A new concept for nanocomposite electrocatalysts: studying the oxygen reduction/evolution reaction and the formic acid oxidation reaction on Pt-based systems

Inaugural dissertation

of the Faculty of Science,

University of Bern

presented by

Jia Du

from China

Supervisor of the doctoral thesis:

Prof. Dr. Matthias Arenz

Department of Chemistry, Biochemistry and Pharmaceutical Sciences

A new concept for nanocomposite electrocatalysts: studying the oxygen reduction/evolution reaction and the formic acid oxidation reaction on Pt-based systems

Inaugural dissertation

of the Faculty of Science,

University of Bern

presented by

Jia Du

from China

Supervisor of the doctoral thesis:

Prof. Dr. Matthias Arenz

Department of Chemistry, Biochemistry and Pharmaceutical Sciences

Accepted by the Faculty of Science.

Bern, 17.06.2022

The Dean

Pof. Dr. Zoltan Balogh

Abstract

Fuel cells are an integral part of the renewable energy concept which involves hydrogen or liquid fuels, e.g., formic acid, as energy carrier. In this thesis, a nanocomposite catalyst concept is developed to prepare fuel cell catalysts. Nanocomposite catalysts are prepared by separately depositing different (two types in this thesis) monometallic nanoparticles onto a support material (carbon black in the thesis). With respect to conventional alloys, the nanocomposites allow to individually control the physical properties of different metal nanoparticles, i.e., particle size, catalyst loading, etc., which benefits from the facile and straightforward preparation method.

The nanocomposite concept is initially introduced to prepare bifunctional Pt-Ir(IrO_2)/C (with various Ir contents) catalysts. $PtIr_y$/C alloy counterparts serve as benchmark. The catalysts are tested in degradation tests, as well as for the oxygen evolution reaction (OER) and the oxygen reduction reaction (ORR). The measurement results show that bifunctional nanocomposite catalysts present both challenges and potentials in comparison with $PtIr_y$/C alloys, in terms of OER and ORR performances. The observed stability improvement for Pt is however at the cost of Ir dissolution, in all the studied bifunctional nanocomposites.

Ir recycling is an important topic associated not only with the use of Ir in fuel cell catalysts to improve the overall catalyst stability. It becomes also essential for the re-use of electrodes from electrolysis cells, which typically contain Ir or IrO_2 at the anode. The observed instability of Ir in the nanocomposite catalysts triggered further investigations towards potential electrochemical Ir recycling schemes. It is shown that by adjusting the applied test protocols a nearly 100% selective Ir dissolution can be achieved. It is further demonstrated that selective Ir dissolution can be achieved in a simple current control setting, which enables simplified electrochemical two electrode setups.

The next part of this thesis extends the nanocomposite concept to prepare potential Pt-based ORR catalysts for proton exchange membrane fuel cells (PEMFCs). Compared with the standard work implemented with rotating disk electrode (RDE), I evaluate the

ORR performance under both low (in RDE) and high (in gas diffusion electrode (GDE) setups) reactant mass transport conditions. The results demonstrate the potential for Pt-Au/C nanocomposites as fuel cell ORR catalyst, as both Pt and Au are stabilized in the nanocomposite and at the same time an improvement of the ORR activity is observed. This is in contrast to Pt-IrO_2/C nanocomposites, displaying only limited performance. Last but not least, by adjusting the added volume of Pt and Au colloidal stock solution, Pt-Au/C nanocomposites with various Au loadings are prepared. The analysis of the formic acid oxidation reaction (FAOR) is combined with detailed characterization by pair distribution function (PDF), scanning transmission electron microscopy-Energy dispersive X-ray spectroscopy (STEM-EDX), *in situ* small-angle X-ray scattering (SAXS), etc., to reveal that nanocomposites mixed with Pt and Au monometallic particles can be used to dynamically prepare *in situ* surface alloys with favorable FAOR performance. These studies are discussed with respect to the conventional preparation of alloy catalysts, highlighting the advantage of the nanocomposite concept to prepare *in situ* surface alloy nanoparticles.

List of publications included in the thesis

*indicates equally contributing first authors.

- Du, J.; Quinson, J.; Zhang, D.; Bizzotto, F.; Zana, A.; Arenz, M. Bifunctional Pt-IrO_2 catalysts for the oxygen evolution and oxygen reduction reactions: alloy nanoparticles versus nanocomposite catalysts. *ACS Catalysis* **2021,** 11 (2), 820-828. https://doi.org/10.1021/acscatal.0c03867.
- Du, J.; Quinson, J.; Zana, A.; Arenz, M. Elucidating Pt-Based nanocomposite catalysts for the oxygen reduction reaction in rotating disk electrode and gas diffusion electrode measurements. *ACS Catalysis* **2021,** 11 (12), 7584-7594. https://doi.org/10.1021/acscatal.1c01496.
- Du, J.; Quinson, J.; Zhang, D.; Wang, B.; Wiberg, G. K. H.; Pittkowski, R. K.; Schröder, J.; Simonsen, S. B.; Kirkensgaard, J. J. K.; Li, Y.; Reichenberger, S.; Barcikowski, S.; Jensen, K. M. Ø.; Arenz, M. Nanocomposite concept for electrochemical *in situ* preparation of Pt-Au alloy nanoparticles for formic acid oxidation. *Submitted to JACS Au (under revision)*
- Nösberger, S.*; Du, J.*; Quinson, J.; Berner, E.; Zana, A.; Wiberg, G. K. H.; Arenz, M. The Gas diffusion electrode setup as a testing platform for evaluating fuel cell catalysts: a comparative RDE-GDE study. *Electrochem. Sci. Adv.* https://doi.org/10.1002/elsa.202100190
- Du, J.*; Zlatar, M.*; Cherevko, S.; Arenz, M. Iridium recycling achieved by the selectively efficient dissolution in the Pt-Ir/C nanocomposites. *In preparation*
- Gridin, V.*; Du, J.*; Arenz, M.; Kramm, U. A comparative GDE-RRDE study of Fe-NC catalyst for the oxygen reduction reaction. *In preparation*

List of publications not included in the thesis

- Alinejad, S.; Inaba, M.; Schröder, J.; Du, J.; Quinson, J.; Zana, A.; Arenz, M. Testing fuel cell catalysts under more realistic reaction conditions: accelerated stress tests in a gas diffusion electrode setup. *J Phys Energy* **2020,** 2 (2). https://doi.org/10.1088/2515-7655/ab67e2.
- Zhang, D.; Du, J.; Quinson, J.; Arenz, M. On the electro-oxidation of small organic molecules: towards a fuel cell catalyst testing platform based on gas diffusion electrode setups. *Journal of Power Sources* **2022,** 522, 230979. https://doi.org/10.1016/j.jpowsour.2022.230979.
- Bagger, A.*; Jensen, K. D.*; Rashedi, M.; Luo, R.; Du, J.; Zhang, D.; Pereira, I. J.; Escudero-Escribano, M.; Arenz, M.; Rossmeisl, J. Fundamental reaction limitations for formic acid oxidation. *Submitted to JACS (under revision)*

List of aberrations

ORR	oxygen reduction reaction
OER	oxygen evolution reaction
FAOR	formic acid oxidation reaction
HOR	hydrogen oxidation reaction
HER	hydrogen evolution reaction
PEMFC	proton exchange membrane fuel cell
PEMFC	polymer electrolyte membrane fuel cell
DFAFC	direct formic acid fuel cell
DMFC	direct methanol fuel cell
URFC	unitized regenerative fuel cell
PEMWE	proton exchange membrane water electrolyzer
AEMFC	anion exchange membrane fuel cell
PGM	platinum group metal
RDE	rotating disk electrode
GDE	gas diffusion electrode
GDL	gas diffusion layer
MEA	membrane electrode assembly
RHE	reversible hydrogen electrode
PTFE	polytetraflfluoroethylene
PEEK	polyetheretherketone
EG	ethylene glycol
GC	glassy carbon
CV	cyclic voltammetry
CA	chronoamperometry
TEM	transmission electron microscopy
IL-TEM	identical location-transmission electron microscopy
TEM-EDX	transmission electron microscopy-energy dispersive X-ray

	spectroscopy
SEM	scanning electron microscopy
SEM-EDX	scanning electron microscopy- energy dispersive X-ray spectroscopy
STEM-EDX	scanning transmission electron microscopy-energy dispersive X-ray spectroscopy
PDF	pair distribution function
SAXS	small-angle X-ray scattering
WAXS	wide-angle X-ray scattering
ICP-MS	inductively coupled plasma-mass spectrometry
XAS	X-ray absorption spectroscopy
ATR-FTIR	attenuated total reflection-Fourier transform infrared spectroscopy
ATR-SEIRAS	attenuated total reflection-surface enhanced infrared absorption spectroscopy
EC-FTIR	electrochemical-Fourier transform infrared spectroscopy
DEMS	differential electrochemical mass spectrometry

Table of Contents

1. Introduction

1.1 Background

1.1.1 Polymer electrolyte membrane fuel cells (PEMFCs)

Due to the increasing depletion of conventional oil-based or gas-based energy sources, fuel cell technologies have been gaining broader interest as clean and efficient energy converters.[1–4] The fuel cell, which was discovered in 1839,[4] is an electrochemical device that can convert the chemical energy of the fed fuel into electricity.[1–4] The fuel is consumed at the anode via electrochemical oxidation, during which the released electrons are externally transferred to the cathode to reduce the oxidant (typically oxygen from air). Both electrodes are separated by an ionic polymer membrane, which serves as electrolyte to conduct protons or hydroxyl ions. The key application of fuel cells is in the transportation sector, however, additional applications including driving portable devices and providing stationary power are reported as well.[2,3,5,6] Fuel cells are mainly classified by their operating temperature and the properties of the applied polymer membrane (electrolyte). Low-temperature fuel cells (80-100°C operating temperature) using polymer electrolyte membranes receive the widest attention due to their conveniency.[4]

Proton exchange membrane fuel cells (PEMFCs) (typically using a Nafion membrane) are the most standard polymer electrolyte membrane fuel cells.[7–9] H_2 fuel is provided and oxidized to protons (hydrogen oxidation reaction, HOR) at the anode, while the O_2 (or air) provided at the cathode is reduced to water (reacting with protons, oxygen reduction reaction, ORR).[7–9] The actual output potential in fuel cells is less than the expected value from thermodynamic considerations due to irreversible losses. These losses include activation loss (in particular in the low current region), ohmic loss (component resistance), and mass transport loss (transport of reactants or/and products).[2]

Despite the fact that PEMFC is a mature technology, the large-scale commercialization

is limited (among other factors) by the supply and the storage of hydrogen fuel.[10,11] Therefore, various types of fuels, e.g., formic acid,[12] methanol,[13] and ethanol,[14] etc., are used to reform hydrogen and thus to overcome the problem of hydrogen supply. Additionally, these liquid fuels can be directly used to power polymer electrolyte membrane fuel cells, i.e., the so-called direct formic acid, methanol, and ethanol fuel cells, etc.[15–21] The amount of required catalyst and the crossover of the supplied fuel (at the anode) to the cathodic side are the most prominent issues for liquid fuel based fuel cells.[3] The liquid fuel can further react with oxygen at the cathode, which leads to a reduced overall efficiency of the fuel cell.[3] Among the liquid fuels, formic acid displays lower toxicity than methanol.[3] Apart from that, formic acid possesses the lowest crossover rate (in comparison to methanol and ethanol) due to the repulsion between formate and sulphonate groups of the Nafion membrane.[3,22] Therefore, direct formic acid fuel cells attract increasing interest as an alternative liquid fuel-based polymer electrolyte membrane fuel cell.

In addition, the proton exchange membrane could be replaced by polymer membranes conducting hydroxyl ions, i.e., anion exchange membrane fuel cells (AEMFCs).[2,3] The overall reaction is the same in basic and acidic media.[3] However, in alkaline media, the crossover rate of liquid fuel is lower than the one under acidic media, as the hydroxyl produced at the cathode, would transfer to the anode side, which is in the opposite movement direction of liquid fuel molecules. Furthermore, alkaline media allows to apply non-noble metal catalysts to proceed a specific reaction, e.g., transition metal catalysts. They are prone to dissolve in acidic media, however, display high dissolution resistance in basic media and can help to reduce the overall price of a fuel cell.[23,24] The dominant issue limiting the development of AEMFCs is the quality of anion membranes, which are unlike proton exchange membranes (e.g. Nafion membranes) not manufactured with mature processes. The ionic conductivity, thermal stability and mechanical stability are mutually restrictive issues that exist in almost all anion exchange membranes. For example, a higher amount of conductive functional groups is needed to guarantee the conductivity of anion exchange membranes, due to the lower

conductivity of hydroxyl ion as compared to protons in the liquid phase.[3] This, however, leads to a poor mechanical stability or/and thermal stability.[3,25,26] To get more information about polymer electrolyte membrane fuel cells, the reader is referred to the following references.[1–6,8,9,11–17,19,21,23,24]

1.2 "State of the art" of the studied reactions

1.2.1 Oxygen reduction reaction (ORR)

1.2.1.1 Fundamentals of the ORR

The ORR is the predominant cathodic reaction in PEMFCs.[1–4] The reaction is presented in formula (1.1), which includes several major steps. A variety of reaction pathways have been proposed in the history of ORR studies. Among which, the oxygen associative and oxygen dissociative pathways are widely accepted[27–30] as shown in the following:

$$O_2 + 4H^+ + 4e^- \rightarrow 2H_2O \quad (1.1)$$

Oxygen associative pathway:

$$O_2(g) + H^+ + e^- \rightarrow HO_2(ads) \quad (1.2)$$

$$HO_2(ads) \leftrightarrow O(ads) + OH(ads) \quad (1.3)$$

$$O(ads) + H^+ + e^- \rightarrow OH(ads) \quad (1.4)$$

$$OH(ads) + H^+ + e^- \rightarrow H_2O(l) \quad (1.5)$$

Oxygen dissociative pathway:

$$O_2(g) \rightarrow 2O(ads) \quad (1.6)$$

$$O(ads) + H^+ + e^- \rightarrow OH(ads) \quad (1.7)$$

$$OH(ads) + H^+ + e^- \rightarrow H_2O(l) \quad (1.8)$$

where (g), (l) and (ads) represent gaseous, liquid and adsorbed phase, respectively. In addition to the two well-accepted pathways, an alternative pathway including H_2O_2 formation is also previously reported. The formed H_2O_2 is however negligible for Pt-based catalysts[31] (small amount of H_2O_2 is generated in the hydrogen underpotential deposition potential region).

According to the oxygen associative pathway,[27,29] i.e., O_2 gets hydrogenated before

dissociation. Nørskov et al. obtained ORR rates of various metals as a function of the calculated OH and O binding energies. The found "volcano" behavior of the ORR activity versus O binding energy is demonstrated in Figure 1.1.

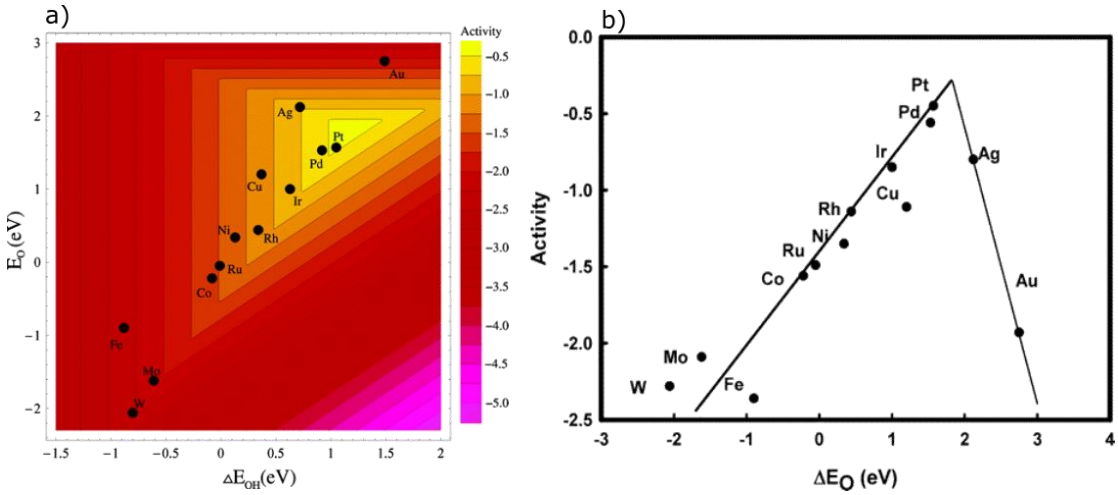

Figure 1.1 Trends in oxygen reduction activity plotted as a function of both the O and the OH binding energy (a) and the "volcano" behavior of oxygen reduction activity plotted as a function of the O binding energy (b). Reprinted with permission from ref. 27. Copyright 2004, American Chemical Society.

One can observe from Figure 1.1a, that the binding energies of O and OH on the various metals are roughly proportionally correlated. In addition, the ORR activity is co-regulated by the binding energy of both O and OH intermediates, which suggests (according to formula (1.2) and (1.5)) that one needs to coordinatively tune the binding strength of the two species on the metal surface to achieve an optimized ORR rate. As seen in Figure 1.1b, the inflection point on the "volcano" plot indicates that the ORR activity from the two sides is determined by different intermediate steps (HO_2 (ads) formation versus OH (ads) reduction). As ΔE_O increases, the formation of HO_2 (ads) gets more difficult (formula (1.2)) and thus the reduction of OH (ads) (formula (1.5)) is easier (the binding energy of the two intermediates are linearly correlated). Therefore, on the right side of the "volcano" plot, the HO_2 (ads) formation step determines the ORR activity, while the OH (ads) reduction step determines the ORR rate on the left side of the "volcano" plot.

1.2.1.2 Electrochemical techniques used to study the ORR

The rotating disk electrode (RDE) method is the most widely applied technique to

evaluate a newly developed catalyst for the ORR. The conveniency of the RDE setup usage and the simplicity of catalyst layer fabrication (on the working electrode) make the RDE technique accessible for most research laboratories. A potentiodynamic protocol, i.e., sweeping the potential with a constant scan rate in a fixed potential region, is well-established and typically used for recording ORR behaviors. The current/potential is then extracted at a given potential/current (after iR, background current and mass transport correction) to elucidate the ORR performance. By applying potentiodynamic protocol, the ORR performance is evaluated under a transient state of the catalyst surface (intrinsic activity),[32,33] and thus deviates from the activity obtained under realistic conditions, which are implemented by using membrane electrode assembly (MEA) setups.[34,35] However, the elaborate infrastructure of (multiple) MEA tests makes it inaccessible for most basic research labs. Therefore, gas diffusion electrodes (GDEs) with various configurations were developed.[36–42] They possess the conveniency of a RDE setup, and allow that ORR measurements are performed under steady state conditions (by applying potentiostatic or galvanostatic protocol) and high reactant mass transport, therefore, bridging the gap between fundamental and practically-related studies and attracting increasing concerns. More detailed information about using the RDE and GDE methods for ORR studies, is given the following chapter.

1.2.1.3 Electrocatalysts for the ORR

As demonstrated in Figure 1.1a, Pt displays the best ORR performance of the different monometals, because the binding energy of hydroxyl and oxygen on the Pt surface exhibits close to optimum values. The low surface-to-volume ratio of single Pt crystals limits their practical applications in fuel cells. However, the results of single Pt crystals offer insight into the influence of Pt structure on the ORR performance. According to previous research using Pt single crystals for ORR studies, the following conclusions could be reached: in aqueous $HClO_4$ electrolyte, the ORR rate follows the sequence of Pt(100) < Pt(111) < Pt(110),[43] in aqueous H_2SO_4 electrolyte , the ORR rate follows a different sequence, i.e., Pt(111) < Pt(100) < Pt(110).[44] Finally, in 0.1 M aqueous KOH

electrolyte , the ORR rate follows the sequence of Pt(100) < Pt(110) < Pt(111).[45] These results indicate that the observed structure-sensitive ORR activity can be predominately ascribed to the specific adsorption of anions ($HClO_4^-$, SO_4^{2-}, HSO_3^- and OH^-, etc.) on the different Pt facets. Therefore, one speaks of spectator species, as they influence the reaction without being a part of it.

To investigate the influence of structure on the ORR further, Pt particles with well-defined structures (shape-controlled Pt particles) were developed. EI-Sayed et al. pioneeringly synthesized Pt cubic particles enclosed by (100) planes.[46] From then on, tremendous work had been reported on the synthesis of shaped Pt particles enclosed with low-index facets.[47,48] Tian et al. synthesized Pt nanocrystals enclosed with high-index facets (730) in 2007,[49] followed by extensive outstanding studies of the synthesis of well-defined particles with high-index facets used for the ORR. However, the biggest issue for shaped particles is their stability, the well-controlled shape is easy to develop into a structure that is thermodynamically stable during the electrochemical measurements.[50]

The effect of Pt particle size on the ORR performance has also been intensively discussed in the literature.[51–60] Shinozaki,[52] Perez-Alonso,[58] Watanabe[60] and Bregoli,[59] etc. reported excellent work and obtained consistent findings: the ORR rate increases with Pt particle size. The proposed properties, i.e., electronic effect,[61] oxide coverage effect,[62] etc. are challenging to unambiguously be distinguished to interpret the particle size effect on the ORR performance. Nevertheless, a basic consensus could be reached: a reduction in particle size leads to an increased number of low coordination sites, i.e., steps, kinks, and edges, which bind oxygen-containing species stronger to maintain stability. Thus more active sites are blocked, and the ORR activity is reduced.[63,64]

In addition to the particle size effect, the interparticle distance (proximity effect) effect on the ORR was being addressed.[57,65–68] Nesselberger et al.[66] reported that the ORR activity improved with a decreased interparticle distance and proposed that the electric double layer structure contributed to the improved performance. A follow-up study investigating Pt high surface area catalysts by Speder et al,[68] demonstrated the same

effect, i.e., a reduced particle distance led to an increase in ORR activity. A recent study carried out by Inaba et al.[57] investigated the particle size and proximity effect on the ORR (demonstrated in Figure 1.2). It was concluded that the particle proximity effect is more notable for small particles and that the reduced oxophilicity and the changed electric double-layer structure with smaller interparticle distance together led to the improvement in ORR activity.

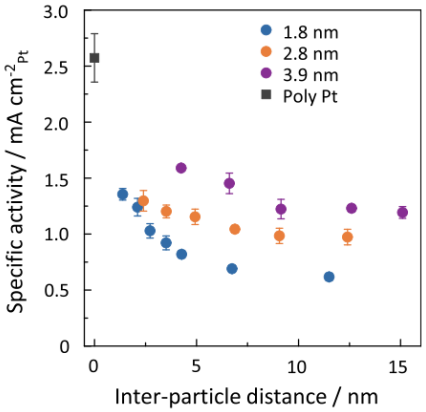

Figure 1.2 ORR specific activity (SA) at 0.9 V_{RHE} of the Pt/Vulcan catalysts with various Pt loadings and Pt nanoparticle sizes determined from the RDE measurements. Reprinted with permission from ref. 57. Copyright 2021, American Chemical Society.

Alloying Pt with other elements to form Pt-based bimetallic materials is a promising strategy to enhance the ORR activity.[69–71] Due to their abundance and low price as compared with Pt, transition metals, e.g., Fe, Co, Ni, and V, etc. are commonly introduced to alloy with Pt. It was seen that the ORR activity could sometimes be significantly improved by applying Pt-transition metal alloys.[70,72] The improved ORR performance is often achieved by modifying the electronic structure (d-band center) of Pt by the introduced elements.[70,72,73] Stamenkovic et al.[70] reported in their study that the optimum ORR performance of Pt-based alloys was dominated by the surface coverage balance of the reactive and blocking species. A "volcano" plot of ORR activity as a function of the d-band center was thereby created and is displayed in Figure 1.3. The Sabatier principle[27,74] could be adopted to rationalize the "volcano" plot, i.e., if the d-band center is close enough to the Fermi level, the overall ORR rate is determined by the OH_{ads} (and specifically adsorbed anions) reduction step. If the d-band center is far

away from the Fermi level, the binding of OH_{ads}, which on the other hand is also a reactive ORR intermediate, is too weak, and thus reduces the ORR activity. Examples of this effect are Pt_3Ti and Pt_3V as shown in Figure 1.3.

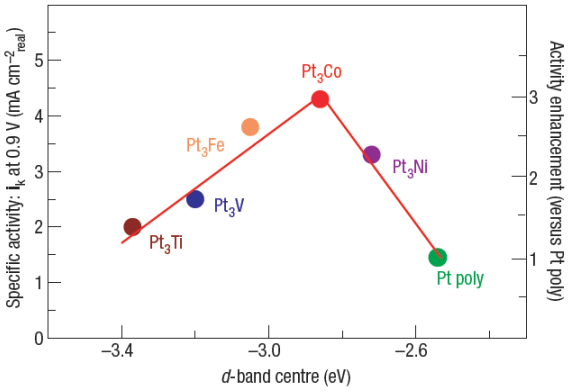

Figure 1.3 Relationships between the catalytic properties and electronic structure of Pt_3M alloys. Reprinted with permission from ref. 70. Copyright 2007, Nature.

In commercial applications, the stability and activity of an ORR catalyst are equally crucial. Transition metals are however prone to be dissolved in acidic media, which results in a poor stability of transition metal-based Pt alloys when tested under acidic conditions. Even though the price of Au is higher than the ones of transition metals, its high acid resistance[75,76] and the fact that it is a non-critical raw material[77] make Au a unique choice for Pt-Au bimetallic systems. Adzic et al.[78] in their pioneering work reported increased durability of Pt modified by Au, and that the ORR activity could concurrently be retained. In the following studies, Wei[79] and Kodama et al.[80] adopted the "edge protection" concept to selectively deposit Au atoms onto low-coordinated Pt sites. The experimental results demonstrated that both the stability and ORR activity were enhanced. The Pt-Au bimetallic structures are not limited to alloys, but there are also other structures reported, e.g., Pt-Au core-shell particles,[81,82] Au-framed Pt particles,[79] Pt deposited onto an Au substrate,[83] etc. The engineering of PtAu structures and the corresponding effect (including strain, ligand, ensemble effects, etc.) leading to a more efficient ORR are demonstrated in Figure 1.4.[84] The ligand and strain effect normally co-exist in Pt-Au core-shell particles, and the shell thickness determines which effect is more dominant. In addition, Pt-Au alloys and core-shell structures, depending on the testing conditions, are dynamically transformed.[84] Nevertheless, even

if the ORR activity and stability can be improved by introducing Au to Pt systems, the overall Au usage should be limited to reduce economic concerns.

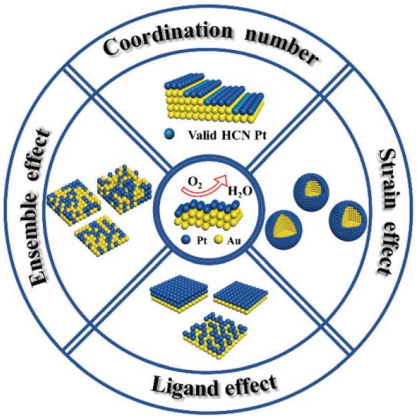

Figure 1.4 Engineering the structure of PtAu electrocatalysts for efficient ORR. Reproduced from ref. 84. Copyright 2020, Royal Society of Chemistry.

Developing non-noble metal catalysts used for ORR study is highly desired since the overall price of fuel cells could be largely reduced.[85] Among different non-noble metal catalysts, a transition metal atom doped with nitrogen and further distributed onto carbon (single atom/site catalysts, expressed as M-N-C) is one of the most promising materials to replace Pt-based catalysts. Fe-N-C is the most widely tested M-N-C material and indeed demonstrates decent ORR performance as compared to commercial Pt catalysts.[86–89] Recently, several studies reported that M-N-C type catalysts not only exhibited satisfactory ORR activity, but their stability was also much improved.[90,91] Therefore, for the commercialization of single-atom catalysts, it is imperative to achieve large-scale production.

1.2.2 Formic acid oxidation reaction (FAOR)

1.2.2.1 Fundamentals of the FAOR

At the anode of DFAFCs[92,93] the oxidation of formic acid takes place. The reaction is described as follows:

$$HCOOH \rightarrow CO_2 + 2H^+ + 2e^- \qquad (1.9)$$

HCOOH is a simpler organic molecule in comparison to CH_3OH, C_2H_5OH, etc., and therefore typically used as a model to investigate the mechanisms and reaction pathways of the electrooxidation of small organic molecules. Even so, there are complicated mechanisms and various reaction pathways involving controversial intermediates, i.e., it is ambiguous to determine if an intermediate is reactive or poisons/inhibits the overall reaction. The proposed mechanisms and possible pathways of the FAOR are summarized in Figure 1.5.[93] Among various reaction pathways of the FAOR, the dual pathway, firstly proposed by Parsons et al.[94,95], has been mostly accepted by researchers. In this reaction scheme, the direct and indirect electrooxidation of FA are described by the formulae (1.10) and (1.11) to (1.12), respectively.

Direct FAO pathway:

$$HCOOH \rightarrow reactive\ intermediates \rightarrow CO_2 + 2H^+ + 2e^- \qquad (1.10)$$

Indirect FAO pathway:

$$HCOOH \rightarrow CO_{ads} + H_2O \qquad (1.11)$$

$$CO_{ads} + OH_{ads} \rightarrow CO_2 + 2H^+ + 2e^- \qquad (1.12)$$

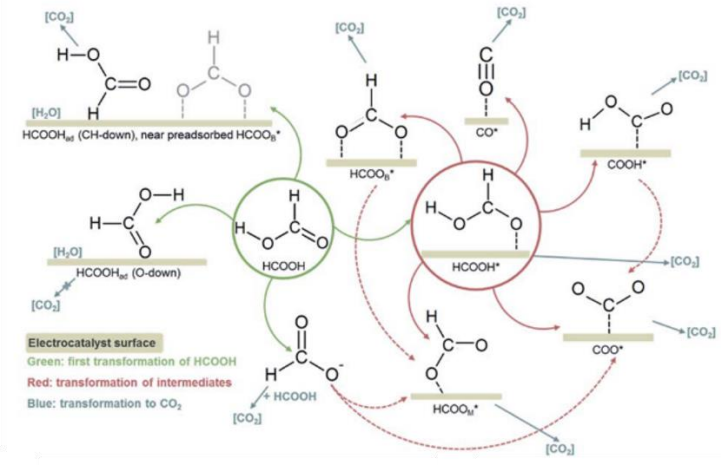

Figure 1.5 The proposed mechanisms of HCOOH electro-oxidation (green: first transformation of HCOOH, red: transformation of inter- mediates, blue: transformation to CO_2). Reproduced from ref. 94 with permission from the Royal Society of Chemistry.

It is well-accepted that adsorbed CO (CO_{ads}) is predominantly a poisoning species for the FAOR.[92,96] Therefore, inhibiting or eliminating the indirect FAOR pathway would

be beneficial for a catalyst. Carboxyl and formate (bridge-bonded, as indicated as $HCOO_B^*$ in Figure 1.5) were previously regarded as precursors to form CO.[97–99] By comparison, the active intermediates in the FAOR are various, e.g., CHO, COOH, HCOO, etc. Among these, formate (HCOO) with a variety of binding forms to the catalyst surface has been intensively discussed in the literature. Vilaplana et al.[99] combined computational and experimental studies and proposed that $HCOO_M^*$ is a reactive intermediate for the FAOR, which was consistent with the conclusion obtained by Zhu et al.[100] By contrast, formate with both atomic oxygens bonded to the catalyst surface ($HCOO_B^*$), was assigned as a poisoning species by Chen et al.[101] with the help of attenuated total reflection-Fourier transform infrared spectroscopy. Wang et al.[102] proposed that $HCOO_B^*$ serves as a catalytic species in the FAOR, as FA would be easier oxidized to CO_2 in the presence of adjacent $HCOO_B^*$.

1.2.2.2 Techniques used to study the FAOR

As for the ORR, the RDE is the most widely used methodology for fundamental studies of the electrooxidation of FA. Only very recently, a GDE setup, which was originally designed to mimic operating conditions of fuel cells and applied for the ORR studies, was adopted to investigate the FAOR by Zhang et al.[103] The study demonstrated that the GDE setup is suitable to study the electrooxidation performance of volatile organic molecules as well. In all reports related to the FAOR, fundamental approaches, e.g., cyclic voltammetry (CV),[104] chronoamperometry (CA)[105] and Tafel plots,[106] etc., are powerful tools to analyze the FAOR. CV provides the basic information of the FAOR in a fast manner and thus is widely used.[104] In Figure 1.6a, the Pt/C model catalyst is taken as an example to elucidate the FAO process under transient state. As seen from the anodic scan, a peak shows up at ~0.57 V_{RHE} corresponding to the electrooxidation of FA to CO_2 through a direct pathway. The indirect FAO pathway proceeds in parallel to form intermediates, e.g. CO, etc., and thus a second peak is observed (~0.92 V_{RHE}) which is ascribed to the electrooxidation of the formed intermediates (CO, etc.). In the cathodic scan, the FAO proceeds on a “clean” catalyst surface and a much higher “intrinsic” activity thereby appears.[106] It is therefore deduced that the smaller the

hysteresis of the peak currents from both scans (the anodic scan is linked to the direct pathway peak current, at ~0.57 V_{RHE}), the lower the degree of poisoning of the catalyst surface.[100] In addition, the relative peak intensities (at ~0.57 V_{RHE} and ~0.92 V_{RHE}, respectively) from the anodic scan indicate which pathway is preferred in the FAOR. That is, when the peak at higher potentials completely disappears, this indicates that the FAOR proceeds completely via the direct pathway. However, in a real FA-based fuel cell, a potentiostatic mode i.e., applying a constant potential, is typically used[21] as depicted in Figure 1.6b.[105] Therefore chronoamperometry reflects more realistically the long-term performance of a FAOR catalyst. An initial high activity can gradually decrease with time as observed in Figure 1.6b. It is hence insufficient to evaluate the performance of a catalyst by only with CV. In addition to the methodology, one can apply different data analyses. In dynamic measurements, Tafel plots (Figure 1.6c) are typically used to analyze the reaction rate in the electrocatalytic process. A lower Tafel slope thereby indicates a faster rate of charge transfer.[93] Furthermore, methods like CO stripping can be helpful to analyze the potential causes for an improved FAOR activity. For example, if the CO oxidation peak of a studied Pt-based catalyst is shifted to more negative potentials as compared to the one from pure Pt/C, this indicates that any CO formed during the FOAR is more facile removed on the Pt-based catalyst surface, which benefits the FAOR performance with respect to the indirect pathway.[107,108]

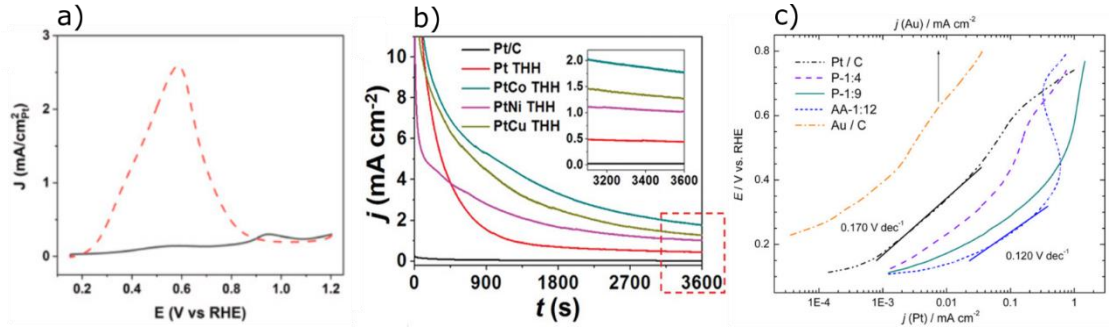

Figure 1.6 CVs of formic acid oxidation with Pt/C recorded in a RDE setup filled up with 1.0 M $HClO_4$ + 0.5 M formic acid. Reproduced from ref. 104 with permission from Elsevier (a), Chronoamperometry curves of formic acid electrooxidation for the different catalysts at 0.5 V in 0.5 M HCOOH + 0.5 M H_2SO_4. Reproduced from ref. 106. Copyright 2020, Wiley (b) and Tafel plots recorded under the quasi steady-state conditions in 0.5 M H_2SO_4 + 0.5 M HCOOH electrolyte tested on Au/C, Pt/C, P-1:4, P-1:9, and AA-1:12 at the scan rate of 1 mV s^{-1}. Reproduced from ref. 107. Copyright 2012, Elsevier (c).

The potential FAOR intermediates have been displayed in Figure 1.5. Their unambiguous identification via pure electrochemical methods however is difficult. Therefore, it is imperative to combine electrochemistry with other techniques for an *in situ* identification of the formed intermediates. Examples for successful combinations are, e.g., *in situ* attenuated total reflection-Fourier transform infrared spectroscopy (ATR-FTIR),[101,109] *in situ* attenuated total reflection-surface enhanced infrared absorption spectroscopy (ATR-SEIRAS),[110] *in situ* electrochemical-Fourier transform infrared spectroscopy (EC-FTIR)[111,112] and *in situ* differential electrochemical mass spectrometry (DEMS),[113,114] which have been proven to be helpful for the *in situ* characterization of FAOR intermediates.

1.2.2.3 Electrocatalysts for the FAOR

Monometallic Pt and Pd based catalysts are both model catalysts for the FAOR.[92] However, they each encounter specific challenges, i.e., Pt is prone to be inhibited by CO intermediates lowering the overall conversion efficiency of the FAOR.[93,94,107] Pd displays higher resistance towards poisoning intermediates, however, its stability, in particular in acidic media, is limited.[92] As the FAOR was studied on Pt-based materials in this thesis, in the following sections mainly Pt-based electrocatalysts are discussed. For Pd-based catalysts, the interested reader is referred to ref.[92]

Studying single Pt crystals in 0.5 M H_2SO_4 + 0.005 M HCOOH, Sun et al.[115] concluded that the maximum dehydrogenation current of the FAOR (anodic scan) follows the trend: Pt (100) < Pt(111) < Pt(110). However, comparing the dehydrogenation current is not the only metric to evaluate a FAOR catalyst. The overpotential and current hysteresis of both scans are equally important parameters. The peak position of the FAOR in the anodic scan follows the order Pt(110) < Pt(111) < Pt(100), while considering the current hysteresis of both scans (serves as an indicator for the poisoning resistance of a catalyst), the order Pt(111) < Pt(110) < Pt(100) is observed. Both obtained trends are extracted from a study of Bagger et al.[116]

As described, the monometallic single crystals are regarded as model systems. Depositing Pt particles onto carbon supports largely improves the utilization of Pt.[117–

[119] The carbon black Vulcan XC-72 is one of the most common carbon supports to immobilize Pt particles. For example, Pt/C catalysts with a Pt loading of 20 % in weight onto carbon black have been intensively studied as FAOR catalysts by several researchers.[117,118] In addition to carbon black supports, alternative supports such as TiO_2 nanotubes etc., have been employed to support metal nanoparticles as well. For example, Pisarek et al.,[120] prepared Pt/TiO_2 and Pd/TiO_2 with the help of a magnetron sputtering technique and tested them for the FAOR. The results showed a higher FAO current for Pd/TiO_2 (per mg of metal) as compared to the Pt/TiO_2 and Pd/Vulcan counterparts.

To reduce the platinum usage and to increase the FAO activity simultaneously, Liang et al.[121] reported that by depositing a monolayer of Pt or Pd onto a metal substrate (Ir, Au, Rh, Ru, Pt and Pd), interesting bimetallic catalysts were obtained. Among the various bimetallic catalysts tested, Pt/Au(111) (a Au(111) substrate decorated with a Pt monolayer) showed the highest FAO activity. Combined with *in situ* infrared refection adsorption spectroscopy and DFT calculations it was shown that the formed CO is easily oxidized by OH, generated from a facilitated water decomposition step.

A common strategy to enhance the FAO activity of Pt-based catalysts is introducing a second element to form bimetallic Pt alloys. Examples for Pt-based alloys include PtAu,[122–124] PtAg,[125,126] PtPd,[120,127] PtBi[128], and PtRu,[129–131] among which, PtBi and PtRu probably have been most extensively studied. Both Bi and Ru are reported to facilitate the removal of CO intermediates due to enhanced adsorption of OH with respect to Pt.[128,131] For instance, Wang et al.[128] reported that PtBi/C alloys displayed comparable peak current in both scan directions as demonstrated in Figure 1.7a. The anodic peak current displays a 10-fold enhancement as compared to Pt/C, which was interpreted as a sign of high resistance towards CO poisoning species. Kormányos et al.[129] recently studied PtRu alloys for the electrooxidation of multiple liquid fuels (isopropanol, methanol, ethanol and formic acid). With similar current densities in anodic and cathodic directions, the electrocatalytic performance of formic acid (Figure 1.7b) was regarded improved as compared to the fuels studied. Despite the optimization of the FAOR performance by Pt-based bimetallic alloys, it is still challenging to assign

the performance improvement to a specific effect, i.e., ligand effect, strain effect, ensemble effect and synergistic effect. Typically, these effects are correlated,[93] similar to the performance increase of ORR catalysts discussed in the previous section.

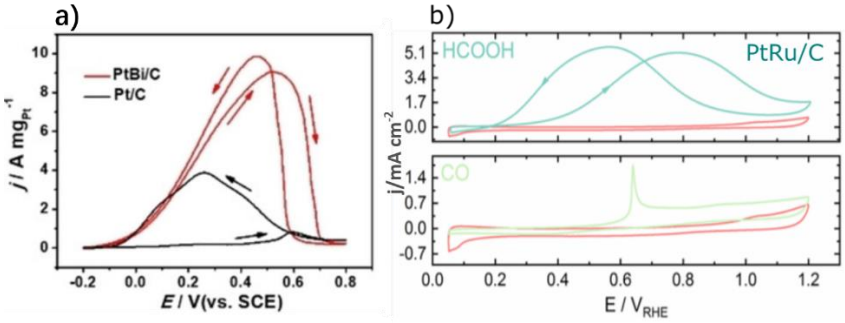

Figure 1.7 CVs of formic acid oxidation on PtBi/C in 0.1 M $HClO_4$+0.25 M HCOOH solution. Reproduced from ref. 129. Copyright 2020, Wiley (a). CVs recorded for PtRu/C in 0.1 M $HClO_4$ solution in presence of HCOOH (top), the red curves for the blanks are recorded in 0.1 M $HClO_4$. Reprinted with permission from ref. 130. Copyright 2020. (b).

Several researchers have investigated Pt-Au systems for the FAOR. In addition to the conventional Pt-Au structures that exhibit impressive FAO performance,[122–124,132–138] recently Xie et al.[139] synthesized AuCuPt alloys followed by selectively de-alloying Cu. In CV tests, the FAO exhibited no CO passivation characteristic, which would be a groundbreaking improvement for Pt-based FAOR catalysts. Duchesne et al.[140] reported a facile colloidal approach to prepare a series of different Pt_xAu_y particles, i.e., Pt_4Au_{96}, Pt_7Au_{93}, $Pt_{17}Au_{83}$ and $Pt_{78}Au_{22}$ (Au-Pt/core-shell structure). The experimental results demonstrated that Pt_xAu_y particles decorated with Pt single atoms at the surface (Pt_4Au_{96} and Pt_7Au_{93}) exhibit an extraordinary FAO performance, which was ascribed to both electronic and ensemble effects to mitigate CO adsorption on the Pt surface.

Despite their promising catalytic activity towards FAO, the low abundance and high price of Pt and Pd limit potential large-scale commercialization. Therefore, similar to ORR catalysts, developing Pt- and Pd-free FAOR catalysts is highly desirable. Alternatively, one can also try to maximize dispersion. Several studies have claimed that reducing the size of metal particles can lead to extraordinary electrocatalytic performance.[137,141] Li's research group recently reported that single-atom catalysts of Rh and Ir exhibiting impressive FAOR performance.[142,143] Their results showed mass

activities of Rh-single-atom catalyst improved by 67 and 28 times as compared to the "state of the art" Pt/C and Pd/C catalysts, respectively. Also, Ir-single-atom catalyst showed improved FAOR performance, i.e., an improvement of 19 and 16 times, respectively. Interestingly, nanoparticle-based Ru/C and Ir/C counterparts are almost inert to the FAOR.[142,143] It is important to point out that there are still only few studies of single-atom catalysts, leaving space for researchers to explore their catalytic performance towards the FAOR.

2. Experimental methodology

In this chapter, the main experimental methods applied in this thesis are discussed. The focus is on rather specific methods, while some standard techniques applied in this thesis are not discussed, because they are typically described in standard textbooks. The chapter starts with the description of the preparation of metal particles and their immobilization on support materials. It follows a section about the main physical characterization techniques of the prepared catalysts. Finally, the electrochemical characterization techniques are discussed.

2.1 Synthesis of monometallic and nanocomposite catalysts

In this thesis the preparation of Pt and Ir nanoparticles was achieved via a surfactant free, ethylene glycol (EG) route, which was performed by myself. For the synthesis of the colloidal Au nanoparticles, organic- and laser-assisted method were applied. These syntheses were performed by collaboration partners. In the EG route, it is necessary to flocculate and re-disperse the colloidal nanoparticles to replace the high boiling point solvent EG with acetone before immobilizing the nanoparticles onto the carbon support.

2.1.1 Synthesis of Pt, Ir nanoparticles by surfactant-free EG approach

The surfactant-free EG approach to produce Pt nanoparticles was firstly reported by Wang et al.[144] In their studies, an oil bath setup was applied to provide the thermal energy to the reaction system. In this thesis, an optimized approach was used employing a microwave reactor which drastically reduces the reaction time.[145] Briefly, the solution of Pt precursor ($H_2PtCl_6 \cdot 6H_2O$ is dissolved in EG) is mixed with NaOH EG solution. The mixture is contained in a microwave reactor and heated up to 160 °C for 3 minutes to obtain the Pt particles. The same method was adopted to prepare Ir or Pt_xIr_y alloy nanoparticles. For this, the $H_2PtCl_6 \cdot 6H_2O$ is simply replaced by $IrCl_3 \cdot xH_2O$ to form Ir nanoparticles or $H_2PtCl_6 \cdot 6H_2O$ and $IrCl_3 \cdot xH_2O$ are added to the reaction vessel simultaneously to form Pt_xIr_y alloy nanoparticles. The size of the Pt nanoparticles can

be adjusted by varying the molar ratio between NaOH and $H_2PtCl_6 \cdot 6H_2O$.[145] Herein, only a fixed molar ratio of 10:1 (OH to Pt) was used leading to Pt nanoparticles of 1.7-2.0 nm in diameter. For the preparation of the colloidal Ir nanoparticles, the same molar ratio between NaOH and $IrCl_3 \cdot xH_2O$ precursor was applied leading to Ir nanoparticles of 1.2-1.5 nm in diameter. Unlike in conventional syntheses using surfactants like PVP, [146,147] in the EG mediated synthesis, the oxidation products of EG, e.g., CO and carboxylic acid, adsorb on the surface of the nanoparticles and stabilize them.[148,149] These species can be easily removed by electrochemical oxidation,150 leading to the terminology "surfactant-free".

2.1.2 Synthesis of colloidal Au nanoparticles

The synthesis of the Au nanoparticles included organic- and laser-assisted methods. As mentioned, I did not perform the synthesis myself. Instead, I used the as synthesized Au nanoparticles for further preparation of the Pt-based catalysts. In the organic-assisted route, oleylamine is used as surfactant to prevent Au nanoparticles (dispersed in hexane) from aggregation.[150] The detailed synthesis method can be found in the appended manuscript. The surfactant oleylamine typically inhibits catalytic reactions and it is therefore necessary to remove it prior to electrochemical applications. In this thesis a thermal treatment was applied, where the carbon supported Au nanoparticles were placed in an oven and exposed to 210 °C for 5 hours to remove the oleylamine. As such procedure undoubtedly renders the overall catalyst preparation more complex and potentially damages the carbon support in later studies, surfactant-free Au nanoparticles (dispersed in water) were thereby used. These nanoparticles were prepared by a laser ablation method. The specific laser-assisted method is described in refs.[151,152]

2.1.3 Deposition of metal nanoparticles onto the carbon support

To deposit the colloidal Pt and Ir nanoparticles suspended in EG, they are firstly flocculated with 1 M HCl and thereafter centrifuged with 5000 rpm to separate the

supernatant and the flocculate of metal nanoparticles. Then the nanoparticles are re-dispersed into acetone. In contrast to EG, the nanoparticles slowly agglomerate in acetone and thus need to be swiftly processed further. For this the carbon support (Vulcan XC72R, throughout this thesis) is dispersed in acetone and homogenized by a horn sonicator for 5 minutes. Then the Pt acetone suspension is added to the carbon acetone suspension under intense sonication. The mixture is sonicated for 10 minutes and thereafter dried with the help of a rotary evaporator to obtain the supported Pt/C catalyst.

The procedure was adopted to prepare Pt-Ir/C and Pt-Au/C nanocomposites. When Pt and Ir nanoparticles serve as building blocks, during the deposition step, Pt and Ir nanoparticle suspensions (in acetone) were added in defined mass ratio to the carbon acetone suspension as simultaneously as possible. After vigorous sonication of the mixture, the rotary evaporation of acetone was applied in the same fashion as for the monometallic catalysts, leading to Pt-Ir/C nanocomposites with individual nanoparticles and specific mass ratios. Similarly, Pt-Au/C nanocomposites with various Au contents (the Pt content was kept constant) were prepared with the surfactant-free Pt and Au nanoparticles as building blocks. The only difference as compared to the Pt-Ir/C preparation was the dispersion step, where vigorous stirring in a beaker was applied instead of sonication was applied. Sonication and stirring are equally efficient to form separate and homogeneous dispersions of metal nanoparticles on the carbon support. However, the low concentration of the Au nanoparticle suspension made the magnetic stirring a better option in the dispersion step. The mixture was left in the hood overnight for solvent removal (the rotary evaporator is less efficient for water removal) to obtain the Pt-Au/C nanocomposites.

The oleylamine-protected Au nanoparticles that were initially used to prepare Pt-Au/C nanocomposite required a different procedure. In this preparation, two steps were employed to support the metal nanoparticles on the carbon. First, the Au nanoparticles were supported with the same procedure as described above. Then the supported Au/C was exposed to a thermal treatment at 210 °C for 5 hours to remove the oleylamine on

the Au surface. Afterwards, the surfactant-free Au/C was dispersed in acetone (oleylamine-protected Au/C is not dispersible in acetone). To complete the Pt-Au/C preparation, i.e., to support Pt nanoparticles onto Au/C, the same procedure as depositing Pt nanoparticles onto a bare carbon support was applied. Separate supporting steps avoid an oxidation of Pt during the thermal treatment, which might trigger substantial Pt dissolution under reductive conditions.

2.2 Physical characterization of the catalysts

Prior to their electrochemical characterization, the physical properties of the as prepared catalysts were determined. For example, the particle size and size distribution were determined and the compositions of the bimetallic catalysts was measured as these properties influence the electrochemical behavior of the catalysts.

2.2.1 Determination of the absolute and relative catalyst compositions

Normalized reaction rates are required for a fair evaluation of a catalyst performance in electrocatalytic reactions. Generally, the normalization is achieved based on the mass of the active phase (metal nanoparticles) or their electrochemically accessible surface area. For both normalizations, the mass of the active phase is required and it is therefore crucial to determine the absolute content of the active phase in a supported catalyst.

2.2.1.1 Inductively coupled plasma-mass spectrometry (ICP-MS)

In this thesis, Pt served as the active phase for the ORR and FAOR studies. For its determination Pt can be digested in aqua regia (a mixture of HCl and HNO_3 with a volume ratio of 3:1) followed by ICP-MS measurements.[153,154] For this, the as-prepared Pt-based catalyst powder was placed in a known amount in a glass tube, followed by heating the glass tube with a Bunsen burner to oxidize and thus remove the carbon support, which could block the cone of the ICP-MS equipment. Afterwards, 5 mL of aqua regia was added to the glass tube to digest the residues (Pt nanoparticles) under stirring. This step lasted for 3 hours and was followed by adding milli-Q water into the

glass tube to dilute the solution to a suitable concentration (20-50 ppb) for the ICP-MS analysis. The same method is applicable to determine the absolute Au content in the catalyst. By contrast, it is more difficult to determine the Ir content as metallic Ir once it is oxidized to Ir oxide will be less likely dissolved in aqua regia.[155] Therefore, the heating step to remove the carbon support should be avoided for Ir-based catalysts (metallic Ir will be thermally oxidized). Instead, the colloidal Ir nanoparticles dispersed in acetone, which were used in the supported step were digested in aqua regia and further processed in ICP-MS measurements to indirectly determine the Ir content in the Ir-based supported catalysts. As one might imagine, Ir can be oxidized during these steps when exposed to air and therefore this method is considered rather an estimation than an accurate determination of the Ir content in a catalyst. Concerning the determination of the metal loading (only works for Pt and Au) in the catalyst layers prepared for the GDE measurements (will be discussed in the following section), the same method is adopted. That is, a piece of catalyst layer (3 mm in diameter) was punched from the pre-prepared larger catalyst layer and immersed into aqua regia overnight. Thereafter, the diluted solution was analyzed with ICP-MS. Note that a pipette tip (or something similar) should be used to press the catalyst layer into the aqua regia to avoid the light catalyst layer floating on top of the liquid.

2.2.1.2 Transmission electron microscopy/Scanning electron microscopy-energy dispersive X-ray spectroscopy (TEM/SEM-EDX)

The relative composition of a bimetallic catalyst is equally important to be determined, as the content of the introduced second phase plays a crucial role in affecting the property of the active phase. ICP-MS is undoubtedly a useful tool to determine the relative composition. Besides that, TEM and SEM equipped with an EDX detector can also provide such information. TEM-EDX concentrates more on the analysis of the as-prepared catalysts, since the sample is prepared by dropping the catalyst ink on the copper grid for TEM imaging. By comparison, SEM-EDX allows to analyze both the as-prepared and the as-measured samples, as the sample holder is suitable for both catalyst powder and catalyst layers (for GDE measurements). Therefore, by analyzing

the relative composition of the bimetallic catalysts via ICP-MS (analysis of the whole sample), TEM-EDX (electron beam travels through the copper grid and thus the whole sample is analyzed),[156] and SEM-EDX (electron beams scans the surface and thus the sample surface is analyzed),[157] one can compare the obtained results from each individual technique, and concurrently evaluate the feasibility of applying such technique.

For the determination of the catalyst compositions, I prepared the samples for the ICP-MS, TEM-EDX and SEM-EDX analyses. The measurements were however carried out by my colleagues. Standard TEM as well as IL-TEM measurements, I conducted myself.

2.2.2 Characterization of particle sizes and size distributions of the studied catalysts

2.2.2.1 Transmission electron microscopy (TEM)

One of the conventional methods to determine the particle size of a catalyst is TEM.[158] For a TEM analysis, a small bit of the as-prepared catalyst powder or the catalyst scraped from the GDL (after vacuum filtration) was dispersed into ethanol. After a homogeneous dispersion was observed with the aid of sonication, a drop of the catalyst dispersion was pipetted onto a copper TEM grid. The TEM imaging can be conducted after the copper grid was dried in ambient environment. The acquired TEM micrographs do not only provide the information of the particle size, but also the number-weighted particle size distribution can be obtained by counting the size of hundreds of metal nanoparticles and constructing a size histogram. However, subjective factors can easily be introduced, especially to the analysis of the number-weighted particle size distribution. The micrographs are a two dimensional display of a three dimensional object. Particles in close vicinity in the micrographs can be located at different sides of the carbon particles and thus be mistaken as agglomerates. Furthermore, particles with a common shape (e.g., spheres) might be more likely to be counted, etc.

2.2.2.2 Identical location-transmission electron microscopy (IL-TEM)

As compared to the conventional TEM method, IL-TEM provides the possibility to detect exactly the same spot of a catalyst before and after an electrochemical treatment. Therefore, it is a well-known technique used in degradation studies to monitor particle migration, dissolution and detachment as degradation mechanisms.[159,160] To carry out IL-TEM, a drop of catalyst ink was deposited onto a gold finder TEM grid, which served as working electrode in the electrochemical treatment. The electrochemical treatment can be performed in a GDE setup (which will be discussed in detail in the following section), as the size of the gold grid exactly fits the working electrode used for GDE measurements. After the electrochemical treatment, the gold grid was transferred back to the TEM to track the potential change of the nanoparticles after exposing them to the electrochemical treatment.

2.2.2.3 Small-angle X-ray scattering (SAXS)

TEM, however, is a local technique, which only displays partial information of the studied catalyst. By comparison, SAXS possesses the merit to analyze the particle size distribution in a macroscopic part of the catalyst.[161] By comparing the average particle size obtained from the TEM and SAXS analysis, it was seen that for populations with small particle size (below 3 nm), the two techniques led to comparable results. However, as a tendency the average particle size determined from the SAXS measurements was a bit larger than the one obtained from a TEM analysis. For particle sizes larger than 3 nm, a larger offset was seen between the two techniques.[42,103] There are three possible causes leading to the observed deviation: Firstly, subjective factors could be introduced for the statistical TEM determination of the average particle size, as discussed in the last section. Secondly, for the TEM analysis, only selected parts of the micrographs can be analyzed, which are then deemed representative for the whole catalyst. By comparison, SAXS measurements probe a macroscopic volume fraction of the catalyst. Additionally, the scattering process is proportional to the sixth power of the particle radius and thus larger particles provide largely enhanced scattering. Last but not least, probability densities determined from SAXS are often plotted volume-weighted, however, the TEM size histogram is number-weighted. Both distributions can be easily

converted into each other. For example, a volume-weighted distribution from a size histogram is obtained by calculating the volume of each individual particle assuming a sphere. The better match in size distribution, especially for populations of large particles after conversion validates the combination of TEM and SAXS for the analysis of the particle size distribution. It is recommended whenever possible to use both techniques to characterize a newly prepared catalyst.

Some factors must be kept in mind for the SAXS fitting, which was done by a collaborator. A suitable background subtraction is key for a good result. If the background signal of the carbon is not subtracted, it will undoubtedly contribute to the size distribution. It is thereby best that the blank sample for the background determination is exposed to the same treatment as the supported catalyst. In addition, for the samples with two different elements, the scattering cross section of each element should be taken into account, which will influence the way the final probability density is displayed.

2.3 Rotating disk electrode (RDE) methodology

The original idea for RDE measurements is to use a planar disk electrode embedded into an insulator, which can rotate during the electrochemical measurements.[162] RDE is popular in ORR studies, as the rotating disk allows to increase and control the rate of dissolved reactant (e.g., O_2) reaching working electrode surface. RDE thereby overcomes the limitation of pure reactant diffusion. A constant and controlled mass transport to the working electrode allows a post-extraction of the pure kinetic reaction parameters.

The polarization curve obtained from RDE measurement can be separated into three potential regions: the pure kinetic-controlled potential region, the pure mass transport-controlled potential region and the mixed-controlled potential region. The current in the pure mass transport-controlled potential region is defined by the Levich equation:[163]

$$i_{dl} = 0.62nFAD_O{}^{2/3}w^{1/2}v^{-1/6}C_O{}^{*} \qquad (2.1)$$

where i_{dl} is the diffusion-limited current, n is the number of electrons, F is the faraday constant, A is the geometric area of the working electrode, D_O is the diffusion coefficient of reactant, w is the rotation speed, v is the kinematic viscosity of electrolyte, and $C_O{}^*$ is the concentration of reactant in the bulk electrolyte.

The kinetic current can be obtained from Koutecky-Levich equation[164] defined as following:

$$\frac{1}{i} = \frac{1}{i_{dl}} + \frac{1}{i_k} \qquad (2.2)$$

where i is the measured current, i_{dl} is the diffusion-limited current, and i_k is the kinetic current. The kinetic current can be determined by correcting the measured current by the diffusion-limited current, which is determined in the mass transport-controlled potential region under defined rotating speed. However, the described method to obtain the kinetic current is only valid in a narrow potential window, i.e., a potential window in which the diffusion-limited current is less than two times higher than the measured current. Otherwise, a substantial error can be introduced due to unstable convection.[165] Re-arranging the Koutecky-Levich equation (2.2) by replacing $i_{dl}$with equation (2.1), the kinetic current can alternatively be obtained by plotting $\frac{1}{i}$ as a function of $\frac{1}{w^{1/2}}$. A linear correlation of the two factors is discernable, and the kinetic current can be extrapolated at an infinite rotation speed, i.e., $w^{-1/2}$ approaching 0, and thus $\frac{1}{i}$ is equal to $\frac{1}{i_k}$. This method allows to analyze reaction kinetics in a wider potential region, e.g., the analysis of the ORR activity in the oxygen transport-controlled potential region.[166]

The RDE methodology is has been adapted to investigate high surface area catalysts by Schmidt et al.[167] The measurements are implemented by dropping a specific amount of catalyst ink onto a glassy carbon (GC) disk, and the dried catalyst thin film on the GC disk is further used in the electrochemical measurements. The method gained high popularity for ORR studies and is intensively applied to elucidate fuel cell catalysts in research laboratories.

2.3.1 Catalyst thin film fabrication on the GC disk

The quality of the catalyst film fabricated on the GC disk has a crucial impact on the determined "intrinsic" activity of a catalyst, e.g., the ORR activity. To obtain a homogeneous catalyst thin film on the GC disk, a finely dispersed and stable catalyst ink needs to be achieved. In this thesis, all catalyst inks prepared for RDE measurements followed a recipe developed by former colleagues.[168] A mixture of isopropanol and Milli-Q water with 1:3 in volume ratio served as dispersing agent. After the catalyst powder was dispersed, 1 M KOH solution (containing 1.6 µL/ml 1 M KOH solution) was added to improve the dispersion and the stability of the catalyst ink. Afterwards, the catalyst ink was further sonicated for ~5 minutes, before fabricating the catalyst thin film on the GC disk. Note that a 1 M KOH solution, instead of Nafion ionomer was added to form the catalyst ink, to avoid the inhibiting effect of Nafion ionomer. The sulfonate anion, which partially comprises the Nafion ionomer, specifically adsorbs on the Pt-based catalyst surface[169,170] thus blocking active sites, which can lead to an underestimation of the "intrinsic" activity of a catalyst. The introduced 1 M KOH can adjust the surface charge distributed on the catalyst, and thus facilitate the formation of a homogeneous catalyst ink.[168]

If a stationary method, i.e., RDE tips are kept in air, is used for drying the catalyst thin film (deposited on the GC disk), the drying can lead to the formation of so-called "coffee rings" at the edge of the GC disk due to capillary forces.[171] In this thesis, therefore, a stationary method with optimized parameters was used, i.e., the RDE tips were dried under an Ar stream saturated with isopropanol and Milli-Q water (1:3 in volume ratio). This method is efficient to obtain homogeneous, "coffee ring"-free catalyst thin films on the GC disk.

2.3.2 RDE measurements in this thesis

The RDE used in the thesis consisted of a rotating shaft and a RDE tip. The RDE tips were homemade by embodying an Ø 5 mm GC disk into a Teflon cylinder. A gold pin was used to connect the RDE tip (GC) with the rotating shaft made up of stainless steel

inside, which is connected to potentiostat to guarantee good electronic conductivity. A glass cell with two chambers was used in the measurements. During the measurements, one needs to guarantee that the distance between working electrode and the tip of the Luggin capillary of the reference electrode is as close as possible to minimize the solution resistance. In addition, the solution resistance is influenced by the concentration and the temperature of the supporting electrolyte, i.e., the higher the temperature and the concentration of the electrolyte, the lower the solution resistance. The RDE measurements in this thesis were performed with 0.1 M $HClO_4$ at room temperature to guarantee sufficient ionic conductivity of the electrolyte, and at the same time avoiding as much as possible the poisoning effects of impurities and anion species in the electrolyte. The small diameter (Ø 5 mm) of the GC disk coated with a small amount of catalyst which leads to a small absolute currents. This allows us to compensate the solution resistance online by using an analog positive feedback scheme. It is however challenging to completely compensate the solution resistance due to the oscillation generated by the potentiostat and the risk of over-compensation, which can destroy the studied catalyst immediately. Thus the resistance was not completely compensated and the remaining uncompensated solution resistance was adjusted in a "normal" range, i.e., below 3 Ω in the RDE measurements of this thesis. If necessary, this solution resistance can be further corrected after the measurements when applying a single frequency AC signal during the measurements. However, the potential offset induced by the small uncompensated solution resistance and the small current in the measurements, e.g., the diffusion limited current of the ORR is ~-1.2 mA at 1600 rpm, which is already much larger than the kinetic current, poses negligible effects on the overall potentials.

2.4 Gas diffusion electrode (GDE) methodology

Benchmarking an ORR catalyst can be easily implemented with a RDE setup. However, the impressive high ORR activity recorded in RDE measurements typically cannot be

transferred to real applications, due to the differences between RDE and MEA (used to constitute a fuel cell) measurements. These differences can be summarized as:

i) Measurement conditions: a potentiodynamic approach is frequently applied for RDE measurements,[172] in which the ORR can proceed on a catalyst surface with limited coverage of oxygen-containing species. By comparison, a potentiostatic or a galvanostatic mode is employed in MEA measurements, i.e., a constant potential or current is applied.[173] Therefore, the oxygenated species are more readily to reach an equilibrium state and thus less active sites are accessible for oxygen adsorption or cleavage on the catalyst surface. ii) Reaction interface: in RDE measurements, the working electrode coated with the catalyst film is in direct contact with protons and the dissolved oxygen in the electrolyte. In the MEA measurements, the reaction however takes place at the boundary of the catalyst surface, the polymer membrane, and oxygen diffusing from the gas diffusion layer (GDL)).[174] iii) Catalyst loading: 10 μg cm^{-2} (based on the geometric area of the working electrode) loaded on the working electrode is a standard catalyst loading for RDE measurements. Increasing the catalyst loading reduces the utilization of the catalyst, in particular once a 3D structure of the catalyst layer is formed. However, the catalyst loading in MEA measurements ranges from ~0.1 mg cm^{-2} to ~0.5 mg cm^{-2} (standard loadings for Pt-based catalysts).[175] In addition, the ORR current reaches the diffusion limited plateau at ~0.85 V_{RHE} in a RDE measurement, due to the intrinsic limitation caused by the solubility and diffusion of oxygen in the electrolyte, therefore, it is challenging to predict the ORR performance of a catalyst in the potential region of 0.6-0.8 V_{RHE}, the potential window relevant for the operation of a fuel cell.[175]

To bridge the gap between RDE and MEA tests, an alternative testing platform combining the merits of both setups i.e., the simplicity of RDE and the applicability (e.g., increased mass transport) of MEA, is desirable. Since Zatilis et al.[38] proposed the concept of floating electrode by using gas diffusion at an interface to improve oxygen transport, and thus obtain oxygen reduction currents with no mass transport limitation, GDE testing platforms with different configurations have been developed.[36–38,40,41] The

existing GDE setups (for ORR studies) can be separated into setups using a polymer membrane and the ones without polymer membrane. Setups without a membrane are known for their simplicity. Meanwhile, the proton transport can be sustained by the liquid electrolyte. Setups with a membrane can be assembled by pressing (or hot pressing) the polymer membrane on top of the catalyst layer to facilitate the proton transport, in particular in the high current region, and thus the membrane-GDE mimics closer to the real condition of PEMFCs. In addition, the introduced polymer membrane can to a great extent minimize the dissolved oxygen (in the electrolyte) to diffuse to catalyst layer, to guarantee that the oxygen is provided via diffusion through the gas diffusion layer. All the different GDE setups can meet the need of improving mass transport. However, only the setup used in this thesis can be applied at elevated temperatures. The GDE setup was first introduced by Wiberg et al.,[176] and was stepwise further adapted to investigate different reactions, i.e., the CO_2 reduction reaction[177] and the oxygen evolution reaction.[178]

2.4.1 Catalyst film fabrication on the GDL

The recipe to prepare catalyst ink was reported previously.[161] Briefly, the catalyst powder was dispersed in a mixture of isopropanol and Milli-Q water with 1:3 in volume ratio, resulting in a concentration of 0.5 g_{Pt} L^{-1} for Pt-based catalysts. Nafion ionomer (D1021, 10 wt. %, Fuel Cell Store) was added to the catalyst ink with the same mass as the carbon support. The mixture was sonicated for ~5 minutes in a sonication bath to obtain a catalyst ink displaying high dispersion.

The composition of the catalyst ink has a crucial effect on the “intrinsic” activity of a catalyst in RDE measurements. The same conclusion was recently reported for GDE measurement,[179] i.e., a standardized carbon to Nafion mass ratio for the compositing catalyst ink might not be optimal for each individual catalyst. A specific ink recipe, e.g., Nafion to support (carbon) mass ratio, for an individual catalyst is essential to obtain the maximum reachable power density for this catalyst. In this thesis, however, the nominal content of Pt and carbon were the same for each studied Pt-based catalyst.

Therefore, the mass ratio of carbon and Nafion was kept at 1 when preparing catalyst ink.

Using vacuum filtration to deposit catalyst ink onto GDL was firstly reported by Yarlagadda et al.,[180] and further adapted in the studies of this thesis. In brief, a GDL (H23C8, Fuel Cell Store) was placed in between a sand core filter and a glass funnel in a vacuum filtration setup. A catalyst ink as described above was diluted to 0.05 g_{Pt} L^{-1} by adding isopropanol and Milli-Q water, to finally lead to a volume ratio of 3:1 (isopropanol: Milli-Q water). The ink was further sonicated for ~5 minutes and poured in the funnel. A vacuum pump was applied to force the catalyst ink through the GDL. In this process the catalyst was deposited onto the GDL, thus forming a GDE, which was then placed in the fume hood for at least 2 hours. The Nafion membrane was pressed on top of GDE (2 tons and lasting for 10 minutes) before the electrochemical measurements. Note: the actual catalyst loading on the GDE might deviate from the nominal value due to nanoparticles detaching from the support (unsupported metal nanoparticles), which can easily pass through the GDL and thus reduce the metal loading on the GDE. It is therefore crucial to determine the catalyst loading on the GDE, e.g. via ICP-MS, especially when the mass of the active phase is used to normalize the measured reaction current. Additionally, acetone can be added to prepare the catalyst ink, e.g., the volume ratio of acetone, isopropanol and Milli-Q water is 1:2:1, to suppress particle loss during vacuum filtration.

2.4.2 GDE measurements in this thesis

The GDE setup used in the thesis consists of two components, i.e., the upper cell body made of polyetheretherketone (PEEK) or polytetraflfluoroethylene (PTFE) and the lower cell body, which is made of stainless steel (used to study the ORR in this thesis) or PTFE (used to study the FAOR in this thesis). The upper cell body contains aqueous electrolyte, in which the counter electrode (Pt mesh) and reference electrode (reversible hydrogen electrode, RHE) are placed. The GDE with the pressed Nafion membrane is placed in between the two cell bodies and serves as working electrode. A schematic

illustration of the GDE setup is available in our previous publications.[178,181]

In the GDE measurements, the reactant gas (e.g., O_2) is firstly humidified by introducing it to a bubbler filled with Milli-Q water. The humidified reactant gas is then streamed through the lower cell body reaching the catalyst layer by passing through the flow field on top of the lower cell body. The Milli-Q water in the bubbler can be replaced by the volatile liquid, e.g., formic acid, and the evaporated liquid is carried by the inert gas, e.g., Ar stream, to the catalyst layer allowing the study of the specific electrocatalytic reaction, e.g., FAOR.

Furthermore, the used GDE setup is small and thus allows to evaluate the performance of a catalyst at elevated temperatures. This can be easily implemented by placing the complete GDE setup (including the bubbler) in a metal box that sits on a heating plate. A temperature sensor connected to the lower metal cell body is used to monitor the temperature of the cell body *in situ* via the potentiostat. Note that using the cell body made of metal is critical to guarantee that the provided heat is homogeneously transferred to the catalyst layer.

The online compensation of solution resistance via the potentiostat is well-established in RDE measurements. However, the online compensation is not sufficient for the ORR measurements carried out with a GDE setup. The remaining uncompensated solution resistance leads to an offset of the measured potential, in particular for the high current region.[36,37] Therefore, a potentiostatic or galvanostatic steady-state protocol is applied for ORR measurements performed in the GDE setup. This allows a post-correction of the potentials caused by the remaining uncompensated solution resistance. The post correction can be done in the analysis program of "EC4 View" using the equation:

$$E_{real} = E_{measured} - iR_u \qquad (2.3)$$

Where R_u is uncompensated solution resistance determined by a single frequency AC signal during the measurements, see above. Therefore, when applying a galvanostatic measurement protocol for the ORR, the real potentials are shifted to larger values when correcting for the uncompensated solution resistance.

3. Discussion of the appended manuscripts

The following chapter offers an overview the work that I accomplished in my thesis and which is published in peer-reviewed journals and where I am first author. These are in total three published/accepted manuscripts, one manuscript that is under revision, and two manuscripts that are in preparation where all measurements have been finished. For each manuscript a short background information is provided and the most important findings are highlighted. Also my role in obtaining the results is specified. Section 3.1 discusses the developed nanocomposite concept versus a conventional alloy concept. BifunctionalPt-Ir/C catalysts were prepared and compared in ORR and OER studies. Section 3.2 presents work investigating commercial Pt/C catalysts for the ORR in a RDE as well as a GDE setup. It is evaluated to which extent the intrinsic activity of a catalyst obtained in RDE measurements can be translated to a more applied environment by using a GDE setup. In section 3.3, the nanocomposite concept is extended to a Pt-Au/C system in a comparative study testing the ORR performance in a RDE and a GDE setup. In section 3.4, Pt-Au/C nanocomposites with different Au contents are further studied for the FAOR. The results demonstrate that the nanocomposites alloy if repetitive potential/current cycles are applied. It is shown that the continuous alloy formation of Pt and Au is induced by and benefits the FAOR. Section 3.5 focuses on the dissolution of Ir during electrochemical treatment and outlines a possible electrochemical recycling scheme. The project was motivated by the severe dissolution of Ir observed in the study presented in section 3.1 and the stability issue of Pt-Ir bifunctional catalysts in practical applications. In the last section 3.6, a non-noble Fe-NC catalyst is tested for the ORR in a RDE setup as well as a GDE in acidic and alkaline conditions and the electrocatalytic performance is compared with that from a Pt/C benchmark catalyst.

3.1 Manuscript I: Bifunctional Pt-IrO_2 catalysts for the oxygen evolution and oxygen reduction reactions: alloy nanoparticles vs. nanocomposite catalysts

Description

Iridium (Ir), one of the platinum group metals (PGMs), is considered highly resistant to corrosion even in the aqua regia. Activated Ir (IrO_2) is used in proton exchange membrane water electrolyzers (PEMWEs) as anode catalyst combining high activity and stability for the oxygen evolution reaction (OER).[182] By comparison ruthenium (Ru) in its activated form (RuO_2) displays outstanding catalytic performance in acidic media, which is however at the cost of its stability due to the formation of easily dissolvable species of RuO_4.[183]

Connecting PEMWEs with an external energy source (such as solar energy) can establish a complete system for hydrogen production and re-employment for electricity generation, i.e., the unitized regenerative fuel cell (URFC).[184] In an URFC, Ir (IrO_2) is typically combined with a Pt-based catalyst to form a bifunctional catalyst, to catalyze OER and ORR, respectively. In addition, Ir (IrO_2) is proposed to "protect" Pt-based catalysts from degradation, in particular under OER operating conditions and/or repetitious start up and shut down conditions.[185] Water is oxidized to oxygen by Ir (IrO_2) and thus decreasing the amount of reactant (water) for carbon (serves as a support for the catalyst) oxidation (carbon is difficult to be oxidized in a dry environment). Carbon oxidation leads to the detachment of Pt-based metal nanoparticles from the carbon support forming aggregates. Furthermore, the carbon surface becomes less accessible. In spite of the high resistance of Ir-based materials under stationary conditions, Ir and IrO_2 suffer from dissolution when switching between oxidating and reducing conditions. When metallic Ir is oxidized and Ir oxide is reduced, repetitively, the oxidation state of Ir is changed between 3+ and 4+ at ~0.9 V_{RHE},[186] and between 5+ and 6+ at ~1.5 V_{RHE}[187] which triggers dissolution.

In the presented work of this section, Pt/C with different weight percent, Pt + xIr/C nanocomposites, and $PtIr_x$/C alloys were prepared. The nanocomposite was developed

as a concept consisting of separately preparing monometallic nanoparticles (herein, Pt and Ir nanoparticles) and co-supporting them onto a support (here carbon). Therefore, the properties of the individual nanoparticles (e.g., the type of particles, the loading of the particles, etc.) can be adjusted without influencing the adjacent co-immobilized metal nanoparticles. The nanocomposite differentiates itself from conventional alloys, where various elements are incorporated into a single metal nanoparticle. Since Pt-Ir catalysts serve as bifunctional catalysts, we compared Pt + xIr/C nanocomposites with $PtIr_x$/C alloys with respect to their stability in accelerated degradation tests, their ORR performance, and their OER performance.

Contribution to the work

My contribution to this work was as follows: I prepared the different catalysts, performed all electrochemical measurements and processed and analyzed the data. In addition, I prepared the first draft of this paper. The TEM characterization and ICP-MS measurements were conducted by the co-authors.

Most important findings

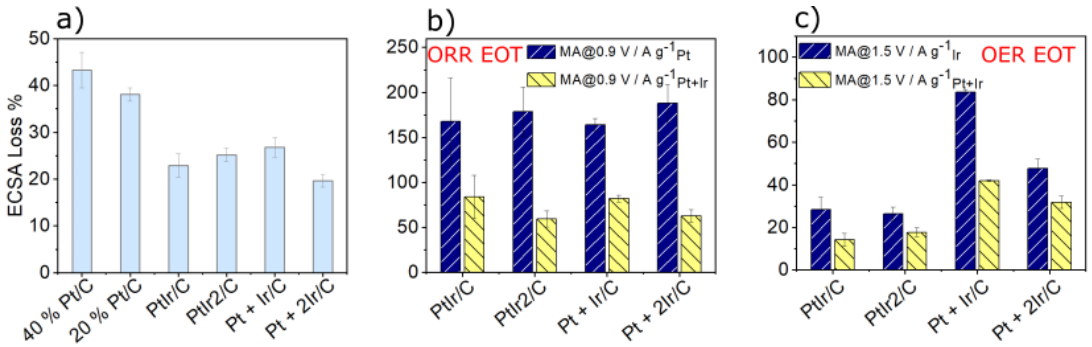

Figure 3.1 Summary of ECSA loss as a function of different investigated catalysts during degradation test (a), ORR activity (b) and OER activity (c) of the studied bifunctional Pt-Ir catalysts (nanocomposites and alloys) after degradation test. EOT: end of test.

The most important findings of this work are summarized in Figure 3.1 and Table 3.1. Figure 3.1 displays the electrochemical performance including stability, ORR activity, and OER activity of the investigated catalysts. Table 3.1 provides an overview of the

relative ratio change in weight composition of the bifunctional Pt-Ir catalysts after being exposed to accelerated degradation tests. The results demonstrate that severe Ir dissolution occurs when exposing the catalysts to alternative oxidative/reductive conditions. In the following, I summarize the key results:

- A clear stability trend is observed as displayed in Figure 3.1a. That is, the catalyst stability improves with introduction of Ir to the Pt catalyst. Less Pt surface area is lost for the bifunctional catalysts in comparison to the monometallic Pt reference. The degree of the durability improvement is not specific to the configuration (nanocomposite vs. alloy) and the loading/ composition (one time vs. two times higher Ir mass than Pt mass) of the bifunctional catalysts. The findings are consistent with the previous reports,[185] i.e., Ir can mitigate the degradation of Pt in bifunctional catalysts.
- Based on the similar loss in ECSA for the bifunctional catalysts, a similar change in the ORR and OER performance (comparing the electrocatalytic activity before and after the degradation test) would be expected. However, Figure 3.1b and Figure 3.1c display a different picture, i.e., Pt + xIr/C nanocomposites display a comparable ORR activity and higher OER activity after the degradation test, as compared to the lower ORR activity and comparable OER activity before the degradation test. Both characteristics (ORR and OER activity) are compared to the ones of the $PtIr_x$/C alloy counterparts.

The improvement in activity (ORR and OER, after degradation) of Pt + xIr/C nanocomposites highlights the advantage of a catalyst configurated with separately supported metal nanoparticles over the conventional bi- and/or tri-metallic structures, i.e., alloys. The degradation of the active nanoparticles impacts less of the adjacent heterogenic nanoparticles if the two components are separately distributed. By comparison in alloys, the different elements are incorporated into the same entity leading to an entangled degradation.

Table 3.1 Summary of relative compositions in weight of Pt and Ir and the change of relative compositions over the degradation test. The relative compositions are determined with TEM-EDX

measurements. BOT: before test. EOT: end of test.

		Ir wt. %	Pt wt. %	wt. Ir/Pt	wt. Ir/Pt change %
PtIr/C	BOT	45 ± 4.8	55 ± 4.8	0.82	73
	EOT	18.2 ± 2.3	81.8 ± 2.3	0.22	
$PtIr_2$/C	BOT	54.8 ± 6.7	45.2 ± 6.7	1.21	82
	EOT	18.2 ± 15	81.8 ± 15	0.22	
Pt + Ir/C	BOT	46.2 ± 2	53.8 ± 2	0.86	65
	EOT	23 ± 5.4	77 ± 5.4	0.3	
Pt + 2Ir/C	BOT	66.8 ± 0.7	33.2 ± 0.7	2.01	77
	EOT	31.6 ± 17	68.4 ± 17	0.46	

- Analyzing the relative weight ratio (Ir/Pt) of the bifunctional catalysts after the degradation tests, one can clearly observe a substantial decline in Ir weight in all the studied bifunctional Pt-Ir catalysts. This indicates that the Pt "protection" is at the expense of Ir dissolution, and thus poses an issue that needs to be addressed for real fuel cell/electrolyzer applications.

Comparing and evaluating the electrocatalytic performance of the studied catalysts, we are able to state that the bifunctional catalysts possess a higher resistance to degradation treatments with respect to the pure Pt/C references. In view of the configuration of the bifunctional catalysts, the nanocomposites display advantages over the alloys, reflected in the higher retainment in performance (ORR and OER) after the degradation tests. However, drawback is also obvious; not only for the nanocomposites, but for all Pt-Ir bifunctional catalysts. Substantial Ir dissolution occurs under harsh electrochemical conditions. It is therefore of high importance to mitigate Ir dissolution and/or recycle the dissolved Ir.

3.2 Manuscript II: The gas diffusion electrode setup as a testing platform for evaluating fuel cell catalysts: a comparative RDE-GDE study

Description

In manuscript I, the presented electrochemical measurements results were obtained with the "state of the art" method, i.e., RDE measurements. The RDE technique is known for its simplicity and is available in most laboratories. The ORR normally occurs on the cathodic side of PEMFCs.[2–4] Using the RDE methodology, one can study the intrinsic ORR activity (upper limit in ORR activity) of a catalyst. However, it is challenging to directly translate the obtained ORR activity to tests in membrane electrode assemblies (MEAs), which constitute a fuel cell. The discrepancy in ORR performances obtained from RDE and MEA measurements can be attributed to several parameters and was already detailed in the last chapter. In the presented work, I compare the performance of industrial catalysts in RDE measurements with those in GDE measurements, which should serve as an intermediate step towards the application of MEAs.

Contribution to the work

I conducted all electrochemical RDE measurements and analyzed the data. Sven Nösberger conducted the electrochemical GDE measurements. Jonathan Quinson, from the University of Copenhagen, did the physical characterization of the commercial Pt/C catalysts, i.e., the TEM imaging and statistical Pt particle evaluation to obtain the number weighted particle size distribution, and the SAXS analysis.

Most important findings

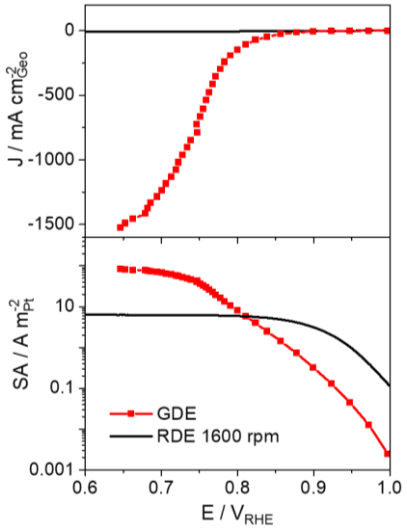

Figure 3.2 Comparison of ORR performance in RDE (black line) and GDE (red line). 46 wt.% TKK Pt/C serves as a represent for comparison.

In the current study, six different commercially available fuel cell Pt/C catalysts were investigated in both RDE and GDE setups. The thorough comparative results can be obtained in the attached manuscript. In the section discussed here, I select one catalyst (46 wt.% TKK Pt/C) as an example, to discuss the different ORR behaviors in different potential windows, obtained from RDE and GDE measurements, respectively. The most important findings of the work are summarized in the following:

- The upper part in Figure 3.2 displays that the obtainable geometric currents in RDE and GDE measurements are substantially different. In RDE, the diffusion limited current is ~-6 mA cm^{-2}, at a rotation speed of 1600 rpm, a typical value in ORR studies. By comparison, a current of ~-1500 mA cm^{-2} is obtained in the GDE measurements. Two factors, i.e., the catalyst loading on the working electrode and the oxygen transport in the system, lead to the observed difference in ORR currents. A mass transport (MT) free diffusion current can be extrapolated in RDE measurement under the assumption of an infinite rotation speed. However, even with infinite rotation the maximum diffusion current under MT-free conditions is only ~-600 mA cm^{-2},[166] due to the limited oxygen solubility in the electrolyte and the much lower catalyst loading (~20 times less)

in comparison to the one used in GDE measurements. This demonstrates the importance to use a GDE setup in catalysts evaluation. In GDE measurements the oxygen solubility issue is eliminated and a much higher catalyst loading can be used.

- Neither the data from RDE nor GDE measurements were mass transport corrected (the lower part in Figure 3.2). The potential region with linear Tafel slope goes down in the GDE measurements to ~0.75 V_{RHE}. In contrast, the potential region with linear Tafel slope is narrowed in the potential range of 0.9-1.0 V_{RHE} in the RDE measurements.
- Ideal data obtained in GDE measurements should exhibit a linear Tafel slope throughout the whole potential window. This is however obviously not the case in the current GDE study. A current plateau as observed in the RDE measurement, can also be seen in the GDE measurements in the potential region where the current reaches ~-1000 mA cm^{-2}. This demonstrates that a limiting factor also exists in this measurement system. Oxygen transport through the GDL should not be an issue, as long as a high gas flow rate can be guaranteed. Therefore, the proton concentration on the catalyst surface, as well as the management of the product (water) might become limiting factors. Consequently, the Nafion content, the humidification of the Nafion and the thickness of the membrane, etc., potentially influence the proton transport. Furthermore, the type of the substrate, the graphitization degree and the porosity of the carbon support pose an impact on the water management. It is thereby extrapolated that by adjusting the mentioned parameters further, an optimization to the present GDE setup can possibly be achieved.

In conclusion, the GDE setup with similar operating conditions as in MEA tests provides an opportunity to evaluate catalysts under more relevant conditions. We therefore can envisage “a scheme” for the design and the application of a newly developed catalyst: catalyst synthesis, RDE measurements to confirm the synthesis

concept, GDE measurements to validate the feasibility of the application of the catalyst, MEA measurements to validate the feasibility of an industrial application. Finally, the large-scale production of the catalyst.

3.3 Manuscript III: Elucidating Pt-based nanocomposite catalysts for the oxygen reduction reaction in rotating disk electrode and gas diffusion electrode measurements

Description

It is well-accepted that among the various materials for the ORR, Pt-based materials exhibit the highest intrinsic ORR activity and thus are utilized at the cathode of PEMFCs.[2–4] Recently, the catalytic performance in the high current region (low potential region) and the stability of the catalysts attract increasing attention in research, as these metrics are important for practical applications.

The catalyst dispersion plays a critical role for the ORR performance in the high current region, i.e., a high dispersion facilitates sufficient oxygen transport to the active sites that is particularly crucial in the high current region. However, to achieve high dispersion, smaller nanoparticles are imperative. This on the other hand accelerates the degradation of the catalyst (lower stability of small nanoparticles).[161,188] Using interparticle effects allows to optimize the particle density on the support (catalyst dispersion) and further exert impact on the Pt stability and ORR rate.

The nanocomposite concept, firstly introduced in manuscript I, allows to investigate the interparticle effect beyond monometallic nanoparticles. Therefore, it is of interest to apply the nanocomposite concept to the Pt-Au system, which is a “hot topic” in ORR studies in the literature.[78–84] With the help of Pt-Au nanocomposites one can elucidate how the interaction between Pt and Au nanoparticles affects the ORR activity and the stability of the catalyst, both properties that are associated with the oxophilicity of Pt.

Contribution to the work

My contribution to this work includes the catalysts preparation, all electrochemical measurements and the data analysis. I also prepared the first draft of the paper. Jonathan Quinson, from the University of Copenhagen, did the physical characterization of the catalysts, i.e., TEM imaging and analysis of the catalyst composition with TEM-EDX,

and the SAXS analysis to evaluate the particle size distributions. The *Ex situ* X-ray absorption spectroscopy (XAS) data was measured and processed by Adam Clark from the SuperXAS beamline at PSI.

Most important findings

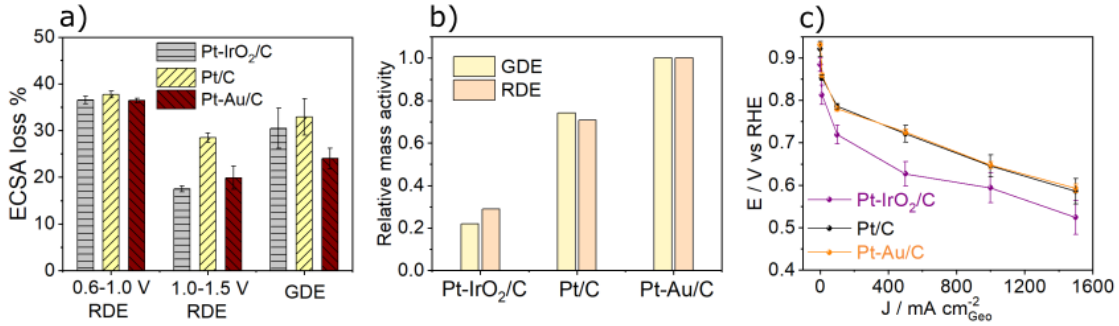

Figure 3.3 Summary of stability comparison (a), ORR activity comparison (b), and ORR activity obtained in a GDE setup (c) of the investigated catalysts. The degradation protocol for GDE measurement incorporating the potential stepping between 0.6 and 1.0 V_{RHE} and the potential cycling between 1.0 and 1.5 V_{RHE}. The ORR mass activity from Pt-Au/C is regarded as a standard to calculate the relative mass activity of the studied catalysts, from RDE and GDE measurements, respectively.

The most important findings of this work are summarized in Figure 3.3. The Figure includes a comparison of the stability and ORR activity of the investigated monometallic Pt/C catalyst, nanocomposites incorporating Pt and Ir (IrO_2, after electrochemical activation) nanoparticles as well as Pt and Au nanoparticles. The performance comparison was first studied in a RDE setup, then the measurements were further carried out in a GDE setup to investigate how much of the obtained performance in the RDE measurements can be transferred to the more realistic situation in the GDE setup. The obtained results are as follows:

- Figure 3.3a depicts that the stability of Pt can be improved by adding Ir (IrO_2) nanoparticles, which is consistent with the study presented in the manuscript I, or by adding Au nanoparticles. This conclusion is confirmed independent of the applied degradation protocol and the applied testing platform. As also presented in the Manuscript I, the stability improvement of Pt is at the cost of Ir dissolution in the Pt-IrO_2/C catalyst. By comparison, in the case of the Pt-Au/C

nanocomposite, Au nanoparticles suffer much less from dissolution. Therefore, Au nanoparticles can be considered more appropriate in terms of improving the durability of Pt nanoparticles. However, it should be noted that the particle size difference between Ir (less than 2 nm) and Au (more than 5 nm) might be a contributing factor in the different dissolution profiles of Ir and Au.

- The interaction of Pt and Au nanoparticles allows to modify the electronic structure of Pt leading to a less oxophilic property of Pt nanoparticles as shown in the XAS measurements (in the appended manuscript) and reflected in the improved stability (Figure 3.3a) as well as improved ORR activity (Figure 3.3b). The ORR activity of Pt-IrO_2/C is however reduced in comparison to the Pt/C reference, despite the observed improvement in stability. OH^*, an intermediate in the ORR, can on the one hand facilitate the ORR, on the other hand it can also act as a poisoning species blocking the active sites required by the ORR. Therefore, the ORR rate is limited by the OH^* formation if the OH^* binding energy on the Pt surface is too weak, and conversely, the ORR rate is limited by the OH^* (OOH^*) reduction if the binding energy is too large. It is reported that the ORR rate on the Pt/Au(111) is determined by the OH^* removal step, while on Pt/Ir(111), it is determined by the OOH^* formation step.[64] An analogous assumption can be made for the current study, i.e., less Pt oxide is formed in the Pt-IrO_2/C system, and thus an improved stability and a lower ORR activity are observed.
- The improved ORR rate for the Pt-Au/C nanocomposite can however not be retained at high current densities as demonstrated in Figure 3.3c. This might be an intrinsic limitation of the studied catalyst, or a limitation of protons and/or water management in the high current region, as discussed in manuscript II.

By carrying out a comparative study in RDE and GDE setups, we could evaluate the performance of the catalysts for both fundamental and applied perspectives. The ORR activity trend of the studied catalysts can be transferred to the more realistic operating

conditions, which proves the feasibility of using GDE setups to evaluate a series of catalysts in basic research. The nanocomposite concept enables us to adjust the individual parameters of the introduced metal nanoparticles and balance the stability and the activity of the catalyst. However, further work is essential to unfold the promises of nanocomposite catalysts in more applied research.

3.4 Manuscript IV: Nanocomposite concept for electrochemical *in situ* preparation of Pt-Au alloy nanoparticles for formic acid oxidation

Description

Hydrogen is one of the most widely used fuels to power PEMFCs for electricity generation.[11] It can alternatively be replaced by liquid fuels, e.g., formic acid, methanol, and ethanol, etc., for the sake of safety and utilize the abundance of liquid fuels. Thus DFAFCs and DMFCs, etc., have been developed.[16,17]

Catalysts may display satisfactory initial performance, the performance however may decrease in longer-term measurements. This can partially be associated with structural changes of the catalyst (irreversible degradation) but also with the formation of poisonous species (reversible degradation). It is therefore crucial to track the dynamic structure of the catalyst during electrochemical tests. For example, with the help of *in situ* transmission electron microscopy, a recent study reported a dynamic conversion of cubic copper nanoparticles taking place under CO_2 electroreduction conditions. The altered morphology of the cubic copper facilitated the generation of C_{2+} products.[189] The finding exemplifies the importance of *in situ* determination of the structure (dynamic structure) of a catalyst.

The nanocomposite concept was first developed and used for the study of bifunctional catalysts, as presented in manuscript I. This concept is further extended to the Pt-Au/C system showing improved ORR performance as presented in manuscript III. The feasibility of performing formic acid oxidation reaction (FAOR) tests and the lack of studies on Pt-Au/C nanocomposites for the FAOR in the literature, motivated us to adopt the Pt-Au nanocomposites for the FAOR. As the nanocomposites exhibited time dependent electrochemical responses, *in situ* small-angle X-ray scattering (*in situ* SAXS) was employed to track the dynamic size distribution of the Pt-Au/C nanocomposites in potentiodynamic tests and to correlate them to the observed catalytic performance.

Contribution to the work

My contribution to this work was as follows: the preparation of the various Pt + xAu/C nanocomposites and catalyst layers for the GDE measurements, the complete electrochemical measurements and the data analysis, the physical characterization of the investigated catalysts (TEM, IL-TEM), the *in situ* SAXS measurements. Furthermore, I prepared the first draft of the paper. The remaining characterizations mentioned in the paper were conducted by the co-authors.

Most important findings

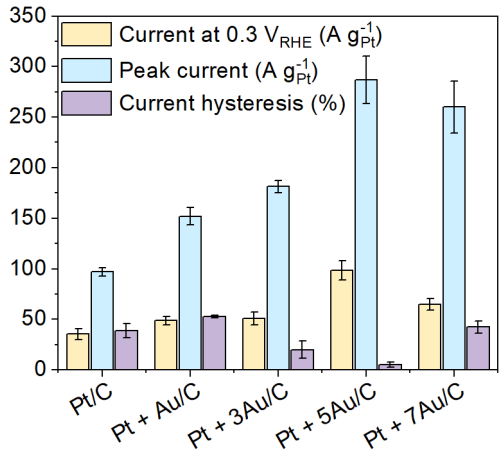

Figure 3.4a FAOR performance comparison of the investigated catalysts. The currents at 0.3 V_{RHE} and peak positions are from the forward scanning. The current hysteresis is calculated from the peak positions in both scanning directions. A detailed specification for the obtained measurement results is available in the appended manuscripts.

Figure 3.4a summarizes the different FAOR characteristics of the studied catalysts. Figure 3.4b displays the dynamic transformation of the particle size distributions during FAOR potentiodynamic tests. Correlating the FAOR performance to the physical property of the catalysts, the following conclusions can be reached:

- It is clearly seen in Figure 3.4a, that the current in the positive-going scan is enhanced with larger Au compositions; both in the peak current and the current at 0.3 V_{RHE}. The highest current is attained when the mass ratio of Pt:Au reaches 1:5. Further increasing the Au composition, however, leads to a reduction in FA

oxidation current. The peak current undoubtedly reflects the FAO rate of a catalyst, however, the current at 0.3 V_{RHE} is an equally crucial parameter for an application, as the working potential of a DFAFE is around 0.3 V_{RHE}.[21] In addition, the current hysteresis is compared, which reflects the tolerance of a catalyst for poisoning. As seen, the Pt + 5Au/C nanocomposite displays the lowest current hysteresis, which indicates that the oxidation current from the forward scan is less passivated and is therefore more similar to the one in backward scan. Thus the catalyst possesses a high poisoning tolerance. In summary, Pt + 5Au/C exhibits the most balanced characteristics for the FAOR.

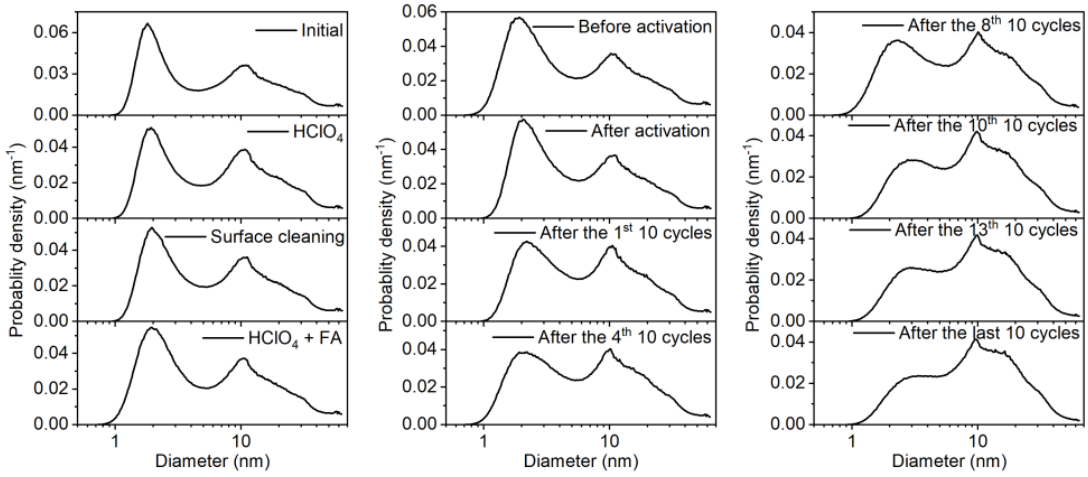

Figure 3.4b Size distributions of Pt + 5Au/C from *in situ* SAXS analysis. The displayed size distribution functions are selected after a certain step of FAOR potentiodynamic test and in an order from the first column to the third column, each column following the top to the bottom sequence.

- Pt + 5Au/C was further investigated using *in situ* SAXS analysis. As seen in Figure 3.4b, with increasing duration of the FAOR potentiodynamic tests the bimodal size distribution of Pt + 5Au/C gradually evolves into a mono-modal distribution. It can be speculated that a transformation into an alloy structure occurs with continuous potential cycling. That is, *in situ* alloy formation occurs that is most likely associated with Pt nanoparticles migrating and coalescing with Au nanoparticles, or/and Pt dissolution and re-deposition onto the Au nanoparticles. The hypothesis is probed by wide-angle X-ray scattering

(WAXS), in which a small shift in the Bragg peaks (Au reflections) is observed after the potentiodynamic test. This allows to distinguish alloy formation from "a simple" Pt re-deposition onto Au islands, as indicated in the STEM-EDX mapping. We therefore can state that by comparing with the study of Guay et al.,[138] *in situ* alloying of Pt and Au occurs during the FAOR potentiodynamic tests leading to the observed improved performance. However, due to the similarities of Pt and Au it is challenging to calculate the lattice constants to quantify the formed alloy.

Pt-Au/C nanocomposites with various Au contents were prepared and tested for the FAOR. It is shown that a five times higher Au mass than Pt mass is the optimal composition for a balanced FAO performance. The improved performance is ascribed to the dynamic change in structure, i.e., the particle size distribution from the initially separate state of Pt and Au gradually evolves to form a Pt-Au surface alloy. *In situ* SAXS study demonstrates that the surface alloy formation is a continuous process. It is therefore suggested for a future study, to combine *in situ* SAXS and WAXS to better quantify the formed alloy as a function of the potential cycling.

3.5 Manuscript V: Iridium recycling achieved by the selectively efficient dissolution in the Pt + xIr/C nanocomposites

Description

As documented, Ir demand is a potential bottleneck in the large-scale commercialization of PEMWEs.[182,190] Therefore, in addition to the reduction of Ir usage in PEMWEs, the recycling of Ir from used electrodes is of paramount importance.

The "state of the art" technologies to extract Ir from its oxide and/or end-of-life materials use boiling concentrated acids.[191–195] The feasibility of Ir dissolution thereby usually comes at the expense of complexity of the treatments and potential hazards for the environment. Despite such harsh treatments, in terms of electrochemical processes the Ir recycling rate from the end-of-life materials is currently only 40-50%, in comparison to ~90% recycling rate of Pt- and Pd-based materials.[190] The sluggish recycling rate of Ir is at least partially associated with the challenge of dissolving Ir oxide via chemical methods. Therefore, there is a high demand for the development of alternative strategies for Ir recycling.

In the presented work, Pt + xIr/C nanocomposites with various compositions were prepared. By alternatively switching the applied oxidative and reductive potentials/currents, the transient dissolution of Pt and Ir was detected. Furthermore, by adjusting the applied electrochemical measurement protocols, a maximum selectivity in Ir dissolution was achieved, suggesting a potential pathway for efficient Ir recycling.

Contribution to the work

My contribution to this work includes the preparation of the Pt + xIr/C nanocomposites, all electrochemical measurements in the half-cell setup and the data analysis. Matej Zlatar, from the Helmholtz Institute Erlangen-Nürnberg for Renewable Energy (IEK-11), carried out all measurements by the scanning flow cell coupled to inductively coupled plasma-mass spectrometry (SFC-ICP-MS) and analyzed these data.

Most important findings

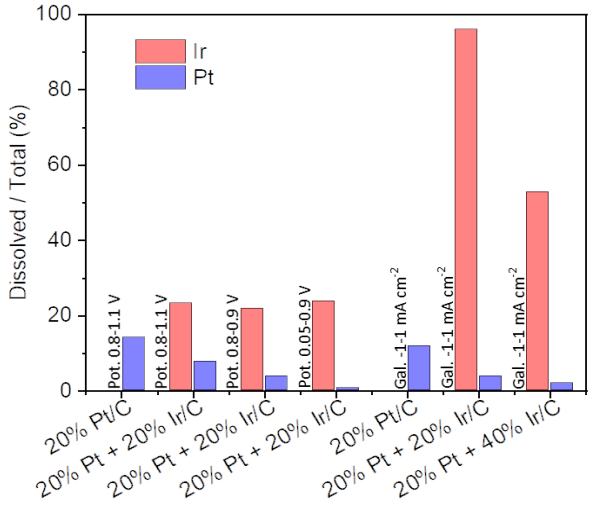

Figure 3.5 Summary of the total metal dissolution rates during SFC-ICP-MS measurements as a function of various samples and treatment protocols. Pot.: potentiostatic holds, Gal.: galvanostatic holds. Pot. 0.8-1.1 V: stepping potential between 0.8 and 1.1 V, each step lasts for 60 s and 7 repeats in total, Pot. 0.8-0.9 V: stepping potential between 0.8 and 0.9 V, each step lasts for 60 s and 7 repeats in total, Pot. 0.05-0.9 V: stepping potential between 0.05 and 0.9 V, each step lasts for 300 s and 3 repeats in total, Gal. -1-1 mA cm^{-2}: stepping current between -1 and 1 mA cm^{-2}, each step lasts for 60 s and 7 repeats in total. The potentials are referred to the reversible hydrogen electrode (RHE) in the measurements.

The most important findings in the presented work of this section are summarized in Figure 3.5. To explain the results, one needs to note that the nanocomposites subjected to the potentiostatic tests consisted of monometallic Pt and Ir nanoparticles, while the nanocomposites subjected to the galvanostatic tests consisted of metallic Pt nanoparticles and activated Ir (IrO_2) nanoparticles. As can be clearly seen, the respective Pt and Ir dissolution rates are to a great extent affected by the applied protocols and the composition/activation of the nanocomposites. In summary the following observations and conclusions were made:

- The pure 20% Pt/C catalyst, which serves as a reference exhibits the highest dissolution rate as compared to the nanocomposites, both under potentiostatic and galvanostatic testing protocols. This indicates that both metallic Ir nanoparticles and IrO_2 nanoparticles can alleviate Pt dissolution. This led to the question if a condition can be found where Ir is selectively dissolved.

- Focusing on 20% Pt + 20% Ir/C in the potentiostatic treatments, it is seen that by lowering the upper potential from 1.1 V to 0.9 V (0.8 V as the lower potential is kept unchanged) in the measurement protocol, Pt dissolution is reduced by half while a similar Ir dissolution is detected. When the lower potential limit is reduced to 0.05 V (keeping the upper limit at 0.9 V), Pt dissolution is minimized while maximum Ir dissolution is reached. It is therefore concluded that by carefully selecting the lower and the upper potential limit (should be below the thermodynamic potential of Pt dissolution[196]), high selectively in Ir dissolution can be achieved.
- Ir dissolution from Ir oxide (IrO_2) was tested as well as it is more relevant for PEMWE recycling schemes. In addition, a current control protocol (galvanostatic protocol) was applied as this is easier to realize in industry. It is seen that conditions can be found where almost all Ir (96 %) can be selectively dissolved while keeping Pt dissolution at a minimum. Comparing the 20% Pt + 40% Ir/C sample to that of 20% Pt + 20% Ir/C, it is shown that Pt dissolution is reduced, however Ir dissolution is less selective.

In conclusion, by adjusting the applied testing protocols, the selective and efficient Ir dissolution can be achieved independent of metallic Ir or activated Ir (IrO_2) nanoparticles are investigated. Current control protocols that alternatively switch between reductive and oxidative currents might be most suitable protocol for applications as no potentiostat is required.

3.6 Manuscript VI: Elucidating Fe-NC catalyst for the oxygen reduction reaction in GDE setup

Description

Even though Pt-based catalysts are the most efficient materials for fuel cells, there is a need for research on alternative materials. The price and the abundance of Pt impede the mass commercialization of fuel cells. Non-noble metal materials with satisfying electrocatalytic performance can potentially replace Pt-based catalysts. Single site catalysts thereby gained interest in the last few years. The most known catalyst of this type for the ORR is Fe-NC, which displays decent ORR performance. The maximum utilization of the metal atoms (active sites), however, comes with the challenge of poor stability in long-term usage, as the atomically dispersed element can easily aggregate due to its high surface energy.[89] Studies to test single site catalysts for a specific reaction are often carried out in a RDE setup. The above mentioned gap between fundamental and applied research is perhaps even larger for this type of catalyst than for Pt/C. Therefore, it is of high interest to compare the evaluation of single site catalysts in RDE configuration to the more realistic environment of a GDE setup. The merits of GDE setup were detailed in the previous sections and are not repeated here.

In the presented work of this section, the single site catalyst Fe-NC is tested for the ORR. The measurements were performed in a RDE as well as in a GDE setup.

Contribution to the work

My contribution to this work includes all electrochemical measurements performed in the GDE setup and the respective data analysis. Vladislav Gridin, from TU Darmstadt, prepared the Fe-NC catalyst and performed the RDE measurements.

Most important findings

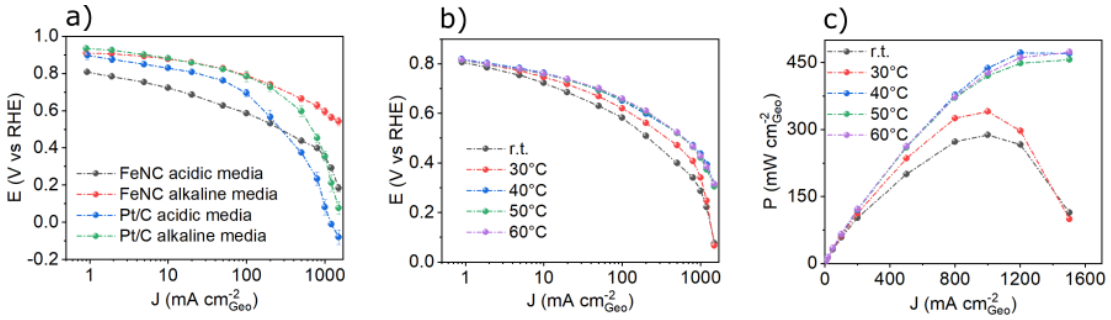

Figure 3.6 Summary of ORR activity comparison between Fe-NC and Pt/C at room temperature (a), ORR Tafel plots (b) and the corresponding power density curves (c) of Fe-NC at different temperatures. The nominal catalyst loadings of Fe-NC and Pt/C (10 wt.%) on the working electrode are 2 $mg_{Fe\text{-}NC}$ cm^{-2} and 0.2 mg_{Pt} cm^{-2}, respectively. 4 M $HClO_4$ and 1 M KOH are used as electrolyte to provide acidia and alkaline media, respectively. All measurements are performed in GDE setup.

The manuscript of this work is at an early stage. Therefore, here only the GDE measurements are discussed. The most important findings are summarized in Figure 3.6. The Figure shows a comparison of the ORR activity between the single site Fe-NC catalyst and a standard ORR Pt/C catalyst with low metal loading (10 wt. %). It is demonstrated how the temperature affects the ORR of Fe-NC in the kinetic (low current) and mass transport influenced (high current) potential region. The following statements can be made:

- In comparison with Pt/C, Fe-NC displays a substantially more pronounced improvement in ORR activity when going from acidic to alkaline media, both in the low and high current region (Figure 3.6a). As reported, peroxide is a predominant ORR product for single site catalysts[197] (this is not the case for Pt/C). However, in alkaline media the produced HO_2^- can be stabilized on the catalyst surface and enabling a complete $4e^-$ transfer to produce water. By comparison, H_2O_2 is easily decomposed to water and oxygen in acidic media.[197] Therefore, Fe-NC displays a substantially higher ORR activity in alkaline media, when compared with Pt/C.
- In the potential window of fuel cell operation (0.6-0.8 V_{RHE}),[175] Pt/C displays a higher ORR activity than Fe-NC in acidic media and comparable performance

in alkaline environment. However, it is necessary to point out that the used 10 wt.% Pt/C catalyst is not a “good” catalyst for the ORR, standard 20 wt.% Pt/C and 30 wt.% Pt/C exhibit higher ORR activity.

- Proton conducting membranes such as Nafion are more mature for applications at elevated temperature (above room temperature) as compared to hydroxide conducting membranes. Therefore, the ORR measurements at different temperatures were easier to be carried out in acidic media and the results are presented in Figure 3.6b. As seen, the overall ORR activity of Fe-NC is improved with temperature, and the improvement is more pronounced in the high current region (above 500 mA cm^{-2}) as compared to the activity recorded below 100 mA cm^{-2}. This result suggests an improvement in reactant/product transport with temperature. The corresponding power density is improved as well, from ~300 mW cm^{-2} at room temperature, to ~450 mW cm^{-2} above 40°C.

In conclusion, using the GDE setup to elucidate a Fe-NC catalyst for the ORR, the benefits and the limitations of Fe-NC are demonstrated. Especially in acidic media, the ORR performance still needs improvement to challenge Pt/C as standard catalyst. However, in alkaline media, Fe-NC demonstrates ample performance and the introduction of hydroxide conducting membranes provides a suitable alternative to standard PEMFCs using Pt at the cathode.

4. Conclusions and perspectives

In this charpter, the overall results of the thesis are discussed and a perspectives for future studies is given.

4.1 Conclusions

In this thesis, the nanocomposite catalyst concept is developed and used to prepare Pt-based catalysts. The nanocomposite catalysts are systematacially tested for the fuel cell reactions, i.e., the ORR and the FAOR. Several achievements in ORR performance are made by introducing "foreign" metallic nanoparticle to the Pt/C, both under fundamental (RDE) and more realistic (GDE) conditions. The demonstrated differences of Au and Ir nanoparticles in affecting the Pt stability inspired to also investigate potential electrochemical Ir recycling schemes by means of efficient and selective Ir dissolution. In addition to the ORR, also the FAOR was studied. Last but not least, also non-noble metal catalysts were studied in a GDE setup and the results were compared to measurements performed with RDE.

First, different Pt-Ir/C bifunctional nanocomposites with various Ir contents were prepared and evaluated for the ORR, OER and their stability performance with the aid of the "state of the art" RDE measurement method (Manuscript I). The obtained performance was compared with the one from $PtIr_x/C$ alloys with identical compositions as the nanocomposites. It is found that the ORR rate is negatively affected (as compared to the Pt/C benchmark) by introducing Ir to the Pt, both in the nanocomposites and the alloys. On the other hand, in all samples containing Ir, the OER activity improves, which somehow compensates the undesired ORR inhibition. The stability of Pt is improved as well, however, at the expense of Ir dissolution. Nevertheless, Pt-Ir/C nanocomposites more effectively prevent the ORR and OER performance from deteriorating in degradation tests than the alloy counterparts.

Ir instability is a typical challenge for Pt-Ir bifunctional catalysts. In this thesis work,

this issue is not solved, however, the results inspired us to investigate possible electrochemical Ir recycling schemes, which goes beyond investigating mitigation strategies for Ir degradation. By adjusting the applied measurement protocols, a selective Ir dissolution of 96% could be achieved. Furthermore, the concept is demonstrated for realistic catalyst films on a GDL (Manuscript V). The results therefore indicate that electrochemical Ir recycling could be more efficient and facile as compared to the standard methods using concentrated acid where a separation of Ir and other metals (Pt) is required.

Second, ORR studies were implemented in a GDE setup which is designed to mimic the operating conditions in a fuel cell more realistically. By testing and comparing the ORR performance of commercial Pt/C catalysts in both fundamental (in the RDE setup) and applied (in the GDE setup) situations (Manuscript II), the limits as well as the potentials of GDE measurement method could be elaborated. Furthermore, the concept of comparative ORR studies using RDE and GDE setups is used to investigate home-made catalysts, i.e., Pt-Ir/C and Pt-Au/C nanocomposites (Manuscript III). The results exhibit the same observations as demonstrated with the commercial Pt/C catalysts. That is, the determined intrinsic ORR activity (kinetically controlled region) is higher in RDE measurements than that in GDE measurements. This result is consistent with comparative RDE and MEA studies, i.e., it is challenging to transfer the impressive intrinsic ORR performance of a studied catalyst to a practical device (MEA). By further extending the potential region to high currents, it is found that the improved ORR rate of Pt-Au/C nanocomposites (in the kinetically controlled region) gradually becomes more comparable to the one of the Pt/C reference. After subjecting the catalysts to degradation treatments, however, the ORR performance is higher than Pt/C. Therefore, it is concluded that introducing Au mainly improves the stability of Pt. Unlike in Pt-Ir/C nanocomposites, the Au content is basically unchanged throughout the degradation measurements.

In the following study, Pt-Au/C nanocomposites were used to study a standard anode reaction, i.e., the FAOR. By combining electrochemical characterization with pair

distribution function (PDF), STEM-EDX, WAXS and *in situ* SAXS, it was demonstrated that during reaction conditions, the initially separate monometallic nanoparticles gradually formed (surface) alloy nanoparticles. Concomitantly with the alloy formation, the FAO characteristics improved. The nanocomposite concept allows a simple balancing of the Au to Pt mass ratio. The best performance was reached with five times more Au than Pt. By comparison, the nanocomposite with less Au nanoparticles (two times higher Au mass than Pt) shows less alloying and thus the characteristics of the FAO are improved in an unbalanced manner. In comparison with the conventional approach for alloy preparation, applying the nanocomposite concept for *in situ* surface alloy formation is facile and straightforward, and requires only the preparation of two kinds of nanoparticles. Apart from that, Pt-Au nanocomposites are suitable for several fuel cell reaction studies and thus are of interest for a broader audience.

Last but not least, the non-noble metal catalyst Fe-NC was elucidated for the ORR in the GDE setup. The studies once more demonstrated the suitability of using GDE for the study of catalyst materials. The measurement results demonstrate a comparable ORR performance for Fe-NC as compared to a Pt/C standard only in alkaline media. By comparison, in acidic media, the ORR performance of the Fe-NC catalyst is inferior to the Pt/C standard, which stresses the room for improvement for single site catalysts for PEMFC applications.

4.2 Perspectives

The concept of nanocomposite catalyst is used throughout the thesis. One of the discussions in section 3.1 focusses on the stability of bifunctional Pt-Ir/C nanocomposites during electrochemical measurements. It is concluded that the improvement of Pt stability is at the cost of Ir dissolution. The stability and the size of metal nanoparticles are closely correlated with each other, i.e., the smaller the particle size, the less stable the metal nanoparticles. It might therefore be interesting to use

larger Ir nanoparticles as starting blocks to prepare Pt-Ir/C nanocomposites to alleviate Ir dissolution and protect Pt from degradation. This raises the question/challenge how to modify the EG approach to prepare “surfactant-free” Ir nanoparticles of different sizes. The approach used for Pt, i.e., regulating the molar ratio of metal precursor and OH concentration did not work to adjust the size of Ir nanoparticles. A size control of “surfactant-free” Ir nanoparticles could be an interesting topic for future investigations. The “size effect” of metal nanoparticles poses an impact on the catalytic activity as well. For example, larger Pt nanoparticles display higher surface normalized ORR activity than the smaller ones. It would be interesting for future studies investigating Pt-Au/C nanocomposites for the ORR to enlarge the size of the Pt nanoparticles from ~1.8 nm (in this thesis) to ~ 5 nm. Such variation can be easily obtained by reducing the molar ratio of OH to Pt precursor, as already reported previously.

The investigation of the Pt-Au/C nanocomposites for the FAOR highlights that alloy formation of Pt and Au plays a significant role for the FAO performance. If, as assumed, surface alloy formation takes place, the usage of Pt would be maximized. In the studies, the size of the Au nanoparticles was roughly five times higher than the size of the Pt nanoparticles. It would be interesting to study the FAOR with nanocomposites consisting of small Au nanoparticles and large Pt nanoparticles to probe if the same performance in FAO is reached. If the structure of the Pt-Au surface alloy on the large Au nanoparticles influences the FAO behavior, using small Au nanoparticles would not show the desired effect. Such measurements could strengthen the hypothesis of a reduction in critical raw material by alloying Pt onto the Au surface. Furthermore, the study of FAOR was carried out in a GDE setup in which the FA was in the form of vapor. However, liquid FA serves as fuel in a DFAFC device. It would be therefore of interest to introduce liquid FA into the GDE setup for FAOR studies. Doing so, the hydrophobic GDL needs to be pre-treated to be more hydrophilic. This can be achieved for example by immersing the GDL into HNO_3 to dope the carbon surface with functional groups (OH- or/and O-).

In addition, the as-developed nanocomposite concept could be extended to other

elements, e.g., Ru. The mono-alcohol approach to prepare “surfactant-free” Ru nanoparticles is well-established and could be adopted to prepare Ru-based nanocomposites. The polymer membrane used in the GDE alleviates Ru dissolution in the acidic media. Therefore, by applying the GDE setup to investigate Ru-based nanocomposites for the OER in acidic media, it might be possible to achieve improved activity and stability, simultaneously.

5. Acknowledgement

Foremost I would like to give my thanks to my supervisor Matthias Arenz for giving me the opportunity to study in his group. I greatly appreciate his valuable guidance through my PhD studies. I feel lucky to be his student.

I would like to thank all my present group members. Gustav, his great discussion with me, his experience in experiments and his support on my data analysis, are all quite helpful for my studies. Damin, his flexible thinking often sheds light on my seemingly hopeless experiments. Shima, Nicolas, Aline, Vlad, Etienne, Ilya, Renan, Sven, Tim, many thanks to all of you for providing me with a pleasant working atmosphere.

I would also like to thank all my former group members. Alessandro, his patient instruction benefits me a lot in the initial stage of my PhD. Francesco, his inspiring suggestions help me so much for my lab work. Johanna, the person I talked the most in the group, thanks for your enthusiastic assistance. Jan, Rebecca, Rahel, thanks to all of you. Additionally, I would like to express my gratitude to Jonathan for his great collaboration with me.

I would like to thank all my Chinese friends I met in Bern. Ping, Huifang, Ying, Qi, Menglong, Yuhui, the time I spent with you banished the darkness from my life. I wish you all the very best.

Last but certainly not least, I would like to give my deepest gratitude to my parents, their support helps me to move forward with more courage.

6. Bibliography

(1) Martínez-Huerta, M. v.; Lázaro, M. J. Electrocatalysts for Low Temperature Fuel Cells. *Catalysis Today* **2017**, *285*, 3–12. https://doi.org/10.1016/j.cattod.2017.02.015.

(2) Lamy, C. Principle of Low-Temperature Fuel Cells Using an Ionic Membrane. In *Electrocatalysts for Low Temperature Fuel Cells: Fundamentals and Recent Trends*; Wiley-VCH Verlag, **2017**, pp 1–33. https://doi.org/10.1002/9783527803873.ch1.

(3) Rajalakshmi, N.; Imran Jafri, R.; Dhathathreyan, K. S. Research Advancements in Low-Temperature Fuel Cells. In *Electrocatalysts for Low Temperature Fuel Cells: Fundamentals and Recent Trends*; Wiley-VCH Verlag, **2017**, pp 35–74. https://doi.org/10.1002/9783527803873.ch2.

(4) Lamy, C. Electrocatalytic Reactions Involved in Low-Temperature Fuel Cells. In *Electrocatalysts for Low Temperature Fuel Cells: Fundamentals and Recent Trends*; Wiley-VCH Verlag, **2017**, pp 75–111. https://doi.org/10.1002/9783527803873.ch3.

(5) Maheshwari, K.; Sharma, S.; Sharma, A.; Verma, S. Fuel Cell and Its Applications: A Review. *International Journal of Engineering Research & Technology* **2018**, 6–9.

(6) Garche, J.; Ju rissen, L. Applications of Fuel Cell Technology: Status and Perspectives. *Interface magazine* **2015**, *24* (2), 39–43. https://doi.org/10.1149/2.F02152if.

(7) Hwan Choi, K.; Sung Kim, H.; Hee Lee, T. *Electrode Fabrication for Proton Exchange Membrane Fuel Cells by Pulse Electrodeposition*; **1998**, Vol. 75.

(8) Vishnyakov, V. M. Proton Exchange Membrane Fuel Cells. *Vacuum* **2006**, *80* (10), 1053–1065. https://doi.org/10.1016/j.vacuum.2006.03.029.

(9) Mohammed, H.; Al-Othman, A.; Nancarrow, P.; Tawalbeh, M.; el Haj Assad, M. Direct Hydrocarbon Fuel Cells: A Promising Technology for Improving Energy Efficiency. *Energy* **2019**, *172*, 207–219.

https://doi.org/10.1016/j.energy.2019.01.105.

(10) Kraytsberg, A.; Ein-Eli, Y. Review of Advanced Materials for Proton Exchange Membrane Fuel Cells. *Energy and Fuels* **2014**, *28* (12), 7303–7330. https://doi.org/10.1021/ef501977k.

(11) Tellez-Cruz, M. M.; Escorihuela, J.; Solorza-Feria, O.; Compañ, V. Proton Exchange Membrane Fuel Cells (Pemfcs): Advances and Challenges. *Polymers*. MDPI September 1, **2021**. https://doi.org/10.3390/polym13183064.

(12) Eppinger, J.; Huang, K. W. Formic Acid as a Hydrogen Energy Carrier. *ACS Energy Letters*. American Chemical Society January 13, **2017**, pp 188–195. https://doi.org/10.1021/acsenergylett.6b00574.

(13) Ranjekar, A. M.; Yadav, G. D. Steam Reforming of Methanol for Hydrogen Production: A Critical Analysis of Catalysis, Processes, and Scope. *Industrial and Engineering Chemistry Research* **2021**, *60* (1), 89–113. https://doi.org/10.1021/acs.iecr.0c05041.

(14) Deluga, G. A.; Salge, J. R.; Schmidt, L. D.; Verykios, X. E. Renewable Hydrogen from Ethanol by Autothermal Reforming. *Science (1979)* **2004**, *303* (5660), 993–997. https://doi.org/10.1126/science.1093045.

(15) Rice, C.; Ha, S.; Masel, R. I.; Waszczuk, P.; Wieckowski, A.; Barnard, T. Direct Formic Acid Fuel Cells. *Journal of Power Sources* **2002**, *111* (1), 83–89. https://doi.org/10.1016/S0378-7753(02)00271-9.

(16) Aslam, N. M.; Masdar, M. S.; Kamarudin, S. K.; Daud, W. R. W. Overview on Direct Formic Acid Fuel Cells (DFAFCs) as an Energy Sources. *APCBEE Procedia* **2012**, *3*, 33–39. https://doi.org/10.1016/j.apcbee.2012.06.042.

(17) Kamarudin, S. K.; Achmad, F.; Daud, W. R. W. Overview on the Application of Direct Methanol Fuel Cell (DMFC) for Portable Electronic Devices. *International Journal of Hydrogen Energy*. August **2009**, pp 6902–6916. https://doi.org/10.1016/j.ijhydene.2009.06.013.

(18) Mallick, R. K.; Thombre, S. B.; Shrivastava, N. K. Vapor Feed Direct Methanol Fuel Cells (DMFCs): A Review. *Renewable and Sustainable Energy Reviews*.

Elsevier Ltd April 1, **2016**, pp 51–74. https://doi.org/10.1016/j.rser.2015.11.039.

(19) Lamy, C.; Rousseau, S.; Belgsir, E. M.; Coutanceau, C.; Léger, J. M. Recent Progress in the Direct Ethanol Fuel Cell: Development of New Platinum-Tin Electrocatalysts. In *Electrochimica Acta*; **2004**, Vol. 49, pp 3901–3908. https://doi.org/10.1016/j.electacta.2004.01.078.

(20) Braunchweig, B.; Hibbitts, D.; Neurock, M.; Wieckowski, A. Electrocatalysis: A Direct Alcohol Fuel Cell and Surface Science Perspective. *Catalysis Today* **2013**, *202* (1), 197–209. https://doi.org/10.1016/j.cattod.2012.08.013.

(21) Yu, X.; Pickup, P. G. Recent Advances in Direct Formic Acid Fuel Cells (DFAFC). *Journal of Power Sources* **2008**, *182* (1), 124–132. https://doi.org/10.1016/j.jpowsour.2008.03.075.

(22) Wang, X.; Hu, J. M.; Hsing, I. M. Electrochemical Investigation of Formic Acid Electro-Oxidation and Its Crossover through a Nafion ® Membrane. *Journal of Electroanalytical Chemistry* **2004**, *562* (1), 73–80. https://doi.org/10.1016/j.jelechem.2003.08.010.

(23) Gottesfeld, S.; Dekel, D. R.; Page, M.; Bae, C.; Yan, Y.; Zelenay, P.; Kim, Y. S. Anion Exchange Membrane Fuel Cells: Current Status and Remaining Challenges. *Journal of Power Sources* **2018**, *375*, 170–184. https://doi.org/10.1016/j.jpowsour.2017.08.010.

(24) Zhang, J.; Zhu, W.; Huang, T.; Zheng, C.; Pei, Y.; Shen, G.; Nie, Z.; Xiao, D.; Yin, Y.; Guiver, M. D. Recent Insights on Catalyst Layers for Anion Exchange Membrane Fuel Cells. *Advanced Science*. John Wiley and Sons Inc August 1, **2021**. https://doi.org/10.1002/advs.202100284.

(25) Xiong, Y.; Fang, J.; Zeng, Q. H.; Liu, Q. L. Preparation and Characterization of Cross-Linked Quaternized Poly(Vinyl Alcohol) Membranes for Anion Exchange Membrane Fuel Cells. *Journal of Membrane Science* **2008**, *311* (1–2), 319–325. https://doi.org/10.1016/j.memsci.2007.12.029.

(26) Li, L.; Zhang, N.; Wang, J. ao; Ma, L.; Bai, L.; Zhang, A.; Chen, Y.; Hao, C.; Yan, X.; Zhang, F.; He, G. Stable Alkoxy Chain Enhanced Anion Exchange

Membrane and Its Fuel Cell. *Journal of Membrane Science* **2022**, *644*. https://doi.org/10.1016/j.memsci.2021.120179.

(27) Nørskov, J. K.; Rossmeisl, J.; Logadottir, A.; Lindqvist, L.; Kitchin, J. R.; Bligaard, T.; Jónsson, H. Origin of the Overpotential for Oxygen Reduction at a Fuel-Cell Cathode. *Journal of Physical Chemistry B* **2004**, *108* (46), 17886–17892. https://doi.org/10.1021/jp047349j.

(28) Russell, A. E. Faraday Discussions: Preface. *Faraday Discussions*. **2008**, pp 9–10. https://doi.org/10.1039/b814058h.

(29) Karlberg, G. S.; Rossmeisl, J.; Nørskov, J. K. Estimations of Electric Field Effects on the Oxygen Reduction Reaction Based on the Density Functional Theory. *Physical Chemistry Chemical Physics* **2007**, *9* (37), 5158–5161. https://doi.org/10.1039/b705938h.

(30) Jinnouchi, R.; Kodama, K.; Hatanaka, T.; Morimoto, Y. First Principles Based Mean Field Model for Oxygen Reduction Reaction. *Physical Chemistry Chemical Physics* **2011**, *13* (47), 21070–21083. https://doi.org/10.1039/c1cp21349k.

(31) Ke, K.; Hatanaka, T.; Morimoto, Y. Reconsideration of the Quantitative Characterization of the Reaction Intermediate on Electrocatalysts by a Rotating Ring-Disk Electrode: The Intrinsic Yield of H2O2 on Pt/C. *Electrochimica Acta* **2011**, *56* (5), 2098–2104. https://doi.org/10.1016/j.electacta.2010.11.086.

(32) Hodnik, N.; Baldizzone, C.; Cherevko, S.; Zeradjanin, A.; Mayrhofer, K. J. J. The Effect of the Voltage Scan Rate on the Determination of the Oxygen Reduction Activity of Pt/C Fuel Cell Catalyst. *Electrocatalysis* **2015**, *6* (3), 237–241. https://doi.org/10.1007/s12678-015-0255-0.

(33) Wiberg, G. K. H.; Arenz, M. Establishing the Potential Dependent Equilibrium Oxide Coverage on Platinum in Alkaline Solution and Its Influence on the Oxygen Reduction. *Journal of Power Sources* **2012**, *217*, 262–267. https://doi.org/10.1016/j.jpowsour.2012.06.019.

(34) Debe, M. K. Electrocatalyst Approaches and Challenges for Automotive Fuel

Cells. *Nature* **2012**, *486* (7401), 43–51. https://doi.org/10.1038/nature11115.

(35) Han, B.; Carlton, C. E.; Kongkanand, A.; Kukreja, R. S.; Theobald, B. R.; Gan, L.; O'Malley, R.; Strasser, P.; Wagner, F. T.; Shao-Horn, Y. Record Activity and Stability of Dealloyed Bimetallic Catalysts for Proton Exchange Membrane Fuel Cells. *Energy and Environmental Science* **2015**, *8* (1), 258–266. https://doi.org/10.1039/c4ee02144d.

(36) Pinaud, B. A.; Bonakdarpour, A.; Daniel, L.; Sharman, J.; Wilkinson, D. P. Key Considerations for High Current Fuel Cell Catalyst Testing in an Electrochemical Half-Cell. *Journal of The Electrochemical Society* **2017**, *164* (4), F321–F327. https://doi.org/10.1149/2.0891704jes.

(37) Ehelebe, K.; Seeberger, D.; Paul, M. T. Y.; Thiele, S.; Mayrhofer, K. J. J.; Cherevko, S. Evaluating Electrocatalysts at Relevant Currents in a Half-Cell: The Impact of Pt Loading on Oxygen Reduction Reaction. *Journal of The Electrochemical Society* **2019**, *166* (16), F1259–F1268. https://doi.org/10.1149/2.0911915jes.

(38) Zalitis, C. M.; Kramer, D.; Kucernak, A. R. Electrocatalytic Performance of Fuel Cell Reactions at Low Catalyst Loading and High Mass Transport. *Physical Chemistry Chemical Physics* **2013**, *15* (12), 4329–4340. https://doi.org/10.1039/c3cp44431g.

(39) Chen, Y. X.; Li, M. F.; Liao, L. W.; Xu, J.; Ye, S. A Thermostatic Cell with Gas Diffusion Electrode for Oxygen Reduction Reaction under Fuel Cell Relevant Conditions. *Electrochemistry Communications* **2009**, *11* (7), 1434–1436. https://doi.org/10.1016/j.elecom.2009.05.023.

(40) Inaba, M.; Jensen, A. W.; Sievers, G. W.; Escudero-Escribano, M.; Zana, A.; Arenz, M. Benchmarking High Surface Area Electrocatalysts in a Gas Diffusion Electrode: Measurement of Oxygen Reduction Activities under Realistic Conditions. *Energy and Environmental Science* **2018**, *11* (4), 988–994. https://doi.org/10.1039/c8ee00019k.

(41) Alinejad, S.; Inaba, M.; Schröder, J.; Du, J.; Quinson, J.; Zana, A.; Arenz, M.

Testing Fuel Cell Catalysts under More Realistic Reaction Conditions: Accelerated Stress Tests in a Gas Diffusion Electrode Setup. *JPhys Energy* **2020**, *2* (2). https://doi.org/10.1088/2515-7655/ab67e2.

(42) Du, J.; Quinson, J.; Zana, A.; Arenz, M. Elucidating Pt-Based Nanocomposite Catalysts for the Oxygen Reduction Reaction in Rotating Disk Electrode and Gas Diffusion Electrode Measurements. *ACS Catalysis* **2021**, *11* (12), 7584–7594. https://doi.org/10.1021/acscatal.1c01496.

(43) Marković, N. M.; Adžić, R. R.; Cahan, B. D.; Yeager, E. B. Structural Effects in Electrocatalysis: Oxygen Reduction on Platinum Low Index Single-Crystal Surfaces in Perchloric Acid Solutions. *Journal of Electroanalytical Chemistry* **1994**, *377* (1–2), 249–259. https://doi.org/10.1016/0022-0728(94)03467-2.

(44) Markovic, N. M.; Gasteiger, H. A.; Ross, P. N. Oxygen Reduction on Platinum Low-Index Single-Crystal Surfaces in Sulfuric Acid Solution: Rotating Ring-Pt(Hkl) Disk Studies. *The Journal of Physical Chemistry* **1995**, *99* (11), 3411–3415. https://doi.org/10.1021/j100011a001.

(45) Markovic, N. M.; Gasteiger, H. A.; Ross, P. N. *Oxygen Reduction on Platinum Low-Index Single-Crystal Surfaces in Alkaline Solution: Rotating Ring Disk Pt(Hkl) Studies*; **1996**.

(46) Ahmadi, T. S.; Wang, Z. L.; Green, T. C.; Henglein, A.; El-Sayed, M. A. Shape-Controlled Synthesis of Colloidal Platinum Nanoparticles. *Science (1979)* **1996**, *272* (5270), 1924–1925. https://doi.org/10.1126/science.272.5270.1924.

(47) Yu, Y. T.; Xu, B. Q. Shape-Controlled Synthesis of Pt Nanocrystals: An Evolution of the Tetrahedral Shape. *Applied Organometallic Chemistry* **2006**, *20* (10), 638–647. https://doi.org/10.1002/aoc.1123.

(48) Tao, A. R.; Habas, S.; Yang, P. Shape Control of Colloidal Metal Nanocrystals. *Small*. March **2008**, pp 310–325. https://doi.org/10.1002/smll.200701295.

(49) Kodambaka, S.; Tersoff, J.; Reuter, M. C.; Ross, F. M. Germanium Nanowire Growth below the Eutectic Temperature. *Science (1979)* **2007**, *316* (5825), 729–732. https://doi.org/10.1126/science.1139105.

(50) Li, D.; Wang, C.; Strmcnik, D. S.; Tripkovic, D. v.; Sun, X.; Kang, Y.; Chi, M.; Snyder, J. D.; van der Vliet, D.; Tsai, Y.; Stamenkovic, V. R.; Sun, S.; Markovic, N. M. Functional Links between Pt Single Crystal Morphology and Nanoparticles with Different Size and Shape: The Oxygen Reduction Reaction Case. *Energy and Environmental Science* **2014**, *7* (12), 4061–4069. https://doi.org/10.1039/c4ee01564a.

(51) Mayrhofer, K. J. J.; Blizanac, B. B.; Arenz, M.; Stamenkovic, V. R.; Ross, P. N.; Markovic, N. M. The Impact of Geometric and Surface Electronic Properties of Pt-Catalysts on the Particle Size Effect in Electrocatalysis. *Journal of Physical Chemistry B* **2005**, *109* (30), 14433–14440. https://doi.org/10.1021/jp051735z.

(52) Shinozaki, K.; Morimoto, Y.; Pivovar, B. S.; Kocha, S. S. Re-Examination of the Pt Particle Size Effect on the Oxygen Reduction Reaction for Ultrathin Uniform Pt/C Catalyst Layers without Influence from Nafion. *Electrochimica Acta* **2016**, *213*, 783–790. https://doi.org/10.1016/j.electacta.2016.08.001.

(53) Mayrhofer, K. J. J.; Strmcnik, D.; Blizanac, B. B.; Stamenkovic, V.; Arenz, M.; Markovic, N. M. Measurement of Oxygen Reduction Activities via the Rotating Disc Electrode Method: From Pt Model Surfaces to Carbon-Supported High Surface Area Catalysts. *Electrochimica Acta* **2008**, *53* (7), 3181–3188. https://doi.org/10.1016/j.electacta.2007.11.057.

(54) Nesselberger, M.; Ashton, S.; Meier, J. C.; Katsounaros, I.; Mayrhofer, K. J. J.; Arenz, M. The Particle Size Effect on the Oxygen Reduction Reaction Activity of Pt Catalysts: Influence of Electrolyte and Relation to Single Crystal Models. *J Am Chem Soc* **2011**, *133* (43), 17428–17433. https://doi.org/10.1021/ja207016u.

(55) Yano, H.; Inukai, J.; Uchida, H.; Watanabe, M.; Babu, P. K.; Kobayashi, T.; Chung, J. H.; Oldfield, E.; Wieckowski, A. Particle-Size Effect of Nanoscale Platinum Catalysts in Oxygen Reduction Reaction: An Electrochemical and 195Pt EC-NMR Study. *Physical Chemistry Chemical Physics* **2006**, *8* (42), 4932–4939. https://doi.org/10.1039/b610573d.

(56) Shao, M.; Peles, A.; Shoemaker, K. Electrocatalysis on Platinum Nanoparticles: Particle Size Effect on Oxygen Reduction Reaction Activity. *Nano Letters* **2011**, *11* (9), 3714–3719. https://doi.org/10.1021/nl2017459.

(57) Inaba, M.; Zana, A.; Quinson, J.; Bizzotto, F.; Dosche, C.; Dworzak, A.; Oezaslan, M.; Simonsen, S. B.; Kuhn, L. T.; Arenz, M. The Oxygen Reduction Reaction on Pt: Why Particle Size and Interparticle Distance Matter. *ACS Catalysis* **2021**, *11* (12), 7144–7153. https://doi.org/10.1021/acscatal.1c00652.

(58) Perez-Alonso, F. J.; McCarthy, D. N.; Nierhoff, A.; Hernandez-Fernandez, P.; Strebel, C.; Stephens, I. E. L.; Nielsen, J. H.; Chorkendorff, I. The Effect of Size on the Oxygen Electroreduction Activity of Mass-Selected Platinum Nanoparticles. *Angewandte Chemie - International Edition* **2012**, *51* (19), 4641–4643. https://doi.org/10.1002/anie.201200586.

(59) Bregoli, L. J. The Influence of Platinum Crystallite Size on the Electrochemical Reduction of Oxygen in Phosphoric Acid. *Electrochimica Acta* **1978**, *23* (6), 489–492. https://doi.org/10.1016/0013-4686(78)85025-7.

(60) Watanabe, M.; Sei, H.; Stonehart, P. *The Influence of Platinum Crystallite Size on the Electroreduction of Oxygen*; Elsevier Sequoia S.A, **1989**, Vol. 261.

(61) Toyoda, E.; Jinnouchi, R.; Hatanaka, T.; Morimoto, Y.; Mitsuhara, K.; Visikovskiy, A.; Kido, Y. The D-Band Structure of Pt Nanoclusters Correlated with the Catalytic Activity for an Oxygen Reduction Reaction. *Journal of Physical Chemistry C* **2011**, *115* (43), 21236–21240. https://doi.org/10.1021/jp206360e.

(62) Takasij, Y.; Ohashi, $ N; Zhang, X.-G.; Murakami, Y.; Minagawa, H.; Sato~, ? S; Yahikozawa, K. *SIZE EFFECTS OF PLATINUM PARTICLES ON THE ELECTROREDUCTION OF OXYGEN*; **1996**, Vol. 41.

(63) Tritsaris, G. A.; Greeley, J.; Rossmeisl, J.; Nørskov, J. K. Atomic-Scale Modeling of Particle Size Effects for the Oxygen Reduction Reaction on Pt. *Catalysis Letters* **2011**, *141* (7), 909–913. https://doi.org/10.1007/s10562-011-0637-8.

(64) Stephens, I. E. L.; Bondarenko, A. S.; Grønbjerg, U.; Rossmeisl, J.;

Chorkendorff, I. Understanding the Electrocatalysis of Oxygen Reduction on Platinum and Its Alloys. *Energy and Environmental Science*. May **2012**, pp 6744–6762. https://doi.org/10.1039/c2ee03590a.

(65) Seidel, Y. E.; Schneider, A.; Jusys, Z.; Wickman, B.; Kasemo, B.; Behm, R. J. Mesoscopic Mass Transport Effects in Electrocatalytic Processes. *Faraday Discuss.* **2009**, *140*, 167–184. https://doi.org/10.1039/B806437G.

(66) Nesselberger, M.; Roefzaad, M.; Fayçal Hamou, R.; Ulrich Biedermann, P.; Schweinberger, F. F.; Kunz, S.; Schloegl, K.; Wiberg, G. K. H.; Ashton, S.; Heiz, U.; Mayrhofer, K. J. J.; Arenz, M. The Effect of Particle Proximity on the Oxygen Reduction Rate of Size-Selected Platinum Clusters. *Nature Materials* **2013**, *12* (10), 919–924. https://doi.org/10.1038/nmat3712.

(67) Fabbri, E.; Taylor, S.; Rabis, A.; Levecque, P.; Conrad, O.; Kötz, R.; Schmidt, T. J. The Effect of Platinum Nanoparticle Distribution on Oxygen Electroreduction Activity and Selectivity. *ChemCatChem* **2014**, *6* (5), 1410–1418. https://doi.org/10.1002/cctc.201300987.

(68) Speder, J.; Altmann, L.; Bäumer, M.; Kirkensgaard, J. J. K.; Mortensen, K.; Arenz, M. The Particle Proximity Effect: From Model to High Surface Area Fuel Cell Catalysts. *RSC Advances* **2014**, *4* (29), 14971–14978. https://doi.org/10.1039/c4ra00261j.

(69) Shao, M.; Chang, Q.; Dodelet, J. P.; Chenitz, R. Recent Advances in Electrocatalysts for Oxygen Reduction Reaction. *Chemical Reviews*. American Chemical Society March 23, **2016**, pp 3594–3657. https://doi.org/10.1021/acs.chemrev.5b00462.

(70) Stamenkovic, V. R.; Mun, B. S.; Arenz, M.; Mayrhofer, K. J. J.; Lucas, C. A.; Wang, G.; Ross, P. N.; Markovic, N. M. Trends in Electrocatalysis on Extended and Nanoscale Pt-Bimetallic Alloy Surfaces. *Nature Materials* **2007**, *6* (3), 241–247. https://doi.org/10.1038/nmat1840.

(71) Marković, N. M.; Schmidt, T. J.; Stamenković, V.; Ross, P. N. Oxygen Reduction Reaction on Pt and Pt Bimetallic Surfaces: A Selective Review. *Fuel Cells* **2001**,

1 (2), 105–116. https://doi.org/10.1002/1615-6854(200107)1:2<105::aid-fuce105>3.0.co;2-9.

(72) Stamenkovic, V.; Mun, B. S.; Mayrhofer, K. J. J.; Ross, P. N.; Markovic, N. M.; Rossmeisl, J.; Greeley, J.; Nørskov, J. K. Changing the Activity of Electrocatalysts for Oxygen Reduction by Tuning the Surface Electronic Structure. *Angewandte Chemie* **2006**, *118* (18), 2963–2967. https://doi.org/10.1002/ange.200504386.

(73) Bligaard, T.; Nørskov, J. K. Ligand Effects in Heterogeneous Catalysis and Electrochemistry. *Electrochimica Acta* **2007**, *52* (18), 5512–5516. https://doi.org/10.1016/j.electacta.2007.02.041.

(74) Bligaard, T.; Nørskov, J. K.; Dahl, S.; Matthiesen, J.; Christensen, C. H.; Sehested, J. The Brønsted-Evans-Polanyi Relation and the Volcano Curve in Heterogeneous Catalysis. *Journal of Catalysis* **2004**, *224* (1), 206–217. https://doi.org/10.1016/j.jcat.2004.02.034.

(75) Jovanovič, P.; Može, M.; Gričar, E.; Šala, M.; Ruiz-Zepeda, F.; Bele, M.; Marolt, G.; Hodnik, N. Effect of Particle Size on the Corrosion Behaviour of Gold in the Presence of Chloride Impurities: An EFC-ICP-MS Potentiodynamic Study. *Coatings* **2019**, *9* (1). https://doi.org/10.3390/coatings9010010.

(76) Cherevko, S.; Topalov, A. A.; Zeradjanin, A. R.; Katsounaros, I.; Mayrhofer, K. J. J. Gold Dissolution: Towards Understanding of Noble Metal Corrosion. *RSC Advances* **2013**, *3* (37), 16516–16527. https://doi.org/10.1039/c3ra42684j.

(77) *COMMITTEE AND THE COMMITTEE OF THE REGIONS* Critical Raw Materials Resilience: Charting a Path towards Greater Security and Sustainability, 1; **2020**.

(78) Zhang, J.; Sasaki, K.; Sutter, E.; Adzic, R. R. Stabilization of Platinum Oxygen-Reduction Electrocatalysts Using Gold Clusters. *Science (1979)* **2007**, *315* (5809), 220–222. https://doi.org/10.1126/science.1134569.

(79) Wei, G. F.; Liu, Z. P. Optimum Nanoparticles for Electrocatalytic Oxygen Reduction: The Size, Shape and New Design. *Physical Chemistry Chemical*

Physics **2013**, *15* (42), 18555–18561. https://doi.org/10.1039/c3cp53758g.

(80) Kodama, K.; Jinnouchi, R.; Takahashi, N.; Murata, H.; Morimoto, Y. Activities and Stabilities of Au-Modified Stepped-Pt Single-Crystal Electrodes as Model Cathode Catalysts in Polymer Electrolyte Fuel Cells. *J Am Chem Soc* **2016**, *138* (12), 4194–4200. https://doi.org/10.1021/jacs.6b00359.

(81) Bian, T.; Zhang, H.; Jiang, Y.; Jin, C.; Wu, J.; Yang, H.; Yang, D. Epitaxial Growth of Twinned Au-Pt Core-Shell Star-Shaped Decahedra as Highly Durable Electrocatalysts. *Nano Letters* **2015**, *15* (12), 7808–7815. https://doi.org/10.1021/acs.nanolett.5b02960.

(82) Chung, D. Y.; Park, S.; Lee, H.; Kim, H.; Chung, Y. H.; Yoo, J. M.; Ahn, D.; Yu, S. H.; Lee, K. S.; Ahmadi, M.; Ju, H.; Abruña, H. D.; Yoo, S. J.; Mun, B. S.; Sung, Y. E. Activity-Stability Relationship in Au@Pt Nanoparticles for Electrocatalysis. *ACS Energy Letters* **2020**, *5* (9), 2827–2834. https://doi.org/10.1021/acsenergylett.0c01507.

(83) Deng, Y. J.; Tripkovic, V.; Rossmeisl, J.; Arenz, M. Oxygen Reduction Reaction on Pt Overlayers Deposited onto a Gold Film: Ligand, Strain, and Ensemble Effect. *ACS Catalysis* **2016**, *6* (2), 671–676. https://doi.org/10.1021/acscatal.5b02409.

(84) Yin, S.; Ding, Y. Bimetallic PtAu Electrocatalysts for the Oxygen Reduction Reaction: Challenges and Opportunities. *Dalton Transactions*. Royal Society of Chemistry April 14, **2020**, pp 4189–4199. https://doi.org/10.1039/d0dt00205d.

(85) Tian, X.; Lu, X. F.; Xia, B. Y.; Lou, X. W. (David). Advanced Electrocatalysts for the Oxygen Reduction Reaction in Energy Conversion Technologies. *Joule*. Cell Press January 15, **2020**, pp 45–68. https://doi.org/10.1016/j.joule.2019.12.014.

(86) Yang, Z.; Wang, Y.; Zhu, M.; Li, Z.; Chen, W.; Wei, W.; Yuan, T.; Qu, Y.; Xu, Q.; Zhao, C.; Wang, X.; Li, P.; Li, Y.; Wu, Y.; Li, Y. Boosting Oxygen Reduction Catalysis with Fe-N 4 Sites Decorated Porous Carbons toward Fuel Cells. *ACS Catalysis* **2019**, *9* (3), 2158–2163. https://doi.org/10.1021/acscatal.8b04381.

(87) Adabi, H.; Shakouri, A.; Ul Hassan, N.; Varcoe, J. R.; Zulevi, B.; Serov, A.; Regalbuto, J. R.; Mustain, W. E. High-Performing Commercial Fe–N–C Cathode Electrocatalyst for Anion-Exchange Membrane Fuel Cells. *Nature Energy* **2021**, *6* (8), 834–843. https://doi.org/10.1038/s41560-021-00878-7.

(88) Zhang, H.; Chung, H. T.; Cullen, D. A.; Wagner, S.; Kramm, U. I.; More, K. L.; Zelenay, P.; Wu, G. High-Performance Fuel Cell Cathodes Exclusively Containing Atomically Dispersed Iron Active Sites. *Energy and Environmental Science* **2019**, *12* (8), 2548–2558. https://doi.org/10.1039/c9ee00877b.

(89) Xu, H.; Wang, D.; Yang, P.; Liu, A.; Li, R.; Li, Y.; Xiao, L.; Ren, X.; Zhang, J.; An, M. Atomically Dispersed M-N-C Catalysts for the Oxygen Reduction Reaction. *Journal of Materials Chemistry A* **2020**, *8* (44), 23187–23201. https://doi.org/10.1039/d0ta08732g.

(90) Yi, J. D.; Xu, R.; Wu, Q.; Zhang, T.; Zang, K. T.; Luo, J.; Liang, Y. L.; Huang, Y. B.; Cao, R. Atomically Dispersed Iron-Nitrogen Active Sites within Porphyrinic Triazine-Based Frameworks for Oxygen Reduction Reaction in Both Alkaline and Acidic Media. *ACS Energy Letters* **2018**, *3* (4), 883–889. https://doi.org/10.1021/acsenergylett.8b00245.

(91) Wang, J.; Huang, Z.; Liu, W.; Chang, C.; Tang, H.; Li, Z.; Chen, W.; Jia, C.; Yao, T.; Wei, S.; Wu, Y.; Li, Y. Design of N-Coordinated Dual-Metal Sites: A Stable and Active Pt-Free Catalyst for Acidic Oxygen Reduction Reaction. *J Am Chem Soc* **2017**, *139* (48), 17281–17284. https://doi.org/10.1021/jacs.7b10385.

(92) Folkman, S. J.; González-Cobos, J.; Giancola, S.; Sánchez-Molina, I.; Galán-Mascarós, J. R. Benchmarking Catalysts for Formic Acid/Formate Electrooxidation. *Molecules*. MDPI AG August 2, **2021**. https://doi.org/10.3390/molecules26164756.

(93) Fang, Z.; Chen, W. Recent Advances in Formic Acid Electro-Oxidation: From the Fundamental Mechanism to Electrocatalysts. *Nanoscale Advances* **2021**, *3* (1), 94–105. https://doi.org/10.1039/d0na00803f.

(94) Kim, J.; Roh, C. W.; Sahoo, S. K.; Yang, S.; Bae, J.; Han, J. W.; Lee, H. Highly

Durable Platinum Single-Atom Alloy Catalyst for Electrochemical Reactions. *Advanced Energy Materials* **2018**, *8* (1). https://doi.org/10.1002/aenm.201701476.

(95) Capon, A. The Oxidation of Formic Acid at Noble Metal Electrodes I. Review of Previous Work. *Journal of Electroanalytical Chemistry* **1973**, *44* (1), 1–7. https://doi.org/10.1016/0368-1874(73)85001-4.

(96) Beden, B.; Bewick, A.; Lamy, C. A COMPARATIVE STUDY OF FORMIC ACID ADSORPTION ON A PLATINUM ELECTRODE BY BOTH ELECTROCHEMICAL AND EMIRS TECHNIQUES; Elsevier Sequoia S.A, **1983**; Vol. 150.

(97) Cuesta, A.; Cabello, G.; Osawa, M.; Gutiérrez, C. Mechanism of the Electrocatalytic Oxidation of Formic Acid on Metals. *ACS Catalysis* **2012**, *2* (5), 728–738. https://doi.org/10.1021/cs200661z.

(98) Qi, Y.; Li, J.; Zhang, D.; Liu, C. Reexamination of Formic Acid Decomposition on the Pt(111) Surface Both in the Absence and in the Presence of Water, from Periodic DFT Calculations. *Catalysis Science and Technology* **2015**, *5* (6), 3322–3332. https://doi.org/10.1039/c5cy00159e.

(99) Ferre-Vilaplana, A.; Perales-Rondón, J. v.; Buso-Rogero, C.; Feliu, J. M.; Herrero, E. Formic Acid Oxidation on Platinum Electrodes: A Detailed Mechanism Supported by Experiments and Calculations on Well-Defined Surfaces. *Journal of Materials Chemistry A* **2017**, *5* (41), 21773–21784. https://doi.org/10.1039/c7ta07116g.

(100) Zhu, X.; Huang, J. Modeling Electrocatalytic Oxidation of Formic Acid at Platinum. *Journal of The Electrochemical Society* **2020**, *167* (1), 013515. https://doi.org/10.1149/2.0152001jes.

(101) Chen, Y. X.; Heinen, M.; Jusys, Z.; Behm, R. J. Bridge-Bonded Formate: Active Intermediate or Spectator Species in Formic Acid Oxidation on a Pt Film Electrode? *Langmuir* **2006**, *22* (25), 10399–10408. https://doi.org/10.1021/la060928q.

(102) Wang, H. F.; Liu, Z. P. Formic Acid Oxidation at Pt/H2O Interface from Periodic DFT Calculations Integrated with a Continuum Solvation Model. *Journal of Physical Chemistry C* **2009**, *113* (40), 17502–17508. https://doi.org/10.1021/jp9059888.

(103) Zhang, D.; Du, J.; Quinson, J.; Arenz, M. On the Electro-Oxidation of Small Organic Molecules: Towards a Fuel Cell Catalyst Testing Platform Based on Gas Diffusion Electrode Setups. *Journal of Power Sources* **2022**, *522*, 230979. https://doi.org/10.1016/j.jpowsour.2022.230979.

(104) Krstajić Pajić, M. N.; Stevanović, S. I.; Radmilović, V. v.; Gavrilović-Wohlmuther, A.; Zabinski, P.; Elezović, N. R.; Radmilović, V. R.; Gojković, S. L.; Jovanović, V. M. Dispersion Effect in Formic Acid Oxidation on PtAu/C Nanocatalyst Prepared by Water-in-Oil Microemulsion Method. *Applied Catalysis B: Environmental* **2019**, *243* (July 2018), 585–593. https://doi.org/10.1016/j.apcatb.2018.10.064.

(105) Huang, L.; Zheng, C. Y.; Shen, B.; Mirkin, C. A. High-Index-Facet Metal-Alloy Nanoparticles as Fuel Cell Electrocatalysts. *Advanced Materials* **2020**, *32* (30). https://doi.org/10.1002/adma.202002849.

(106) Obradović, M. D.; Rogan, J. R.; Babić, B. M.; Tripković, A. v.; Gautam, A. R. S.; Radmilović, V. R.; Gojković, S. L. Formic Acid Oxidation on Pt-Au Nanoparticles: Relation between the Catalyst Activity and the Poisoning Rate. *Journal of Power Sources* **2012**, *197*, 72–79. https://doi.org/10.1016/j.jpowsour.2011.09.043.

(107) Wang, Y.; Xiong, Z.; Xia, Y. Branched PdAu Nanowires with Superior Electrocatalytic Formic Acid Oxidation Activities. *RSC Advances* **2017**, *7* (64), 40462–40469. https://doi.org/10.1039/c7ra02115a.

(108) Peng, Y.; Li, L.; Tao, R.; Tan, L.; Qiu, M.; Guo, L. One-Pot Synthesis of Au@Pt Star-like Nanocrystals and Their Enhanced Electrocatalytic Performance for Formic Acid and Ethanol Oxidation. *Nano Research* **2018**, *11* (6), 3222–3232. https://doi.org/10.1007/s12274-017-1851-5.

(109) Zhang, J.; Chen, M.; Li, H.; Li, Y.; Ye, J.; Cao, Z.; Fang, M.; Kuang, Q.; Zheng, J.; Xie, Z. Stable Palladium Hydride as a Superior Anode Electrocatalyst for Direct Formic Acid Fuel Cells. *Nano Energy* **2018**, *44*, 127–134. https://doi.org/10.1016/j.nanoen.2017.11.075.

(110) Samjeské, G.; Osawa, M. Current Oscillations during Formic Acid Oxidation on a Pt Electrode: Insight into the Mechanism by Time-Resolved IR Spectroscopy. *Angewandte Chemie - International Edition* **2005**, *44* (35), 5694–5698. https://doi.org/10.1002/anie.200501009.

(111) Chen, Y. X.; Ye, S.; Heinen, M.; Jusys, Z.; Osawa, M.; Behm, R. J. Application of In-Situ Attenuated Total Reflection-Fourier Transform Infrared Spectroscopy for the Understanding of Complex Reaction Mechanism and Kinetics: Formic Acid Oxidation on a Pt Film Electrode at Elevated Temperatures. *Journal of Physical Chemistry B* **2006**, *110* (19), 9534–9544. https://doi.org/10.1021/jp057463h.

(112) Cappellari, P. S.; García, G.; Florez-Montaño, J.; Barbero, C. A.; Pastor, E.; Planes, G. A. Enhanced Formic Acid Oxidation on Polycrystalline Platinum Modified by Spontaneous Deposition of Gold. Fourier Transform Infrared Spectroscopy Studies. *Journal of Power Sources* **2015**, *296*, 290–297. https://doi.org/10.1016/j.jpowsour.2015.07.005.

(113) Smith, S. P. E.; Casado-Rivera, E.; Abruña, H. D. Application of Differential Electrochemical Mass Spectrometry to the Electrocatalytic Oxidation of Formic Acid at a Modified Bi/Pt Electrode Surface. *Journal of Solid State Electrochemistry* **2003**, *7* (9), 582–587. https://doi.org/10.1007/s10008-003-0385-9.

(114) Baltruschat, H. Differential Electrochemical Mass Spectrometry. *J Am Soc Mass Spectrom* **2004**, *15* (12), 1693–1706. https://doi.org/10.1016/j.jasms.2004.09.011.

(115) Sun, S.-G.; Yang, Y.-Y. Studies of Kinetics of HCOOH Oxidation on Pt(100), Pt(110), Pt(111), Pt(510) and Pt(911) Single Crystal Electrodes. *Journal of*

Electroanalytical Chemistry **1999**, *467* (1–2), 121–131. https://doi.org/10.1016/S0022-0728(99)00032-7.

(116) Bagger, A.; Jensen, K. D.; Rashedi, M.; Luo, R.; Du, J.; Zhang, D.; Pereira, I. J.; Escudero-Escribano, M.; Arenz, M.; Rossmeisl, J. Fundamental Reaction Limitations for Formic Acid Oxidation. *ChemRxiv* **2022**. https://doi.org/10.26434/chemrxiv-2022-t4lqn.

(117) Shi, H.; Liao, F.; Zhu, W.; Shao, C.; Shao, M. Effective PtAu Nanowire Network Catalysts with Ultralow Pt Content for Formic Acid Oxidation and Methanol Oxidation. *International Journal of Hydrogen Energy* **2020**, *45* (32), 16071–16079. https://doi.org/10.1016/j.ijhydene.2020.04.003.

(118) Menshikov, V. S.; Novomlinsky, I. N.; Belenov, S. v.; Alekseenko, A. A.; Safronenko, O. I.; Guterman, V. E. Methanol, Ethanol, and Formic Acid Oxidation on New Platinum-Containing Catalysts. *Catalysts* **2021**, *11* (2), 1–18. https://doi.org/10.3390/catal11020158.

(119) Hsieh, C. te; Hsiao, H. T.; Tzou, D. Y.; Yu, P. Y.; Chen, P. Y.; Jang, B. S. Electro-Oxidation of Methanol and Formic Acid on Platinum Nanoparticles with Different Oxidation Levels. *Materials Chemistry and Physics* **2015**, *149*, 359–367. https://doi.org/10.1016/j.matchemphys.2014.10.030.

(120) Pisarek, M.; Kedzierzawski, P.; Andrzejczuk, M.; Holdyński, M.; Mikolajczuk-Zychora, A.; Borodziński, A.; Janik-Czachor, M. TiO2 Nanotubes with Pt and Pd Nanoparticles as Catalysts for Electro-Oxidation of Formic Acid. *Materials* **2020**, *13* (5). https://doi.org/10.3390/ma13051195.

(121) Liang, Z.; Song, L.; Elnabawy, A. O.; Marinkovic, N.; Mavrikakis, M.; Adzic, R. R. Platinum and Palladium Monolayer Electrocatalysts for Formic Acid Oxidation. *Topics in Catalysis* **2020**, *63* (7–8), 742–749. https://doi.org/10.1007/s11244-020-01264-5.

(122) Shi, H.; Liao, F.; Zhu, W.; Shao, C.; Shao, M. Effective PtAu Nanowire Network Catalysts with Ultralow Pt Content for Formic Acid Oxidation and Methanol Oxidation. *International Journal of Hydrogen Energy* **2020**, *45* (32), 16071–

16079. https://doi.org/10.1016/j.ijhydene.2020.04.003.

(123) Xu, J. B.; Zhao, T. S.; Liang, Z. X. Carbon Supported Platinum-Gold Alloy Catalyst for Direct Formic Acid Fuel Cells. *Journal of Power Sources* **2008**, *185* (2), 857–861. https://doi.org/10.1016/j.jpowsour.2008.09.039.

(124) Zhang, S.; Shao, Y.; Liao, H. G.; Liu, J.; Aksay, I. A.; Yin, G.; Lin, Y. Graphene Decorated with PtAu Alloy Nanoparticles: Facile Synthesis and Promising Application for Formic Acid Oxidation. *Chemistry of Materials* **2011**, *23* (5), 1079–1081. https://doi.org/10.1021/cm101568z.

(125) Lu, Y.; Chen, W. PdAg Alloy Nanowires: Facile One-Step Synthesis and High Electrocatalytic Activity for Formic Acid Oxidation. *ACS Catalysis* **2012**, *2* (1), 84–90. https://doi.org/10.1021/cs200538g.

(126) Han, S. H.; Liu, H. M.; Bai, J.; Tian, X. L.; Xia, B. Y.; Zeng, J. H.; Jiang, J. X.; Chen, Y. Platinum-Silver Alloy Nanoballoon Nanoassemblies with Super Catalytic Activity for the Formate Electrooxidation. *ACS Applied Energy Materials* **2018**, *1* (3), 1252–1258. https://doi.org/10.1021/acsaem.8b00004.

(127) Capon, A. The Oxidation of Formic Acid at Noble Metal Electrodes Part 4. Platinum + Palladium Alloys. *Journal of Electroanalytical Chemistry* **1975**, *65* (1), 285–305. https://doi.org/10.1016/0368-1874(75)85124-0.

(128) Wang, C. Y.; Yu, Z. Y.; Li, G.; Song, Q. T.; Li, G.; Luo, C. X.; Yin, S. H.; Lu, B. A.; Xiao, C.; Xu, B. bin; Zhou, Z. Y.; Tian, N.; Sun, S. G. Intermetallic PtBi Nanoplates with High Catalytic Activity towards Electro-Oxidation of Formic Acid and Glycerol. *ChemElectroChem* **2020**, *7* (1), 239–245. https://doi.org/10.1002/celc.201901818.

(129) Kormányos, A.; Speck, F. D.; Mayrhofer, K. J. J.; Cherevko, S. Influence of Fuels and PH on the Dissolution Stability of Bifunctional PtRu/C Alloy Electrocatalysts. *ACS Catalysis* **2020**, *10* (19), 10858–10870. https://doi.org/10.1021/acscatal.0c02094.

(130) Yu, X.; Manthiram, A. Catalyst-Selective, Scalable Membraneless Alkaline Direct Formate Fuel Cells. *Applied Catalysis B: Environmental* **2015**, *165*, 63–

67. https://doi.org/10.1016/j.apcatb.2014.09.069.

(131) Marković, N. M.; Gasteiger, H. A.; Ross, P. N.; Jiang, X.; Villegas, I.; Weaver, M. J. Electro-Oxidation Mechanisms of Methanol and Formic Acid on Pt-Ru Alloy Surfaces. *Electrochimica Acta* **1995**, *40* (1), 91–98. https://doi.org/10.1016/0013-4686(94)00241-R.

(132) Liao, M.; Li, W.; Xi, X.; Luo, C.; Gui, S.; Jiang, C.; Mai, Z.; Chen, B. H. Highly Active Aucore@Ptclustercatalyst for Formic Acid Electrooxidation. *Journal of Electroanalytical Chemistry* **2017**, *791*, 124–130. https://doi.org/10.1016/j.jelechem.2017.03.024.

(133) Chen, C. H.; Liou, W. J.; Lin, H. M.; Wu, S. H.; Borodzinski, A.; Stobinski, L.; Kedzierzawski, P. Palladium and Palladium Gold Catalysts Supported on MWCNTs for Electrooxidation of Formic Acid. In *Fuel Cells*; **2010**, Vol. 10, pp 227–233. https://doi.org/10.1002/fuce.200900117.

(134) Xue, Q.; Bai, X. Y.; Zhao, Y.; Li, Y. N.; Wang, T. J.; Sun, H. Y.; Li, F. M.; Chen, P.; Jin, P.; Yin, S. bin; Chen, Y. Au Core-PtAu Alloy Shell Nanowires for Formic Acid Electrolysis. *Journal of Energy Chemistry* **2021**, *65*, 94–102. https://doi.org/10.1016/j.jechem.2021.05.034.

(135) Park, I. S.; Lee, K. S.; Choi, J. H.; Park, H. Y.; Sung, Y. E. Surface Structure of Pt-Modified Au Nanoparticles and Electrocatalytic Activity in Formic Acid Electro-Oxidation. *Journal of Physical Chemistry C* **2007**, *111* (51), 19126–19133. https://doi.org/10.1021/jp0739566.

(136) Kristian, N.; Yan, Y.; Wang, X. Highly Efficient Submonolayer Pt-Decorated Au Nano-Catalysts for Formic Acid Oxidation. *Chemical Communications* **2008**, *1* (3), 353–355. https://doi.org/10.1039/b714230g.

(137) Zhang, G. R.; Zhao, D.; Feng, Y. Y.; Zhang, B.; Su, D. S.; Liu, G.; Xu, B. Q. Catalytic Pt-on-Au Nanostructures: Why Pt Becomes More Active on Smaller Au Particles. *ACS Nano* **2012**, *6* (3), 2226–2236. https://doi.org/10.1021/nn204378t.

(138) Oko, D. N.; Zhang, J.; Garbarino, S.; Chaker, M.; Ma, D.; Tavares, A. C.; Guay,

D. Formic Acid Electro-Oxidation at PtAu Alloyed Nanoparticles Synthesized by Pulsed Laser Ablation in Liquids. *Journal of Power Sources* **2014**, *248*, 273–282. https://doi.org/10.1016/j.jpowsour.2013.09.045.

(139) Xie, Y.; Dimitrov, N. Ultralow Pt Loading Nanoporous Au-Cu-Pt Thin Film as Highly Active and Durable Catalyst for Formic Acid Oxidation. *Applied Catalysis B: Environmental* **2020**, *263*. https://doi.org/10.1016/j.apcatb.2019.118366.

(140) Duchesne, P. N.; Li, Z. Y.; Deming, C. P.; Fung, V.; Zhao, X.; Yuan, J.; Regier, T.; Aldalbahi, A.; Almarhoon, Z.; Chen, S.; Jiang, D. en; Zheng, N.; Zhang, P. Golden Single-Atomic-Site Platinum Electrocatalysts. *Nature Materials* **2018**, *17* (11), 1033–1039. https://doi.org/10.1038/s41563-018-0167-5.

(141) Gamler, J. T. L.; Ashberry, H. M.; Skrabalak, S. E.; Koczkur, K. M. Random Alloyed versus Intermetallic Nanoparticles: A Comparison of Electrocatalytic Performance. *Advanced Materials* **2018**, *30* (40). https://doi.org/10.1002/adma.201801563.

(142) Xiong, Y.; Dong, J.; Huang, Z. Q.; Xin, P.; Chen, W.; Wang, Y.; Li, Z.; Jin, Z.; Xing, W.; Zhuang, Z.; Ye, J.; Wei, X.; Cao, R.; Gu, L.; Sun, S.; Zhuang, L.; Chen, X.; Yang, H.; Chen, C.; Peng, Q.; Chang, C. R.; Wang, D.; Li, Y. Single-Atom Rh/N-Doped Carbon Electrocatalyst for Formic Acid Oxidation. *Nature Nanotechnology* **2020**, *15* (5), 390–397. https://doi.org/10.1038/s41565-020-0665-x.

(143) Li, Z.; Chen, Y.; Ji, S.; Tang, Y.; Chen, W.; Li, A.; Zhao, J.; Xiong, Y.; Wu, Y.; Gong, Y.; Yao, T.; Liu, W.; Zheng, L.; Dong, J.; Wang, Y.; Zhuang, Z.; Xing, W.; He, C. T.; Peng, C.; Cheong, W. C.; Li, Q.; Zhang, M.; Chen, Z.; Fu, N.; Gao, X.; Zhu, W.; Wan, J.; Zhang, J.; Gu, L.; Wei, S.; Hu, P.; Luo, J.; Li, J.; Chen, C.; Peng, Q.; Duan, X.; Huang, Y.; Chen, X. M.; Wang, D.; Li, Y. Iridium Single-Atom Catalyst on Nitrogen-Doped Carbon for Formic Acid Oxidation Synthesized Using a General Host–Guest Strategy. *Nature Chemistry* **2020**, *12* (8), 764–772. https://doi.org/10.1038/s41557-020-0473-9.

(144) Wang, Y.; Ren, J.; Deng, K.; Gui, L.; Tang, Y. Preparation of Tractable Platinum, Rhodium, and Ruthenium Nanoclusters with Small Particle Size in Organic Media. *Chemistry of Materials* **2000**, *12* (6), 1622–1627. https://doi.org/10.1021/cm0000853.

(145) Quinson, J.; Inaba, M.; Neumann, S.; Swane, A. A.; Bucher, J.; Simonsen, S. B.; Theil Kuhn, L.; Kirkensgaard, J. J. K.; Jensen, K. M.; Oezaslan, M.; Kunz, S.; Arenz, M. Investigating Particle Size Effects in Catalysis by Applying a Size-Controlled and Surfactant-Free Synthesis of Colloidal Nanoparticles in Alkaline Ethylene Glycol: Case Study of the Oxygen Reduction Reaction on Pt. *ACS Catalysis* **2018**, *8* (7), 6627–6635. https://doi.org/10.1021/acscatal.8b00694.

(146) Das, R. S.; Singh, B.; Banerjee, R.; Mukhopadhyay, S. PVP Stabilized Pt Nano Particles Catalyzed De-Oxygenation of Phenoxazine Group by Hydrazine in Physiological Buffer Media: Surfactant Competes with Reactants for the Same Surface Sites. *Journal of the Chemical Society. Dalton Transactions* **2013**, *42* (2), 4068–4080. https://doi.org/10.1039/c2dt32007j.

(147) Safo, I. A.; Dosche, C.; Oezaslan, M. TEM, FTIR and Electrochemistry Study: Desorption of PVP from Pt Nanocubes. *Zeitschrift fur Physikalische Chemie* **2018**, *232* (9–11), 1319–1333. https://doi.org/10.1515/zpch-2018-1147.

(148) Schrader, I.; Warneke, J.; Neumann, S.; Grotheer, S.; Swane, A. A.; Kirkensgaard, J. J. K.; Arenz, M.; Kunz, S. Surface Chemistry of "Unprotected" Nanoparticles: A Spectroscopic Investigation on Colloidal Particles. *Journal of Physical Chemistry C* **2015**, *119* (31), 17655–17661. https://doi.org/10.1021/acs.jpcc.5b03863.

(149) Bock, C.; Paquet, C.; Couillard, M.; Botton, G. A.; MacDougall, B. R. Size-Selected Synthesis of PtRu Nano-Catalysts: Reaction and Size Control Mechanism. *J Am Chem Soc* **2004**, *126* (25), 8028–8037. https://doi.org/10.1021/ja0495819.

(150) Zhang, Z.; Xin, L.; Qi, J.; Wang, Z.; Li, W. Selective Electro-Conversion of Glycerol to Glycolate on Carbon Nanotube Supported Gold Catalyst. *Green*

Chemistry **2012**, *14* (8), 2150–2152. https://doi.org/10.1039/c2gc35505a.

(151) Kohsakowski, S.; Seiser, F.; Wiederrecht, J. P.; Reichenberger, S.; Vinnay, T.; Barcikowski, S.; Marzun, G. Effective Size Separation of Laser-Generated, Surfactant-Free Nanoparticles by Continuous Centrifugation. *Nanotechnology* **2020**, *31* (9). https://doi.org/10.1088/1361-6528/ab55bd.

(152) Letzel, A.; Reich, S.; dos Santos Rolo, T.; Kanitz, A.; Hoppius, J.; Rack, A.; Olbinado, M. P.; Ostendorf, A.; Gökce, B.; Plech, A.; Barcikowski, S. Time and Mechanism of Nanoparticle Functionalization by Macromolecular Ligands during Pulsed Laser Ablation in Liquids. *Langmuir* **2019**, *35* (8), 3038–3047. https://doi.org/10.1021/acs.langmuir.8b01585.

(153) Speder, J.; Altmann, L.; Roefzaad, M.; Bäumer, M.; Kirkensgaard, J. J. K.; Mortensen, K.; Arenz, M. Pt Based PEMFC Catalysts Prepared from Colloidal Particle Suspensions-a Toolbox for Model Studies. *Physical Chemistry Chemical Physics* **2013**, *15* (10), 3602–3608. https://doi.org/10.1039/c3cp50195g.

(154) Speder, J.; Spanos, I.; Zana, A.; Kirkensgaard, J. J. K.; Mortensen, K.; Altmann, L.; Bäumer, M.; Arenz, M. From Single Crystal Model Catalysts to Systematic Studies of Supported Nanoparticles. *Surface Science* **2015**, *631*, 278–284. https://doi.org/10.1016/j.susc.2014.05.024.

(155) BALCERZAK, M. Sample Digestion Methods for the Determination of Traces of Precious Metals by Spectrometric Techniques. *Analytical Sciences* **2002**, *18* (7), 737–750. https://doi.org/10.2116/analsci.18.737.

(156) Kumar, P. S.; Pavithra, K. G.; Naushad, Mu. Characterization Techniques for Nanomaterials. In *Nanomaterials for Solar Cell Applications*; Thomas, S., Sakho, E. H. M., Kalarikkal, N., Oluwafemi, S. O., Wu, J., Eds.; Elsevier, **2019**, pp 97–124. https://doi.org/10.1016/B978-0-12-813337-8.00004-7.

(157) Sun, D.; Siddiqui, M. O. R.; Iqbal, K. Specialty Testing Techniques for Smart Textiles. In *Smart Textile Coatings and Laminates*; Smith, W. C., Ed.; Elsevier, **2019**, pp 99–116. https://doi.org/10.1016/B978-0-08-102428-7.00004-3.

(158) Pyrz, W. D.; Buttrey, D. J. Particle Size Determination Using TEM: A Discussion

of Image Acquisition and Analysis for the Novice Microscopist. *Langmuir* **2008**, *24* (20), 11350–11360. https://doi.org/10.1021/la801367j.

(159) Mayrhofer, K. J. J.; Ashton, S. J.; Meier, J. C.; Wiberg, G. K. H.; Hanzlik, M.; Arenz, M. Non-Destructive Transmission Electron Microscopy Study of Catalyst Degradation under Electrochemical Treatment. *Journal of Power Sources* **2008**, *185* (2), 734–739. https://doi.org/10.1016/j.jpowsour.2008.08.003.

(160) Zana, A.; Speder, J.; Roefzaad, M.; Altmann, L.; Bäumer, M.; Arenz, M. Probing Degradation by IL-TEM: The Influence of Stress Test Conditions on the Degradation Mechanism. *Journal of The Electrochemical Society* **2013**, *160* (6), F608–F615. https://doi.org/10.1149/2.078306jes.

(161) Schröder, J.; Quinson, J.; Mathiesen, J. K.; Kirkensgaard, J. J. K.; Alinejad, S.; Mints, V. A.; Jensen, K. M. Ø.; Arenz, M. A New Approach to Probe the Degradation of Fuel Cell Catalysts under Realistic Conditions: Combining Tests in a Gas Diffusion Electrode Setup with Small Angle X-Ray Scattering. *Journal of The Electrochemical Society* **2020**, *167* (13), 134515. https://doi.org/10.1149/1945-7111/abbdd2.

(162) Neyhouse, B. J.; Brushett, F. R. From the Synthesis Vial to the Full Cell: Electrochemical Methods for Characterizing Active Materials for Redox Flow Batteries. In *Reference Module in Earth Systems and Environmental Sciences*; Elsevier, **2021**. https://doi.org/https://doi.org/10.1016/B978-0-12-819723-3.00058-5.

(163) Hirt, T. J.; Palmer, H. B. *Quantitative Determination of Carbon Suboxide by Gas Chromatography Department of Fuel Technology Rotating Disk Electrodes Sir: The Use of Rotating Disk Elec*; **1954**, Vol. 223.

(164) Koutecky, J. and B. G. L. The Application of the Rotating Disc Electrode to Studies of Kinetic and Catalytic Processes. *Zhurnal Fizicheskoi Khimii* **1958**, *32* (7), 1565–1575.

(165) Shinozaki, K.; Zack, J. W.; Pylypenko, S.; Pivovar, B. S.; Kocha, S. S. Oxygen Reduction Reaction Measurements on Platinum Electrocatalysts Utilizing

Rotating Disk Electrode Technique. *Journal of The Electrochemical Society* **2015**, *162* (12), F1384–F1396. https://doi.org/10.1149/2.0551512jes.

(166) Zana, A.; Wiberg, G. K. H.; Deng, Y. J.; Østergaard, T.; Rossmeisl, J.; Arenz, M. Accessing the Inaccessible: Analyzing the Oxygen Reduction Reaction in the Diffusion Limit. *ACS Applied Materials and Interfaces* **2017**, *9* (44), 38176–38180. https://doi.org/10.1021/acsami.7b13902.

(167) Schmidt, T. J.; Gasteiger, H. A.; Stäb, G. D.; Urban, P. M.; Kolb, D. M.; Behm, R. J. Characterization of High-Surface-Area Electrocatalysts Using a Rotating Disk Electrode Configuration. *Journal of The Electrochemical Society* **1998**, *145* (7), 2354–2358. https://doi.org/10.1149/1.1838642.

(168) Inaba, M.; Quinson, J.; Arenz, M. PH Matters: The Influence of the Catalyst Ink on the Oxygen Reduction Activity Determined in Thin Film Rotating Disk Electrode Measurements. *Journal of Power Sources* **2017**, *353*, 19–27. https://doi.org/10.1016/j.jpowsour.2017.03.140.

(169) Subbaraman, R.; Strmcnik, D.; Paulikas, A. P.; Stamenkovic, V. R.; Markovic, N. M. Oxygen Reduction Reaction at Three-Phase Interfaces. *ChemPhysChem* **2010**, *11* (13), 2825–2833. https://doi.org/10.1002/cphc.201000190.

(170) Kodama, K.; Jinnouchi, R.; Suzuki, T.; Murata, H.; Hatanaka, T.; Morimoto, Y. Increase in Adsorptivity of Sulfonate Anions on Pt (111) Surface with Drying of Ionomer. *Electrochemistry Communications* **2013**, *36*, 26–28. https://doi.org/10.1016/j.elecom.2013.09.005.

(171) Shinozaki, K.; Zack, J. W.; Pylypenko, S.; Pivovar, B. S.; Kocha, S. S. Oxygen Reduction Reaction Measurements on Platinum Electrocatalysts Utilizing Rotating Disk Electrode Technique. *Journal of The Electrochemical Society* **2015**, *162* (12), F1384–F1396. https://doi.org/10.1149/2.0551512jes.

(172) Pedersen, C. M.; Escudero-Escribano, M.; Velázquez-Palenzuela, A.; Christensen, L. H.; Chorkendorff, I.; Stephens, I. E. L. Benchmarking Pt-Based Electrocatalysts for Low Temperature Fuel Cell Reactions with the Rotating Disk Electrode: Oxygen Reduction and Hydrogen Oxidation in the Presence of

CO (Review Article). *Electrochimica Acta* **2015**, *179*, 647–657. https://doi.org/10.1016/j.electacta.2015.03.176.

(173) Gasteiger, H. A.; Panels, J. E.; Yan, S. G. Dependence of PEM Fuel Cell Performance on Catalyst Loading. In *Journal of Power Sources*; **2004**, Vol. 127, pp 162–171. https://doi.org/10.1016/j.jpowsour.2003.09.013.

(174) O'Hayre, R.; Prinz, F. B. The Air/Platinum/Nafion Triple-Phase Boundary: Characteristics, Scaling, and Implications for Fuel Cells. *Journal of The Electrochemical Society* **2004**, *151* (5), A756. https://doi.org/10.1149/1.1701868.

(175) Gasteiger, H. A.; Kocha, S. S.; Sompalli, B.; Wagner, F. T. Activity Benchmarks and Requirements for Pt, Pt-Alloy, and Non-Pt Oxygen Reduction Catalysts for PEMFCs. *Applied Catalysis B: Environmental* **2005**, *56* (1-2 SPEC. ISS.), 9–35. https://doi.org/10.1016/j.apcatb.2004.06.021.

(176) Wiberg, G. K. H.; Fleige, M.; Arenz, M. Gas Diffusion Electrode Setup for Catalyst Testing in Concentrated Phosphoric Acid at Elevated Temperatures. *Review of Scientific Instruments* **2015**, *86* (2). https://doi.org/10.1063/1.4908169.

(177) de Jesus Gálvez-Vázquez, M.; Moreno-García, P.; Xu, H.; Hou, Y.; Hu, H.; Montiel, I. Z.; Rudnev, A. v.; Alinejad, S.; Grozovski, V.; Wiley, B. J.; Arenz, M.; Broekmann, P.; Moreno-García, P. Environment Matters: CO2RR Electrocatalyst Performance Testing in a Gas-Fed Zero-Gap Electrolyzer. *ACS Catalysis* **2020**, *10* (21), 13096–13108. https://doi.org/10.1021/acscatal.0c03609.

(178) Schröder, J.; Mints, V. A.; Bornet, A.; Berner, E.; Fathi Tovini, M.; Quinson, J.; Wiberg, G. K. H.; Bizzotto, F.; El-Sayed, H. A.; Arenz, M. The Gas Diffusion Electrode Setup as Straightforward Testing Device for Proton Exchange Membrane Water Electrolyzer Catalysts. *JACS Au* **2021**, *1* (3), 247–251. https://doi.org/10.1021/jacsau.1c00015.

(179) Nösberger, S.; Du, J.; Quinson, J.; Berner, E.; Zana, A.; Wiberg, G. K. H.; Arenz, M. The Gas Diffusion Electrode Setup as a Testing Platform for Evaluating Fuel Cell Catalysts: A Comparative RDE-GDE Study. *Electrochemical Science Advances* **2022**. https://doi.org/10.1002/elsa.202100190.

(180) Yarlagadda, V.; McKinney, S. E.; Keary, C. L.; Thompson, L.; Zulevi, B.; Kongkanand, A. Preparation of PEMFC Electrodes from Milligram-Amounts of Catalyst Powder. *Journal of The Electrochemical Society* **2017**, *164* (7), F845–F849. https://doi.org/10.1149/2.1461707jes.

(181) Alinejad, S.; Quinson, J.; Schröder, J.; Kirkensgaard, J. J. K.; Arenz, M. Carbon-Supported Platinum Electrocatalysts Probed in a Gas Diffusion Setup with Alkaline Environment: How Particle Size and Mesoscopic Environment Influence the Degradation Mechanism. *ACS Catalysis* **2020**, *10* (21), 13040–13049. https://doi.org/10.1021/acscatal.0c03184.

(182) She, L.; Zhao, G.; Ma, T.; Chen, J.; Sun, W.; Pan, H. On the Durability of Iridium-Based Electrocatalysts toward the Oxygen Evolution Reaction under Acid Environment. *Advanced Functional Materials*. John Wiley and Sons Inc January 1, **2022**. https://doi.org/10.1002/adfm.202108465.

(183) Yu, J.; He, Q.; Yang, G.; Zhou, W.; Shao, Z.; Ni, M. Recent Advances and Prospective in Ruthenium-Based Materials for Electrochemical Water Splitting. *ACS Catalysis* **2019**, *9* (11), 9973–10011. https://doi.org/10.1021/acscatal.9b02457.

(184) Pu, Z.; Zhang, G.; Hassanpour, A.; Zheng, D.; Wang, S.; Liao, S.; Chen, Z.; Sun, S. Regenerative Fuel Cells: Recent Progress, Challenges, Perspectives and Their Applications for Space Energy System. *Applied Energy* **2021**, *283*. https://doi.org/10.1016/j.apenergy.2020.116376.

(185) Jang, S. E.; Kim, H. Effect of Water Electrolysis Catalysts on Carbon Corrosion in Polymer Electrolyte Membrane Fuel Cells. *J Am Chem Soc* **2010**, *132* (42), 14700–14701. https://doi.org/10.1021/ja104672n.

(186) Cherevko, S.; Geiger, S.; Kasian, O.; Mingers, A.; Mayrhofer, K. J. J. Oxygen Evolution Activity and Stability of Iridium in Acidic Media. Part 1. - Metallic Iridium. *Journal of Electroanalytical Chemistry* **2016**, *773*, 69–78. https://doi.org/10.1016/j.jelechem.2016.04.033.

(187) Cherevko, S.; Geiger, S.; Kasian, O.; Mingers, A.; Mayrhofer, K. J. J. Oxygen

Evolution Activity and Stability of Iridium in Acidic Media. Part 2. - Electrochemically Grown Hydrous Iridium Oxide. *Journal of Electroanalytical Chemistry* **2016**, *774*, 102–110. https://doi.org/10.1016/j.jelechem.2016.05.015.

(188) Alinejad, S.; Quinson, J.; Schröder, J.; Kirkensgaard, J. J. K.; Arenz, M. Carbon-Supported Platinum Electrocatalysts Probed in a Gas Diffusion Setup with Alkaline Environment: How Particle Size and Mesoscopic Environment Influence the Degradation Mechanism. *ACS Catalysis* **2020**, *10* (21), 13040–13049. https://doi.org/10.1021/acscatal.0c03184.

(189) Grosse, P.; Yoon, A.; Rettenmaier, C.; Herzog, A.; Chee, S. W.; Roldan Cuenya, B. Dynamic Transformation of Cubic Copper Catalysts during CO2 Electroreduction and Its Impact on Catalytic Selectivity. *Nature Communications* **2021**, *12* (1), 1–11. https://doi.org/10.1038/s41467-021-26743-5.

(190) Minke, C.; Suermann, M.; Bensmann, B.; Hanke-Rauschenbach, R. Is Iridium Demand a Potential Bottleneck in the Realization of Large-Scale PEM Water Electrolysis? *International Journal of Hydrogen Energy* **2021**, *46* (46), 23581–23590. https://doi.org/10.1016/j.ijhydene.2021.04.174.

(191) Raleigh Gilchrist, B.; Wickers, E.; Gilchrist, R.; Wichers, E. *A Procedure for the Separation of the Six Platinum Metals from One Another and for Their Gravimetric Determination1·2*; UTC, **2022**, Vol. 15, pp 2565–2573. https://doi.org/10.1021/ja01315a075.

(192) Lee, J.; Kim, Y. Chemical Dissolution of Iridium Powder Using Alkali Fusion Followed by High-Temperature Leaching. *Materials Transactions* **2011**, *52* (11), 2067–2070. https://doi.org/10.2320/matertrans.M2011202.

(193) Federer, J. I. *Purification of Iridium by an Oxidation-Dissolution Process*; **1974**.

(194) WET CHEMICAL ETCHING - BASICS www.microchemicals.com/downloads/application_notes.html.

(195) Kobayashi, Y.; Yamada, S.; Nagai, T. New Dissolution Process of Iridium to Hydrochloric Acid. In *Treatise on Process Metallurgy*; Elsevier Ltd., **2019**, Vol.

3, pp 197–200. https://doi.org/10.1007/978-3-030-05740-4_19.

(196) Hodnik, N.; Baldizzone, C.; Polymeros, G.; Geiger, S.; Grote, J. P.; Cherevko, S.; Mingers, A.; Zeradjanin, A.; Mayrhofer, K. J. J. Platinum Recycling Going Green via Induced Surface Potential Alteration Enabling Fast and Efficient Dissolution. *Nature Communications* **2016**, *7*, 1–6. https://doi.org/10.1038/ncomms13164.

(197) Ramaswamy, N.; Mukerjee, S. Fundamental Mechanistic Understanding of Electrocatalysis of Oxygen Reduction on Pt and Non-Pt Surfaces: Acid versus Alkaline Media. *Advances in Physical Chemistry*. **2012**. https://doi.org/10.1155/2012/491604.

7. Appended manuscripts

The manuscripts I-III discussed in chapter 3 alongside with the respective supplementary information are reprinted with permission. Manuscript IV and V have not yet been published are also included in this chapter.

Manuscript I

ACS Catalysis

pubs.acs.org/acscatalysis

Research Article

Bifunctional Pt-IrO_2 Catalysts for the Oxygen Evolution and Oxygen Reduction Reactions: Alloy Nanoparticles versus Nanocomposite Catalysts

Jia Du, Jonathan Quinson, Damin Zhang, Francesco Bizzotto, Alessandro Zana, and Matthias Arenz*

Cite This: *ACS Catal.* 2021, 11, 820−828

Read Online

ACCESS | Metrics & More | Article Recommendations | Supporting Information

ABSTRACT: In the present study, different concepts for the development of bifunctional oxygen reduction reaction/oxygen evolution reaction (ORR/OER) electrocatalysts are explored and compared. Bifunctional ORR/OER catalysts are often suggested to improve the stability during startup and shutdown of fuel cells. Furthermore, they have been proposed for the so-called unitized regenerative fuel cells (URFCs) that would allow a closed loop system to use and produce hydrogen on demand. We compare the electrocatalytic performance of conventional Pt_xIr_y alloy nanoparticles (NPs) with Pt−IrO_2 NP composites (nanocomposites), both immobilized onto a commercial carbon support. The Pt−IrO_2 nanocomposites thereby consist of a mixture of Pt NPs and IrO_2 NPs. By probing the electrocatalytic performance before and after exposing the electrocatalysts to accelerated degradation tests (ADTs), it is shown that the Pt−IrO_2 nanocomposite concept offers advantages but also some disadvantages over the conventional alloy concept. In particular, it is shown that while the nanocomposites are initially less active for the ORR because of an interparticle effect, their performance is less affected by the ADTs. However, all the tested catalysts experience a decline of the Ir/Pt ratio upon ADT treatment, highlighting the limiting value of Ir as an OER catalyst for startup−shutdown protection in fuel cells as well as the challenging stability requirements for URFCs.

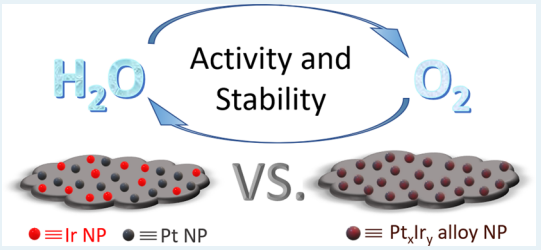

KEYWORDS: *bimetallic electrocatalysts, nanocomposite electrocatalysts, alloy nanoparticles, accelerated degradation test, startup−shutdown degradation, fuel cells, unitized regenerative fuel cells*

INTRODUCTION

Electrochemical energy conversion is one of the main applications of electrocatalysis.[1−3] The most studied technologies and reactions are the electrochemical water splitting to produce hydrogen as an energy carrier as well as the reconversion of such "green hydrogen" (provided the electricity is based on renewable sources such as wind or solar power) in fuel cells to deliver electricity on demand.[4−7] In addition, a number of new reactions such as electrochemical carbon dioxide reduction[8,9] or the production of valuable chemicals[10,11] recently received increasing attention. While the main application of fuel cells is often seen in the mobile automotive sector[12] with a recent focus shift to larger trucks,[13] there is also great potential for applications such as power backup,[14] residential areas,[15] or range extenders for batteries.[16]

In proton exchange membrane fuel cells (PEMFCs), most conversion losses arise at the cathode where the oxygen reduction reaction (ORR) takes place.[17] The electrocatalyst of choice for the cathode currently consists of bimetallic Pt nanoparticles (NPs), mainly PtCo, immobilized onto a carbon support.[18,19] The alloying optimizes the adsorption strength of the ORR reaction intermediates (O_{ad}, OH_{ad}, and OOH_{ad}) on Pt and thus the ORR rate.[20,21] However, also other Pt-based bimetallic electrocatalysts are investigated for PEMFCs like PtIr.[22] Ir is equally scarce and recently has become even more expensive than Pt.[23] The motivation behind developing PtIr catalysts is not necessarily the optimization of the binding energy of reaction intermediates but rather the fact that Ir-oxide is an active catalyst for the oxygen evolution reaction (OER).[24,25] Bifunctional ORR/OER electrocatalysts are suggested to improve the stability of PEMFC cathode catalysts because under high potential excursions reached during startup and shutdown, the OER competes with and thus mitigates the oxidation of the carbon support to carbon dioxide, the latter being extremely detrimental to the catalyst stability. Furthermore, bifunctional ORR/OER electrocatalysts are suggested for the so-called unitized regenerative fuel cells (URFCs). URFCs are a concept for a closed loop system that can use hydrogen fuel to produce electricity as well as regenerate the hydrogen fuel when connected to an external

Received: September 4, 2020
Revised: December 3, 2020
Published: January 4, 2021

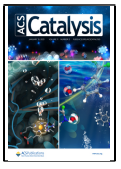

https://dx.doi.org/10.1021/acscatal.0c03867
ACS Catal. 2021, 11, 820−828

energy source.[26−28] URFCs allow for two operation modes: a charge (electrolyzer) mode, and a discharge (fuel cell) mode. To sustain both operation modes, bifunctional catalysts are required. A distinction, however, can be made between two concepts, the constant-gas (CG) and the constant-electrode (CE) configuration.[28] In the CG configuration, the URFC consists of an oxygen electrode to sustain the ORR and OER and a hydrogen electrode for hydrogen oxidation and hydrogen evolution reactions (HOR/HER). By comparison, in the CE configuration, the two electrodes are a HOR/OER and an ORR/HER electrode. The advantages of the classical CG configuration are that H_2 and O_2 mixing is avoided and fast switching between the two modes is possible.[28] In the CG configuration using proton conducting membranes, most approaches for URFCs use bifunctional catalysts composed of Pt and IrO_2. Thereby, different types have been investigated ranging from simple mixtures of Pt and IrO_2[29] to Pt_xIr_y alloys,[30] Pt NPs deposited onto IrO_2 black,[31] nickel−platinum/cobalt−iridium two-dimensional (2D) nanoframes,[32] or IrO_2 deposited onto Pt black.[33] More recently, composite materials have also been discussed.[34] One of the main challenges in employing URFCs is the stability requirements[35] of the catalyst at these harsh conditions changing from oxidative to reductive conditions.

In the present study, we use our previously introduced toolbox approach[36−39] to compare different concepts for bifunctional ORR/OER electrocatalysts. Pt_xIr_y alloy NPs as well as composites consisting of separated Pt and IrO_2 NPs (Pt−IrO_2 nanocomposites) are investigated, both systems in the immobilized form using a commercial carbon support. Carbon supported monometallic Pt NPs serve as a reference system. The electrocatalysts are probed for their electrocatalytic performance for ORR and OER. Furthermore, accelerated degradation tests (ADTs) are performed, exposing the electrocatalysts repeatedly to a series of reductive and oxidative currents. The influence of these ADT treatments is examined with respect to the type of catalysts (alloys vs nanocomposites), electrochemically active Pt surface area (ECSA) loss, as well as ORR and OER activity. In addition, the influence of ADT treatments on the catalyst composition is probed.

EXPERIMENTAL SECTION

Chemicals and Gases. The following chemicals were used for catalyst synthesis and characterization: ethylene glycol (EG, 99.8%, Sigma-Aldrich), sodium hydroxide (NaOH, 98.9%, Fisher Chemical), hexa-chloroplatinic(IV) acid hexahydrate ($H_2PtCl_6{\cdot}6H_2O$, 99.9%, Alfa Aesar), iridium(III) chloride ($IrCl_3{\cdot}xH_2O$, Sigma-Aldrich, >99.8%), 30% hydrochloric acid (HCl, Suprapur, Merck), 65% nitric acid (HNO_3, Suprapur, Merck), and acetone (99.5 + %, Alfa Aesar). Commercial carbon black (Vulcan XC72R) was employed as a carbon support in catalyst synthesis. Ultrapure water (resistivity>18.2 MΩ·cm, total organic carbon <5 ppb) from a Milli-Q system (Millipore) was used for acid/base dilutions, catalyst ink formulation, and electrochemical cell cleaning. Isopropanol (99.7 + %, Alfa Aesar), 70% perchloric acid ($HClO_4$, Suprapur, Merck), potassium hydroxide hydrate ($KOH{\cdot}H_2O$, Suprapur, Merck) were used for the catalyst ink formulation and electrolyte preparation. The following gases from Air Liquide were used for electrochemical measurements: Ar (99.999%), O_2 (99.999%), and CO (99.97%).

Synthesis of Supported Monometallic Pt NPs, Pt_xIr_y Alloy NPs, and Pt−IrO_2 Nanocomposites. Bifunctional electrocatalysts were synthesized via the toolbox method that we previously reported.[36−39] The synthesis approach consists of two main steps: First NPs were prepared assisted by a microwave reactor via an alkaline EG route, and then in the second step, the NPs were immobilized onto a carbon support.

The colloidal Pt or Ir NP synthesis in alkaline EG was conducted by mixing 5 mL of NaOH EG solution (0.4 M) with 5 mL of $H_2PtCl_6{\cdot}6H_2O$ or $IrCl_3{\cdot}xH_2O$ EG solution (0.04 M) in a microwave reaction vessel and heating the mixture to 160 °C for 3 min in the microwave reactor to obtain colloidal Pt or Ir NPs in EG with a concentration of 3.9 g_{Pt} L^{-1} and 3.85 g_{Ir} L^{-1}, respectively. Pt_xIr_y alloy NPs were synthesized according to a previously reported method.[40] For PtIr alloy NPs, 2.5 mL of $H_2PtCl_6{\cdot}6H_2O$ EG solution (0.04 M) and 2.54 mL of $IrCl_3{\cdot}xH_2O$ EG solution (0.04 M) were mixed with 5.04 mL of NaOH EG solution (0.4 M), and the mixture was heated to 160 °C for 3 min in a microwave reactor to obtain alloyed colloidal PtIr NPs in EG with a concentration of 1.936 g_{Pt} L^{-1} and 1.936 g_{Ir} L^{-1}. For the preparation of $PtIr_2$ alloy NPs, the synthesis procedure was similar but with different Pt and Ir precursor contents, that is, 1.5 mL of $H_2PtCl_6{\cdot}6H_2O$ EG solution (0.04 M) and 3.05 mL of $IrCl_3{\cdot}xH_2O$ EG solution (0.04 M) were mixed with 4.55 mL of NaOH EG solution (0.4 M), followed by heating the mixture to 160 °C for 3 min in the microwave reactor to obtain colloidal $PtIr_2$ alloy NPs in EG with a concentration of 1.288 g_{Pt} L^{-1} and 2.576 g_{Ir} L^{-1}. All colloidal NP suspensions looked dark brown after synthesis.

In order to immobilize the NPs on carbon, 1 M HCl was added to the colloidal NP suspension (V_{HCl}: V_{NPs} = 3: 1), inducing particle flocculation. The mixture was thereafter centrifuged at 5000 rpm for 10 min once, the supernatant was discarded, and the floc was re-dispersed in acetone to obtain NP acetone solution with the same concentration as before flocculation in EG. To immobilize the monometallic Pt NPs, 5.5 mg of carbon (Vulcan XC72R) was dispersed in 10 mL of acetone, the carbon suspension was sonicated with a horn sonicator (QSONICA sonicator, 500 W, 50 kHz, with alternation of 1 s sonication and 1 s resting) until it showed stable dispersion (∼3 min), then Pt NP acetone solution of 352 or 940 μL was added and further sonicated for 10 min (during which the vial was immersed in ice water to avoid overheating of the dispersion), and finally, the acetone was evaporated from the mixture with the help of a rotary evaporator (room temperature, 200 mbar) until the catalyst was completely dried and the respective 20 wt % Pt/C or 40 wt % Pt/C was obtained. The same procedure was employed to obtain immobilized Pt_xIr_y alloy NPs. In brief, the same amount (5.5 mg) of carbon was dispersed in 10 mL of acetone; after sonication, the PtIr alloy NPs dispersed in 710 μL of acetone or the $PtIr_2$ alloy NPs dispersed in 1068 μL of acetone were added and further sonicated for 10 min, and the solvent evaporated in a rotary evaporator, and the PtIr alloy/C or $PtIr_2$ alloy/C catalysts were obtained. Concerning the supported Pt−IrO_2 nanocomposites, Pt NP acetone solution and Ir NP acetone solution were added to the sonicated carbon acetone suspension (5.5 mg in 10 mL acetone) one by one: first, 352 μL of Pt NP acetone solution and then 357 or 714 μL of Ir NP acetone solution. The mixture was further sonicated and the solvent evaporated, and nanocomposites with Pt to Ir NP ratios of 1: 1 and 1: 2 based on metal weight were obtained. Pt

https://dx.doi.org/10.1021/acscatal.0c03867
ACS Catal. 2021, 11, 820−828

weight loading on the carbon support thereby is fixed to 20 wt %.

Transmission Electron Microscopy and Energy-Dispersive X-ray Spectroscopy. For the transmission electron microscopy (TEM) analysis, a Jeol 2100 transmission electron microscope operated at 200 kV equipped with an energy-dispersive X-ray spectroscopy (EDX) detector was used. The samples were prepared by dropping the catalyst dispersion diluted in ethanol on carbon-coated copper TEM grids (Quantifoil). For TEM after electrochemical treatments, the samples were collected from the rotating disk electrode (RDE) for preparation of TEM grids. Images were recorded at different magnifications (at least x300 000, x400 000, and x500 000) in at least three randomly selected areas. The composition of the samples was evaluated by measuring the relative ratio of Pt and Ir in at least three and typically five different randomly selected areas.

Inductively Coupled Plasma Mass Spectrometry. The Pt loading in the Pt/C catalysts was determined via an indirect Pt proof.[41] The actual content of Pt and Ir in the bifunctional catalysts was evaluated by inductively coupled plasma mass spectrometry (ICP-MS, NexION 2000 ICP-MS). The Ir loading in the bifunctional catalyst was indirectly evaluated by measuring the Ir content lost during the immobilization procedure. That is the amount of Ir NPs remaining in the supernatant after flocculation by HCl, and the Ir NPs remaining in the re-dispersing solvent acetone were determined by ICP-MS after dissolution in aqua regia (volume ratio of HCl: HNO_3 = 3: 1). The volume was adjusted to 20 mL with milli-Q water. ICP-MS was carried out using a cyclonic spray chamber and a PFA nebulizer. The radio-frequency power for the plasma was held at 1300 W with a gas flow of 15 L min^{-1}.

Electrochemical Measurements. All electrochemical measurements were performed using a computer-controlled potentiostat (ECi 200, Nordic Electrochemistry) and a glass cell equipped with three electrodes. A 5 mm mirror-polished glassy carbon (GC) disk embedded in a Teflon tip [homogeneous thin films of Pt-based catalysts on GC were prepared by pipetting different amounts of each catalyst ink on GC to lead the same loading of Pt (10 $\mu g\ cm^{-2}$) and drying in air] was used as the working electrode and a platinum wire as the counter electrode. All potentials were measured with respect to a reversible hydrogen electrode (RHE). The electrolyte was 0.1 M $HClO_4$ prepared by diluting 70% $HClO_4$ with milli-Q water. The effective solution resistance was compensated to below 3 Ω via an analogue positive feedback scheme. Prior to all electrochemical measurements and ADTs, the electrolyte was de-aerated by purging with Ar. The supported monometallic Pt NPs were cleaned by potential cycling between 0.05 and 1.20 V_{RHE} at a scan rate of 500 mV s^{-1} until stable cyclic voltammograms (CVs) could be observed. The supported Pt_xIr_y alloy NPs and Pt−IrO_2 nanocomposites were cleaned by potential cycling between 0.10 and 0.30 V_{RHE} at a scan rate of 100 mV s^{-1} for 20 cycles (in order not to oxidize Ir to obtain the exact value of the ECSA originating from Pt as well as Ir; once Ir is oxidized, the CO stripping method for the Ir ECSA determination does not work, as Ir oxide does not adsorb CO).[42]

After cleaning, for each bimetallic catalyst layer, the following automized measurement procedure was applied using a macroscript of the potentiostat software: CO stripping, Ir activation, CO stripping, ORR activity determination, OER activity determination, ADT treatment, ORR activity determination, OER activity determination, and CO stripping. The activities are determined with respect to the metal mass (mass activity) as well as with respect to the electrochemically active surface area (specific activity).

Ir activation was performed by holding the potential at 1.60 V_{RHE} for 8 min, followed by cycling the electrode potential between 0.05 and 1.20 V_{RHE} for around 100 cycles to clean the catalyst surface until a stable CV with the typical features of Pt was obtained.

The ECSA was determined via the oxidation charge in CO monolayer stripping experiments.[43] Two different ECSAs were determined, the ECSA of the pristine catalyst in the reduced state and the ECSA after Ir activation. In the reduced state, Ir as well as Pt adsorb CO and the charge from the CO monolayer stripping relates to the total (Ir + Pt) ECSA, whereas after activation, the oxidized Ir NPs do not adsorb CO and only the Pt ECSA is determined, as demonstrated in previous studies showing that after electrochemical activation, the Ir NPs cannot be easily reduced again;[42] even after holding at low potentials in hydrogen atmosphere for 30 min, only around 10% of the initial Ir surface area was determined in CO stripping. To determine the total ECSA, the electrode was held at 0.15 V_{RHE} in a CO-saturated electrolyte for 2 min. Thereafter, the electrolyte was saturated with Ar to replace the excess CO in the electrolyte. The adsorbed CO monolayer was oxidized to CO_2 by scanning the potential from 0.15 to 1.10 and 1.40 V_{RHE}, respectively, for Pt/C and the different bifunctional PtIr catalysts. The scan rate was 50 mV s^{-1}. After activating the different bifunctional PtIr catalysts, a second CO stripping curve was recorded in the same manner, however at a reduced potential window between 0.15 and 1.10 V_{RHE}. To calculate the Pt ECSA, a reference monolayer oxidation charge value of 396 $\mu C\ cm_{Pt}^{-2}$ was used[44] and for Ir, 358 $\mu C\ cm_{Ir}^{-2}$ was used.[45] The Ir surface area was estimated by subtracting the Pt surface area from the total surface area, leading to nominal Ir surface areas up to 225 $m^2\ g_{Ir}^{-1}$ for all the different PtIr catalysts, which even slightly exceed the ECSA of Ir NPs deposited onto a planar support.[42] The thus-determined nominal Ir surface area might be slightly overestimated because of currents related to irreversible (hydro) oxide formation on Ir.[46] 225 $m^2\ g_{Ir}^{-1}$ corresponds to an average particle size about 1.2 nm, which is in agreement with the particle size determined in small-angle X-ray scattering but slightly lower than the average size determined by TEM.[42] In addition, this estimation disregards the shielding of parts of the particle surface due to the particle support interface. The likely overestimation of the Ir surface area leads to an underestimation of the specific OER activity but does not influence any of the conclusions made. Representative CO stripping curves for a pristine and activated Pt−IrO_2 nanocomposite are presented in Figure S1. It can be clearly seen that the area under the CO stripping curve is significantly higher in the pristine nanocomposite catalyst (Pt plus Ir surface area) as compared to after activation (Pt surface area).

In order to determine the ORR activity, measurements were conducted in an O_2-saturated electrolyte at a scan rate of 50 mV s^{-1} and a rotation speed of 1600 rpm.[43] The polarization curves were corrected by background subtraction (CVs recorded in an Ar-saturated electrolyte at the identical scan rate). The specific activity was analyzed and compared at 0.90 V_{RHE} from positive going scan direction on a polarization curve normalized by the Pt area. The mass activity was analyzed and

https://dx.doi.org/10.1021/acscatal.0c03867
ACS Catal. 2021, 11, 820−828

compared at 0.90 V_{RHE} normalized by Pt content and total metal content, respectively.

In order to determine the OER activity, the potential was scanned between 1.00 and 1.70 V_{RHE} at a scan rate of 10 mV s^{-1} and a rotation speed of 1600 rpm. The OER specific activity was analyzed based on the current at 1.50 V_{RHE} during the positive going scan direction normalized by the total surface area, while for the mass activity, the current at 1.50 V_{RHE} was normalized by Pt content (Pt/C catalysts), Ir content, and total metal content (PtIr bimetallic catalysts).

ADT Protocol. The stability of the catalysts was scrutinized employing ADTs with a current control protocol. The protocol was developed based on the simulation of load cycling and was mainly designed to probe startup−shutdown conditions in fuel cells, for which bifunctional ORR/OER catalysts have been suggested. A similar degradation protocol for this purpose was employed in a previous work of Dahn and co-workers.[47] The degradation test was conducted in the O_2-saturated $HClO_4$ electrolyte maintaining a rotation of 1600 rpm. The current was stepped between 0 and −5 mA cm_{geo}^{-2}, which is roughly the diffusion-limited current used during ORR in a RDE measurement at 1600 rpm, with a rest time of 1 s. This procedure was repeated for 5 times followed by a current step to 1 mA cm_{geo}^{-2} for 1 s. The abovementioned procedure was regarded as a basic unit, and this unit was repeated for 300 times, as schematized in Figure 1. The ECSA, ORR activity, and OER activity were recorded before and after applying the ADT. ADTs solely focusing on URFC application usually employ an equal number of excursions to oxidizing and reducing conditions.

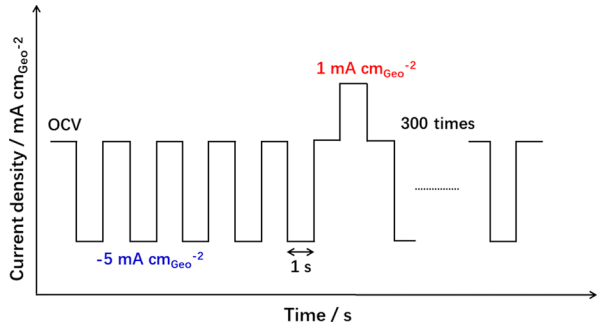

Figure 1. Scheme of the ADT protocol applying steps between different current densities. All measurements were performed in oxygen-saturated 0.1 M $HClO_4$ solution at room temperature applying a rotation rate of 1600 rpm.

RESULTS AND DISCUSSION

As outlined in the introduction, the aim of this study is to utilize our colloidal toolbox approach[36−39] to compare the performance and stability of two different concepts for bifunctional ORR/OER catalysts, that is, Pt_xIr_y alloy NPs and nanocomposites composed of a mixture of monometallic Pt and Ir NPs. The catalysts were investigated after supporting them on commercial high surface area carbon support (Vulcan XC72R). For both approaches, two nominal weight compositions were prepared, that is, Pt: Ir = 1: 1 and Pt: Ir = 1: 2 (due to the very similar molecular weights of Pt and Ir, i.e., 195.084 u and 192.217 u; in the following, we do not explicitly distinguish between weight and atomic ratios). For each bifunctional catalyst, the Pt loading on the carbon support was kept at 20 wt %. This resulted in nanocomposites with 20 wt % Pt and 20 wt % Ir NPs and 20 wt % Pt and 40 wt % Ir NPs on carbon as well as Pt_xIr_y alloy NPs that follow the same composition and metal weight as the nanocomposites. Monometallic Pt NPs with 20 and 40 wt % loading served as the benchmark. In the following, the catalysts are denominated as 20% Pt/C, 40% Pt/C, Pt + Ir/C, Pt + 2 Ir/C, PtIr/C, and $PtIr_2$/C.

We start the discussion with the physical characterization of the as-prepared catalysts. In Figure 2, representative TEM

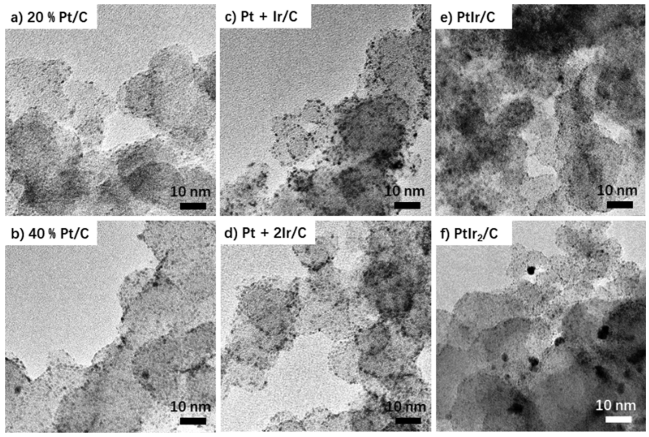

Figure 2. TEM micrographs of the as-prepared catalyst samples. (a,b) Supported monometallic Pt NPs with 20 and 40 wt % loading, respectively. (c,d) Supported Pt−Ir nanocomposites with 20−20 wt % and 20−40 wt % loading, respectively. (e,f) Supported PtIr alloy and $PtIr_2$ alloy NPs with the same metal loading as the nanocomposites.

micrographs of each catalyst are presented. It can be seen that the NPs are round in shape and well dispersed on the carbon support. The size (diameter) of the individual Pt, Ir, and Pt_xIr_y NPs is in the range of 1−3 nm. For the monometallic and nanocomposite catalysts, an increase in total metal loading from 20 to 40 wt % (Pt/C, Figure 2a, b) and from 40 to 60 wt % (Pt + Ir/C and Pt + 2 Ir/C, Figure 2c, d) leads to a slight increase in NP agglomeration. The fact that the Pt ECSA determined by CO stripping of the individual catalysts deviates less than 10% from each other (see Table S2) confirms that the agglomeration is not significant. EDX analysis of the nanocomposite catalysts further indicates that nominal (Pt: Ir of 1: 1 and 1: 2, respectively) and obtained compositions (Pt: Ir of 1.08: 0.92 and 1.00: 2.00, respectively) are in good agreement; see Table S4. The results therefore demonstrate the true nature of the nanocomposites with a mix of individual Pt and Ir NPs immobilized on the carbon support. By contrast, in the case of the Pt_xIr_y alloy NPs, only the PtIr alloy (1: 1 ratio at 40 wt % total metal loading) contains the targeted metal ratio; see EDX analysis in Table S4. An increase to a nominal Pt: Ir ratio of 1: 2 (associated with an increase in total metal loading on the support to 60 wt %; $PtIr_2$/C sample) leads to a deviation of the established composition from the nominal one: a Pt: Ir composition of 0.90: 1.10 is determined by EDX significantly deviating from the targeted 1: 2 ratio. The large deviation from the nominal composition indicates that the mixing of Pt and Ir during the particle formation is insufficient. In addition, the formation of some agglomerated NPs on the carbon support can be seen in the TEM micrograph shown in Figure 2. However, the Pt ECSA is not largely affected by these agglomerates (see Table S2), while the overall metal area

https://dx.doi.org/10.1021/acscatal.0c03867
ACS Catal. 2021, 11, 820−828

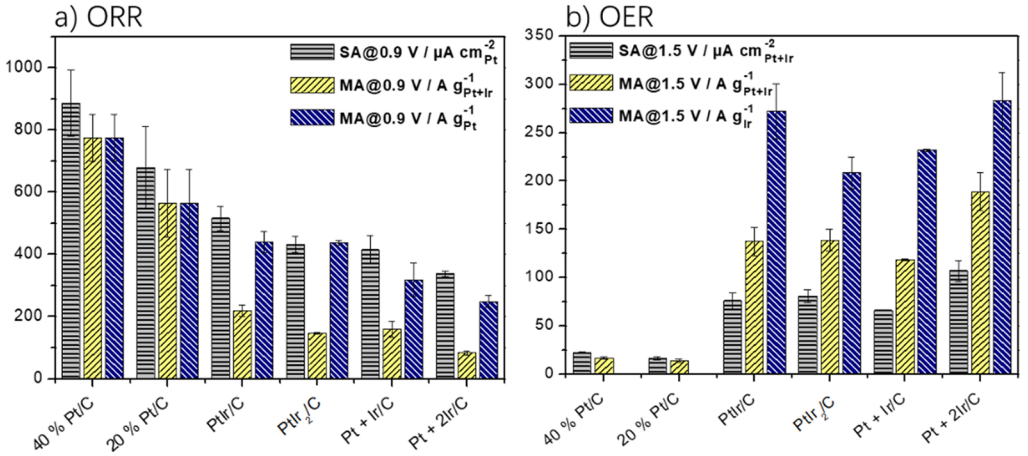

Figure 3. Comparison of the electrochemical activity of supported monometallic Pt NPs, Pt_xIr_y alloy NPs, and Pt−IrO_2 nanocomposites before the ADT. (a) ORR performance and (b) OER performance. The ORR activity is determined with a scan rate of 50 mV s^{-1} and 1600 rpm applying a potential range of 0.05−1.10 V_{RHE}, while the OER activity is determined with a scan rate of 10 mV s^{-1} and 1600 rpm applying a potential range of 1.00−1.70 V_{RHE}. Concerning the OER performance of the Pt/C catalysts, the mass activity normalized to the total metal content equals the mass activity normalized to the Pt content. All measurements are performed at room temperature. As error, the standard deviation from three measurements on different catalyst films is given.

before the formation of the Ir-oxide phase is lower on the $PtIr_2$/C than on the Pt + 2Ir/C catalyst (the ratio between Pt and Ir and their loading on the electrode are the same), as shown in Figure S1b. Last but not least, the results show that for this specific example of bimetallic catalysts, the catalyst composition can be more accurately tuned using a nanocomposite approach than using an alloying approach.

As discussed in the introduction, bifunctional oxygen catalysts that can catalyze the ORR as well as the OER are suggested to mitigate the degradation during startup and shutdown of fuel cells and are required for URFCs in CG configuration. Therefore, we evaluated the specific activity and mass activity for the ORR as well as the OER. Concentrating first on the ORR activities, Figure 3a, it should be noted that Ir oxide[48] is not active for the ORR (in order to form bifunctional catalysts, the Ir was activated to Ir oxide, see experimental section). As a consequence, the specific activity of the ORR is normalized to the Pt ECSA, whereas the mass activity of the ORR is given based on normalization to the Pt mass as well as the total metal mass (Pt and Ir) to account for the fact that the mass activity is mainly used to account for the catalyst cost for a certain reaction. The results clearly show that the addition of Ir to the catalyst decreases the specific activity as well as the mass activity of the ORR, independent of normalization and regardless of whether a nanocomposite or alloy catalyst is prepared. This is a particularly interesting finding for the specific activity of the nanocomposite catalysts. As the specific activity is normalized to the Pt ECSA, which is not affected by the co-immobilization of the Ir NPs (see Table S1), a constant specific activity would be expected in case there is no electronic particle−particle interaction. Instead, the results indicate that the electronic properties of the Pt NPs are affected by the adjacent Ir-oxide NPs. These particle−particle interactions may arise because of direct contact between Pt and Ir-oxide particles[31,32,35] or by reducing the interparticle distance to very small distances.[49−51] As an example of the former, it has been found that the deposition of Pt NPs onto an IrO_x support leads to lattice contraction and inhibition of the H_{upd} region of Pt.[31,52] The fact that no H_{upd} region is observed points to particle−particle interactions due to the particle proximity effect. This phenomenon so far was observed only for monometallic Pt clusters and NPs. In these cases, a decrease in the interparticle distance led to the enhancement of the ORR because of reduced oxophilicity as well as reduced Pt dissolution.[49−51] This is in line with the results obtained in the present work for monometallic Pt NPs. The ORR specific activity for the 40% Pt/C as compared to the 20% Pt/C is increased, that is, 886 ± 50 µA cm $_{Pt}^{-2}$ vs 679 ± 132 µA cm_{Pt}^{-2} (Table S1). As the ECSA of both catalysts is very similar, the difference in specific activity directly translates into a corresponding difference in mass activity, that is, 774.5 ± 74.5 A g_{Pt}^{-1} and 564.5 ± 109.4 A g_{Pt}^{-1}, respectively (Table S1). By comparison, the ORR on Pt seems to be inhibited by the adjacent Ir-oxide NPs. According to the Sabatier principle for the ORR,[53] this finding indicates an increase in oxophilicity of the Pt NPs due to Pt−IrO_2 particle−particle interactions. For the Pt + 2Ir/C nanocomposite, a specific activity of 338 ± 9 µA cm_{Pt}^{-2} and a mass activity of 249 ± 18.3 A g_{Pt}^{-1} were determined (see Table S1), which is only half the activity of the monometallic 20% Pt/C catalyst.

It should be noted that the Pt_xIr_y alloy NPs exhibit a decreased ORR performance as well, both in Pt area-normalized ORR activity and mass-normalized ORR activity; see Table S1. The results therefore show that the different bifunctional ORR/OER catalysts suffer from ORR inhibition due to the addition of Ir (IrO_2) to the catalyst.

We next studied the OER performance of the bifunctional catalysts. Thereby, we probed the OER activity based on the oxidation currents observed at 1.50 V_{RHE} in linear scan voltammetry measurements. As Pt is not very active for the OER[54] (see Figure 3b), the monometallic Pt catalysts serve only as a comparison. It is seen that, as expected, the OER performance is considerably boosted by the introduction of activated Ir (IrO_2). Among the investigated catalysts, the Pt + 2Ir/C shows the highest specific activity for the OER, which in a URFC may compensate for the lower activity of this catalyst for the ORR. For the other three catalysts, only a small difference in specific activity between the supported Pt_xIr_y alloy NPs and the Pt−IrO_2 nanocomposites is seen. The same trend is observed for the mass activity normalized to the total metal

https://dx.doi.org/10.1021/acscatal.0c03867
ACS Catal. 2021, 11, 820−828

loading. Interestingly, normalizing the mass activity to the Ir loading, which can be considered the only active component for the OER, the trend slightly changes. The mass activity for the PtIr/C catalyst, 272 ± 28.4 A g_{Ir}^{-1}, becomes almost the same as the mass activity for the Pt + 2Ir/C sample, 283 ± 29.2 A g_{Ir}^{-1} (Table S1).

Overall, the differences in pristine OER activity between the catalysts are relatively small and no specific bifunctional catalyst stands out as the most promising and preferred candidate for future deployment. A different conclusion is reached when the stability and resulting changes in performance are considered. The stability of the catalysts was evaluated by employing an ADT based on a current control protocol, that is, fixed currents were applied instead of the conventional potential control. To take into account the bifunctional nature of the catalysts, reductive as well as oxidative currents were applied, albeit the oxidative currents were limited to avoid extensive carbon corrosion. The stability determination based on the loss in the electrochemically available Pt surface area determined by CO stripping is summarized in Figure 4.

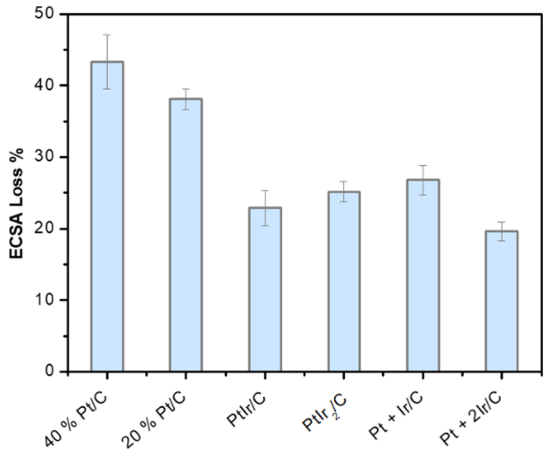

Figure 4. Comparison of the loss in the electrochemically available Pt surface area for the supported monometallic Pt NPs, Pt_xIr_y alloy NPs, and Pt−IrO_2 nanocomposites after an ADT with a current control protocol. As error, the standard deviation for three measurements on different catalyst films is given.

Representative CO stripping curves for all catalysts at the beginning of test (BOT) and at the end of test (EOT) are shown in Figure S2. In Figure S5, TEM micrographs of the degraded catalysts are shown. Based on the Pt ECSA loss, one can clearly state that Ir not only increases the OER activity but also boosts the stability of the catalysts. The ECSA loss for supported Pt_xIr_y alloy NPs and the Pt−IrO_2 nanocomposites is in the range between 19.6 ± 1.3 and 26.8 ± 2.1%, which is roughly half of the ECSA loss seen without Ir, that is, 38.1 ± 1.4% for 20% Pt/C and 43.3 ± 3.8 for 40% Pt/C; see also Table S2. Furthermore, as a general trend, the ECSA loss seems to decrease with the Ir content. The catalyst stability can also be analyzed based on the CVs recorded in the Ar-saturated electrolyte before and after subjecting the catalyst to the ADTs; see Figure S3. After the degradation test, both the H_{upd} potential region (underpotentially deposited hydrogen, 0.05−0.40 V_{RHE}) and the Pt redox potential region (ca. 0.60−1.10 V_{RHE}) "shrink" as compared with the CVs of the pristine catalyst. The TEM micrographs of the degraded Pt/C catalysts (see Figure S5) clearly indicate particle growth which can be related to electrochemical Ostwald ripening and/or particle migration and coalescence.[52] Furthermore, particle detachment might occur which is difficult to identify using conventional TEM. Interestingly, the TEM micrographs indicate differences in the degradation behavior between the different bimetallic catalysts. The Pt_xIr_y alloy NPs experience particle growth as well, whereas the Pt−IrO_2 nanocomposites seem to experience less degradation, in particular, the Pt + Ir/C catalyst. The results therefore confirm the general ability of IrO_2 to reduce the degradation of Pt/C catalysts. They also indicate differences in the concept between "alloying" and nanocomposites. This becomes even more evident considering the EOT activities.

The inflicted change in ORR and OER performance due to the ADTs is summarized in Figure 5. We thereby concentrate on the bifunctional catalysts. After the ADTs, all bifunctional catalysts display a similar ORR mass activity, in particular if the mass activity is based on the (initial) Pt loading. This is in contrast to the results of the pristine catalysts before applying the ADTs reported in Figure 3a where the supported Pt_xIr_y alloy NPs displayed higher mass activities than the supported Pt−IrO_2 nanocomposites. Regarding OER mass activity, the influence of the ADTs is even more pronounced. While the Pt ECSA loss is similar for the supported Pt_xIr_y alloy NPs and the Pt−IrO_2 nanocomposites, a significant difference is detected in OER activity; see Figure 5b. In agreement with the TEM micrographs in Figure S5, the Pt−IrO_2 nanocomposites exhibit a significantly higher mass activity than the supported Pt_xIr_y alloy NPs. The difference between alloy NPs and nanocomposites is most pronounced for the Pt + Ir/C catalyst. After the ADTs, it exhibits the highest OER, even though the pristine nanocomposite had a lower OER mass activity than the supported Pt_xIr_y alloy NPs. The mass activity values after ADTs are 83.6 ± 0.9 A g_{Ir}^{-1} and 41.8 ± 0.4 A g_{Ir+Pt}^{-1}, whereas the mass activity values for the supported PtIr alloy NPs are only 28.4 ± 5.7 A g_{Ir}^{-1} and 14.2 ± 2.9 A g_{Ir+Pt}^{-1}. That is, the mass activity of the nanocomposite is after the ADTs, roughly a factor of three higher than that of the respective alloy NPs; see Table S3 for a complete comparison.

The stabilizing effect of Ir is often discussed in the context of a boosted OER activity. That is, the oxidative current forced onto the catalyst is not provided by carbon oxidation but the OER instead. However, IrO_2 is prone to dissolution as well, as it can experience a change in the valence state between +3 and +4 in the potential range ∼0.80−1.00 V_{RHE}.[52] A change in the valence state requires a current, and therefore this process might compete with the OER and carbon corrosion. A rough estimation shows that the currents in each step of the ADT protocol are sufficient to switch the oxidation of ca. half of all Ir atoms in the samples. Our hypothesis to explain the difference in performance degradation between Pt_xIr_y alloy NPs and Pt−IrO_2 nanocomposites is that the stability of IrO_2 is key and that separating IrO_2 from Pt offers significant advantages. In the Pt_xIr_y alloy NPs systems, Pt and Ir are incorporated in the same particle, that is, once IrO_2 is subjected to degradation, inevitably Pt is as well. In the Pt−IrO_2 nanocomposite system, the effect of the ADTs on Pt and Ir can be separated. Thus, the Pt + 2Ir/C catalyst is least affected by the ADTs with respect to ORR performance. Pt is "protected" by IrO_2, however, at the expense of a high relative loss in OER activity. By comparison, in the Pt + Ir/C nanocomposite, the Pt NPs are less "protected", and the ORR activity loss is higher, but the OER activity loss is lower. The protective function of IrO_2

https://dx.doi.org/10.1021/acscatal.0c03867
ACS Catal. 2021, 11, 820−828

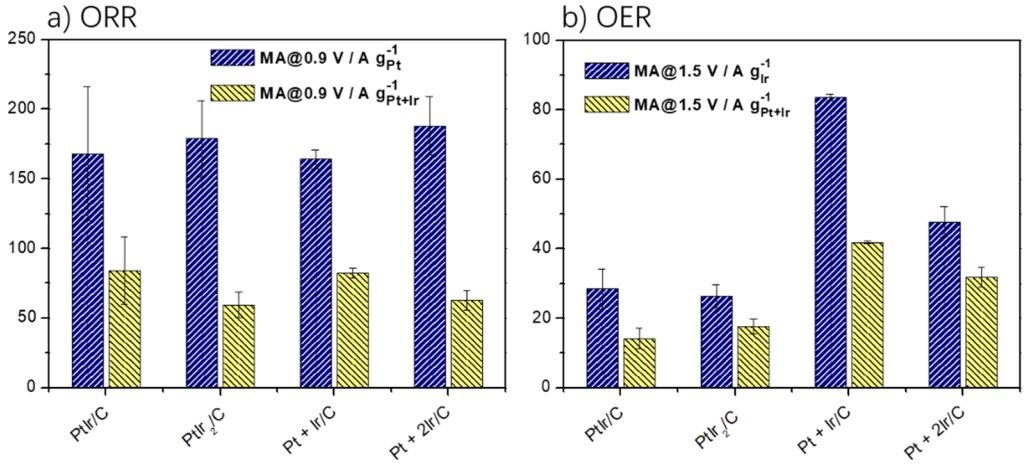

Figure 5. Comparison of the electrochemical mass activity of supported Pt_xIr_y alloy NPs and Pt−IrO_2 nanocomposites after the ADTs. (a) ORR performance and (b) OER performance. The ORR activity is determined with a scan rate of 50 mV s^{-1} and 1600 rpm applying a potential range of 0.05−1.10 V_{RHE}, while the OER activity is determined with a scan rate of 10 mV s^{-1} and 1600 rpm applying a potential range of 1.00−1.70 V_{RHE}. As error, the standard deviation from three measurements on different catalyst films is given.

comes at least in part from the change in the valence state between +3 and +4, which requires a charge, but also triggers Ir dissolution.[46]

To substantiate this hypothesis, we analyzed the compositional changes of the catalysts upon applying the ADTs with EDX. As mentioned above, in the pristine Pt−IrO_2 nanocomposites and the PtIr/C, the determined metal composition is close to the nominal value. We confirmed the results also by ICP-MS measurements; see Table S5. Although the ICP-MS measurements have limitations as discussed in detail in the experimental part Inductively Coupled Plasma Mass Spectrometry, we can follow the Ir and Pt ratio in the catalyst as well as the "washing" supernatant. The results furthermore show that during the "washing" procedure for NP flocculation, only few (less than 4%) NPs are lost into the supernatant. The composition of the pristine $PtIr_2$/C, however, deviates from the nominal one (the Ir/Pt is only 1.21).

The results show that after applying the ADTs, the ratio between Ir and Pt substantially decreases in all bifunctional catalysts. The changes of Ir/Pt before and after the degradation test are summarized in Table S4. The results suggest that the increase in IrO_2 in the catalyst leads also to an increase in disproportional Ir loss. Separating Pt and IrO_2 NPs in a nanocomposite allows for a fine tuning of the electrochemical properties of the bifunctional catalyst and thus offers advantages for their optimization. The best overall stability and ORR/OER performance is established for the nanocomposite catalysts based on 20 wt % Pt and 20 wt % Ir. For this catalyst, minor particle agglomeration is observed after applying ADTs (see Figure S5), and the relative loss of Ir is lowest (see Table S4). Last but not least, the differences between the different catalysts (alloy and nanocomposite) could in part be due to differences in the interaction with the carbon support. However, probing the carbon support in the different catalysts before and after the ADT (Figure S6), no significant differences between the catalysts were seen.

CONCLUSIONS

Supported monometallic Pt NPs, Pt_xIr_y alloy NPs, and Pt−IrO_2 nanocomposites were prepared and measured to investigate ORR/OER performance and stability. The results indicate that the monometallic Pt NPs exhibit the best ORR performance of the investigated catalysts, that is, the ORR performance is decreased by adding Ir to the catalyst. In the case of the nanocomposite catalysts, the results indicate an electronic particle proximity effect between Pt and IrO_2 NPs, leading to an increase in oxophilicity of the Pt NPs. The opposite activity trend is found for the OER. The increase in OER activity when introducing Ir to a Pt/C catalyst is accompanied with an increase in stability. Applying an ADT protocol to study the employment of bifunctional Pt−IrO_2 catalysts to mitigate degradation under startup and shutdown, it is seen that the bifunctional catalysts suffer from severe degradation at such challenging conditions. This will also have a direct consequence when applying such catalysts in URFCs in CG configuration when switching between OER and ORR mode and questions their stable long-term operation. Part of the severe degradation might be mitigated by more stable support materials other than carbons; however, the problem of a declining ratio between Ir and Pt most likely will need to be solved. Last but not least, our results provide evidence that nanocomposite materials show interesting electrochemical properties and might be a suitable strategy to address these stability challenges. Although being far from stable, Pt−IrO_2 nanocomposites allow for careful optimization of ORR and OER properties and offer advantages over the conventional approach of alloying Pt and Ir.

ASSOCIATED CONTENT

Supporting Information

The Supporting Information is available free of charge at https://pubs.acs.org/doi/10.1021/acscatal.0c03867.

Additional experimental data, CVs, CO stripping curves, tables showing the specific and mass activities for ORR and OER, ECSA values in the beginning and at the end of the ADTs, a summary of the EDX and ICP-MS data as well as TEM micrographs of the degraded catalyst, and a summary of Raman data from the catalysts in the beginning and at the end of the ADTs (PDF)

https://dx.doi.org/10.1021/acscatal.0c03867
ACS Catal. 2021, 11, 820−828

AUTHOR INFORMATION

Corresponding Author

Matthias Arenz − *Department of Chemistry and Biochemistry, University of Bern, Bern 3012, Switzerland;* orcid.org/0000-0001-9765-4315; Email: matthias.arenz@dcb.unibe.ch

Authors

Jia Du − *Department of Chemistry and Biochemistry, University of Bern, Bern 3012, Switzerland*

Jonathan Quinson − *Department of Chemistry, University of Copenhagen, Copenhagen 2100, Denmark;* orcid.org/0000-0002-9374-9330

Damin Zhang − *Department of Chemistry and Biochemistry, University of Bern, Bern 3012, Switzerland*

Francesco Bizzotto − *Department of Chemistry and Biochemistry, University of Bern, Bern 3012, Switzerland*

Alessandro Zana − *Department of Chemistry and Biochemistry, University of Bern, Bern 3012, Switzerland*

Complete contact information is available at: https://pubs.acs.org/10.1021/acscatal.0c03867

Notes

The authors declare no competing financial interest.

ACKNOWLEDGMENTS

This work was supported by the Swiss National Science Foundation (SNSF) via project No. 200021_184742. J. D. acknowledges funding from the China Scholarship Council (CSC). S. B. Simonsen and L. Theil Kuhn, Technical University of Denmark, are thanked for access to TEM, Tom Vosch for the Raman measurements, and Wouter van Beek from the ESRF for measuring XRD on the catalyst samples.

REFERENCES

(1) She, Z. W.; Kibsgaard, J.; Dickens, C. F.; Chorkendorff, I.; Nørskov, J. K.; Jaramillo, T. F. Combining Theory and Experiment in Electrocatalysis: Insights into Materials Design. *Science* **2017**, *355*, No. eaad4998.

(2) Peng, L.; Wei, Z. Catalyst Engineering for Electrochemical Energy Conversion from Water to Water: Water Electrolysis and the Hydrogen Fuel Cell. *Engineering.* **2020**, *6*, 653−679.

(3) Sievers, G. W.; Jensen, A. W.; Quinson, J.; Zana, A.; Bizzotto, F.; Oezaslan, M.; Dworzak, A.; Kirkensgaard, J. J. K.; Smitshuysen, T. E. L.; Kadkhodazadeh, S.; Juelsholt, M.; Jensen, K. M. Ø.; Anklam, K.; Wan, H.; Schäfer, J.; Čépe, K.; Escudero-Escribano, M.; Rossmeisl, J.; Quade, A.; Brüser, V.; Arenz, M. Self-Supported Pt−CoO Networks Combining High Specific Activity with High Surface Area for Oxygen Reduction. *Nat. Mater.* **2020**, DOI: 10.1038/s41563-020-0775-8.

(4) McCrory, C. C. L.; Jung, S.; Ferrer, I. M.; Chatman, S. M.; Peters, J. C.; Jaramillo, T. F. Benchmarking Hydrogen Evolving Reaction and Oxygen Evolving Reaction Electrocatalysts for Solar Water Splitting Devices. *J. Am. Chem. Soc.* **2015**, *137*, 4347−4357.

(5) Siracusano, S.; Hodnik, N.; Jovanovic, P.; Ruiz-Zepeda, F.; Šala, M.; Baglio, V.; Aricò, A. S. New Insights into the Stability of a High Performance Nanostructured Catalyst for Sustainable Water Electrolysis. *Nano Energy* **2017**, *40*, 618−632.

(6) Carmo, M.; Fritz, D. L.; Mergel, J.; Stolten, D. A Comprehensive Review on PEM Water Electrolysis. *Int. J. Hydrogen Energy* **2013**, *38*, 4901−4934.

(7) Deng, Y.-J.; Tripkovic, V.; Rossmeisl, J.; Arenz, M. Oxygen Reduction Reaction on Pt Overlayers Deposited onto a Gold Film: Ligand, Strain, and Ensemble Effect. *ACS Catal.* **2016**, *6*, 671−676.

(8) Whipple, D. T.; Kenis, P. J. A. Prospects of CO2 Utilization via Direct Heterogeneous Electrochemical Reduction. *J. Phys. Chem. Lett.* **2010**, *1*, 3451−3458.

(9) Dutta, A.; Rahaman, M.; Luedi, N. C.; Mohos, M.; Broekmann, P. Morphology Matters: Tuning the Product Distribution of CO2 Electroreduction on Oxide-Derived Cu Foam Catalysts. *ACS Catal.* **2016**, *6*, 3804−3814.

(10) Davies, B. J. V.; Arenz, M.; Rossmeisl, J.; Escudero-Escribano, M. Electrochemical Synthesis of High-Value Chemicals: Detection of Key Reaction Intermediates and Products Combining Gas Chromatography-Mass Spectrometry and in Situ Infrared Spectroscopy. *J. Phys. Chem. C* **2019**, *123*, 12762−12772.

(11) Šarić, M.; Davies, B. J. V.; Schjødt, N. C.; Dahl, S.; Moses, P. G.; Escudero-Escribano, M.; Arenz, M.; Rossmeisl, J. Catalyst Design Criteria and Fundamental Limitations in the Electrochemical Synthesis of Dimethyl Carbonate. *Green Chem.* **2019**, *21*, 6200−6209.

(12) Pollet, B. G.; Staffell, I.; Shang, J. L. Current Status of Hybrid, Battery and Fuel Cell Electric Vehicles: From Electrochemistry to Market Prospects. *Electrochim. Acta* **2012**, *84*, 235−249.

(13) Gangloff, J. J.; Kast, J.; Morrison, G.; Marcinkoski, J. Design Space Assessment of Hydrogen Storage Onboard Medium and Heavy Duty Fuel Cell Electric Trucks. *J. Electrochem. Energy Convers. Storage* **2017**, DOI: 10.1115/1.4036508.

(14) Sønderskov, S. H.; Rasmussen, D.; Ilsøe, J.; Blom-Hansen, D.; Munk-Nielsen, S. Detecting Performance Outliers in Fuel Cell Backup Power Systems. In *2019 21st European Conference on Power Electronics and Applications (EPE '19 ECCE Europe)*; 2019; 1−10. DOI: 10.23919/EPE.2019.8915057.

(15) Di Marcoberardino, G.; Chiarabaglio, L.; Manzolini, G.; Campanari, S. A Techno-Economic Comparison of Micro-Cogeneration Systems Based on Polymer Electrolyte Membrane Fuel Cell for Residential Applications. *Appl. Energy* **2019**, *239*, 692−705.

(16) Álvarez Fernández, R.; Corbera Caraballo, S.; Beltrán Cilleruelo, F.; Lozano, J. A. Fuel Optimization Strategy for Hydrogen Fuel Cell Range Extender Vehicles Applying Genetic Algorithms. *Renew. Sustainable Energy Rev.* **2018**, *81*, 655−668.

(17) Gasteiger, H. A.; Kocha, S. S.; Sompalli, B.; Wagner, F. T. Activity Benchmarks and Requirements for Pt, Pt-Alloy, and Non-Pt Oxygen Reduction Catalysts for PEMFCs. *Appl. Catal. B: Environ.* **2005**, *56*, 9−35.

(18) Marković, N. M.; Schmidt, T. J.; Stamenković, V.; Ross, P. N. Oxygen Reduction Reaction on Pt and Pt Bimetallic Surfaces: A Selective Review. *Fuel Cells* **2001**, 105.

(19) Stephens, I. E. L.; Bondarenko, A. S.; Grønbjerg, U.; Rossmeisl, J.; Chorkendorff, I. Understanding the Electrocatalysis of Oxygen Reduction on Platinum and Its Alloys. *Energy Environ. Sci.* **2012**, *5*, 6744−6762.

(20) Jia, Q.; Caldwell, K.; Strickland, K.; Ziegelbauer, J. M.; Liu, Z.; Yu, Z.; Ramaker, D. E.; Mukerjee, S. Improved Oxygen Reduction Activity and Durability of Dealloyed PtCox Catalysts for Proton Exchange Membrane Fuel Cells: Strain, Ligand, and Particle Size Effects. *ACS Catal.* **2015**, *5*, 176−186.

(21) Antolini, E.; Salgado, J. R. C.; Giz, M. J.; Gonzalez, E. R. Effects of Geometric and Electronic Factors on ORR Activity of Carbon Supported Pt-Co Electrocatalysts in PEM Fuel Cells. *Int. J. Hydrogen Energy* **2005**, *30*, 1213−1220.

(22) Kuriganova, A. B.; Leont'ev, I. N.; Smirnova, N. V. PtIr/C Catalysts Synthesized by Electrochemical Dispersion Method for Proton Exchange Membrane Fuel Cells. *Russ. J. Electrochem.* **2018**, *54*, 561−565.

(23) Carmo, M.; Keeley, G. P.; Holtz, D.; Grube, T.; Robinius, M.; Müller, M.; Stolten, D. PEM Water Electrolysis: Innovative Approaches towards Catalyst Separation, Recovery and Recycling. *Int. J. Hydrogen Energy* **2019**, *44*, 3450−3455.

(24) Ali, I.; AlGhamdi, K.; Al-Wadaani, F. T. Advances in Iridium Nano Catalyst Preparation, Characterization and Applications. *J. Mol. Liq.* **2019**, *280*, 274−284.

(25) Spöri, C.; Kwan, J. T. H.; Bonakdarpour, A.; Wilkinson, D. P.; Strasser, P. The Stability Challenges of Oxygen Evolving Catalysts:

Towards a Common Fundamental Understanding and Mitigation of Catalyst Degradation. *Angew. Chem., Int. Ed.* **2017**, *56*, 5994−6021.
(26) Altmann, S.; Kaz, T.; Friedrich, K. A. Bifunctional Electrodes for Unitised Regenerative Fuel Cells. *Electrochim. Acta* **2011**, *56*, 4287−4293.
(27) Sadhasivam, T.; Dhanabalan, K.; Roh, S. H.; Kim, T. H.; Park, K. W.; Jung, S.; Kurkuri, M. D.; Jung, H. Y. A Comprehensive Review on Unitized Regenerative Fuel Cells: Crucial Challenges and Developments. *Int. J. Hydrogen Energy* **2017**, *42*, 4415−4433.
(28) Regmi, Y. N.; Peng, X.; Fornaciari, J. C.; Wei, M.; Myers, D. J.; Weber, A. Z.; Danilovic, N. A Low Temperature Unitized Regenerative Fuel Cell Realizing 60% Round Trip Efficiency and 10 000 Cycles of Durability for Energy Storage Applications. *Energy Environ. Sci.* **2020**, *13*, 2096−2105.
(29) Ioroi, T.; Kitazawa, N.; Yasuda, K.; Yamamoto, Y.; Takenaka, H. Iridium Oxide/Platinum Electrocatalysts for Unitized Regenerative Polymer Electrolyte Fuel Cells. *J. Electrochem. Soc.* **2000**, *147*, 2018.
(30) Ioroi, T.; Yasuda, K. Platinum-Iridium Alloys as Oxygen Reduction Electrocatalysts for Polymer Electrolyte Fuel Cells. *J. Electrochem. Soc.* **2005**, *152*, A1917.
(31) Yao, W.; Yang, J.; Wang, J.; Nuli, Y. Chemical Deposition of Platinum Nanoparticles on Iridium Oxide for Oxygen Electrode of Unitized Regenerative Fuel Cell. *Electrochem. Commun.* **2007**, *9*, 1029−1034.
(32) Godínez-Salomón, F.; Albiter, L.; Mendoza-Cruz, R. P. Rhodes, C. Bimetallic Two-Dimensional Nanoframes: High Activity Acidic Bifunctional Oxygen Reduction and Evolution Electrocatalysts. *ACS Appl. Energy Mater.* **2020**, *3*, 2404−2421.
(33) Ioroi, T.; Kitazawa, N.; Yasuda, K.; Yamamoto, Y.; Takenaka, H. IrO2-Deposited Pt Electrocatalysts for Unitized Regenerative Polymer Electrolyte Fuel Cells. *J. Appl. Electrochem.* **2001**, *31*, 1179−1183.
(34) Moriau, L. J.; Bele, M.; Vižintin, A.; Ruiz-Zepeda, F.; Petek, U.; Jovanovič, P.; Šala, M.; Gaberščcek, M.; Hodnik, N. Synthesis and Advanced Electrochemical Characterization of Multifunctional Electrocatalytic Composite for Unitized Regenerative Fuel Cell. *ACS Catal.* **2019**, *9*, 11468−11483.
(35) da Silva, G. C.; Mayrhofer, K. J. J.; Ticianelli, E. A.; Cherevko, S. Dissolution Stability: The Major Challenge in the Regenerative Fuel Cells Bifunctional Catalysis. *J. Electrochem. Soc.* **2018**, *165*, F1376.
(36) Speder, J.; Altmann, L.; Roefzaad, M.; Bäumer, M.; Kirkensgaard, J. J. K.; Mortensen, K.; Arenz, M. Pt Based PEMFC Catalysts Prepared from Colloidal Particle Suspensions-a Toolbox for Model Studies. *Phys. Chem. Chem. Phys.* **2013**, *15*, 3602−3608.
(37) Neumann, S.; Grotheer, S.; Tielke, J.; Schrader, I.; Quinson, J.; Zana, A.; Oezaslan, M.; Arenz, M.; Kunz, S. Nanoparticles in a Box: A Concept to Isolate, Store and Re-Use Colloidal Surfactant-Free Precious Metal Nanoparticles. *J. Mater. Chem. A* **2017**, *5*, 6140−6145.
(38) Quinson, J.; Inaba, M.; Neumann, S.; Swane, A. A.; Bucher, J.; Simonsen, S. B.; Theil Kuhn, L.; Kirkensgaard, J. J. K.; Jensen, K. M.; Oezaslan, M.; Kunz, S.; Arenz, M. Investigating Particle Size Effects in Catalysis by Applying a Size-Controlled and Surfactant-Free Synthesis of Colloidal Nanoparticles in Alkaline Ethylene Glycol: Case Study of the Oxygen Reduction Reaction on Pt. *ACS Catal.* **2018**, *8*, 6627−6635.
(39) Quinson, J.; Neumann, S.; Wannmacher, T.; Kacenauskaite, L.; Inaba, M.; Bucher, J.; Bizzotto, F.; Simonsen, S. B.; Theil Kuhn, L.; Bujak, D.; Zana, A.; Arenz, M.; Kunz, S. Colloids for Catalysts: A Concept for the Preparation of Superior Catalysts of Industrial Relevance. *Angew. Chem., Int. Ed.* **2018**, *57*, 12338−12341.
(40) Spanos, I.; Rellán, C. P.; Altmann, L.; Bäumer, M.; Arenz, M. PtxCo1-X Alloy NPs Prepared by Colloidal Tool-Box Synthesis: The Effect of de-Alloying on the Oxygen Reduction Reaction Activity. *Int. J. Hydrogen Energy* **2014**, *39*, 9143.
(41) Bucher, J.; Quinson, J.; Mingers, A. M.; Zhang, D.; Arenz, M. On the Facile and Accurate Determination of the Pt Content in Standard Carbon Supported Pt Fuel Cell Catalysts. *Anal. Chim. Acta* **2020**, *1101*, 41−49.
(42) Bizzotto, F.; Quinson, J.; Zana, A.; Kirkensgaard, J. J. K.; Dworzak, A.; Oezaslan, M.; Arenz, M. Ir Nanoparticles with Ultrahigh Dispersion as Oxygen Evolution Reaction (OER) Catalysts: Synthesis and Activity Benchmarking. *Catal. Sci. Technol.* **2019**, *9*, 6345−6356.
(43) Inaba, M.; Quinson, J.; Bucher, J. R.; Arenz, M. On the Preparation and Testing of Fuel Cell Catalysts Using the Thin Film Rotating Disk Electrode Method. *J. Visualized Exp.* **2018**, *2018*, 57105.
(44) Mayrhofer, K. J. J.; Strmcnik, D.; Blizanac, B. B.; Stamenkovic, V.; Arenz, M.; Markovic, N. M. Measurement of Oxygen Reduction Activities via the Rotating Disc Electrode Method: From Pt Model Surfaces to Carbon-Supported High Surface Area Catalysts. *Electrochim. Acta* **2008**, *53*, 3181−3188.
(45) Alia, S. M.; Hurst, K. E.; Kocha, S. S.; Pivovar, B. S. Mercury Underpotential Deposition to Determine Iridium and Iridium Oxide Electrochemical Surface Areas. *J. Electrochem. Soc.* **2016**, *163*, F3051−F3056.
(46) Gómez, R.; Weaver, M. J. Electrochemical Infrared Studies of Monocrystalline Iridium Surfaces. Part 2: Carbon Monoxide and Nitric Oxide Adsorption on Ir(110). *Langmuir* **1998**, *14*, 2525−2534.
(47) Crowtz, T. C.; Dahn, J. R. Screening Bifunctional Pt Based NSTF Catalysts for Durability with the Rotating Disk Electrode: The Effect of Ir and Ru. *J. Electrochem. Soc.* **2018**, *165*, F854.
(48) Chang, C. H.; Yuen, T. S.; Nagao, Y.; Yugami, H. Electrocatalytic Activity of Iridium Oxide Nanoparticles Coated on Carbon for Oxygen Reduction as Cathode Catalyst in Polymer Electrolyte Fuel Cell. *J. Power Sources* **2010**, *195*, 5938−5941.
(49) Nesselberger, M.; Roefzaad, M.; Fayçal Hamou, R.; Ulrich Biedermann, P.; Schweinberger, F. F.; Kunz, S.; Schloegl, K.; Wiberg, G. K. H.; Ashton, S.; Heiz, U.; Mayrhofer, K. J. J.; Arenz, M. The Effect of Particle Proximity on the Oxygen Reduction Rate of Size-Selected Platinum Clusters. *Nat. Mater.* **2013**, *12*, 919−924.
(50) Speder, J.; Altmann, L.; Bäumer, M.; Kirkensgaard, J. J. K.; Mortensen, K.; Arenz, M. The Particle Proximity Effect: From Model to High Surface Area Fuel Cell Catalysts. *RSC Adv.* **2014**, *4*, 14971−14978.
(51) Sandbeck, D. J. S.; Secher, N. M.; Inaba, M.; Quinson, J.; Sørensen, J. E.; Kibsgaard, J.; Zana, A.; Bizzotto, F.; Speck, F. D.; Paul, M. T. Y.; Dworzak, A.; Dosche, C.; Oezaslan, M.; Chorkendorff, I.; Arenz, M.; Cherevko, S. The Dissolution Dilemma for Low Pt Loading Polymer Electrolyte Membrane Fuel Cell Catalysts. *J. Electrochem. Soc.* **2020**, *167*, 164501.
(52) da Silva, G. C.; Mayrhofer, K. J. J.; Ticianelli, E. A.; Cherevko, S. The Degradation of Pt/IrOx Oxygen Bifunctional Catalysts. *Electrochim. Acta* **2019**, *308*, 400−409.
(53) Nørskov, J. K.; Rossmeisl, J.; Logadottir, A.; Lindqvist, L.; Kitchin, J. R.; Bligaard, T.; Jónsson, H. Origin of the Overpotential for Oxygen Reduction at a Fuel-Cell Cathode. *J. Phys. Chem. B* **2004**, *108*, 17886−17892.
(54) Reier, T.; Oezaslan, M.; Strasser, P. Electrocatalytic Oxygen Evolution Reaction (OER) on Ru, Ir, and Pt Catalysts: A Comparative Study of Nanoparticles and Bulk Materials. *ACS Catal.* **2012**, *2*, 1765−1772.

https://dx.doi.org/10.1021/acscatal.0c03867
ACS Catal. 2021, 11, 820−828

Supporting Information of Manuscript I

Supporting Information

Bifunctional Pt-IrO_2 Catalysts for the Oxygen Evolution and Oxygen Reduction Reactions: Alloy Nanoparticles vs. Nanocomposite Catalysts

Jia Du [a], Jonathan Quinson[b], Damin Zhang[a], Francesco Bizzotto [a], Alessandro Zana [a], Matthias Arenz [a] *

[a] Department of Chemistry and Biochemistry, University of Bern, Freiestrasse 3, 3012 Bern, Switzerland

[b] Department of Chemistry, University of Copenhagen, Universitetsparken 5, 2100 Copenhagen Ø, Denmark

* corresponding author: matthias.arenz@dcb.unibe.ch

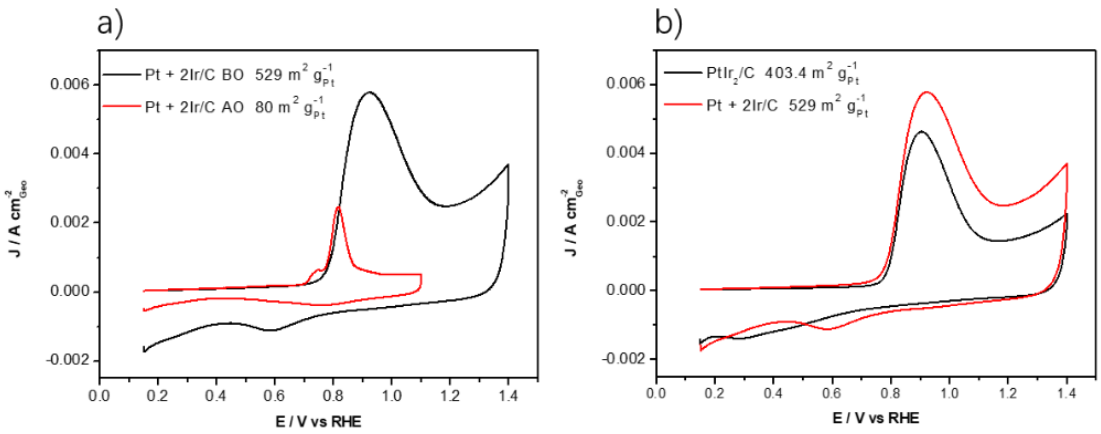

Figure S1. a) Comparison of electrochemical active area before (black line) and after (red line) Ir activation based on the area under CO stripping plot. The Pt + 2Ir/C nanocomposite (20 wt.% Pt 40 wt.% Ir/C) serves as an example. b) Comparison of electrochemical active area between-Pt + 2Ir/C (red line) and $PtIr_2$/C (black line) based on the area under CO stripping plot before Ir is activated. BO: before activation, AO: after activation.

Table S1. ORR and OER performances of supported monometallic Pt NPs, Pt_xIr_y alloy NPs and Pt – IrO_2 nanocomposites before ADTs. The ORR activity is determined at a potential of 0.90 V_{RHE} while the OER activity is determined at a potential of 1.50 V_{RHE}. The given error is the standard deviation of three independent measurements.

	Activity	20 % Pt/C	40 % Pt/C	PtIr/C	$PtIr_2$/C	Pt + Ir/C	Pt + 2Ir/C
ORR	$SA_{0.9\ V}$ ($\mu A\ cm_{Pt}^{-2}$)	679 ± 132	886 ± 50	516 ± 39	432 ± 26	415 ± 45	338 ± 9
	$MA_{0.9\ V}$ ($A\ g_{Pt}^{-1}$)	564.5 ± 109.4	774.5 ± 74.5	439.7 ± 33.7	437.8 ± 8.7	319 ± 52	249 ± 18.3
	$MA_{0.9\ V}$ ($A\ g_{Pt+Ir}^{-1}$)	564.5 ± 109.4	774.5 ± 74.5	218.5 ± 17.5	146.7 ± 2.7	159.3 ± 25.7	83.2 ± 6.1
OER	$SA_{1.5\ V}$ ($\mu A\ cm_{Pt+Ir}^{-2}$)	16.3 ± 1.8	22 ± 1	76 ± 8.2	80.5 ± 6.7	66.1 ± 0.4	107 ± 10.9
	$MA_{1.5\ V}$ ($A\ g_{Pt/Ir}^{-1}$)	13.7 ± 1.6	16.7 ± 0.9	272 ± 28.4	208.4 ± 16.6	231.6 ± 0.9	283 ± 29.2
	$MA_{1.5\ V}$ ($A\ g_{Pt+Ir}^{-1}$)	13.7 ± 1.6	16.7 ± 0.9	137.3 ± 14.9	138.8 ± 11.3	118.5 ± 1	189 ± 19.8

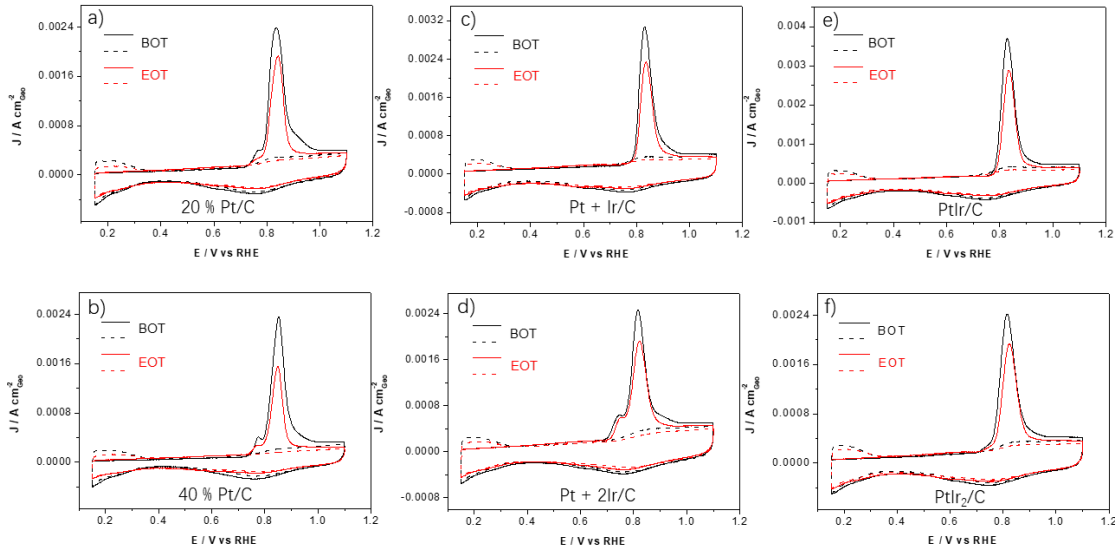

Figure S2. Initial and final CO stripping curves (solid line) as well as the subsequent CV (dashed line) of the supported monometallic Pt NPs, Pt_xIr_y alloy NPs and Pt – IrO_2 nanocomposites. The current is measured with a scan rate of 50 mV s^{-1}. BOT: before test, EOT: end of test.

Table S2. ECSA determined from CO stripping measurement before and after ADTs with current control protocol together with ECSA retained and loss (%) of the supported monometallic Pt NPs, Pt_xIr_y alloy NPs and Pt – IrO_2 nanocomposites. The error is the standard deviation of three independent measurements. BOT: before test, EOT: end of test.

Stability \ Catalysts		20 % Pt/C	40 % Pt/C	PtIr/C	$PtIr_2$/C	Pt + Ir/C	Pt + 2Ir/C
ECSA ($m^2\ g_{Pt}^{-1}$)	BOT	83.1 ± 3.6	74.8 ± 1.8	85.3 ± 2.1	75.1 ± 1.3	82.4 ± 2.8	77 ± 2.6
	EOT	51.5 ± 3.4	42.4 ± 3.0	65.8 ± 2.7	56.2 ± 2.5	60.3 ± 3.7	61.9 ± 3.6
Retained %		61.9 ± 1.4	56.7 ± 3.7	77.1 ± 2.5	74.8 ± 1.4	73.2 ± 2.1	80.4 ± 1.3
Loss %		38.1 ± 1.4	43.3 ± 3.8	22.9 ± 2.5	25.2 ± 1.4	26.8 ± 2.1	19.6 ± 1.3

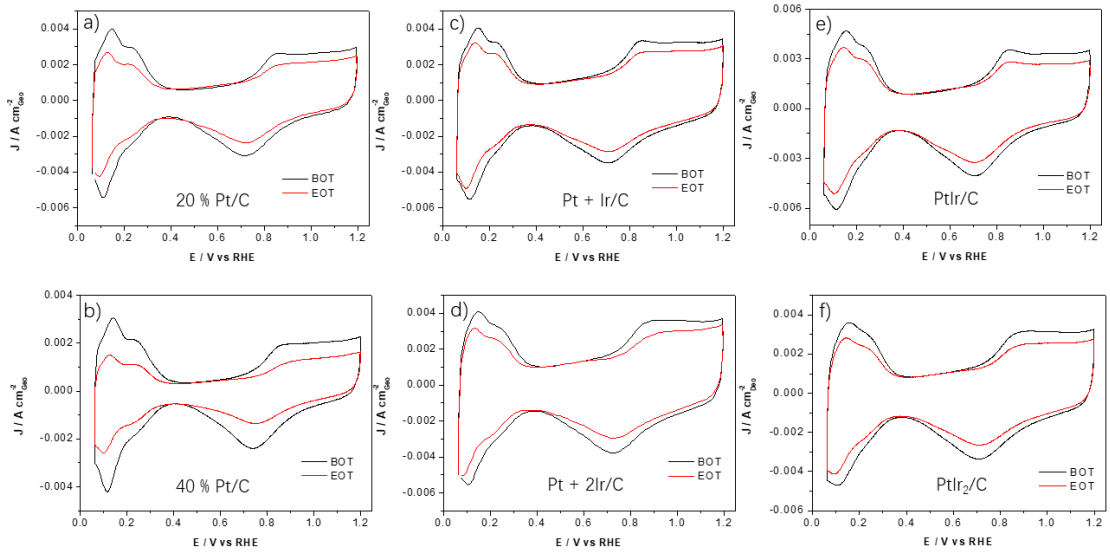

Figure S3. The CVs of the supported monometallic Pt NPs, Pt_xIr_y alloy NPs and Pt – IrO_2 nanocomposites recorded before and after ADTs. The scan rate is 50 mV s^{-1}. BOT: before test, EOT: end of test.

Table S3. ORR and OER performances of the supported Pt_xIr_y alloy NPs and Pt – IrO_2 nanocomposites after ADTs. ORR activity is determined at the potential of 0.90 V_{RHE} while OER activity is determined at the potential of 1.50 V_{RHE}. The error is the standard deviation of three independent measurements.

	Activity	PtIr/C	$PtIr_2$/C	Pt + Ir/C	Pt + 2Ir/C
ORR	$MA_{0.9\ V}$ ($A\ g_{Pt}^{-1}$)	168 ± 48	178.8 ± 27.3	164 ± 7	188 ± 21
	$MA_{0.9\ V}$ ($A\ g_{Pt+Ir}^{-1}$)	84 ± 24	59.5 ± 9	82.1 ± 3.6	62.6 ± 7.1
OER	$MA_{1.5\ V}$ ($A\ g_{Ir}^{-1}$)	28.4 ± 5.7	26.4 ± 3.2	83.6 ± 0.9	47.7 ± 4.4
	$MA_{1.5\ V}$ ($A\ g_{Pt+Ir}^{-1}$)	14.2 ± 2.9	17.6 ± 2.1	41.8 ± 0.4	31.8 ± 2.9

The effect of the ADTs on the catalysts can also be expressed as relative performance change for the ORR and OER, respectively, see Figure S4. It is seen that the ORR mass activity loss (%) for both supported Pt_xIr_y alloy NPs is around 60 %, for the Pt + Ir/C nanocomposite is around 49 % and only 25 % for the Pt + 2Ir/C nanocomposite. Also the OER mass activity loss is higher for the alloy NPs than for the nanocomposite, i.e. both supported Pt_xIr_y alloy NPs almost 90 % as compared to 64 % and 83 % for the Pt + Ir/C and Pt + 2Ir/C nanocomposite, respectively. Previous reports indicated that for Ir and Pt bifunctional catalyst systems (Pt and Ir were sputter deposited onto a nanostructured thin film catalyst support with Pt on the bottom), an increasing Ir loading improves the durability both with respect to ORR and OER activity[1]. In our present study, this cannot be confirmed as a general rule.

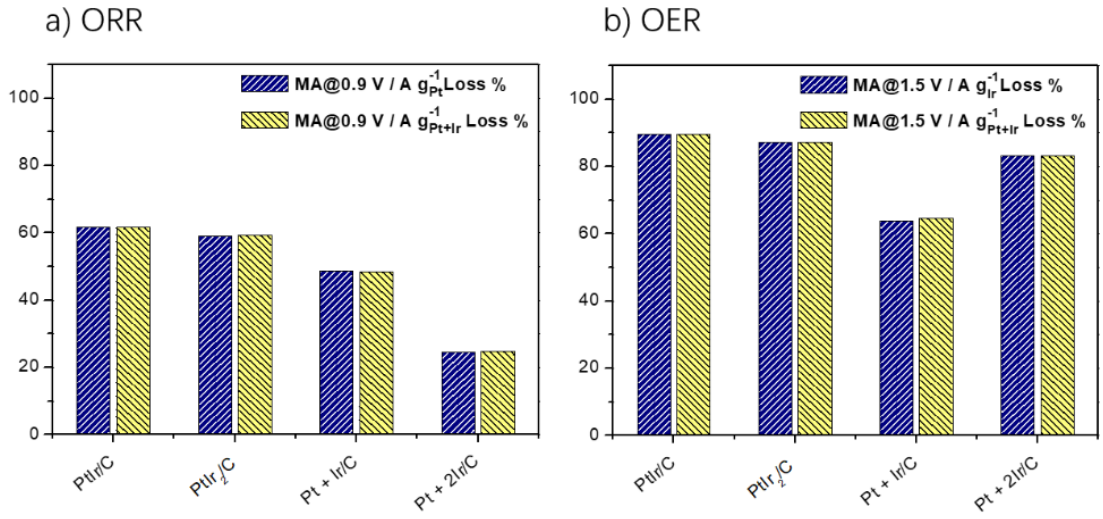

Figure S4. MA loss in percentage of ORR a) and OER b) calculated based on the average electrochemical activity values before and after ADTs of the bifunctional catalysts.

Table S4. EDX data for weight compositions of Ir and Pt together with the calculated Ir / Pt ratio and the change of Ir / Pt ratio during ADTs of the bifunctional catalysts. The calculation based on the average EDX data of Ir and Pt weight compositions. The error is the standard deviation of five independent measurements. BOT: before test, EOT: end of test.

		Ir wt. %	Pt wt. %	wt. Ir/Pt	wt. Ir/Pt change %
PtIr/C	BOT	45 ± 4.8	55 ± 4.8	0.82	73
	EOT	18.2 ± 2.3	81.8 ± 2.3	0.22	
$PtIr_2$/C	BOT	54.8 ± 6.7	45.2 ± 6.7	1.21	82
	EOT	18.2 ± 15	81.8 ± 15	0.22	
Pt + Ir/C	BOT	46.2 ± 2	53.8 ± 2	0.86	65
	EOT	23 ± 5.4	77 ± 5.4	0.3	
Pt + 2Ir/C	BOT	66.8 ± 0.7	33.2 ± 0.7	2.01	77
	EOT	31.6 ± 17	68.4 ± 17	0.46	

Table S5. ICP-MS measurement data of the concentration of Pt NPs, Ir NPs, Pt_xIr_y alloy NPs. For each sample, the concentration of NPs in acetone as well as in the supernatant from precipitation procedure was measured, respectively. The measurement was repeated for two times of each sample, font with the same color is from the same measurement.

Sample \ Concentration		Nominal concentration		Measured concentration	
		Pt (ppb)	Ir (ppb)	Pt (ppb)	Ir (ppb)
Pt Ir 5 ppb		5	5	5.140	5.140
Pt Ir 10 ppb		10	10	10.164	10.192
Pt Ir 30 ppb		30	30	30.038	30.056
Pt Ir 50 ppb		50	50	50.057	50.234
Pt	Acetone 1	20	0	17.607	0.145
	Acetone 2	20	0	18.506	0.091
	Supernatant 1	0	0	0.623	0.047
	Supernatant 2	0	0	0.383	0.039
Ir	Acetone 1	0	15	0.628	14.362
	Acetone 2	0	15	0.621	13.309
	Supernatant 1	0	0	1.039	0.253
	Supernatant 2	0	0	0.717	0.276
PtIr	Acetone 1	25	25	21.316	17.809
	Acetone 2	25	25	21.536	17.820
	Supernatant 1	0	0	0.594	0.466
	Supernatant 2	0	0	0.601	0.468
$PtIr_2$	Acetone 1	15	30	14.413	22.766
	Acetone 2	15	30	14.151	22.588
	Supernatant 1	0	0	0.165	0.316
	Supernatant 2	0	0	0.174	0.336

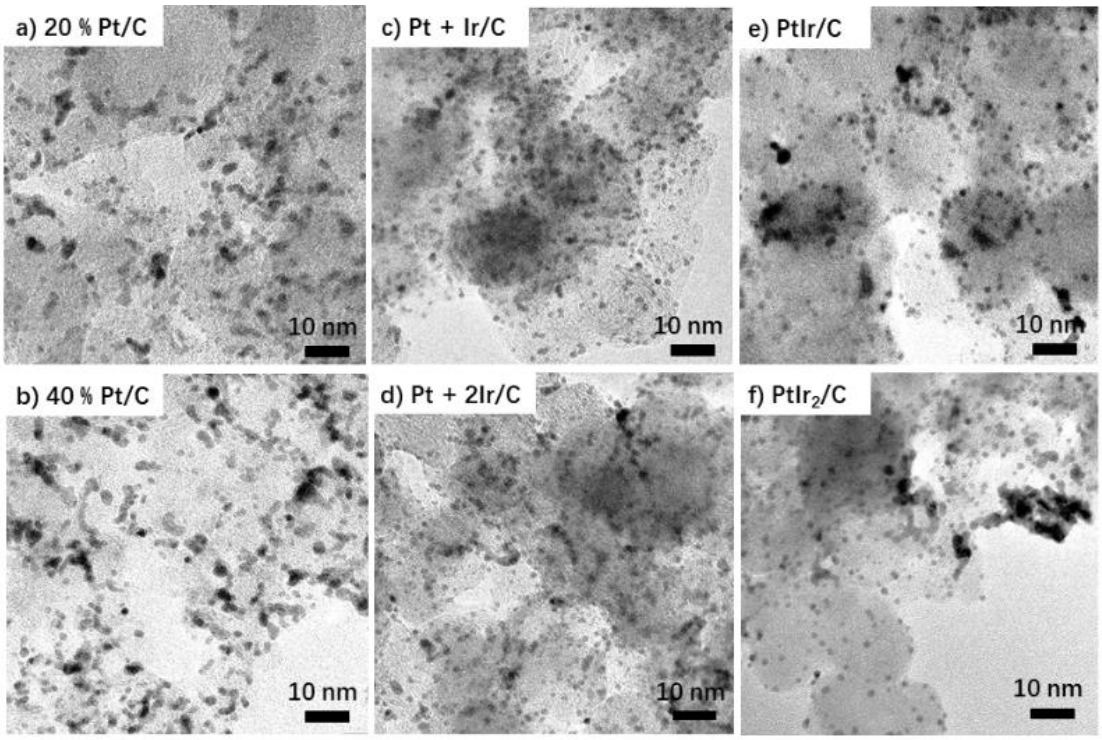

Figure S5. TEM micrographs of the degraded catalyst samples. (a, b) Supported monometallic Pt NPs, (c, d) Supported Pt – IrO_2 nanocomposites and (e, f) Supported Pt_xIr_y alloy NPs.

Samples		I_D/I_G	$\sigma(I_D/I_G)$
20% Pt/C	as prepared	0.98	0.01
	current control	0.96	0.01
Pt + 2Ir/C	as prepared	0.97	0.02
	current control	1.00	0.04
40% Pt/C	as prepared	0.95	0.01
	current control	0.95	0.02
Pt + Ir/C	as prepared	0.96	0.01
	current control	0.94	0.01
$PtIr_2$/C	as prepared	0.96	0.01
	current control	0.94	0.04
PtIr/C	as prepared	0.95	0.01
	current control	0.96	0.02
Carbon (Vulcan XC72R)		1.06	0.06

Figure S6. Intensity ratios between D and G peak in the Raman spectra of the different catalyst samples. The Raman spectra were recorded with an excitation wavelength of 488 nm according to the procedure in ref.[2]

References

(1) Ioroi, T.; Yasuda, K. Platinum-Iridium Alloys as Oxygen Reduction Electrocatalysts for Polymer Electrolyte Fuel Cells. *J. Electrochem. Soc.* **2005**,

152 (10), A1917. https://doi.org/10.1149/1.2006547.

(2) Zana, A.; Speder, J.; Reeler, N. E. A.; Vosch, T.; Arenz, M. Investigating the Corrosion of High Surface Area Carbons during Start/Stop Fuel Cell Conditions: A Raman Study. *Electrochim. Acta* **2013**, *114*. https://doi.org/10.1016/j.electacta.2013.10.097.

Manuscript II

RESEARCH ARTICLE
doi.org/10.1002/elsa.202100190

Chemistry Europe
European Chemical Societies Publishing

Received: 24 October 2021
Revised: 9 March 2022
Accepted: 2 April 2022

The gas diffusion electrode setup as a testing platform for evaluating fuel cell catalysts: A comparative RDE-GDE study

Sven Nösberger[1] | **Jia Du**[1] | **Jonathan Quinson**[2] | **Etienne Berner**[1] | **Alessandro Zana**[1] | **Gustav K.H. Wiberg**[1] | **Matthias Arenz**[1]

[1]Department of Chemistry, Biochemistry, and Pharmaceutical Sciences, University of Bern, Bern, Switzerland

[2]Department of Chemistry, University of Copenhagen, Copenhagen Ø, Denmark

Correspondence
Matthias Arenz, Department of Chemistry, Biochemistry and Pharmaceutical Sciences, University of Bern, Freiestrasse 3, 3012 Bern, Switzerland.
Email: matthias.arenz@unibe.ch

Sven Nösberger and Jia Du are equally contributing first authors.

Funding information
the Swiss National Science Foundation (SNSF), Grant/Award Number: 200021_184742; the Marie Skłodowska-Curie, Grant/Award Number: 840523

Abstract

Gas diffusion electrode (GDE) setups have been recently introduced as a new experimental approach to test the performance of fuel cell catalysts under high mass transport conditions, while maintaining the simplicity of rotating disk electrode (RDE) setups. In contrast to experimental RDE protocols, for investigations using GDE setups only few systematic studies have been performed. In literature, different GDE arrangements were demonstrated, for example, with and without an incorporated proton exchange membrane. Herein, we chose a membrane-GDE approach for a comparative RDE–GDE study, where we investigate several commercial standard Pt/C fuel cell catalysts with respect to the oxygen reduction reaction (ORR). Our results demonstrate both the challenges and the strengths of the new fuel cell catalyst testing platform. We highlight the analysis and the optimization of catalyst film parameters. That is, instead of focusing on the intrinsic catalyst ORR activities that are typically derived in RDE investigations, we focus on parameters, such as the catalyst ink recipe, which can be optimized for an individual catalyst in a much simpler manner as compared to the elaborative membrane electrode assembly (MEA) testing. In particular, it is demonstrated that ~50% improvement in ORR performance can be reached for a particular Pt/C catalyst by changing the Nafion content in the catalyst layer. The study therefore stresses the feasibility of the GDE approach used as an intermediate "testing step" between RDE and MEA tests when developing new fuel cell catalysts.

KEYWORDS
gas diffusion electrode (GDE) setups, fuel cell catalysts, oxygen reduction reaction (ORR), rotating disk electrode (RDE) setups

RESEARCH ARTICLE
doi.org/10.1002/elsa.202100190
Chemistry Europe
European Chemical Societies Publishing

1 | INTRODUCTION

Despite the substantial advancements of fuel cells in the last decade, their cost and the lack of a hydrogen infrastructure are still inhibiting factors for mass commercialization. Concerning fuel cell catalysts, the amount of Pt (precious metal) used and its resistance against degradation are major factors that still need further improvement.[1–5] To reduce the costs, the catalyst layers need to be improved in a way that they provide maximal power by minimal Pt (precious metal) content. Additional challenges are the scarcity of the active catalyst materials and the limited conversion efficiency (as compared to battery storage).[6] Developing new and improved oxygen reduction reaction (ORR) catalysts with lower precious metal content that achieve higher power densities is therefore crucial. One major challenge thereby is the implementation of new catalysts established in fundamental research to applications in fuel cells. Despite the fact that many promising catalysts meet performance targets identified in rotating disk electrode (RDE) measurements, there are few examples of successful implementation to membrane electrode assembly (MEA) testing.[7]

In fundamental research, most fuel cell catalysts are investigated with a RDE setup.[8] However, due to the limited mass transport, inherent to RDE setups, the potential ranges at which the kinetics of an ORR catalyst can be investigated is narrow. In addition, different catalyst loadings and testing parameters are used for RDE measurements compared to MEAs, that is, the typical catalyst loading for RDE is 5–20 $\mu g_{Pt}/cm^2$, while for MEAs it is 100–500 $\mu g_{Pt}/cm^2$, which leads to different thicknesses in catalyst layers.[8–10] In RDE measurements, the catalyst layer may contain Nafion (or similar proton conducting polymer) binder. However, due to the liquid electrolyte, this is not required for proton transport. By comparison, Nafion is an essential component for catalyst layers in MEAs. Furthermore, RDE testing protocols are performed potentiodynamically, while MEAs testing is carried out under potentiostatic or galvanostatic conditions.[9] All these differences limit the transferability of results gained with an RDE setup toward an application in fuel cells. There is a lack of evidence that all high-performing fuel cell catalysts measured with the RDE setup can unfold their full potential in MEAs.[7,11,12]

To facilitate the full exploitation of results and knowledge obtained in fundamental research, new measurement setups with increased mass transport properties have been introduced.[7,13–19] These setups allow to apply more realistic conditions in the catalyst testing and at the same time should be widely applicable in standard research laboratories. The GDE approach fulfils these criteria.[18,20–23] Most importantly, mass transport limitations which are inherent to RDE measurements, can be avoided in the GDE approach by distributing the reactant, for example, oxygen gas, directly through a gas diffusion layer (GDL). In the article, the used membrane-based GDE setup, no direct contact between catalyst layer and liquid electrolyte exists. A polymer electrolyte membrane separates the catalyst layer, which in the current study contains a fixed Pt loading of 208 $\mu g_{Pt}/cm^2$, and the electrolyte. A major challenge for the GDE approach is to develop and standardize procedures for catalyst testing.[23] Therefore, it is of interest to systematically compare the inherent performance of Pt/C catalysts as determined by RDE measurements with their performance as catalyst film in membrane-GDE measurements. In the presented study, we thus, compare the ORR performance of six different commercial Pt/C catalysts in a GDE setup and use RDE measurements as benchmark for their *intrinsic* ORR activity. The aim is to investigate which factors are essential to transfer the *intrinsic* ORR activity of Pt/C catalysts to catalyst layers that eventually will be used in MEAs. The experimental protocol (e.g., catalyst ink composition, coating methods, and measurement procedures) in the RDE measurements utilizes previous insights on establishing *intrinsic* activities, whereas the GDE protocol is oriented toward MEA testing. However, both experimental protocols fulfil the respective testing criteria to reach the fundamental and applied research standard, as closely as possible.[8,24–26] With this study, it is demonstrated that a GDE approach allows a straight-forward optimization of a given catalyst film under conditions relevant for applications. On the other hand, GDE testing using standardized ink recipes might not uncover the full potential of a respective catalyst.

2 | MATERIALS AND METHODS

2.1 | Small angle X-ray scattering (SAXS)

Small angle X-ray scattering (SAXS) measurements were conducted using a SAXSLab instrument as previously described[22] and are detailed in Supporting information. The SAXS data were fitted assuming a power law and polydisperse spheres. The background corrected scattering data were fitted using a power law to take into account the behavior at low q value and a model of polydisperse spheres, described by a volume-weighted log-normal distribution. Some data were best fitted by adding a second model of polydisperse spheres also described by a volume-weighted log-normal distribution. The scattering data and related fits are reported in Supporting information Figure S1 and the values obtained for the fitting parameters are reported in Supporting information Table S1.

RESEARCH ARTICLE
doi.org/10.1002/elsa.202100190
Chemistry Europe
European Chemical Societies Publishing

2.2 | Transmission electron microscopy (TEM) and scanning electron microscopy with energy dispersive X-ray spectroscopy (SEM-EDS)

A Jeol 2100 transmission electron microscope (TEM) operated at 200 kV was used for the TEM analysis. The samples were prepared by suspending the commercial catalyst powders in ethanol and then dropping the sample suspension onto carbon-coated copper TEM grids (copper or nickel grids, Quantifoil). Micrographs were recorded at three different magnifications at least, and in at least three randomly selected areas. At least 200 nanoparticle diameters were evaluated using the software ImageJ to evaluate the size distribution.

The SEM-EDS cross-section measurements were performed as described earlier[21] using a Zeiss GeminiSEM 450 with SmartSEM 6.05 software and EDS Photodetector Ultim max 65 from Oxford Instruments using AZTec 4.2 software. As scan parameters for the EDS maps, a WD (working distance) between 8.4 and 8.8 mm, accelerating voltage of 15 kV and a probe current of 200 pA were used.

2.3 | Electrochemical characterization

2.3.1 | Catalyst ink and film formation for the RDE measurements

The inks for the RDE measurements were prepared from the respective dried catalyst powder and dispersed in a mixture of Milli-Q water and isopropanol (V_{water}: V_{IPA} = 3:1). To the ink, 1.6 µL/mL 1 M KOH (aq) was added and then homogenized in a sonicator bath for 10 min. The resulting homogeneous catalyst ink had a total Pt concentration of 0.218 g_{Pt}/L.

Thin catalysts films were prepared by pipetting 9 µL (0.218 g_{Pt}/L) of each catalyst ink onto a newly polished glassy carbon (GC) disc. The disk was then dried under Ar gas stream humidified with IPA and H_2O, the disc was kept stationary in the drying step. The resulting films had a Pt loading of 10 $\mu g/cm^2$ and were dried at ambient atmosphere for further electrochemical measurements.

2.3.2 | Catalyst ink and film preparation for the GDE measurements

Catalysts inks were prepared from different dried catalyst powders and dispersed in a mixture of Milli-Q water and isopropanol (mixture volume ratio of 3:1). To disperse the powder, the mixture was sonicated for 5 min at room temperature. Subsequently, Nafion solution was added so that the ink contained a mass C:Nafion ratio of 1. The ink was sonicated again for 5 min. The final inks had a Pt concentration of 0.5 mg/mL for all catalysts.

The catalyst films were produced by a vacuum filtration of the catalyst ink onto GDL. To conduct the vacuum filtration, the ink was first diluted by Milli-Q water to a Pt concentration of 0.05 mg/mL (mixture volume ratio 1:3). The ink was then added to a vacuum apparatus and filtrated through an MPL-coated GDL (Freudenberg H23C8). The resulting catalyst films (Ø = 4 cm) were stored in petri dishes. From this film-coated GDL, a disk (Ø = 3 mm) was extruded and used as GDE. All investigated GDEs prepared from the commercially available Pt/C catalysts had a Pt loading of 208 ug_{Pt}/cm^2 on the GDL.

2.3.3 | Rotating disk electrode (RDE) measurements

All RDE electrochemical measurements were performed at room temperature with a computer controlled potentiostat (ECi 200, Nordic Electrochemistry ApS) and a glass cell equipped with three electrodes as previously reported.[26–28] The working electrode (WE) was a GC disk (5 mm in diameter) embedded into a Teflon tip.

A Pt wire served as counter electrode (CE) and a reversible hydrogen electrode (RHE) served as a reference electrode. An aqueous 0.1 M perchloric acid electrolyte was used, which was saturated with argon prior to the start of the electrochemical measurements. The solution resistance was measured with a superposed AC signal (5 mV, 5 kHz) and was compensated down to 2 Ω.

The analytical procedure to electrochemically analyze the Pt/C catalyst layers was repeated for all six investigated Pt/C catalysts and included the following steps: Surface cleaning, Ar background, ORR activity, and CO stripping to determine Pt active surface area. The Pt catalyst surface was cleaned under an argon atmosphere by cycling the potential between 0.05 V_{RHE} and 1.20 V_{RHE} for three cycles to remove the possible organic residue on the catalyst film. Thereafter, the upper potential was reduced to 1.10 V_{RHE} and the cycling was continued until reaching a stable cyclic voltammogram (CV) (~50 cycles in total). The scan rate was 0.50 V/s. The initial higher potential limit served to reduce the total number of potential sweeps. Afterwards, an Ar background was measured in a potential range between 0.05 V_{RHE} and 1.10 V_{RHE} with a scan rate of 0.05 V/s in Ar saturated electrolyte. Prior to the ORR performance measurements, the electrolyte was purged with O_2 for 10 min. During the ORR activity measurement, the potential window and the scan rate were the same as that

RESEARCH ARTICLE
doi.org/10.1002/elsa.202100190
Chemistry Europe
European Chemical Societies Publishing

applied for Ar background measurements, while the RDE had a rotation speed of 1600 rpm.

To determine the electrochemical active surface area (ECSA) of the investigated catalysts, the oxidation charge obtained from a CO monolayer stripping experiments was analyzed. In brief, the electrode was held at 0.05 V_{RHE} in CO saturated electrolyte for 2 min. Subsequently, the electrolyte was saturated with Ar (~10 min) to purge the electrolyte from CO. The potential was swept from 0.05 to 1.10 V_{RHE} with a scan rate of 50 mV/s to oxidize the adsorbed CO monolayer to CO_2. The ECSA was then calculated from the ration of resulting oxidative charge (Q_{CO}), after background subtraction, and the oxidation charge of a monolayer, 400 μC/ cm_{Pt}^2, and finally normalized to the mass of the Pt (m_{Pt}).[29]

$$ECSA = \frac{Q_{CO}}{400\mu C\, cm_{Pt}^{-2}} \frac{1}{mPt}.$$

The ORR data were analysed from the background corrected polarization curves. The background polarization curves were recorded in Ar-purged electrolyte. The ORR activity was then evaluated at 0.90 V_{RHE} from positive going scans. The mass activity (MA) was obtained by normalizing the activity by the Pt mass. The specific activity (SA) was obtained by normalizing the measured current density (mA/cm_{Geo}^2) to the ECSA.

2.3.4 | Measurements in the gas diffusion electrode setup

The GDE-setup was assembled as follows:[13] A 3 mm disc was punched out of the catalyst film covered by GDL. The catalyst containing disc was placed into an MPL-coated GDL disc (Ø = 2 cm, Freudenberg H23C8) which had a 3 mm hole in the middle. A Nafion membrane was placed on top (Nafion 117, thickness 183um). With a tablet press (pressure range: 0–15T), the whole stack was pressed together at a pressure of two tonnes and a duration of 10 min. Afterwards, a GDL (Freudenberg H23) was placed into the gas flow field of the lower cell body, followed by the stack containing the GDE and the Nafion membrane. Finally, the upper cell body was placed on top of the Nafion membrane. The two body parts were held in place by a clamp. The compartments of the upper cell body were filled with 15 mL of 4 M perchloric acid. Finally, an RHE RE and the CE (Pt wire) were put into the electrolyte.

All electrochemical measurements were performed at 30°C with a computer controlled potentiostat (ECi 240, Nordic Electrochemistry ApS) and a GDE-setup as reported.[13] The analytical procedure to electrochemically analyse the Pt/C catalyst layers was the same for all six investigated Pt/C catalysts and included the following steps: First, the GDE was purged from the backside (through the GDL) with argon gas. Doing so, the catalyst was cleaned by potential cycles between 0.05 and 1.10 V_{RHE} at a scan rate of 0.2 V/s until a stable CV could be observed (~50 cycles). Afterwards, a CO stripping measurement was performed followed by electrochemical impedance spectroscopy (EIS) and ORR-activity measurements. To conclude the investigations, a second CO stripping measurement was performed. Throughout the entire experiment, a bubbler was used to humidify the gas and the membrane. During the whole measurement, the solution resistance was measured by superimposing an AC signal of 5 kHz and an amplitude of 5 mV.

CO stripping measurements were conducted to determine the ECSA. In essence, the catalyst layer got covered by CO gas which adsorbed onto the Pt surface. Afterwards, the catalyst was purged with Ar to remove the excess of CO. As a next step, a CV was recorded (scan rate: 50 mV/s), which records the oxidative current originating from the oxidation of CO to CO_2. Finally, multiple CVs under Ar atmosphere were conducted until the Ar background was regained. The value of the ECSA was then obtained, as described in "Section 2.3.3".

Prior to the ORR activity measurements, oxygen was flowed through the pipes for 10 min. For the last 5 min, a potential of 0.80 V_{RHE} was applied. This ensured that all gas lines were fully filled with oxygen and that the catalyst layer was equally wet over the entire surface. The ORR-activity measurements were conducted in potential control mode with a potential range between 1.00 V_{RHE} and 0.10 V_{RHE}. The potential was preset to 1.00 V_{RHE} and then lowered in steps of 25 mV until 0.10V_{RHE} are reached. At every step, the potential was held constant for 1 min to reach steady-state conditions. For analysis, the measured current was averaged over the last 10 s. The online solution resistance was determined from the superimposed AC signal (5 kHz, 5 mV). All ORR activity measurements were postcorrected for the potential errors introduced by the solution resistance using this online measurement, see Supporting information Figure S2 for example. The EIS measurements served to back up the online correction in case of failure or uncertainties.

3 | RESULTS AND DISCUSSION

We start with the physical characterization of the investigated Pt/C fuel cell catalysts. All examined catalysts are commercially available and can serve as benchmarks in studies investigating new, home-made fuel cell catalysts. Their Pt to C ratio (Pt loading), as indicated by the supplier, ranges from roughly 20 wt.% up to 70 wt.%. In Figure 1,

RESEARCH ARTICLE
doi.org/10.1002/elsa.202100190
Chemistry Europe
European Chemical Societies Publishing

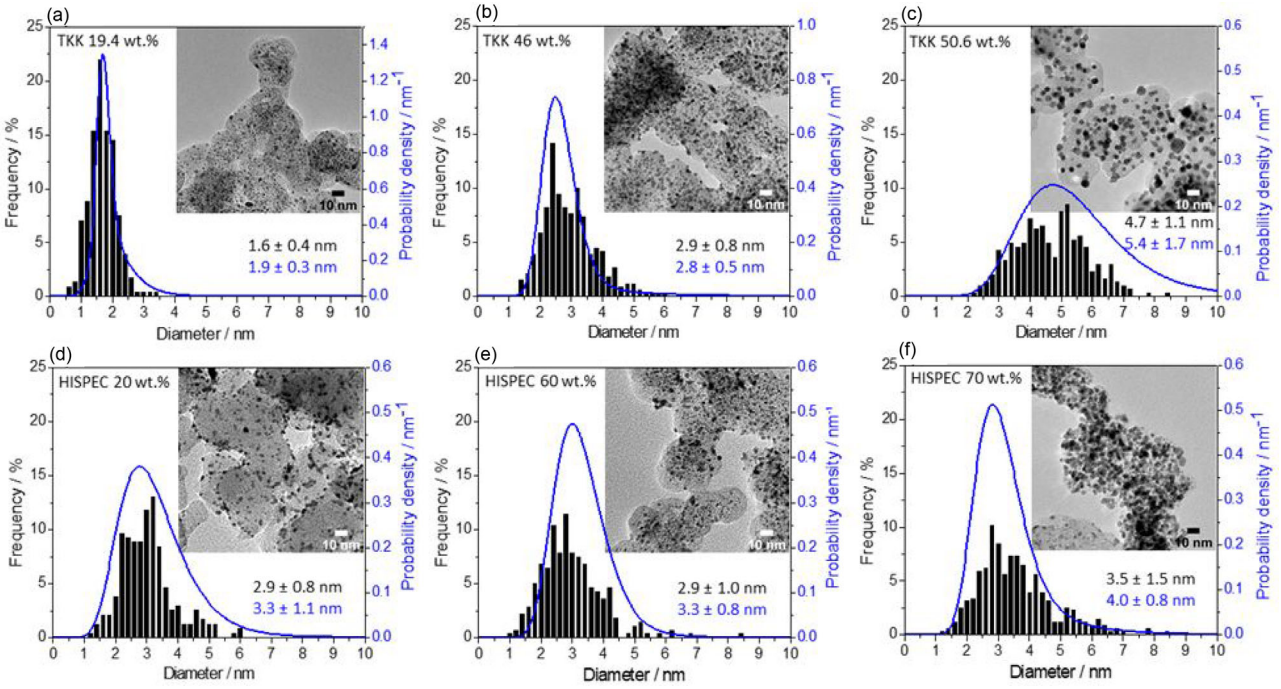

FIGURE 1 Pt particle size distribution of the investigated commercial Pt/C determined from TEM micrographs (at least 200 particles were counted) and probability density function derived from the SAXS analysis. The insets display representative TEM micrographs of each commercial Pt/C catalyst. The average particle size with the font in black is determined from TEM measurements while the blue font indicates the average particle size determined from the SAXS measurements. The Pt-to-C ratio (Pt loading) of each Pt/C catalyst is indicated in the upper left corner

we present representative TEM micrographs to demonstrate the physical characteristics of each Pt/C catalyst. In addition, size histograms and average particle sizes derived from a TEM analysis as well as probability density functions derived from fitting the SAXS data are shown. As Figure 1 shows, within the accuracy (error) of the measurements, both methods lead to the same average particle size. However, with a closer look at the size retrieved, the average Pt particle size determined from TEM is slightly smaller (except for TKK 46 wt.% Pt/C) in comparison to the values derived from the SAXS analysis. This difference can be explained by the fact that the particle size distributions are based on different analyses that are sensitive to different sizes in different ways: For the TEM analysis, one determines the relative number of particles with the same size based on defined bin sizes, and only relatively few individual NPs are accounted for. In contrast, SAXS analysis is performed in a larger volume of sample and substantially more NPs are considered for the size evaluation. Additionally, the size retrieved from TEM is often number- or surface-weighted, whereas it is volume-weighted for SAXS, that is, SAXS is more sensitive to the contribution of larger NP sizes. This explains why SAXS analysis leads to an estimated diameter slightly larger than for TEM analysis in this study. Nevertheless, due to the good agreement of the results obtained by both analysis techniques in the present study, we do not distinguish in the following between the two methods when referring to the average particle size and size distribution.

The analysis shows that the average particle sizes range from roughly 2 to 5 nm (Figure 1). In addition, the carbon support of each investigated catalyst is relatively homogeneously decorated by Pt particles; in particular, the TKK 19.4 wt.% Pt/C sample. The limited particle agglomeration on the carbon support of this catalysts is also reflected by the very narrow size distribution with a standard deviation of only 0.4 nm in the TEM analysis. As expected, it can be clearly seen that at increased Pt loadings, the carbon support is more densely covered with Pt particles and agglomeration increases. Characteristically in the TEM micrographs of the HISPEC 60 wt.% and 70 wt.% Pt/C samples, some darker spots are seen that most likely are related to the slightly agglomerated Pt particles and the size distribution exhibits a clearly discernable tail towards larger sizes (also the size distribution of the TKK 50.6 wt.% Pt/C sample displays such a feature).

In Figure 2, SEM-EDS cross-sections of pristine GDEs prepared from three representative Pt/C catalysts are shown. The general structure of the GDEs consisting of a porous GDL covered by a carbon MPL and the respective Pt/C catalyst layer is clearly discernable. While the MPL's thickness is measured constantly to be around 20 µm, the

RESEARCH ARTICLE
doi.org/10.1002/elsa.202100190
Chemistry Europe
European Chemical Societies Publishing

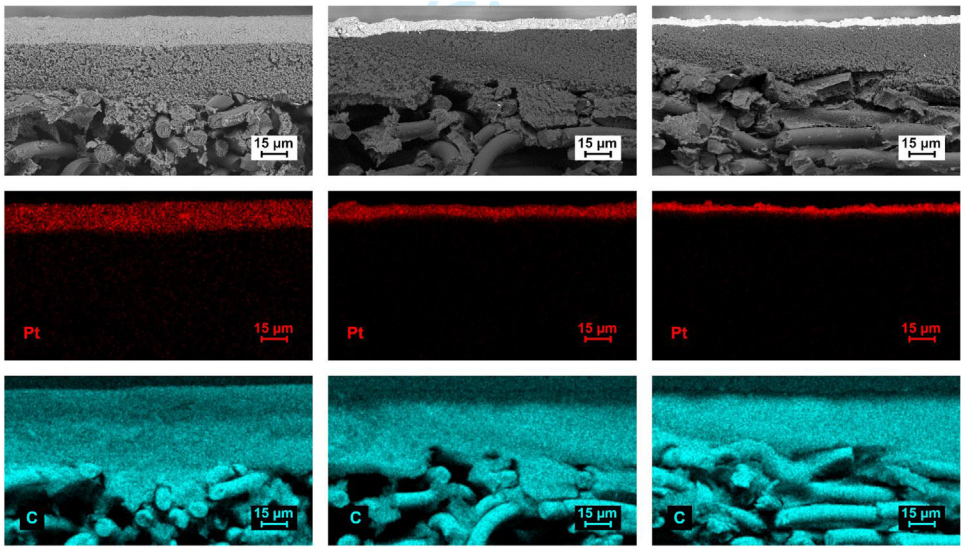

FIGURE 2 Comparison of SEM-EDS cross-sections of three GDEs prepared with different Pt/C catalysts. (Left) HISPEC 20 wt.%, (middle) TKK 46 wt.%, and (right) HISPEC 70 wt.%. The SEM micrographs were recorded with the BSE detector. Due to the different metal loading on the carbon support in the Pt/C catalysts, the fixed Pt loading on the GDL (208 ug_{Pt}/cm^2) leads to different thicknesses of the catalyst film

thickness of the Pt/C catalyst layer varies with the Pt loading on the carbon support (Pt to carbon ratio) of the respective catalyst. At low Pt loading (20 wt.%), the catalyst film is about 16 ± 1 µm, whereas it is less than 5 µm on average at very high Pt loading (70 wt.%). In other words, higher Pt loadings (Pt to carbon ratio) of the Pt/C catalyst lead to substantially denser (thinner) catalyst layers. Furthermore, the SEM micrographs imply that under current conditions, the vacuum filtration method of the Pt/C catalysts with high Pt wt.% leads to less homogeneous catalyst films on the GDL.

In previous work of our and other groups, the TKK 46 wt.% Pt/C sample was used as a benchmark or reference catalyst.[14,16,17,30] Therefore, in the following, we discuss the GDE measurements with this catalyst. In the upper part of Figure 3, representative CVs of the TKK 46 wt.% Pt/C samples recorded in the two setups are compared. In both cases, the typical "electrochemical features" of a Pt/C catalyst are depicted. In the low potential region of the CVs (0.05–0.35 V_{RHE}), both hydrogen adsorption (negative scanning direction) and desorption (positive scanning direction) are visible, typically referred to as H_{upd} peaks. However, the H_{upd} peaks in the CV of the GDE measurements differ from the ones in the RDE, which are typical for measurements in aqueous perchloric acid electrolyte. In particular, the CV recorded in the GDE setup, the "second" peak at around 0.25 V_{RHE} is less pronounced, and the hydrogen evolution reaction (HER) starts earlier, around 0.07 V_{RHE}. In contrast to these differences, the adjacent potential region between 0.35 V_{RHE} and 0.60 V_{RHE}, the double layer region defined by capacitive currents from

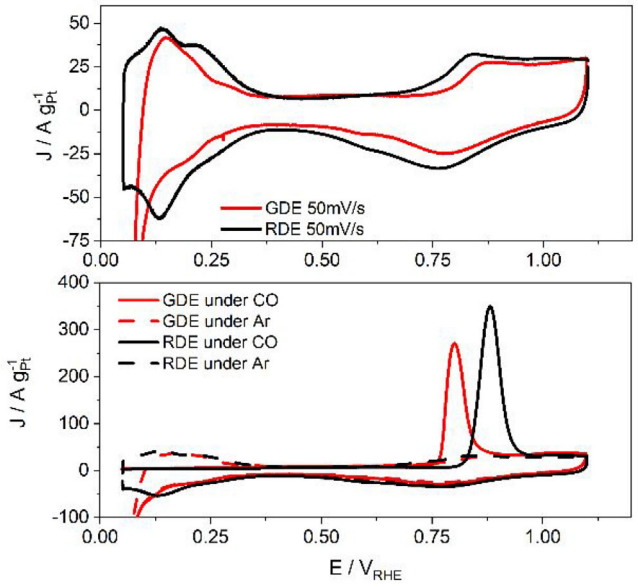

FIGURE 3 In the upper graph, representative examples of CVs of the same TKK 46 wt.% Pt/C catalyst recorded in an inert (Ar purging) atmosphere are shown, whereas in the lower graph, representative CO stripping measurements of the same catalyst are shown. The CVs are normalized to the Pt loading on the electrode to take account of the different films thicknesses. The measurements recorded in the RDE setup are represented by a black line, while the measurements recorded in the GDE setup are represented by a red line. The scan rate was 50 mV/s for both GDE and RDE

charging and discharging the interphase, displays identical double layer capacities in both setups. Finally, in the potential region of Pt oxidation and reduction (0.60–1.10 V_{RHE}),

RESEARCH ARTICLE
doi.org/10.1002/elsa.202100190
Chemistry Europe
European Chemical Societies Publishing

the Pt oxidation and reduction peaks in the CV recorded with the GDE setup are shifted toward higher potentials. These observed differences are most likely a consequence of the different local ion environments, that is, an aqueous electrolyte and a membrane electrolyte environment. In the GDE setup, the catalyst is surrounded by a solid Nafion electrolyte, whereas it is surrounded by a liquid aqueous electrolyte in the RDE setup. The earlier onset of the HER in the GDE setup might be related to the reduced local partial pressure of hydrogen. Furthermore, the reference electrode in the GDE setup is in aqueous electrolyte, while the measured catalyst is not. This might lead to slight shifts in referenced and "experienced" potentials, which is known to substantially influence the determination of the intrinsic ORR activity.[29]

The different reaction environments manifest itself also in the CO stripping measurements that are typically used to determine the electrochemically active Pt surface area,[31] see lower graph in Figure 3. The CO oxidation peaks recorded in both setups are clearly shifted against each other. Interestingly, in the GDE setup, the CO stripping peak appears at lower potentials than in the RDE setup (ca. 0.8 vs. 0.9 V_{RHE}). Thus, the shift is more pronounced and in opposite direction as compared to the potential difference in hydrogen evolution or oxide formation observed in the CVs recorded in Ar atmosphere. It should be pointed out that this shift is not related to an incomplete CO monolayer formation, as can be seen from the absence of H_{upd} features in the forward going CO stripping scan. Therefore, it can be argued that the shift in the CO stripping peak is related to a reduced anion blocking in the GDE membrane-catalyst environment.[32] Interestingly, the peak position observed in the CO stripping curve recorded in the GDE setup is similar to the one observed in an MEA measurement by Harzer et al.,[33] although it needs to be stressed out that a direct comparison is difficult due to the different catalyst and different experimental parameters such as scan rate and temperature. In addition, the CO stripping shows a smaller ECSA for the catalyst layer in the GDE setup compared with the RDE setup, which is consistent with the observation in the H_{upd} region, that is, the overall peak area in the H_{upd} region in GDE measurement is smaller than the one from RDE measurement.

To investigate this effect systematically, in Figure 4, the ECSA values obtained from the CO stripping measurements are compared for the different Pt/C catalysts measured in both setups. The ECSA is plotted versus their "theoretical" ECSA, which is calculated from the TEM size histograms assuming that the Pt NPs are perfect, free-standing spheres, that is, no Pt surface area is blocked by the carbon support. The ECSA values of some Pt/C samples can also be compared to previous measurements.[34] The diagonal line in Figure 4 indicates where measured and "theoretical" ECSA values are equal. It is seen that there is in general a good agreement between the measured ECSAs and the expected ECSA based on the particle size distribution. However, as a general trend the ECSA values determined in the GDE setup are lower than the ones obtained in the RDE measurements. This general trend is visualized in Figure 4 by fitting linear trendlines to the data points. The maximum difference in ECSA from RDE and GDE is approximately 20%. This systematic difference could be the result of different factors. First, it may be that during the vacuum filtration some Pt got lost, resulting in a smaller CO-oxidation current when normalized to the assumed catalyst loading. Second, Nafion which needs to be added to the catalyst ink preparation for the GDE, might block some active sites. Nafion is known to partially block the active surface area of the active catalyst phase and, thus, reduces the ECSA.[35] For the RDE measurements, no Nafion was used as its only function is to glue the catalyst film to the GC.[36]

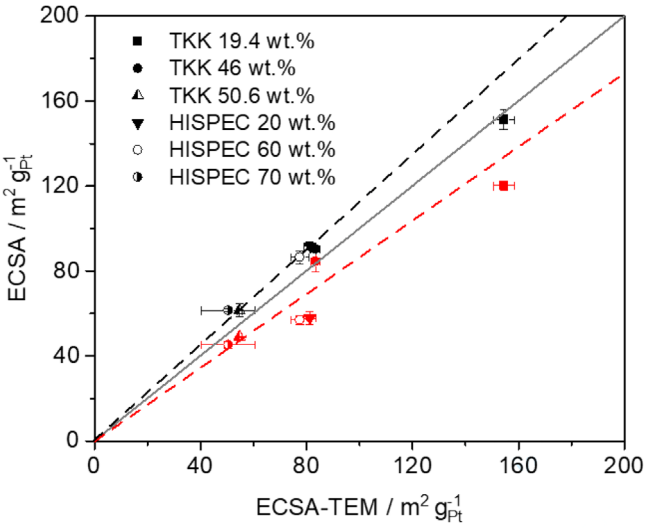

FIGURE 4 Comparison of ECSA values obtained from RDE (black dots) and GDE (red dots) measurements with the ECSA calculated from the Pt particle distribution shown in the TEM micrographs, indicated as ECSA-TEM. The ECSA-TEM values were calculated based on 200–400 randomly distributed Pt particles in the TEM micrographs of each catalyst. The given error with respect to the ECSA-TEM is the standard error of the counted Pt particles in TEM micrographs, while the given error from measured ECSA values is the standard deviation of at least three independent measurements of each catalyst

In Figure 5, the electrochemical response of the Pt/C benchmark catalyst in O_2 saturated atmosphere is presented from measurements by both setups, that is, the RDE and the GDE setup. The goal of an RDE characterization is to determine the intrinsic kinetic ORR activity of a catalyst. Such task is challenging as in the past even the results of

RESEARCH ARTICLE
doi.org/10.1002/elsa.202100190
Chemistry Europe
European Chemical Societies Publishing

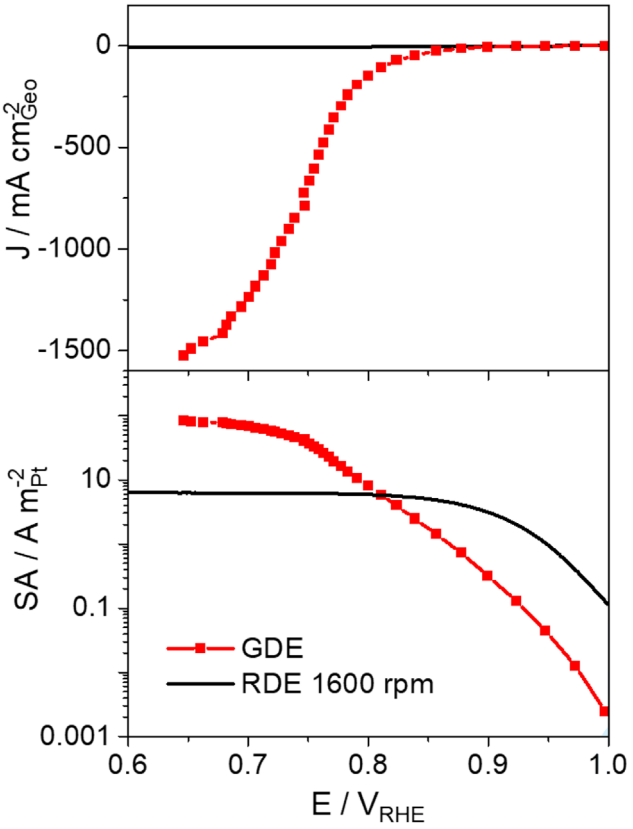

FIGURE 5 Comparison of the ORR performance of TKK 46 wt.% Pt/C measured in a GDE (red) and RDE setup (black). Upper graph, excerpt of the geometric ORR current densities

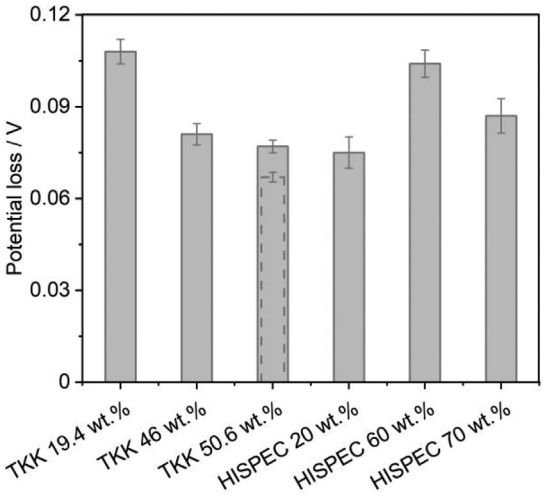

FIGURE 6 Comparison of the corresponding potential loss at a current of 5 A/m$_{Pt}^2$ from RDE and GDE. The potential loss is a result of subtraction between the averaged corresponding potential in RDE and GDE. The bar from TKK 50.6 wt.% Pt/C with the dashed edge is a measurement result with cleaning the catalyst surface in Ar saturated electrolyte in RDE, while the same catalyst with a bar of solid edge is a measurement result companied with an optimized cleaning procedure (O_2 saturated electrolyte). The given error is the standard deviation for the difference in averaged corresponding potential at the current of 5 A/m$_{Pt}^2$ between RDE and GDE

relatively "simple" Pt/C catalysts had been varying by one order of magnitude.[9] As a result, benchmarks, such as polycrystalline Pt, have been introduced and several works on measurement procedures and best practices have been published.[8,25,26,29,31,37] The basic assumption is that procedures and conditions can be defined where all catalysts exhibit their maximum performance. Focusing first on the measurement limitations of the RDE setup, it is seen that the maximum ORR current density which can be reached (at 1600 rpm) is around 6 mA/cm$^2_{Geo.}$ The broad current plateau indicates that in a wide potential region, the ORR is limited by mass transport through the hydrodynamic layer at the electrode interface.[38] By contrast, in the GDE setup, a current density up to 1400 mA/cm$^2_{Geo}$ can be reached in the same potential region because oxygen gas can directly diffuse through the GDL to the catalyst layer. Thus, the maximum current density achieved in the present study is comparable to the ones reported from MEA tests, for example, at 0.7 V, 1500 mA/cm^2 could be reached in H_2-O_2 MEA tests using a Pt-Co/C catalyst.[39,40] A GDE setup is, thus, particularly apt at investigating catalysts with higher current densities and lower potentials, which reflect more realistic conditions that are closer to the operational window of a fuel cell. It should be mentioned though, that the maximum current density reached in the GDE setup varied up to 50% between the different samples, highlighting the influence of the catalyst layer on the obtained results.

To further compare the results, the current densities were normalized to the ECSA derived from the CO stripping measurements, thus, avoiding any influence from uncertainties in catalyst loading. This specific ORR activity is shown as a Tafel plot in Figure 5. The Tafel plot shows that the potential region with kinetic behavior, that is, linear Tafel slope is substantially larger in a GDE setup as compared to a RDE measurement; it stretches from around 1 V_{RHE} down to roughly 0.75 V_{RHE} whereas the kinetically controlled potential region ends at around 0.90 V_{RHE}, in a RDE measurement. However, it is also seen, that the SA obtained in the low-current regime (above 0.80 V_{RHE}) of RDE measurements is substantially higher than the one measured in the GDE setup. This difference in SA was observed for all six investigated Pt/C catalysts and is summarized in Figure 6. Comparing the performance of the different Pt/C catalysts with a standardized procedure at a fixed current density of 5 A/m$_{Pt}^2$, a potential shift in the range of 0.067 V_{RHE} and 0.108 V_{RHE} is observed between the two approaches which constitutes a substantial difference of around one order in magnitude.

To investigate the reason for this significant reduction in SA measured in the GDE setup, we applied a steady-state

RESEARCH ARTICLE
doi.org/10.1002/elsa.202100190
Chemistry Europe
European Chemical Societies Publishing

protocol using an RDE. Supporting information Figure S3 shows that by applying a steady-state protocol in an RDE measurement, the SA at 0.9 V_{RHE} drops down to a similar SA, that is, 0.4 A/m^2_{Pt} as was measured in the GDE setup at the same potential. This indicates that the substantial differences in determined specific ORR activities in the GDE setup are at least partially caused by the steady-state protocol used for GDE measurements. In the GDE measurements, we started the measurements at 1.00 V_{RHE} and went stepwise more negative to 0.10 V_{RHE}, where each step took 1 min. Thus, at each potential, we can assume steady-state conditions. In contrast, in the dynamic potential cycling typically used for RDE measurements, no steady-state condition is reached, leading to an apparent higher activity. The effect is also well-known from RDE measurements, where a profound influence of the scan rate on the ORR activity is reported and a hysteresis in activity between positive and negative sweeps is observed.[9,41] Furthermore, in a RDE measurement, the kinetic current density is obtained after correcting for mass transport limitations.[42] All these arguments point toward that in the intrinsic ORR activities derived from RDE measurements might overestimate the performance in a fuel cell, where steady-state conditions are applied. The GDE setup, by comparison, is not particularly designed to investigate catalysts under dynamic conditions and applying a similar protocol using a GDE setup is not feasible. Any uncompensated resistance (iR drop) leads not only to a shift in potential but also to a current-dependent change in the scan rate. Potentiostatic or galvanostatic measurements by comparison can be corrected for the iR drop in a straightforward manner but face the challenge of a more or less pronounced time dependence in the recorded current or potential. Hence in the current work, we choose to average the currents recorded in a set time interval, see section 2. Instead of investigating the catalysts properties at 0.90 V_{RHE}, the focus is set to lower voltages with higher current densities, which reflects more realistic conditions, that is, in the range between 0.70 V_{RHE} and 0.80 V_{RHE}. This range equals the operational window for a real fuel cell and is, thus, especially important. For the GDE measurements, we adopted a procedure of Yarlagadda et al.[43] to prepare Pt/C films on top of a GDL using the same Pt loading and a standardized ink composition for all Pt/C catalysts. Furthermore, the same automized testing protocol has been applied, see section 2. The activity results then can be compared at either a fixed potential or at fixed current density. Apart from these systematic differences between RDE and GDE measurements which should lead to a constant shift in activity between all catalysts, the different measurement results of the 50.6 wt.% catalyst in Figure 6 indicate that an automized and standardized procedure might not always be suitable to ensure that each catalyst exhibits its optimal, intrinsic performance in a GDE measurement. For example, an improved cleaning procedure in oxygen might improve the performance (in the specific case shown here, in the RDE measurements) while for other catalysts it might lead to slight degradation, for example, in case of small particles. Furthermore, the SEM-EDS cross-sections demonstrate substantially different thicknesses of the Pt/C catalyst films depending on the Pt loading on the carbon support.

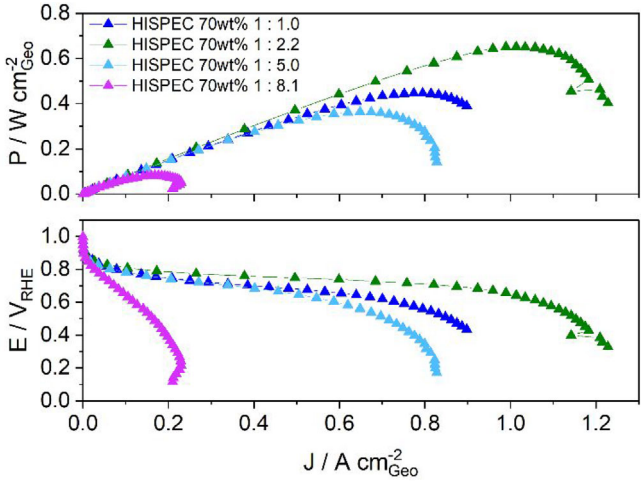

FIGURE 7 Comparison of different carbon to Nafion ratios (C:N) of HISPEC 70 wt.%. The power density of HISPEC 70 wt.% strongly depends on the amount of Nafion added to the ink. The standard procedure suggests a C:N ratio of 1:1. However, measurements made with the GDE setup show higher power density for a C:N ratio of 1:2.2. By adding significantly more Nafion, the power density drops down

Furthermore, in comparative RDE measurements, typically the same ink composition is used for all Pt/C catalysts without optimization for a specific catalyst. However, a fixed carbon to Nafion (C:N) mass ratio, might not be the best recipe for all the different catalysts. The different Pt loadings on the carbon support, the different Pt particle size distributions as well as different carbon supports might require specific ink compositions for every single catalyst to optimize the performance in the GDE setup; knowledge that is commonly known for MEA measurements and is part of the optimization of fuel cell catalyst layers.[44]

To investigate this hypothesis, we analyzed the specific ORR activity (SA) of a moderately performing catalyst, that is, the HISPEC 70 wt.% at different C:N mass ratios. As demonstrated in Figure 7, the conventional ink recipe (C:N = 1:1) does not lead to the best performance of the HISPEC 70 wt.% catalyst. The obtained maximum power density strongly depends on the C:N ratio in the ink (Figure 7). By changing the C:N ratio, the maximum power density can be almost doubled from about 0.4 to about 0.7 W/cm^2. A

RESEARCH ARTICLE
doi.org/10.1002/elsa.202100190
Chemistry Europe
European Chemical Societies Publishing

standardized ink recipe, therefore, leads to an "underperformance" of certain catalysts. For a meaningful comparison of different catalysts in a GDE, it is therefore, important to consider optimizing the ink composition for every single catalyst.

To demonstrate this conclusion even further, and to analyze which characteristics are crucial for a good performance of a specific Pt/C catalyst, we also analyzed the influence of the Pt to Nafion (Pt:N) ratio of this specific catalyst by introducing additional carbon support in the catalyst ink. In the plot in Figure 8, it is demonstrated that at 0.9 V_{RHE}, the ORR performance increases with increasing C:N ratio. With regards to the Pt:N ratio, it seems that the ORR performance increases with increasing ratio as well. However, this behavior changes as soon as higher current densities are reached. At 0.8 V_{RHE}, the highest ORR current density was reached with a Pt:N ratio of 1 instead of a ratio more than 2 at 0.9 V_{RHE}. Furthermore, it is shown that at this Pt:N ratio, the C:N ratio does not have a substantial influence on the current density anymore. This trend gets even more pronounced at 0.7 V_{RHE}. The highest current density for the HISPEC 70 wt.% catalyst were obtained with a Pt:N ratio of 1 (by adding carbon support to the ink) *and* a C:N ratio of 1.

4 | CONCLUSIONS

In the presented work, the ORR performance of six commercial Pt/C catalysts is compared in a GDE setup. As benchmark, the same catalysts are compared in RDE measurements according to standardized procedures that are assumed to showcase the *intrinsic* ORR activity of the respective catalysts. The results are summarized in Table 1. The work clearly demonstrates the challenges but also the strengths of the GDE approach. In the last 10 years, several RDE studies demonstrated the importance of the film quality for obtaining the intrinsic ORR activity of a catalyst, research work that is still ongoing.[45] At the same time, the popularity of the RDE approach is at least partially owed to its simplicity and the availability of all required instruments. The presented GDE measurements indicate that the influence of the film quality on the obtained results in this approach is at least equally important as in the RDE approach. However, to find broad application, a simple and straight-forward film preparation method should be applied, such as the vacuum filtration technique, that only requires standard equipment that is available in most research laboratories and leads to reproducible results in film quality. Most likely, as for the RDE approach, further work on establishing standardized procedures and the use of benchmarks will be essential to obtain meaningful results.

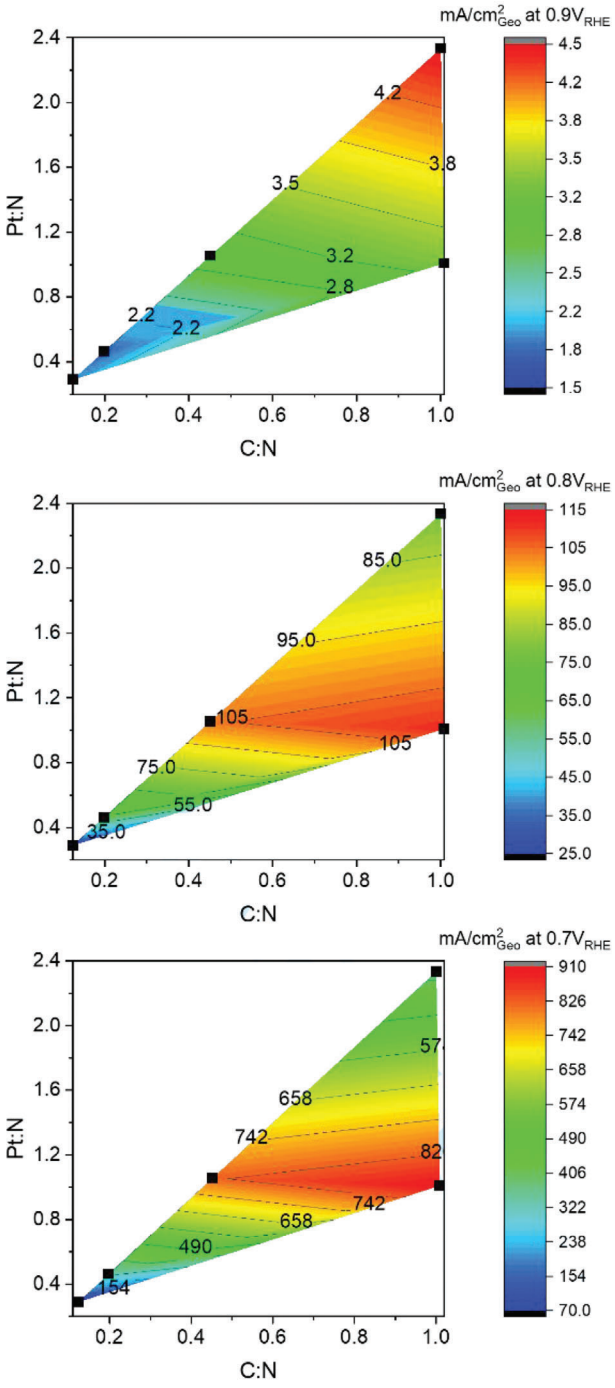

FIGURE 8 Comparison of the influence of Pt:N and C:N ratios on ORR activities of HISPEC 70 wt.% at 0.9 V_{RHE}, 0.8 V_{RHE}, and 0.7 V_{RHE}. At 0.9 VRHE, both Pt:N and C:N ratio determine the obtained current density of HISPEC 70wt.%. A high Pt:N ratio and a C:N ratio around 1 gave the highest current densities. However, at lower voltages the Pt:N ratio becomes the key ratio. There is a clear trend toward a Pt:N ratio of 1. The ORR activities are averaged values of three measurements. The black squares indicate the calculated C:N and Pt:N ratios of all analyzed catalyst films based on which the contour plots are made

TABLE 1 Summary of the RDE and GDE results. The font in red from TKK 50.6 wt.% is the result with potential cycling in O_2 for catalyst surface cleaning

Catalyst	Pt NP size (nm)		Theoretical M ECSA (m^2/g_{Pt})	ECSA (m^2/g_{Pt})		MA (A/g_{Pt})		SA (A/m_P)			
	TEM	SAXS	Based onTEM	RDE	GDE	RDE (0.9 V)	GDE (0.9 V)	RDE (0.9 $V_{Pos.}$)	RDE (0.9 $V_{Neg.}$)	GDE (0.9 V)	GDE (0.8 V)
TKK 19.4 wt.%	1.6 ± 0.4	1.9 ± 0.3	175	151.3 ± 7.5	120.1 ± 2.3	163.4 ± 59	12.2 ± 0.6	330	3.37 ± 0.49	1.08 ± 0.39	0.1	2.75
TKK 46 wt.%	2.9 ± 0.8	2.8 ± 0.5	96.5	90.3 ± 1.1	84.6 ± 5	108.4 ± 11.8	26.7 ± 0.9	660	5.84 ± 0.99	1.20 ± 0.13	0.3	7.8
TKK 50.6 wt.%	4.7 ± 1.1	5.4 ± 1.7	59.5	61.4 ± 3.3	49 ± 0.2	55.3 ± 7.4	16.8 ± 0.4	364	3.18 ± 0.28 4.20 ± 0.36	0.90 ± 0.11 1.68 ± 0.14	0.3	7.43
HISPEC 20 wt.%	2.9 ± 0.8	3.3 ± 1.1	96.5	91.8 ± 2.1	57.8 ± 3.2	175.3 ± 8.3	19.4 ± 2.7	517	5.64 ± 1.21	1.91 ± 0.09	0.3	8.95
HISPEC 60 wt.%	2.9 ± 1	3.3 ± 0.8	96.5	86.5 ± 3.4	57 ± 2	174.7 ± 17.3	9.7 ± 0.1	280	5.69 ± 1.14	2.02 ± 0.20	0.2	5
HISPEC 70 wt.%	3.5 ± 1.5	4 ± 0.8	79.8	61.5 ± 0.7	45.3 ± 1.6	113.2 ± 40	21.4 ± 0.7	379	6.77 ± 2.00	1.84 ± 0.65	0.5	8.4

On the other hand, the results clearly demonstrate the potential of the GDE approach to bridge RDE and MEA measurements, thus, helping to commercialize new ORR catalysts. Most importantly, the GDE approach allows focusing on relevant current densities that are inaccessible in RDE measurements. Moreover, the optimization of characteristics, such as the ink recipe or the applied catalyst loading on the GDL for each individual catalyst, is feasible in a much simpler manner than in elaborate MEA testing. Therefore, the GDE approach has the clear potential to reach similar popularity as the RDE approach.

ACKNOWLEDGMENTS

This work was supported by the Swiss National Science Foundation (SNSF) via the project No. 200021_184742. Jia Du acknowledges funding from the China Scholarship Council (CSC). Jonathan Quinson acknowledges the European Union's Horizon 2020 research and innovation program under the Marie Skłodowska-Curie grant agreement No. 840523 (CoSolCat). S. B. Simonsen and L. Theil Kuhn, Technical University of Denmark, are thanked for access to TEM. The Niels Bohr Institute, University of Copenhagen, for access to SAXS equipment and in particular J. J. K. Kirkensgaard.

CONFLICT OF INTERESTS

The authors declare no conflict of interest.

ORCID

Etienne Berner https://orcid.org/0000-0002-4902-2687
Gustav K.H. Wiberg https://orcid.org/0000-0003-1884-604X
Matthias Arenz https://orcid.org/0000-0001-9765-4315

REFERENCES

1. T. Yoshida, K. Kojima, *Electrochem. Soc. Interface* **2015**, *24*, 45–49.
2. F. R. Nikkuni, B. Vion-Dury, L. Dubau, F. Maillard, E. A. Ticianelli, M. Chatenet, *Appl. Catal. B Environ.* **2014**, *156–157*, 301–306.
3. D. J. Myers, A. Jeremy Kropf, E. C. Wegener, H. Mistry, N. Kariuki, J. Park, *J. Electrochem. Soc.* **2021**, *168*, 044510.
4. H. A. Baroody, E. Kjeang, *J. Electrochem. Soc.* **2021**, *168*, 044524.
5. D. J. S. Sandbeck, N. M. Secher, M. Inaba, J. Quinson, J. E. Sørensen, J. Kibsgaard, A. Zana, F. Bizzotto, F. D. Speck, M. T. Y. Paul, A. Dworzak, C. Dosche, M. Oezaslan, I. Chorkendorff, M. Arenz, S. Cherevko, *J. Electrochem. Soc.* **2020**, *167*, 164501.
6. O. Gröger, H. A. Gasteiger, J.-P. Suchsland, [J. Electrochem. Soc., 162, A2605 (2015)]. *J. Electrochem. Soc.* **2016**, *163*, X3–X3.
7. B. Han, C. E. Carlton, A. Kongkanand, R. S. Kukreja, B. R. Theobald, L. Gan, R. O'Malley, P. Strasser, F. T. Wagner, Y. Shao-Horn, *Energy Environ. Sci.* **2015**, *8*, 258–266.
8. K. Shinozaki, J. W. Zack, R. M. Richards, B. S. Pivovar, S. S. Kocha, *J. Electrochem. Soc.* **2015**, *162*, F1114. https://doi.org/10.1149/2.1071509jes.

9. H.A. Gasteiger, S. S. Kocha, B. Sompalli, F. T. Wagner, *Appl. Catal. B* **2005**, *56*, 9–35. https://doi.org/10.1016/j.apcatb.2004.06.021.
10. H. A. Gasteiger, J. E. Panels, S. G. Yan, *J. Power Sources* **2004**, *127*, 162–171.
11. D. Siegmund, S. Metz, V. Peinecke, T. E. Warner, C. Cremers, A. Grevé, T. Smolinka, D. Segets, U. P. Apfel, *JACS Au* **2021**, *1*, 527–535.
12. T. Yoshizumi, H. Kubo, M. Okumura, *SAE Int*. **2021**. https://doi.org/10.4271/2021-01-0740.
13. G. K. H. Wiberg, M. Fleige, M. Arenz, *Rev. Sci. Instrum.* **2015**, *86*. https://doi.org/10.1063/1.4908169
14. M. Inaba, A. W. Jensen, G. W. Sievers, M. Escudero-Escribano, A. Zana, M. Arenz, *Energy Environ. Sci.* **2018**, *11*. http://doi.org/10.1039/C8EE00019K
15. C. Zalitis, A. Kucernak, X. Lin, J. Sharman, *ACS Catal*. **2020**, *10*, 4361–4376.
16. C. M. Zalitis, D. Kramer, A. R. Kucernak, *Phys. Chem. Chem. Phys.* **2013**. https://doi.org/10.1039/c3cp44431g.
17. L. Pan, S. Ott, F. Dionigi, P. Strasser, *Curr. Opin. Electrochem.* **2019**, *18*, 61–71.
18. K. Ehelebe, D. Seeberger, M. T. Y. Paul, S. Thiele, K. J. J. Mayrhofer, S. Cherevko, *J. Electrochem. Soc.* **2019**, *166*, F1259–F1268.
19. B. A. Pinaud, A. Bonakdarpour, L. Daniel, J. Sharman, D. P. Wilkinson, *J. Electrochem. Soc.* **2017**. https://doi.org/10.1149/2.0891704jes.
20. S. Alinejad, M. Inaba, J. Schröder, J. Du, J. Quinson, A. Zana, M. Arenz, *J. Phys. Energy* **2020**, *2*, 024003.
21. J. Schröder, V. A. Mints, A. Bornet, E. Berner, M. Fathi Tovini, J. Quinson, G. K. H. Wiberg, F. Bizzotto, H. A. El-Sayed, M. Arenz, *JACS Au* **2021**, *1*, 247–251.
22. J. Schröder, J. Quinson, J. K. Mathiesen, J. J. K. Kirkensgaard, S. Alinejad, V. A. Mints, K. M. ∅. Jensen, M. Arenz, *J. Electrochem. Soc.* **2020**, *167*, 134515.
23. K. Ehelebe, N. Schmitt, G. Sievers, A. W. Jensen, A. Hrnjić, P. C. Jiménez, P. Kaiser, M. Geuß, Y.-P. Ku, P. Jovanovič, K. J. J. Mayrhofer, B. Etzold, N. Hodnik, M. Escudero-Escribano, M. Arenz, S. Cherevko, *ACS Energy Lett*. **2022**, *7*, 816–826.
24. M. Inaba, J. Quinson, J. R. Bucher, M. Arenz, *J. Vis. Exp.* **2018**, *133*, e57105.
25. S.S. Kocha, K. Shinozaki, J. W. Zack, D. J. Myers, N. N. Kariuki, T. Nowicki, V. Stamenkovic, Y. Kang, D. Li, D. Papageorgopoulos, *Electrocatalysis* **2017**, *8*, 366–374.
26. M. Inaba, J. Quinson, M. Arenz, *J. Power Sources* **2017**, *353*, 19–27.
27. J. Du, J. Quinson, D. Zhang, F. Bizzotto, A. Zana, M. Arenz, *ACS Catal*. *11*, 820–828.
28. J. Du, J. Quinson, A. Zana, M. Arenz, *ACS Catal*. *11*, 7584–7594.
29. K. J. J. Mayrhofer, D.Strmcnik, B.B.Blizanac, V.Stamenkovic, M.Arenz, N.M.Markovic, *Electrochim. Acta* **2008**, *53*, 3181–3188.
30. G. K. H. Wiberg, M. Fleige, M. Arenz, *Rev. Sci. Instrum.* **2015**, *86*.
31. M. Inaba, J. Quinson, J. R. Bucher, M. Arenz, *J. Vis. Exp.* **2018**, *2018*, 57105.
32. D. Zhang, J. Du, J. Quinson, M. Arenz, *ChemRxiv. Prepr.* **2021**. http://doi.org/10.33774/chemrxiv-2021-j5vb5.
33. G. S. Harzer, J. N. Schwämmlein, A. M. Damjanović, S. Ghosh, H. A. Gasteiger, *J. Electrochem. Soc.* **2018**, *165*, F3118–F3131.
34. M. Nesselberger, S. Ashton, J. C. Meier, I. Katsounaros, K. J. Mayrhofer, M. Arenz, *J. Am. Chem. Soc.* **2011**, *133*, 17428–1733.
35. K. Kodama, A. Shinohara, N. Hasegawa, K. Shinozaki, R. Jinnouchi, T. Suzuki, T. Hatanaka, Y. Morimoto, *J. Electrochem. Soc.* **2014**, *161*, F649–F652.
36. I. Takahashi, S. S. Kocha, *J. Power Sources* **2010**, *195*, 6312–6322.
37. D. Voiry, M. Chhowalla, Y. Gogotsi, N. A. Kotov, Y. Li, R. M. Penner, R. E. Schaak, P. S. Weiss, *ACS Nano* **2018**, *12*, 9635–9638.
38. A. J. Bard, L. R. Faulkner, *Electrochemical Methods: Fundamentals and Applications*. Wiley-VCH Verlag, Germany**1980**.
39. X. Tian, X. F. Lu, B. Y. Xia, X. W. Lou (David), . *Joule* **2020**, *4*, 45–68.
40. L. Chong, J. Wen, J. Kubal, F. G. Sen, J. Zou, J. Greeley, M. Chan, H. Barkholtz, W. Ding, D. J. Liu, *Science (80-.)*. **2018**, *362*, 1276–1281.
41. U. A. Paulus, T. J. Schmidt, H. A. Gasteiger, R. J. Behm, *Res. gate* **2014**, *495*, 134–145.
42. N. M. Markovíc, P. N. Ross, *Surf. Sci. Rep.* **2002**, *45*, 117–229.
43. V. Yarlagadda, S. E. McKinney, C. L. Keary, L. Thompson, B. Zulevi, A. Kongkanand, *J. Electrochem. Soc.* **2017**, *164*, F845–F849.
44. T. Yoshizumi, H. Kubo, M. Okumura, in *SAE Technical Paper* **2021**.https://doi.org/10.4271/2021-01-0740.
45. M. Inaba, Y. Kamitaka, K. Kodama, *J. Electroanal. Chem.* **2021**, *886*, 115115.

SUPPORTING INFORMATION

Additional supporting information may be found in the online version of the article at the publisher's website.

How to cite this article: Sven Nösberger, Jia Du, Jonathan Quinson, Etienne Berner, Alessandro Zana, Gustav K.H. Wiberg, & Matthias Arenz. *Electrochem Sci Adv*. **2022**, e2100190. https://doi.org/10.1002/elsa.202100190

Supporting Information of Manuscript II

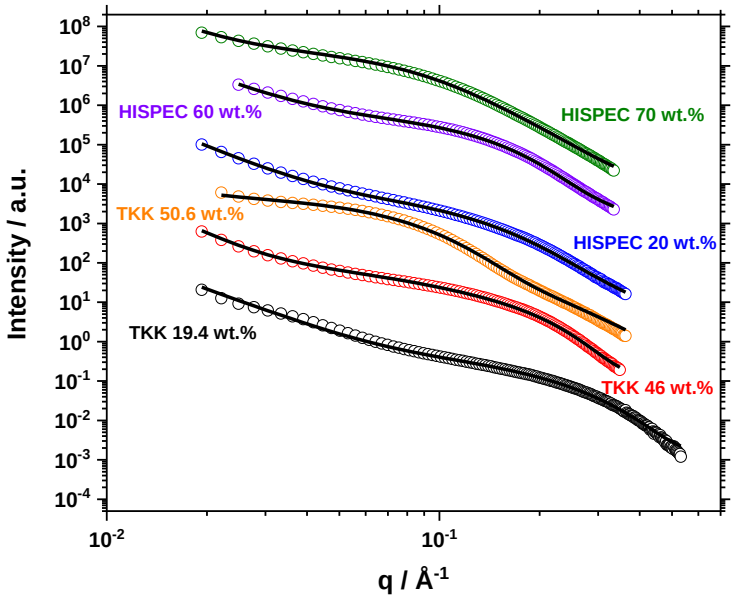

Figure S1: Background subtracted SAXS data and the related fits for the different samples, as indicated.

Table S1 SAXS fitting parameters for fits corresponding to *Figure S*.

Sample	A*10⁶	n	R_1 (Å)	σ_1	C_1	R_2 (Å)	σ_2	C_2	d / nm [a]	σ / nm [b]
TKK 19.4 wt.%	115	3.1	8.6	0.12	0.002	10.1	0.3	0.005	1.9	0.3
TKK 46 wt.%	8	4.0	13.0	0.20	0.025	20.0	0.4	0.018	2.8	0.5
TKK 50.6 wt.%	40	3.3	26.0	0.30	0.110	-	-	-	5.4	1.7
HISPEC 20 wt.%	100	3.5	15.5	0.33	0.030	-	-	-	3.3	1.1
HISPEC 60 wt.%	150	3.3	16.0	0.25	0.038	-	-	-	3.3	0.8
HISPEC 70 wt.%	52	3.5	15.0	0.25	0.015	25.0	0.3	0.063	4.0	0.8

(a) evaluated as $0.2\ \varphi_{A1}\ e^{\left(\ln(R_1)+\frac{{\sigma_1}^2}{2}\right)} + \ 0.2\ \varphi_{A2}\ e^{(\ln(R_2)+\frac{{\sigma_2}^2}{2})}$

(b) evaluated $0.2\ \sqrt{{\varphi_{A1}}^2\ [(e^{{\sigma_1}^2}-1).\ e^{(2.\ln(R_1)+{\sigma_1}^2)} + \ {\varphi_{A2}}^2\ [(e^{{\sigma_2}^2}-1).\ e^{(2.\ln(R_2)+{\sigma_2}^2)}}$

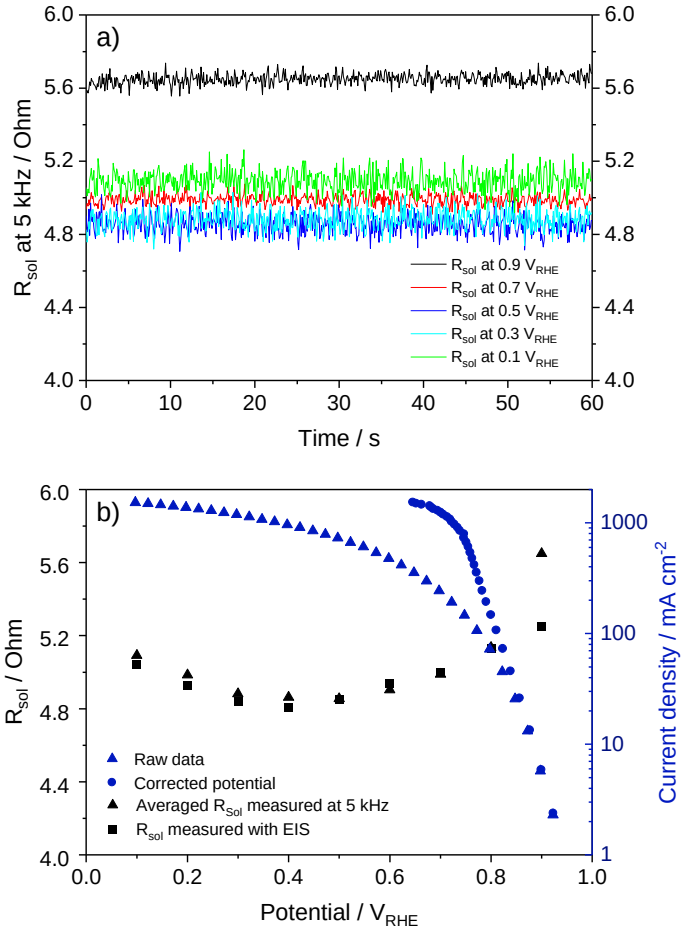

Figure S2: a) Example of online measurement of the solution resistance R_{Sol} in GDE setup with 5 kHz at different potentials; no compensation applied. b) Comparison of average R_{Sol} values from online measurement (black triangles) with R_{Sol} determined from Nyquist plot of EIS measurements (black squares). Measured (blue triangles) and post corrected (blue circles) ORR current densities. All measurements performed with TKK 2-3nm 46wt.% Pt/C catalyst.

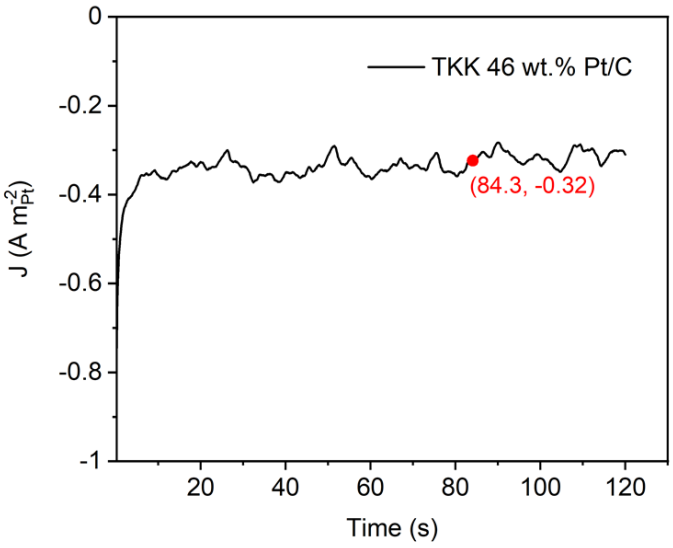

Figure S3: ORR activity determination under steady state. Potential sweeping (50 mV s^{-1}) was conducted for 4 cycles with different rotation speeds (900, 1600, 2500 and 3600 rpm, 1 cycle for each rotation speed) in O_2 saturated 0.1 M $HClO_4$, followed by potential jumping to 0.9 V_{RHE} and holding for 2 min. The corresponding current was recorded and normalized by Pt ECSA.

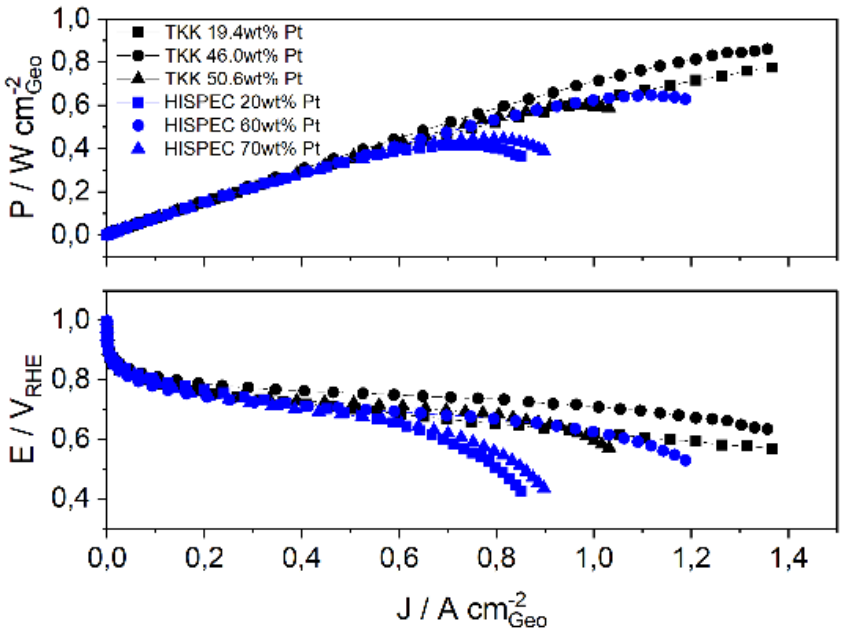

Figure S4: Comparison of the performance of all investigated catalysts in a GDE setup. The black lines represent catalysts manufactured by Tanaka Kikinzoku Kogyo K.K, the blue lines represent catalysts manufactured by Alfa Aesar. The figure shows the averaged power density of at least three measurements of the same catalyst.

Manuscript III

ACS Catalysis

pubs.acs.org/acscatalysis

Research Article

Elucidating Pt-Based Nanocomposite Catalysts for the Oxygen Reduction Reaction in Rotating Disk Electrode and Gas Diffusion Electrode Measurements

Jia Du, Jonathan Quinson, Alessandro Zana, and Matthias Arenz*

Cite This: *ACS Catal.* 2021, 11, 7584–7594

Read Online

ACCESS | Metrics & More | Article Recommendations | Supporting Information

ABSTRACT: In the present study, we compare different nanoparticle (NP) composites (nanocomposites) as potential electrocatalysts for the oxygen reduction reaction (ORR). The nanocomposites consist of a mixture of Pt and Ir NPs and Pt and Au NPs, respectively, that are immobilized onto a high surface area carbon support. Pt NPs supported on the same carbon support serve as a benchmark. The performance testing was performed in a conventional rotating disk electrode (RDE) setup as well as in a recently introduced gas diffusion electrode (GDE) setup, providing high mass transport conditions. The ORR activity is determined, and the degradation is tested using accelerated degradation tests. It is shown that with respect to the benchmark, the Pt-Au nanocomposite concept exhibits improved ORR activity as well as improved stability both in the RDE and GDE measurements. By comparison, the Pt-Ir nanocomposite exhibits improved stability but lower ORR activity. By combining the GDE approach with small-angle X-ray scattering, it is shown that the improved stability of the Pt-Au nanocomposite can be assigned to a reduced Pt particle growth due to the adjacent Au NPs. The results demonstrate that nanocomposites could be an alternative catalyst design strategy complementing the state-of-the-art alloying concepts.

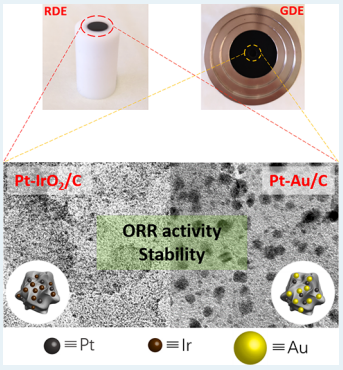

KEYWORDS: *nanocomposite electrocatalysts, oxygen reduction reaction, gas diffusion electrode setup, accelerated degradation tests, small-angle X-ray scattering*

INTRODUCTION

Due to its importance for fuel cells, the oxygen reduction reaction (ORR) is one of the most studied reactions in electrocatalysis. Independently, if a fuel cell is operated with hydrogen or liquid fuels such as methanol and operates under acidic or alkaline conditions, a substantial part of its performance loss (as compared to the thermodynamic cell potential) is due to the sluggish ORR at its cathode catalyst. In acidic proton exchange membrane fuel cells (PEMFCs), state-of-the-art ORR catalysts are based on Pt-alloy catalysts,[1−5] e.g., PtCo nanoparticles (NPs) supported on a high surface area carbon support. The "kinetic activity" of the ORR catalyst has direct consequences for the conversion efficiency; however, catalyst stability and performance under high mass transport conditions (high current densities) are equally important properties a "good ORR catalyst" must fulfill. Most research studies concerning Pt-based ORR catalysts for PEMFCs are concerned with an accurate control and optimization of the active Pt phase at the atomic level that determines the kinetics. Substantial achievements have been reported for the initial kinetic activity that needs to be sustained under operation conditions. One of the most imminent challenges therefore is the changing reaction environment, i.e., going from reductive conditions during operation to slightly oxidizing under open-circuit (idling) conditions to (if not prevented) highly oxidizing conditions during start-up and shutdown. Such dynamic conditions not only lead to the dissolution of Pt but they also induce segregation and dissolution of less noble components in Pt-alloys.[6]

An alternative approach that has been recently introduced is to concentrate on a statistical distribution of surface sites in high entropy alloy (HEA) catalysts with the goal of optimizing the likelihood for highly active surface sites.[7] As compared to conventional bimetallic or trimetallic Pt-based catalysts, the HEA approach is less mature and, to date, is more of fundamental interest. Not only is the synthesis of nanomaterials with random surface arrangements of the different constituents extremely difficult, also characterizing and maintaining the surface composition are challenging.

By comparison, the synthesis of monometallic nanomaterials is considerably more straightforward. In the presented work, we therefore pursue the concept of composite catalysts

Received: April 1, 2021
Revised: May 27, 2021
Published: June 9, 2021

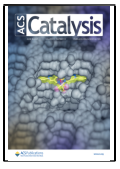

consisting of different monometallic NPs, i.e., nanocomposite catalysts, which are currently of primarily fundamental interest as well. The main difference to the established alloying concept is the focus—in addition to the atomic structure—on mesoscopic properties such as the particle density on the support, i.e., the interparticle distance.[8−11] As stated above, in addition to the kinetic performance, the effective mass transport of the reactant and product in the catalyst layer is equally crucial to optimize the power density, e.g., for mobile applications of PEMFCs. For this, non-active NP components could, for example, be used to optimize the catalyst performance without inhibiting the dispersion of the active sites as well as the oxygen mass transport resistance; the latter is often a problem for high-performing alloy catalysts that tend to exhibit a large particle size and associated large oxygen transport resistance.[12] To investigate the promising nanocomposite concept further, we chose to investigate two different nanocomposite catalysts, i.e., a nanocomposite consisting of carbon-supported Pt and activated (oxidized) Ir NPs and a nanocomposite consisting of carbon-supported Pt and Au NPs, in the following referred to as Pt-IrO_2/C and Pt-Au/C. A standard Pt/C catalyst serves as a benchmark.[13,14] In Pt-based alloy catalysts, the addition of both Ir and Au is reported to improve the ORR performance.[15,16] The performance of the nanocomposite catalysts is investigated in conventional rotating disk electrode (RDE) measurements[13,17,18] as well as in recently introduced gas diffusion electrode (GDE) measurements,[19−25] which, in contrast to the RDE measurements, provide realistic catalyst loadings as well as realistic mass transport conditions. In addition to the activity, the degradation was tested using accelerated degradation tests (ADTs). It is shown that both nanocomposites, i.e., Pt-IrO_2/C and Pt-Au/C, exhibit improved degradation resistance; however, only in the case of Pt-Au/C, the ORR activity is improved as well.

EXPERIMENTAL SECTION

Chemicals and Gases. The following chemicals were used for catalyst synthesis and characterization: hexa-chloroplatinic-(IV) acid hexahydrate ($H_2PtCl_6{\cdot}6H_2O$, 99.9%, Alfa Aesar), iridium(III) chloride ($IrCl_3{\cdot}xH_2O$, >99.8%, Sigma-Aldrich), gold(III) chloride ($AuCl_3$, ≥99.99% trace metal basis, Sigma-Aldrich), ethylene glycol (EG, 99.8%, Sigma-Aldrich), sodium hydroxide (NaOH, 98.9%, Fisher Chemical), oleylamine (technical grade, 70%, Sigma-Aldrich), 1-octadecene (technical grade, 90%, Sigma-Aldrich), lithium triethylborohydride ($LiBEt_3H$, superhydride solution, 1 M in THF, Sigma-Aldrich), 30% hydrochloric acid (HCl, Suprapur, Merck), and acetone (99.5+%, Alfa Aesar). Commercial carbon black (Vulcan XC72R) was employed as a carbon support in the catalyst synthesis. Ultrapure water (resistivity, >18.2 MΩ cm; total organic carbon (TOC), <5 ppb) from a Milli-Q system (Millipore) was used for acid/base dilutions, catalyst ink formulation, and electrochemical cell cleaning. Isopropanol (IPA, 99.7+%, Alfa Aesar), 70% perchloric acid ($HClO_4$, Suprapur, Merck), and potassium hydroxide hydrate ($KOH{\cdot}H_2O$, Suprapur, Merck) were used for the catalyst ink formulation and electrolyte preparation. The following gases from Air Liquide were used for electrochemical measurements: Ar (99.999%), O_2 (99.999%), and CO (99.97%).

Synthesis of Monometallic Pt/C, Pt-IrO_2/C Nanocomposite, and Pt-Au/C Nanocomposite Catalysts. The synthesis approach followed a colloidal approach and consisted of two main steps: the synthesis of colloidal NPs and their immobilization on a carbon support. Concerning the synthesis of carbon-supported monometallic Pt NPs and Pt-IrO_2 nanocomposite catalysts, we applied a surfactant-free colloidal approach[26] and referred to our recent work.[27] In short, mixing 400 mM NaOH EG with 40 mM $H_2PtCl_6{\cdot}6H_2O$ or $IrCl_3{\cdot}xH_2O$ EG solution in a microwave reaction vessel and heating the mixture to 160 °C for 3 min in a microwave reactor led to the formation of colloidal Pt or Ir NPs in EG with concentrations of 3.90 g_{Pt} L^{-1} and 3.85 g_{Ir} L^{-1}, respectively. To immobilize the NPs on the carbon support, 1 M HCl was added to the colloidal NPs, inducing particle flocculation. The mixture was thereafter centrifuged at 5000 rpm for 10 min, the supernatant was discarded, and the floc was redispersed in acetone to obtain an NP dispersion in acetone with the same concentration as before the flocculation in EG. To prepare a monometallic Pt/C catalyst, the carbon support (Vulcan XC72R) suspension was prepared with a concentration of 0.50 g L^{-1} in acetone and homogenized by a horn sonicator (QSONICA sonicator, 500 W, 50 kHz, with alternation of 1 s sonication and 1 s resting) for 5 min. Then, the Pt NPs dispersed in acetone were added and further sonicated for 5 min. After the homogenization of the mixture, the solvent was evaporated with a rotary evaporator at room temperature and 200 mbar, applying a continuous sonication until the catalyst was completely dried and 20 wt % Pt/C was obtained. A similar procedure was employed to obtain the immobilized Pt-IrO_2/C nanocomposite catalyst. Here, Pt NPs dispersed in acetone and Ir NPs dispersed in acetone were added to the sonicated carbon acetone suspension one by one, whereafter the same procedure was applied. The nominal Pt-to-Ir metal ratio in the nanocomposite was 1:2 based on weight. The Pt loading was kept as in the benchmark, i.e., 20 wt %.

Concerning the preparation of supported Pt-Au/C nanocomposite catalysts, we applied the same approach for obtaining surfactant-free colloidal Pt NPs. However, for the preparation of Au NPs, we used the method reported previously by Zhang et al.[28] In short, $AuCl_3$ (151.7 mg) was dissolved in a mixture of 1-octadecene (16 mL) and oleylamine (4 mL) under an Ar atmosphere. The system was protected by the Ar atmosphere and heated to 60 °C, followed by a quick injection of the reducing agent $LiBEt_3H$ (1.5 mL). The temperature was kept at 60 °C for 10 min, whereafter the solution was cooled down to room temperature. Thereafter, the system was exposed to air, and ethanol was added to separate Au NPs with centrifugation at 5000 rpm for 10 min. The as-prepared Au NPs were redispersed in hexane at a concentration of 0.82 g_{Au} L^{-1}. To immobilize the monometallic Au NPs, carbon was dispersed in hexane and sonicated with the horn sonicator as mentioned above until a stable dispersion was obtained (∼10 min). Then, the Au NPs dispersed in hexane were added and the suspension was sonicated further for 10 min, and thereafter, hexane was evaporated with a rotary evaporator until the catalyst was completely dried, obtaining 40 wt % Au/C. To remove the ligand (oleylamine), the dried Au/C powder was heated in an oven (Nabertherm, 30−3000 °C) at 210 °C for 5 h. If the ligand is not removed from the Au surface, then Au/C cannot be dispersed in acetone, which will inevitably influence the subsequent immobilization step of the Pt NPs (that were dispersed in acetone after flocculation with 1 M HCl) onto Au/C. Another point needs to be noted: to obtain the carbon supported Pt-IrO_2 nanocomposite, the Pt NPs and Ir NPs were

https://doi.org/10.1021/acscatal.1c01496
ACS Catal. 2021, 11, 7584−7594

added one by one to the carbon suspension in acetone. In the procedure of the carbon-supported Pt-Au nanocomposite, instead of adding Pt NPs and Au NPs simultaneously during the immobilization procedure, first, Au/C was obtained, which may have suffered from the thermal treatment for ligand removal. The Pt NPs were immobilized on the ligand-free Au/C to avoid exposing the Pt NPs to the thermal treatment, which may induce the complete oxidation of Pt. The immobilization procedure of the Pt NPs on the ligand-free Au/C followed the same procedure as described above, i.e., mixing, sonication, and solvent evaporation. The prepared Pt-Au/C nanocomposite had a nominal Pt to Au metal weight ratio of 1:2 and a Pt loading of 20 wt %.

Catalyst Ink Formation and Catalyst Layer Preparation for RDE Measurements. To obtain inks for the RDE measurements, the respective dried catalyst powder was dispersed in a mixture of Milli-Q water and IPA (V_{water}:V_{IPA} = 3:1) containing 1.6 μL/mL 1 M KOH(aq.)[17] and homogenized in a sonicator bath for 10 min, resulting in a homogeneous catalyst ink with a total Pt concentration of 0.275 g L^{-1}. A total of 7.14 μL of the respective catalyst ink was pipetted onto glassy carbon (GC) disks to obtain a fixed Pt loading of 10 $\mu g\ cm_{geo}^{-2}$ for all samples. The GC tips were dried at ambient atmosphere for further electrochemical measurements. By obtaining cyclic voltammograms (CVs) between 0.05 and 1.60 V_{RHE}, the appearance of the broad oxidation peak (centered at around 1.40 V_{RHE}) as well as the oxide reduction peak (centered at around 1.20 V_{RHE}) can be the indication of the presence of Au in the catalyst (see Figure S1). The Pt weight loading on the carbon support in the mentioned electrocatalysts therefore is fixed to 20 wt %.

Gas Diffusion Electrode (GDE) Cell Setup. An in-house gas diffusion electrode setup as described before[19,22,24,29] was used in the electrochemical measurements. A GDE setup with a lower cell body made of stainless steel and a flow field was used. The GDE was placed above the flow field with a Nafion membrane (Nafion 117, 183 μm thick, Fuel Cell Store) facing upward. The upper cell body was made of polytetrafluoroethylene (PTFE). A platinum mesh and a reversible hydrogen electrode (RHE) were used as a counter electrode and a reference electrode, respectively. The counter electrode was placed inside a glass capillary tube with a glass frit on the bottom, which can avoid the trapping of gas bubbles in the hole of the Teflon cell and hence improves the reproducibility of the measurements.

Catalyst Ink Formation and Catalyst Layer Preparation for GDE. The recipe of the catalyst ink for the GDE measurements was reported previously.[24] The catalyst ink was formed by dispersing the catalysts in a mixture of Milli-Q water and IPA (V_{water}:V_{IPA} = 3:1) to obtain the concentration of Pt of 0.50 g L^{-1}. Nafion (D1021, 10 wt %, Fuel Cell Store) was added to the catalyst ink in a weight ratio between Nafion and carbon of 1. Then, the solution was sonicated in a sonication bath for around 5 min to obtain a stable dispersion.

A H23C8 gas diffusion layer (GDL) was punched from a larger GDL sheet and placed into a vacuum filtration setup between a glass funnel and a sand core filter. This was placed on top of a collecting bottle as reported by Yarlagadda et al.[30] Separate vacuum filtration setups were used for the Pt-IrO_2/C and Pt-Au/C nanocomposite catalysts to avoid cross-contamination. For the Pt-IrO_2/C nanocomposite catalyst, a setup with a sand core filter of 42 mm in diameter was used, while for monometallic Pt/C and Pt-Au/C nanocomposite catalysts, a setup with a sand core filter of 15 mm in diameter was used. The catalyst ink was diluted from a concentration of 0.50 $g_{Pt}\ L^{-1}$ to 0.05 $g_{Pt}\ L^{-1}$ by adding Milli-Q water and IPA (the final volume ratio between Milli-Q water and IPA was 1:3 to increase the speed of vacuum filtration). The diluted catalyst ink was filled into the funnel and a vacuum pump was used to deposit the catalyst on top of the GDL. With this deposition procedure, in all cases, a nominal Pt loading of 208 $\mu g\ cm_{geo}^{-2}$ on the GDL was obtained. After preparing the catalyst layer on the GDL, a Nafion membrane was pressed on top of the GDE. For this, a Teflon sheet, a GDL without MPL (Ø 2 cm), a GDL with MPL (Ø 2 cm with a hole of Ø 3 mm), the catalyst on the GDL from the vacuum filtration (Ø 3 mm), a Nafion membrane, and the second Teflon sheet were placed in this order one by one on top of a Teflon block. Then, a second Teflon block was placed on top, and everything was placed between two metal blocks and pressed at 2 tons for 10 min.

Electrochemical Measurements. All electrochemical measurements were recorded with a computer-controlled potentiostat (ECi 200, Nordic Electrochemistry) at room temperature. The RDE measurements were performed using the same setup employed in our previous work,[18] i.e., in a glass cell equipped with three electrodes. A GC RDE tip with a diameter of 5 mm was used as a working electrode (WE) and a platinum wire as a counter electrode (CE). All potentials were measured with respect to a trapped hydrogen reversible hydrogen electrode (RHE) as a reference electrode (RE). As an aqueous electrolyte, 0.1 M $HClO_4$ was used, which was saturated with Ar before the electrochemical measurements. For the Pt-IrO_2/C nanocomposite, the Ir NPs were activated by the holding potential at 1.60 V_{RHE} for 8 min. After activation, the catalyst was exposed to potential cycling between 0.05 and 1.20 V_{RHE} until a stable CV with the basic features of Pt was obtained. For the monometallic Pt/C and Pt-Au/C nanocomposite catalysts, the same potential cycling was applied; however, no activation was performed. During the potential cycling, the cell resistance between the WE and RE (~25 Ω) was compensated to an effective value of around 3 Ω using the analog positive feedback scheme of the potentiostat.

In the RDE setup, the activity and stability tests were separately conducted, i.e., for each catalyst, at least three different tips were used for activity measurements and three different tips were used for the stability measurements. For the ORR activity measurements, a macroscript was designed with EC4DAQ potentiostat software to automatically record a series of cyclic voltammograms (CVs), CO stripping curves, and ORR polarization curves.[18] The CVs were recorded in an Ar-saturated electrolyte in the potential region between 0.05 and 1.10 V_{RHE} with a scan rate of 50 mV s^{-1}. CO stripping measurements were carried out to determine the Pt area; basically, the electrode was held at 0.15 V_{RHE} in a CO-saturated electrolyte for 2 min. Then, the electrolyte was purged with Ar and held at 0.15 V_{RHE} for 10 min to replace the excess CO in the electrolyte, and the adsorbed CO monolayer was oxidized to CO_2 by cycling the potential from 0.15 to 1.10 V_{RHE} at a scan rate of 50 mV s^{-1}. The electrochemically active surface area (ECSA; Pt area) was calculated based on a reference oxidation charge value from polycrystalline Pt of 396 $\mu C\ cm_{Pt}^{-2}$. For the Pt-Ir/C nanocomposite, as Ir was pre-activated (Ir was oxidized to IrO_2), the contribution from Ir for ECSA determination is negligible as reported previously.[31] Because the interaction between CO and the Au surface is quite weak as well, the same is the case for the Pt-Au/C

https://doi.org/10.1021/acscatal.1c01496
ACS Catal. 2021, 11, 7584−7594

nanocomposite. To confirm this, we conducted the CO stripping measurement with pure Au/C in which the gold content was the same as the Pt-Au/C nanocomposite. The measurement exhibited only a very small CO oxidation peak centered at around 1.10 V_{RHE} with a calculated surface area below 5 m^2 g_{Au}^{-1}. The ORR activity measurements were conducted in an O_2-saturated electrolyte at a scan rate of 50 mV s^{-1} and a rotation speed of 1600 rpm. The specific activity was normalized by the Pt surface area and compared at 0.85 V_{RHE} from the polarization curve recorded in the negative-going scan direction (corrected by background subtraction recorded under an inert atmosphere). The mass activity was normalized by the Pt content and compared at 0.85 V_{RHE} as well.

To determine the stability of the Pt-based electrocatalysts, accelerated degradation tests (ADT) were employed using four different protocols in the RDE measurements. The first three protocols were performed in a potential control mode in an Ar-saturated electrolyte. One protocol simulates load cycling conditions, stepping the electrode potential between 0.60 and 1.00 V_{RHE} with a rest time of 3 s at each potential. The treatment lasted for 9000 cycles. The second protocol simulates start-up/shutdown conditions by cycling the electrode potential between 1.00 and 1.50 V_{RHE} with a scan rate of 500 mV s^{-1}. The total treatment lasted for 9000 cycles as well. These protocols are based on the FCCJ recommendations.[32,33] The third protocol was designed as a combination of the above two protocols, cycling the electrode potential between 0.40 and 1.40 V_{RHE} with a scan rate of 1000 mV s^{-1}, and the total treatment lasted for 3600 cycles.[34] The fourth protocol was performed in current control alternating reductive and oxidative currents and was adapted from our previous stability study of bifunctional ORR−OER catalysts.[27] The measurements were conducted in the O_2-saturated electrolyte, maintaining a rotation of 1600 rpm. The current was stepped between 0 and −5 mA cm_{geo}^{-2} with a holding time of 1 s for each current, repeating this cycle for five times and followed by a current stepped to 1 mA cm_{geo}^{-2} for 1 s. The above procedure was regarded as a basic unit and this unit was repeated 300 times. Sketches of the different degradation protocols are summarized in Figure S2. The stability of catalysts was evaluated by the change in Pt ECSA that was recorded by CO stripping measurements before and after applying the ADT protocols.

For the electrochemical measurements in the GDE setup, 4 M $HClO_4$ was used as an electrolyte in the upper compartment above the Nafion membrane.[22] Prior to the electrochemical measurements, the electrode was purged with Ar gas, and the catalyst (Pt/C and Pt-Au/C nanocomposite) was cleaned by potential cycling between 0.15 and 1.20 V_{RHE} until a stable CV with the basic features of Pt was obtained (∼50 cycles). In the case of the Pt-Ir/C nanocomposite, the potential was held at 1.60 V_{RHE} for 8 min to activate Ir. After the activation procedure, the potential was cycled between 0.15 and 1.20 V_{RHE} for further cleaning of the catalyst surface. During the cleaning procedure, the resistance between the working and reference electrodes (∼10 Ω) was compensated to an effective value of around 1 Ω using the analog positive feedback scheme of the potentiostat.

The ORR activity and stability tests of the catalysts were performed with the same catalyst layer. For each catalyst, at least three measurements were repeated to obtain an acceptable reproducibility of the data. The automatized measurement procedure was applied using a macroscript of potentiostat software for each catalyst, i.e., CVs, CO stripping, ORR activity determination, ADT treatment, ORR activity determination, CO stripping, and CVs. The ORR activity before the ADT treatment is referred to as the beginning of treatment (BOT) activity, and the one measured after the ADT treatment is referred to as the end of treatment (EOT) activity. The measurement conditions during the CVs and CO stripping measurements were the same as those in the RDE measurements described above. To establish the ORR activity in a GDE setup, it is not ideal to sweep the electrode potential as done in RDE measurements as the high current densities lead to considerable iR drops even if a compensation is used. This does not only distort the potential but also the scan speed. Therefore, we adopted a protocol introduced by Pinaud et al.[20,21] using steady-state measurements in current control mode (galvanostatic). The current was stepwise increased, i.e., −1, −10, −100, −500, −1000, and −1500 mA cm_{geo}^{-2}, with a hold time of 30 s each. As for the ORR performance, the working electrode potential at each current density was averaged over the last 5 s of the current hold. Despite the fact that the iR was compensated to a value around 1 Ω, a post-measurement resistance correction is necessary for each current to obtain the correct electrode potential, i.e., the residual solution resistance was recorded online using the AC signal (5 kHz, 5 mV) and the formula of $E_{real} = E_{measured} - iR_u$ was applied to obtain the real working electrode potential. After the ADT treatment, the same ORR measurement protocol was employed once more to compare the ECSA loss with the ORR activity loss. The ADT treatment was adopted for the GDE setup[35] and consisted of a combination of simulating load cycling conditions and start-up/shutdown conditions. For this, the electrode potential was stepped 25 times between 0.60 and 1.00 V_{RHE} (the hold time for each potential was 3 s) followed by two potential cycles between 1.00 and 1.50 V_{RHE} at a scan rate of 500 mV s^{-1}. The treatment was performed in an O_2 atmosphere and repeated 20 times. A scheme of the degradation protocol is shown in Figure S2. The Pt surface area was determined by CO stripping measurements (as listed in the macroscript) before and after the degradation test to evaluate the stability of each catalyst.

Transmission Electron Microscopy (TEM) and Energy Dispersive X-ray Spectroscopy (EDX). A JEOL 2100 transmission electron microscope operated at 200 kV and equipped with an EDX detector was used for the TEM analysis. The samples before electrochemical treatment were prepared by suspending the catalyst powder in ethanol and dropping the mixture onto carbon-coated copper TEM grids (Quantifoil). The samples after the electrochemical treatments were collected from the rotating disk electrode (RDE) and dissolved in acetone for the preparation of TEM grids. Micrographs were recorded at different magnifications (at least ×300,000, ×400,000, and ×500,000) in at least three randomly selected areas. The composition of the samples was evaluated by determining the relative ratio of Ir/Pt and Au/Pt by EDX in at least three different randomly selected areas.

The composition of the supported nanocomposites on the gas diffusion layer (GDL) was evaluated with EDX as well, however recorded in a scanning electron microscope. For this, the GDL with the filtered nanocomposite on top was put on a sticky carbon tape, which was then put on an SEM metal holder. The analysis was conducted with a Zeiss Gemini 450 scanning electron microscope equipped with an Oxford

https://doi.org/10.1021/acscatal.1c01496
ACS Catal. 2021, 11, 7584−7594

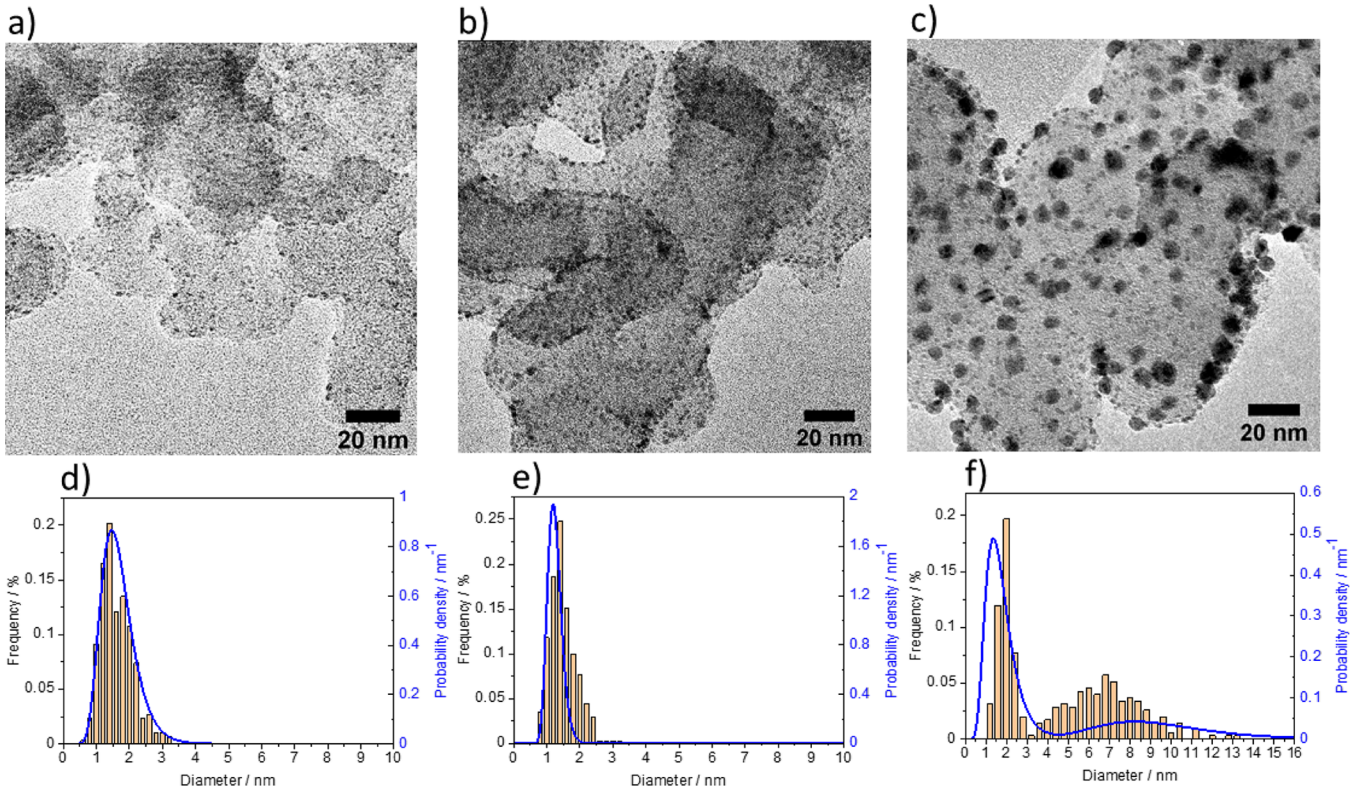

Figure 1. TEM micrographs and size distributions of the investigated catalysts. (a, d) Supported monometallic Pt NPs with a metal loading of 20 wt %, (b, e) supported nanocomposite with 20 wt % Pt NPs and 40 wt % Ir NPs (Pt-IrO_2/C), and (c, f) supported nanocomposite with 20 wt % Pt NPs and 40 wt % Au NPs (Pt-Au/C). The histograms are based on the statistical analysis of 350 individual particles of each as-prepared catalyst from TEM and the volume-weighted probability density of the particle size is derived from SAXS measurements.

Instruments Ultim Max 65 EDX detector at a voltage of 25 kV. Five independent areas on the GDL were selected for each sample. Software AZtec 4.2 (Oxford Instruments) was used to acquire the EDX spectra and to determine sample composition.

Small Angle X-ray Scattering (SAXS). SAXS measurements were performed at the Niels Bohr Institute at the University of Copenhagen with a SAXSLab instrument as previously detailed.[24,29,31] The instrument is equipped with a 100XL+ microfocus sealed X-ray tube from Rigaku, producing a photon beam with a wavelength of 1.54 Å. A 2D 300 K Pilatus detector (Dectris) was used to record the scattering patterns. The two-dimensional scattering data were azimuthally averaged, normalized by the incident radiation intensity, the sample exposure time, and the transmission, and then corrected for background and detector inhomogeneities using SAXGUI reduction software. The samples with NPs on the GDL were sealed between two mica windows and the background measurement was performed with the same GDL without any NPs. The radially averaged intensity $I(q)$ is expressed as a function of the scattering vector $q = 4\pi \cdot \sin(\theta)/\lambda$, where λ is the wavelength and 2θ is the scattering angle. A power law was used for fitting scattering data after background correction, and the scattering data were fitted with polydisperse spheres as a model and described by a volume-weighted log-normal distribution. The scattering data are fitted to the expression:

$$I(q) = A \cdot q^{-n} + C_1 \cdot \int P_{s1}(q, R) V_1(R) D_1(R) \mathrm{d}R + C_2 \cdot \int P_{s2}(q, R) V_2(R) D_2(R) \mathrm{d}R$$

where $A \cdot q^{-n}$ is the power law in which A and n are free parameters, C_1 and C_2 are scaling constants, P_{s1} and P_{s2} are the sphere form factors, V_1 and V_2 are the particle volumes, and D_1 and D_2 are the log-normal size distributions. The sphere form factor is expressed as:

$$P_s(q, R) = \left(3\frac{\sin(qR) - qR\cos(qR)}{(qR)^3}\right)^2$$

and the log-normal distribution is expressed as:

$$D(R) = \frac{1}{R\sigma\sqrt{2\pi}} e^{(-[\ln(R/R_0)]^2/2\sigma^2)}$$

The fitting was conducted with a home-written MATLAB code. The values obtained for free parameters in the model are listed in Table S1, and the corresponding fits are shown in Figure S3.

Ex Situ X-ray Absorption Spectroscopy (XAS). Ex situ X-ray absorption spectroscopy measurements at the Pt L_3 edge were carried out at the SuperXAS beamline at the Swiss Light Source (Villigen, Switzerland). The incident photon beam was provided by a 2.9 T superbend magnet and collimated by a Rh-coated mirror as 2.5 mrad. Subsequently, the X-ray beam was monochromatized by a Si (111) channel-cut Quick-EXAFS monochromator.[36] The beam was focused by a rhodium-coated toroidal mirror with a beam size of approximately 1.0

https://doi.org/10.1021/acscatal.1c01496
ACS Catal. 2021, 11, 7584−7594

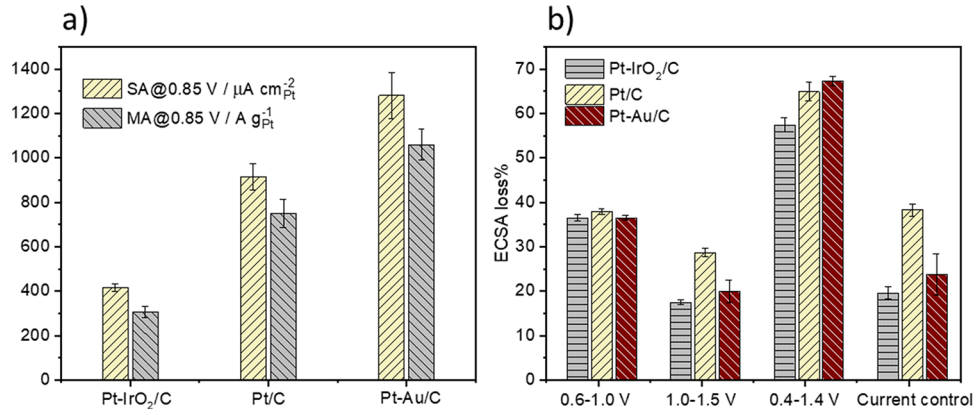

Figure 2. Comparison of the electrochemical performance of the supported monometallic Pt NPs and nanocomposites with the RDE approach. (a) ORR activity and (b) stability are evaluated with four different degradation protocols. The data of the ECSA loss for the current control protocol applied to Pt-IrO_2/C and Pt/C are taken from ref 27. The ORR activity is determined from the negative sweeping polarization curve at 0.85 V_{RHE}, and a scan rate of 50 mV s^{-1} and a rotation speed of 1600 rpm are applied in a potential region of 0.05−1.10 V_{RHE}. The error is the standard deviation from three independent measurements on each catalyst.

mm × 0.2 mm at the sample position. The Rh-coated mirrors also act to suppress higher-order harmonics. Each sample was measured in transmission geometry for 10 min in QEXAFS mode. The acquired data were then processed using ProQEXAFS, allowing for energy calibration, interpolation, and averaging.[37] The samples for ex situ X-ray absorption spectroscopy measurements were vacuum-filtered on GDL, and a higher nominal Pt loading of 400 μg cm_{geo}^{-2} was utilized to obtain a sufficient signal from ex situ X-ray absorption spectroscopy measurements.

RESULTS AND DISCUSSION

This study aims to investigate nanocomposite materials as potential electrocatalysts for the ORR. For this, we performed measurements with a conventional RDE setup as well as in a GDE setup: the latter is to obtain more applied conditions with realistic catalyst loading, a membrane catalyst interface, and realistic mass transport conditions. Two different nanocomposites were investigated in the current study, i.e., Pt-IrO_2/C and Pt-Au/C Pt. Pt/C (20 wt %) serves as a benchmark. To achieve comparative results, the active phase in all catalysts, i.e., the Pt loading, was kept at 20 wt %. The nominal loading of the second metal component was fixed at 40 wt %, i.e., the nanocomposite catalysts had the compositions of 20 wt % Pt + 40 wt % Ir and 20 wt % Pt + 40 wt % Au, respectively.

Representative TEM micrographs of the investigated catalysts are presented in Figure 1, together with histograms of their particle size distribution and the probability density of their particle size derived from SAXS measurements. The average particle sizes are also summarized in Tables S1 and S2. It can be seen that the Pt NPs in the Pt/C benchmark catalyst exhibit an average diameter of 1.7 ± 0.5 nm and are homogeneously distributed on the carbon support. By comparison, for the Pt-IrO_2/C nanocomposite, it is difficult to distinguish the Pt and Ir NPs. All NPs have a similar size, but it is apparent that the support is covered more densely. In the size histogram, no clearly distinguishable size populations are apparent. The best fit of the SAXS data, however, leads to two size populations with average sizes of 3.2 ± 1.7 and 1.2 ± 0.2 nm, which may be assigned to Pt and Ir NPs, respectively. However, the larger average size of the Pt NPs as compared to the Pt/C reference sample indicates that an unambiguous separation of the size population of the Pt and Ir NPs is not possible and that some smaller Pt NPs are accounted for in the "Ir size population". For the Pt-Au/C nanocomposite, the Pt and Au NPs are clearly distinguishable. Large and small NPs "co-decorate" the carbon support evenly with very few parts with agglomerated NPs. The two size populations are clearly distinguishable in the size histogram as well as the probability density function retrieved from SAXS. The small particles have an average size of 1.7 ± 0.7 nm and are thus assigned to Pt NPs. The average size of the larger particles is 9.4 ± 2.9 nm and is assigned to Au NPs. The satisfactory dispersion and full utilization of the active Pt NP phase are demonstrated by CO stripping measurements (see Figure S4). The results indicate comparable electrochemically accessible surface areas of Pt for each investigated catalyst independently if determined by the RDE measurements or in the GDE setup; only the Pt-IrO_2/C nanocomposite exhibits slightly lower ECSA values. Furthermore, it is seen that the ECSA values determined by the RDE measurements tend to be slightly larger than the ones determined in the GDE, which can be explained by the required addition of Nafion to the catalyst inks for the preparation of the GDE layers (without Nafion, no proton conduction is established in the catalyst layers); i.e., the Nafion partially blocks the Pt surface, leading to lower ECSA values.[38] Last but not least, the EDX analysis of the nanocomposites reveals that the obtained metal compositions with determined weight ratios of 2.03 and 1.95 for Ir/Pt and Au/Pt (Table S5), respectively, are close to the targeted value of 2. Thus, it can be concluded that the surfactant-free colloidal approach indeed allows for an accurate preparation of different nanocomposite catalysts.[27]

It is widely accepted that IrO_2 is not a good catalyst for the ORR. Au on its own also performs badly for the ORR in acidic conditions, with H_2O_2 or HO_2^- being the final product of the reaction.[39−41] However, in previous studies, it was reported that Pt-Au core−shell structures,[42] Pt-Au alloy structures,[15] and Au-modified Pt structures[43] can not only increase the ORR rate but also the stability. We evaluated the ORR performance of the investigated catalysts both in specific activity (SA) and mass activity (MA), i.e., normalized by the Pt surface area and Pt mass, respectively. The polarization curves and Tafel plots (from the positive scan direction) are shown in the Supporting Information (Figure S5). It is known that the

https://doi.org/10.1021/acscatal.1c01496
ACS Catal. 2021, 11, 7584−7594

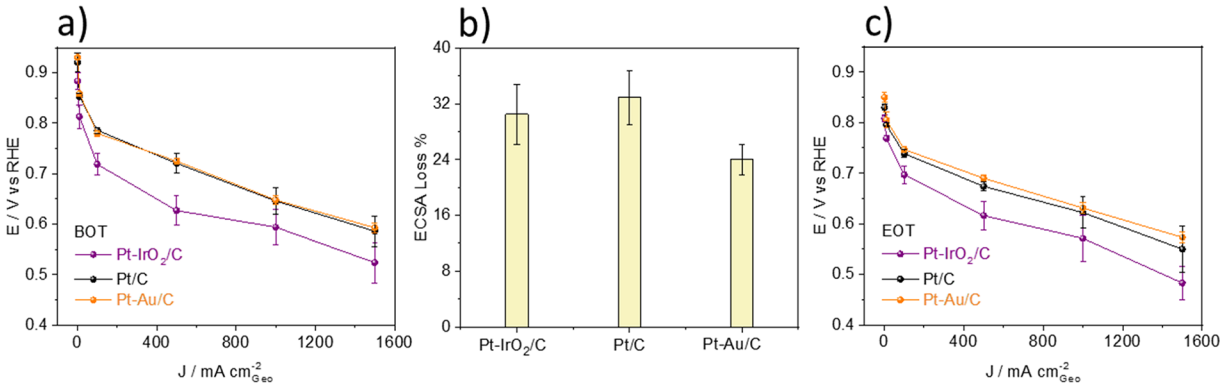

Figure 3. Comparison of the electrochemical performance of the supported monometallic Pt NPs and nanocomposites with the GDE approach. (a) ORR activity before degradation test, (b) loss in the available Pt surface area, and (c) ORR activity after degradation test. The ORR activity is determined with current control mode, and six constant currents are applied on each measurement step for activity evaluation. The stability is determined in an O_2 atmosphere with a mixed degradation protocol of potential stepping between 0.60 and 1.00 V_{RHE} followed by potential cycling between 1.00 and 1.50 V_{RHE}, and the whole procedure is repeated 20 times. The error is the standard deviation from three independent measurements on each catalyst. BOT: before test; EOT: end of test.

investigation of the ORR performance under transient conditions leads to an overestimation of the activity in comparison to the performance under steady-state conditions.[44−47] This leads to a hysteresis between the negative- and positive-going scan directions[48] and is also reflected in the higher ORR rates determined by the RDE measurements as compared to the measurements in the GDE setup. To alleviate this difference, here, we determined the ORR activities from the RDE measurements of the polarization curves recorded in the negative scan direction instead of the typically chosen positive scan direction. In Figure 2, the performance of the different catalysts determined in RDE measurements is summarized. It is seen that the activity trends for SA and MA are identical. The ORR activity is decreased by mixing Ir NPs to a Pt/C catalyst in agreement with our previous study,[27] while the same amount of Au NPs clearly enhances the ORR performance. For Pt-IrO_2/C, a SA of 416 ± 16 $\mu A\ cm_{Pt}^{-2}$ and an MA activity of 307 ± 26 A g_{Pt}^{-1} were determined (see also Table S3), which are less than half of the Pt/C benchmark activities, i.e., 915 ± 58 $\mu A\ cm_{Pt}^{-2}$ and 750 ± 63 A g_{Pt}^{-1}. On the contrary, for Pt-Au/C, a SA of 1280 ± 102 $\mu A\ cm_{Pt}^{-2}$ and an MA of 1060 ± 71 A g_{Pt}^{-1} were determined, i.e., around 1.4 times higher than for the benchmark catalyst. The ORR activity of Pt-based catalysts is in general considered to be correlated to the adsorption energies of the O*, OH*, and OOH* intermediates,[49] here referred to as oxophilicity. In agreement with our previous study,[27] we therefore assume that the reduced ORR activity of the Pt-IrO_2/C nanocomposite can be ascribed to the more oxophilic nature of Pt NPs adjacent to IrO_2 particles. Concurrently, the improved activity of Pt-Au/C suggests that the electronic properties of Pt NPs are affected in a different way (i.e., less oxophilic) by the adjacent Au NPs. To test this hypothesis, we performed ex situ XANES measurement determining the white line (WL) intensity at the Pt L_3 edge, which corresponds closely to the density of unoccupied states and thus the oxidation state of the Pt.[50] As shown in Figure S6, the Pt-Au/C nanocomposite indeed exhibits lower WL intensity than the Pt/C benchmark, indicating a lower oxophilicity. As a result, the active Pt surface sites in the Pt-Au/C nanocomposite are less blocked by the ORR intermediates than in the case on the Pt/C benchmark, leading to an improved ORR activity. It should be mentioned though that the ex situ-determined WL intensity of the non-activated Pt-IrO_2/C nanocomposite is comparable to the one of the Pt/C benchmark (Figure S6) and that for a more detailed study, in situ XANES is required.

The trend in stability observed in the RDE measurements is less straightforward and depends on the applied ADT protocol. Based on the literature and our previous work,[27,51] one might expect an improvement in stability when adding Ir NPs to the Pt/C benchmark catalyst. Such improvement is indeed observed when choosing an ADT protocol that applies highly oxidizing conditions (see Figure 2). However, for simulated load cycle conditions, no effect on the stability is detected. Furthermore, the effect in cycling stability (cycling the electrode potential between 0.40 and 1.40 V_{RHE} with a scan rate of 1000 mV s^{-1}) is only small. The findings for the Pt-Au/C nanocomposite are similar, i.e., a general improved stability is observed except that the cycling stability seems to be even slightly lower than for the Pt/C benchmark. The largest improvement in stability for the Pt-Au/C nanocomposite is an improvement by 38% as compared to the benchmark in the current control ADT (see also Figure 2b and Table S4). In contrast to the Pt-IrO_2/C nanocomposite, the Au/Pt ratio is not affected by the ADT treatment as shown by EDX analysis (see Table S5). The analysis of the TEM micrographs of the degraded catalysts, as displayed in Figure S7, clearly indicates particle growth, in particular, in the Pt/C benchmark catalyst.

Particle growth is normally associated with particle migration and coalescence and/or electrochemical Ostwald ripening.[52] However, it is difficult to distinguish between the two degradation mechanisms. In addition, carbon support oxidation occurs in cycling between oxidizing and reducing potentials,[53] which leads to Pt area loss due to particle loss. In Figure S7c,g, a lower NP density on the support might indicate particle detachment, but it is difficult to exactly quantify the extent with conventional TEM.

As discussed in Introduction, the RDE technique is known for its simplicity and is widely used for fundamental research. The liquid electrolyte environment and low reactant mass transport however limit the extrapolation of the results to real devices.[54] Measurements in GDE setups combine the advantages of RDE with more realistic conditions close to the ones in membrane electrode assemblies (MEAs). Therefore, we compared the results of the RDE measurements to investigations performed in our recently developed GDE setup.

https://doi.org/10.1021/acscatal.1c01496
ACS Catal. 2021, 11, 7584−7594

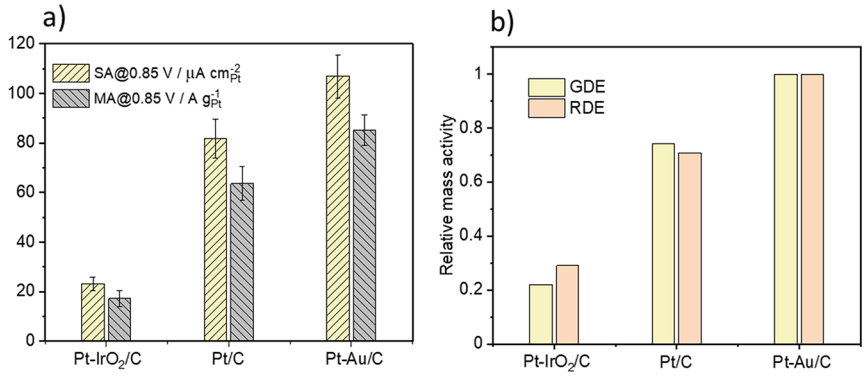

Figure 4. (a) Comparison of the ORR activity at 0.85 V_{RHE} determined with the GDE approach and (b) comparison of the relative mass activity determined with GDE and RDE measurements. The SA and MA values at 0.85 V_{RHE} from the GDE measurement are before degradation test and are extracted from three independent measurements. For the relative mass activities, the activities are normalized to the one of Pt-Au/C. The activity determined by the RDE approach at 0.85 V_{RHE} is determined from the negative-going polarization curve.

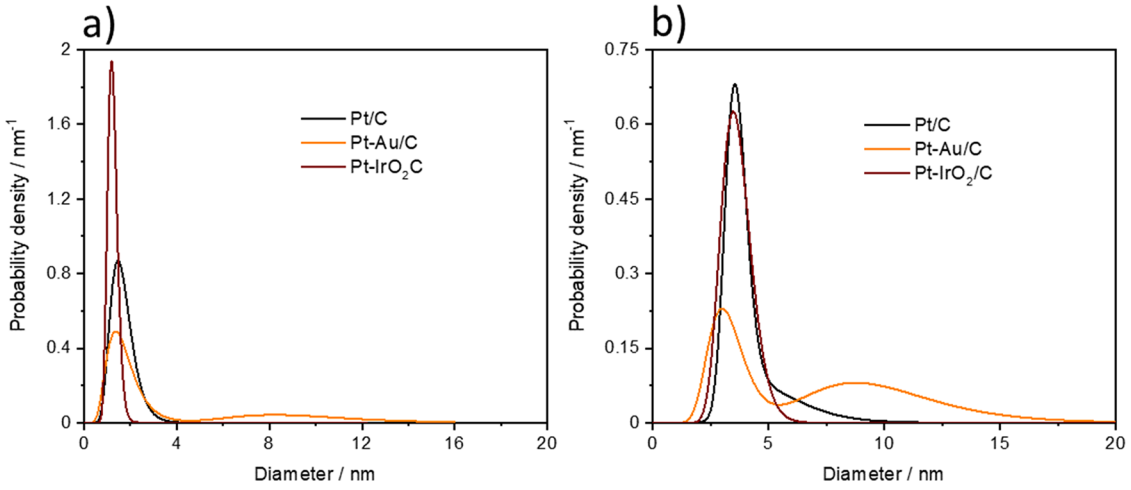

Figure 5. Particle size distributions, plotted as the volume-weighted probability density derived from SAXS analysis, of the investigated catalysts: (a) before and (b) after degradation test.

All catalyst layers were prepared with a realistic Pt loading of 208 μg cm_{geo}^{-2} on the GDL and the catalyst composition was confirmed by EDX (the obtained metal compositions in wt % were Ir/Pt = 2.10 and Au/Pt = 1.90 for Pt-IrO_2/C and Pt-Au/C; see also Table S5). The electrochemically active Pt area of each catalyst layer was determined with CO stripping measurements and representative CO oxidation plots shown in Figure S4. It can be seen that the electrochemically active Pt area in all catalyst layers is similar and the performance of the different catalysts can be compared to each other.

The BOT ORR activity data are presented in Figure 3a, and the respective Tafel plots (estimation) are shown in Figure S8, demonstrating that the Tafel slopes are basically consistent with the ones obtained in the RDE measurement. From the GDE data, it is apparent that in agreement with the RDE data and as compared to the Pt/C benchmark, the Pt-IrO_2/C nanocomposite indeed exhibits a substantially inhibited ORR performance over a wide range of current densities up to 1500 mA cm_{geo}^{-2}. By comparison, the activity improvement for the Pt-Au/C nanocomposite is limited to very low current densities (−1 and −10 mA cm_{geo}^{-2}), but at higher current densities, i.e., ≥100 mA cm_{geo}^{-2}, no improvement as compared to the Pt/C benchmark is seen. Nevertheless, in Figure 4, it is demonstrated that at low current densities, i.e., high electrode potentials (here, 0.85 V_{RHE}), the activity trends observed in the RDE and GDE are indeed comparable and consistent, although the absolute values differ.

The comparison between RDE and GDE therefore exemplifies the importance of performing measurements under realistic conditions as the improvement in kinetic ORR activity seen for the Pt-Au/C nanocomposite in the RDE measurements can be confirmed in the GDE measurements, but at the same time, it is highly unlikely that these improvements exhibit any relevance for conditions in applications.

By performing the ADT and comparing the loss in Pt ECSA, the observed trends in stability are similar to the ones observed in the RDE measurements (the ADT consisted of a combination of load-cycle and start-stop simulations). However, one needs to keep in mind that the conditions in an aqueous electrolyte environment are different from those in a membrane electrolyte environment. For example, Ehelebe et al. recently reported that while Pt ions can be transported away from a catalyst layer, the Pt dissolution rates in GDE experiments are considerably lower than in an aqueous electrolyte environment; placing a membrane onto the catalyst layer reduced the dissolution rate even further.[25] In our study, both the Pt-IrO_2/C and Pt-Au/C nanocomposites exhibit improved stability as compared to the Pt/C benchmark (Figure 3b). A small difference exists, however, i.e., the Pt-Au/

https://doi.org/10.1021/acscatal.1c01496
ACS Catal. 2021, 11, 7584−7594

C nanocomposite appears to be slightly more stable than the Pt-IrO_2/C nanocomposite. Interestingly, the improved stability of the Pt-Au/C nanocomposite (as compared to Pt/C) results in a distinguishable improvement in the EOT ORR activity over the whole investigated current density range (see Figure 3c). By comparison, the improved stability of the Pt-IrO_2/C nanocomposite does not lead to any improved EOT ORR activity as compared to Pt/C.

In addition to more realistic reaction conditions, the GDE investigations also allow an ex situ analysis of the used (degraded) catalyst layers with SAXS.[24,29] Comparing the particle size distributions derived from SAXS at BOT and EOT indicates that the improved stability and ORR activity of the Pt-Au/C nanocomposite can be assigned to a reduced Pt particle growth (see Figure 5 and Table S2). A reduced particle growth in the Pt-Au/C nanocomposite as compared to the Pt/C benchmark is consistent with the lower loss in Pt ECSA and the less oxophilic nature of the Pt NPs adjacent to the Au NPs as discussed in Results and Discussion (RDE measurement part). Furthermore, a reduced particle growth is consistent with a reduced loss in oxygen transfer resistance at high current densities.[12] The weight ratio between Au and Pt therefore only changes slightly, i.e., from 1.90 to 1.80 (Table S5), indicating a low amount of Pt dissolution (or Pt and Au dissolve in equal amounts). Interestingly, in the case of the Pt-IrO_2/C nanocomposite, the improved stability is at the cost of a change in the Ir/Pt weight ratio, which significantly decreases to a value of 0.99 (Table S5), indicating severe Ir dissolution during the ADT.

CONCLUSIONS

In our study, we compare the ORR performance (activity and stability) of two nanocomposite catalysts, i.e., Pt-IrO_2/C and Pt-Au/C, to a Pt/C benchmark. The Pt loading, Pt particle size, and therefore the Pt ECSA in all catalysts could be kept constant. By comparing the performance with the state-of-the-art RDE approach, it is concluded that both the introduction of IrO_2 and Au NPs to a Pt/C catalyst alleviates the degradation of the Pt NPs, the active phase for the ORR. In the case of IrO_2, however, the improvement in stability is at the expense of a decrease in ORR activity. By comparison, Au NPs seem to boost the stability and ORR activity of the Pt NPs likewise. Under conditions more closely comparable to MEAs, i.e., in a GDE setup, it is seen that the performance improvement of the Pt-Au/C nanocomposite is limited to very low current densities and cannot be sustained under high current density conditions most relevant for applications. Nevertheless, the Pt-Au/C nanocomposite offers a significant advantage that might be more realistically transferred to applications, i.e., its improved stability. The GDE measurements indicate that, ultimately, the improved stability might also lead to an improved ORR performance over the lifetime of the fuel cell. By comparison, the results indicate that stabilization of fuel catalysts by IrO_2 might not be a promising approach as the stability improvement is at the expense of Ir dissolution and is therefore more likely a short-term effect.

ASSOCIATED CONTENT

Supporting Information

The Supporting Information is available free of charge at https://pubs.acs.org/doi/10.1021/acscatal.1c01496.

CVs, CO stripping curves, SAXS fits, Tafel plots, XANES spectra, degradation protocols, tables of particle size analysis from SAXS measurement, specific and mass activities for ORR from RDE and GDE approaches, ECSA values at the beginning and end of the ADTs, and summary of the EDX data and TEM micrographs of the degraded catalyst with different protocols (PDF)

AUTHOR INFORMATION

Corresponding Author

Matthias Arenz − *Department of Chemistry, Biochemistry and Pharmaceutical Sciences, University of Bern, Bern 3012, Switzerland;* orcid.org/0000-0001-9765-4315; Email: matthias.arenz@dcb.unibe.ch

Authors

Jia Du − *Department of Chemistry, Biochemistry and Pharmaceutical Sciences, University of Bern, Bern 3012, Switzerland;* orcid.org/0000-0002-2387-1912

Jonathan Quinson − *Department of Chemistry, University of Copenhagen, Copenhagen Ø 2100, Denmark;* orcid.org/0000-0002-9374-9330

Alessandro Zana − *Department of Chemistry, Biochemistry and Pharmaceutical Sciences, University of Bern, Bern 3012, Switzerland*

Complete contact information is available at: https://pubs.acs.org/10.1021/acscatal.1c01496

Notes

The authors declare no competing financial interest.

ACKNOWLEDGMENTS

This work was supported by the Swiss National Science Foundation (SNSF) via the project no. 200021_184742. J.D. acknowledges funding from the China Scholarship Council (CSC). S. B. Simonsen and L. Theil Kuhn, Technical University of Denmark, are thanked for the access to TEM. The authors are thankful to The Niels Bohr Institute, Universtity of Copenhagen, for the access to SAXS equipment and, in particular, J. K. K. Kirkensgaard. The authors thank Adam Clark from the SuperXAS beamline (X10DA) of the Swiss Light Source (SLS) for measuring and analyzing the XAS samples.

REFERENCES

(1) Sievers, G. W.; Jensen, A. W.; Quinson, J.; Zana, A.; Bizzotto, F.; Oezaslan, M.; Dworzak, A.; Kirkensgaard, J. K.; Smitshuysen, T. E. L.; Kadkhodazadeh, S.; Juelsholt, M.; Jensen, K. M. Ø.; Anklam, K.; Wan, H.; Schäfer, J.; Čépe, K.; Escudero-Escribano, M.; Rossmeisl, J.; Quade, A.; Brüser, V.; Arenz, M. Self-Supported Pt−CoO Networks Combining High Specific Activity with High Surface Area for Oxygen Reduction. *Nat. Mater.* **2021**, 208.

(2) Stamenkovic, V. R.; Mun, B. S.; Arenz, M.; Mayrhofer, K. J. J.; Lucas, C. A.; Wang, G.; Ross, P. N.; Markovic, N. M. Trends in Electrocatalysis on Extended and Nanoscale Pt-Bimetallic Alloy Surfaces. *Nat. Mater.* **2007**, *6*, 241.

(3) Chattot, R.; Le Bacq, O.; Beermann, V.; Kühl, S.; Herranz, J.; Henning, S.; Kühn, L.; Asset, T.; Guétaz, L.; Renou, G.; Drnec, J.; Bordet, P.; Pasturel, A.; Eychmüller, A.; Schmidt, T. J.; Strasser, P.; Dubau, L.; Maillard, F. Surface Distortion as a Unifying Concept and Descriptor in Oxygen Reduction Reaction Electrocatalysis. *Nat. Mater.* **2018**, 827.

(4) Han, B.; Carlton, C. E.; Kongkanand, A.; Kukreja, R. S.; Theobald, B. R.; Gan, L.; O'Malley, R.; Strasser, P.; Wagner, F. T.;

Shao-Horn, Y. Record Activity and Stability of Dealloyed Bimetallic Catalysts for Proton Exchange Membrane Fuel Cells. *Energy Environ. Sci.* **2015**, *8*, 258−266.
(5) Stephens, I. E. L.; Bondarenko, A. S.; Grønbjerg, U.; Rossmeisl, J.; Chorkendorff, I. Understanding the Electrocatalysis of Oxygen Reduction on Platinum and Its Alloys. *Energy Environ. Sci.* **2012**, 6744.
(6) Mayrhofer, K. J. J.; Hartl, K.; Juhart, V.; Arenz, M. Degradation of Carbon-Supported Pt Bimetallic Nanoparticles by Surface Segregation. *J. Am. Chem. Soc.* **2009**, *131*, 16348.
(7) Batchelor, T. A. A.; Pedersen, J. K.; Winther, S. H.; Castelli, I. E.; Jacobsen, K. W.; Rossmeisl, J. High-Entropy Alloys as a Discovery Platform for Electrocatalysis. *Joule* **2019**, *3*, 834−845.
(8) Nesselberger, M.; Roefzaad, M.; Fayçal Hamou, R.; Ulrich Biedermann, P.; Schweinberger, F. F.; Kunz, S.; Schloegl, K.; Wiberg, G. K. H.; Ashton, S.; Heiz, U.; Mayrhofer, K. J. J.; Arenz, M. The Effect of Particle Proximity on the Oxygen Reduction Rate of Size-Selected Platinum Clusters. *Nat. Mater.* **2013**, *12*, 919.
(9) Speder, J.; Altmann, L.; Bäumer, M.; Kirkensgaard, J. J. K.; Mortensen, K.; Arenz, M. The Particle Proximity Effect: From Model to High Surface Area Fuel Cell Catalysts. *RSC Adv.* **2014**, *4*, 14971.
(10) Huang, J.; Zhang, J.; Eikerling, M. H. Particle Proximity Effect in Nanoparticle Electrocatalysis: Surface Charging and Electrostatic Interactions. *J. Phys. Chem. C* **2017**, *121*, 4806−4815.
(11) Liu, H.; Mun, B. S.; Thornton, G.; Isaacs, S. R.; Shon, Y.-S.; Ogletree, D. F.; Salmeron, M. Electronic Structure of Ensembles of Gold Nanoparticles: Size and Proximity Effects. *Phys. Rev. B: Condens. Matter Mater. Phys.* **2005**, *72*, 155430−155435.
(12) Kongkanand, A.; Mathias, M. F. The Priority and Challenge of High-Power Performance of Low-Platinum Proton-Exchange Membrane Fuel Cells. *J. Phys. Chem. Lett.* **2016**, *7*, 1127−1137.
(13) Kocha, S. S.; Shinozaki, K.; Zack, J. W.; Myers, D. J.; Kariuki, N. N.; Nowicki, T.; Stamenkovic, V.; Kang, Y.; Li, D.; Papageorgopoulos, D. Best Practices and Testing Protocols for Benchmarking ORR Activities of Fuel Cell Electrocatalysts Using Rotating Disk Electrode. *Electrocatalysis* **2017**, *8*, 366−374.
(14) Gasteiger, H. A.; Kocha, S. S.; Sompalli, B.; Wagner, F. T. Activity Benchmarks and Requirements for Pt, Pt-Alloy, and Non-Pt Oxygen Reduction Catalysts for PEMFCs. *Appl. Catal., B* **2005**, 9.
(15) Lopes, P. P.; Li, D.; Lv, H.; Wang, C.; Tripkovic, D.; Zhu, Y.; Schimmenti, R.; Daimon, H.; Kang, Y.; Snyder, J.; Becknell, N.; More, K. L.; Strmcnik, D.; Markovic, N. M.; Mavrikakis, M.; Stamenkovic, V. R. Eliminating Dissolution of Platinum-Based Electrocatalysts at the Atomic Scale. *Nat. Mater.* **2020**, 1207.
(16) Ioroi, T.; Yasuda, K. Platinum-Iridium Alloys as Oxygen Reduction Electrocatalysts for Polymer Electrolyte Fuel Cells. *ECS Trans.* **2006**, *1*, 129−136.
(17) Inaba, M.; Quinson, J.; Arenz, M. PH Matters: The Influence of the Catalyst Ink on the Oxygen Reduction Activity Determined in Thin Film Rotating Disk Electrode Measurements. *J. Power Sources* **2017**, *353*, 19−27.
(18) Inaba, M.; Quinson, J.; Bucher, J. R.; Arenz, M. On the Preparation and Testing of Fuel Cell Catalysts Using the Thin Film Rotating Disk Electrode Method. *J. Visualized Exp.* **2018**, *2018*, 57105.
(19) Wiberg, G. K. H.; Fleige, M.; Arenz, M. Gas Diffusion Electrode Setup for Catalyst Testing in Concentrated Phosphoric Acid at Elevated Temperatures. *Rev. Sci. Instrum.* **2015**, *86*, No. 024102.
(20) Pinaud, B. A.; Bonakdarpour, A.; Daniel, L.; Sharman, J.; Wilkinson, D. P. Key Considerations for High Current Fuel Cell Catalyst Testing in an Electrochemical Half-Cell. *J. Electrochem. Soc.* **2017**, F321.
(21) Ehelebe, K.; Seeberger, D.; Paul, M. T. Y.; Thiele, S.; Mayrhofer, K. J. J.; Cherevko, S. Evaluating Electrocatalysts at Relevant Currents in a Half-Cell: The Impact of Pt Loading on Oxygen Reduction Reaction. *J. Electrochem. Soc.* **2019**, *166*, F1259−F1268.
(22) Inaba, M.; Jensen, A. W.; Sievers, G. W.; Escudero-Escribano, M.; Zana, A.; Arenz, M. Benchmarking High Surface Area Electrocatalysts in a Gas Diffusion Electrode: Measurement of Oxygen Reduction Activities under Realistic Conditions. *Energy Environ. Sci.* **2018**, *11*, 988−994.
(23) Sievers, G. W.; Jensen, A. W.; Brüser, V.; Arenz, M.; Escudero-Escribano, M. Sputtered Platinum Thin-Films for Oxygen Reduction in Gas Diffusion Electrodes: A Model System for Studies under Realistic Reaction Conditions. *Surfaces* **2019**, *2*, 336−348.
(24) Schröder, J.; Quinson, J.; Mathiesen, J. K.; Kirkensgaard, J. J. K.; Alinejad, S.; Mints, V. A.; Jensen, K. M.; Arenz, M. A New Approach to Probe the Degradation of Fuel Cell Catalysts under Realistic Conditions: Combining Tests in a Gas Diffusion Electrode Setup with Small Angle X-Ray Scattering. *J. Electrochem. Soc.* **2020**, *167*, 134515.
(25) Ehelebe, K.; Knöppel, J.; Bierling, M.; Mayerhöfer, B.; Böhm, T.; Kulyk, N.; Thiele, S.; Mayrhofer, K. J. J.; Cherevko, S. Platinum Dissolution in Realistic Fuel Cell Catalyst Layers. *Angew. Chem., Int. Ed.* **2021**, 8882.
(26) Quinson, J.; Kunz, S.; Arenz, M. Beyond Active Site Design: A Surfactant-Free Toolbox Approach for Optimized Supported Nanoparticle Catalysts. *ChemCatChem* **2021**, *13*, 1692.
(27) Du, J.; Quinson, J.; Zhang, D.; Bizzotto, F.; Zana, A.; Arenz, M. Bifunctional Pt-IrO_2 Catalysts for the Oxygen Evolution and Oxygen Reduction Reactions: Alloy Nanoparticles versus Nanocomposite Catalysts. *ACS Catal.* **2021**, *11*, 820−828.
(28) Zhang, Z.; Xin, L.; Qi, J.; Wang, Z.; Li, W. Selective Electro-Conversion of Glycerol to Glycolate on Carbon Nanotube Supported Gold Catalyst. *Green Chem.* **2012**, *14*, 2150−2152.
(29) Alinejad, S.; Quinson, J.; Schröder, J.; Kirkensgaard, J. J. K.; Arenz, M. Carbon-Supported Platinum Electrocatalysts Probed in a Gas Diffusion Setup with Alkaline Environment: How Particle Size and Mesoscopic Environment Influence the Degradation Mechanism. *ACS Catal.* **2020**, *10*, 13040.
(30) Yarlagadda, V.; McKinney, S. E.; Keary, C. L.; Thompson, L.; Zulevi, B.; Kongkanand, A. Preparation of PEMFC Electrodes from Milligram-Amounts of Catalyst Powder. *J. Electrochem. Soc.* **2017**, *164*, F845−F849.
(31) Bizzotto, F.; Quinson, J.; Zana, A.; Kirkensgaard, J. J. K.; Dworzak, A.; Oezaslan, M.; Arenz, M. Ir Nanoparticles with Ultrahigh Dispersion as Oxygen Evolution Reaction (OER) Catalysts: Synthesis and Activity Benchmarking. *Catal. Sci. Technol.* **2019**, 6345−6356.
(32) Ohma, A.; Shinohara, K.; Iiyama, A.; Yoshida, T.; Daimaru, A. Membrane and Catalyst Performance Targets for Automotive Fuel Cells by FCCJ Membrane, Catalyst, MEA WG. *ECS Trans.* **2011**, *41*, 775−784.
(33) Pizzutilo, E.; Geiger, S.; Grote, J.-P.; Mingers, A.; Mayrhofer, K. J. J.; Arenz, M.; Cherevko, S. On the Need of Improved Accelerated Degradation Protocols (ADPs): Examination of Platinum Dissolution and Carbon Corrosion in Half-Cell Tests. *J. Electrochem. Soc.* **2016**, *163*, F1510.
(34) Mayrhofer, K. J. J.; Meier, J. C.; Ashton, S. J.; Wiberg, G. K. H.; Kraus, F.; Hanzlik, M.; Arenz, M. Fuel Cell Catalyst Degradation on the Nanoscale. *Electrochem. Commun.* **2008**, *10*, 1144−1147.
(35) Alinejad, S.; Inaba, M.; Schröder, J.; Du, J.; Quinson, J.; Zana, A.; Arenz, M. Testing Fuel Cell Catalysts under More Realistic Reaction Conditions: Accelerated Stress Tests in a Gas Diffusion Electrode Setup. *J. Phys.: Energy* **2020**, *2*, No. 024003.
(36) Müller, O.; Nachtegaal, M.; Just, J.; Lützenkirchen-Hecht, D.; Frahm, R. Quick-EXAFS Setup at the SuperXAS Beamline for *in Situ* X-Ray Absorption Spectroscopy with 10 ms Time Resolution. *J. Synchrotron Radiat.* **2016**, *23*, 260−266.
(37) Clark, A. H.; Imbao, J.; Frahm, R.; Nachtegaal, M. *ProQEXAFS*: A Highly Optimized Parallelized Rapid Processing Software for QEXAFS Data. *J. Synchrotron Radiat.* **2020**, *27*, 551−557.
(38) Kodama, K.; Shinohara, A.; Hasegawa, N.; Shinozaki, K.; Jinnouchi, R.; Suzuki, T.; Hatanaka, T.; Morimoto, Y. Catalyst Poisoning Property of Sulfonimide Acid Ionomer on Pt (111) Surface. *J. Electrochem. Soc.* **2014**, *161*, F649−F652.

https://doi.org/10.1021/acscatal.1c01496
ACS Catal. 2021, 11, 7584−7594

(39) Jusys, Z.; Behm, R. J. The Effect of Anions and PH on the Activity and Selectivity of an Annealed Polycrystalline Au Film Electrode in the Oxygen Reduction Reaction-Revisited. *ChemPhysChem* **2019**, 3276.
(40) Ohta, N.; Nomura, K.; Yagi, I. Adsorption and Electroreduction of Oxygen on Gold in Acidic Media: In Situ Spectroscopic Identification of Adsorbed Molecular Oxygen and Hydrogen Superoxide. *J. Phys. Chem. C* **2012**, 14390.
(41) Wang, Y.; Laborda, E.; Ward, K. R.; Tschulik, K.; Compton, R. G. A Kinetic Study of Oxygen Reduction Reaction and Characterization on Electrodeposited Gold Nanoparticles of Diameter between 17 Nm and 40 Nm in 0.5 M Sulfuric Acid. *Nanoscale* **2013**, *5*, 9699.
(42) Chung, D. Y.; Park, S.; Lee, H.; Kim, H.; Chung, Y.-H.; Yoo, J. M.; Ahn, D.; Yu, S.-H.; Lee, K.-S.; Ahmadi, M.; Ju, H.; Abruña, H. D.; Yoo, S. J.; Mun, B. S.; Sung, Y.-E. Activity−Stability Relationship in Au@Pt Nanoparticles for Electrocatalysis. *ACS Energy Lett.* **2020**, 2827−2834.
(43) Kodama, K.; Jinnouchi, R.; Takahashi, N.; Murata, H.; Morimoto, Y. Activities and Stabilities of Au-Modified Stepped-Pt Single-Crystal Electrodes as Model Cathode Catalysts in Polymer Electrolyte Fuel Cells. *J. Am. Chem. Soc.* **2016**, *138*, 4194−4200.
(44) Uribe, F. A.; Zawodzinski, T. A., Jr. A Study of Polymer Electrolyte Fuel Cell Performance at High Voltages. Dependence on Cathode Catalyst Layer Composition and on Voltage Conditioning. *Electrochim. Acta* **2002**, *47*, 3799−3806.
(45) Pašti, I. A.; Gavrilov, N. M.; Mentus, S. V. Electrocatalytic Behavior of Pt/WO_3 Composite Layers Formed Potentiodynamically on Tungsten Surfaces. *Int. J. Electrochem. Sci.* **2017**, *12*, 5772−5791.
(46) Wiberg, G. K. H.; Arenz, M. Establishing the Potential Dependent Equilibrium Oxide Coverage on Platinum in Alkaline Solution and Its Influence on the Oxygen Reduction. *J. Power Sources* **2012**, *217*, 262.
(47) Hodnik, N.; Baldizzone, C.; Cherevko, S.; Zeradjanin, A.; Mayrhofer, K. J. J. The Effect of the Voltage Scan Rate on the Determination of the Oxygen Reduction Activity of Pt/C Fuel Cell Catalyst. *Electrocatalysis* **2015**, *6*, 237−241.
(48) Shinozaki, K.; Zack, J. W.; Richards, R. M.; Pivovar, B. S.; Kocha, S. S. Oxygen Reduction Reaction Measurements on Platinum Electrocatalysts Utilizing Rotating Disk Electrode Technique: I. Impact of Impurities, Measurement Protocols and Applied Corrections. *J. Electrochem. Soc.* **2015**, *162*, F1144.
(49) Nørskov, J. K.; Rossmeisl, J.; Logadottir, A.; Lindqvist, L.; Kitchin, J. R.; Bligaard, T.; Jónsson, H. Origin of the Overpotential for Oxygen Reduction at a Fuel-Cell Cathode. *J. Phys. Chem. B* **2004**, 17886.
(50) Teliska, M.; Murthi, V. S.; Mukerjee, S.; Ramaker, D. E. Correlation of Water Activation, Surface Properties, and Oxygen Reduction Reactivity of Supported Pt−M/C Bimetallic Electrocatalysts Using XAS. *J. Electrochem. Soc.* **2005**, *152*, A2159.
(51) Crowtz, T. C.; Dahn, J. R. Screening Bifunctional Pt Based NSTF Catalysts for Durability with the Rotating Disk Electrode: The Effect of Ir and Ru. *J. Electrochem. Soc.* **2018**, F854.
(52) Schlögl, K.; Hanzlik, M.; Arenz, M. Comparative IL-TEM Study Concerning the Degradation of Carbon Supported Pt-Based Electrocatalysts. *J. Electrochem. Soc.* **2012**, B677.
(53) Ashton, S. J.; Arenz, M. A DEMS Study on the Electrochemical Oxidation of a High Surface Area Carbon Black. *Electrochem. Commun.* **2011**, *13*, 1473.
(54) Kodama, K.; Nagai, T.; Kuwaki, A.; Jinnouchi, R.; Morimoto, Y. Challenges in Applying Highly Active Pt-Based Nanostructured Catalysts for Oxygen Reduction Reactions to Fuel Cell Vehicles. *Nat. Nanotechnol.* **2021**, 140.

https://doi.org/10.1021/acscatal.1c01496
ACS Catal. 2021, 11, 7584−7594

Supporting Information of Manuscript III

Supporting Information

Elucidating Pt-Based Nanocomposite Catalysts for the Oxygen Reduction Reaction in Rotating Disk Electrode and Gas Diffusion Electrode Measurements

Jia Du[a], Jonathan Quinson[b], Alessandro Zana[a], Matthias Arenz[a] *

[a] Department of Chemistry, Biochemistry and Pharmaceutical Sciences, University of Bern, Freiestrasse 3, 3012 Bern, Switzerland

[b] Department of Chemistry, University of Copenhagen, Universitetsparken 5, 2100 Copenhagen Ø, Denmark

* corresponding author: matthias.arenz@dcb.unibe.ch

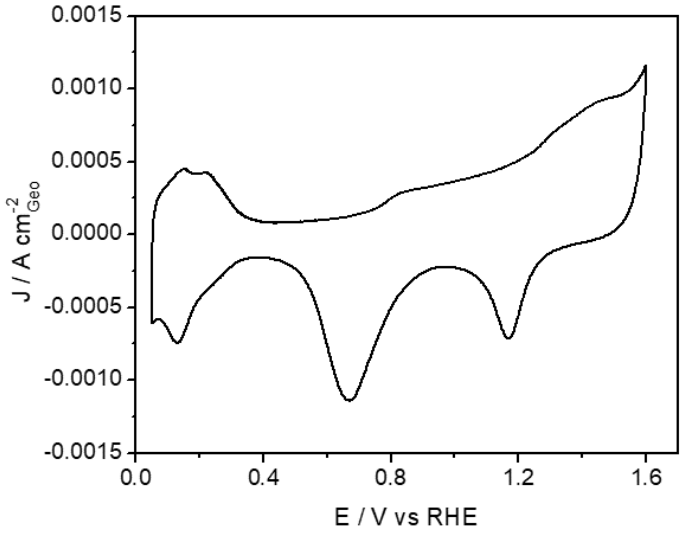

Figure S1. CV of the Pt-Au/C nanocomposite recorded at room temperature in $HClO_4$ aqueous electrolyte. The scan rate was 50 mV s^{-1}.

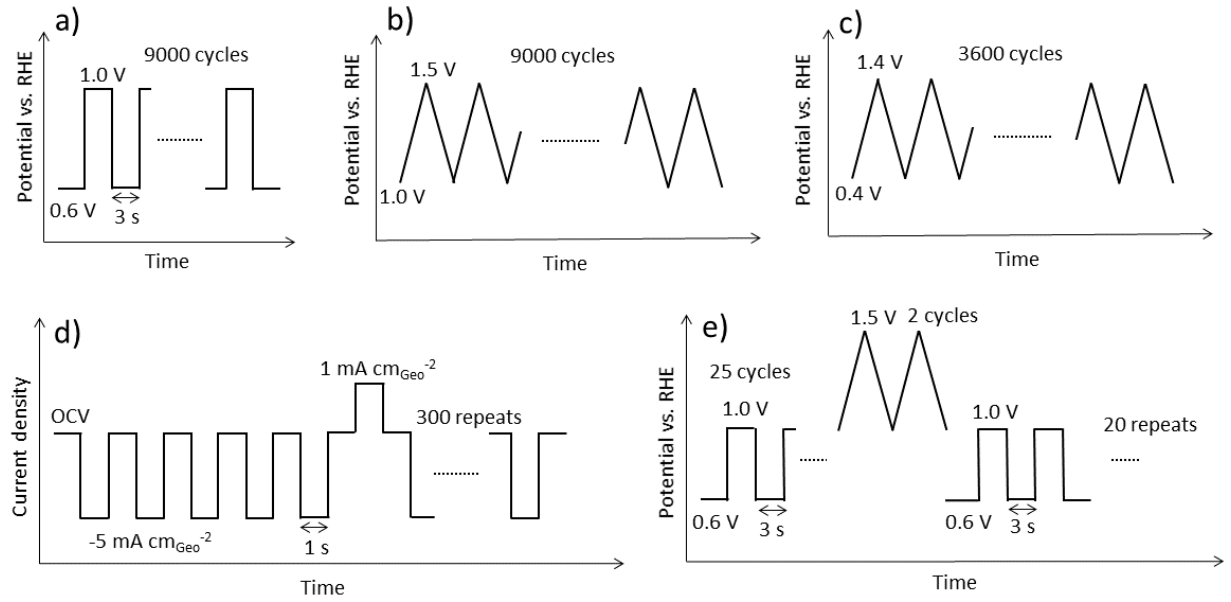

Figure S2. Schemes of the different applied ADT protocols in the RDE (a, b, c and d) and the GDE (e) measurements. The protocols of the RDE measurements were performed in Ar atmosphere (a, b and c) as well as O_2 atmosphere (d), while the protocol with a mixture of potential holding and potential cycling of the GDE measurement were performed in O_2 atmosphere.

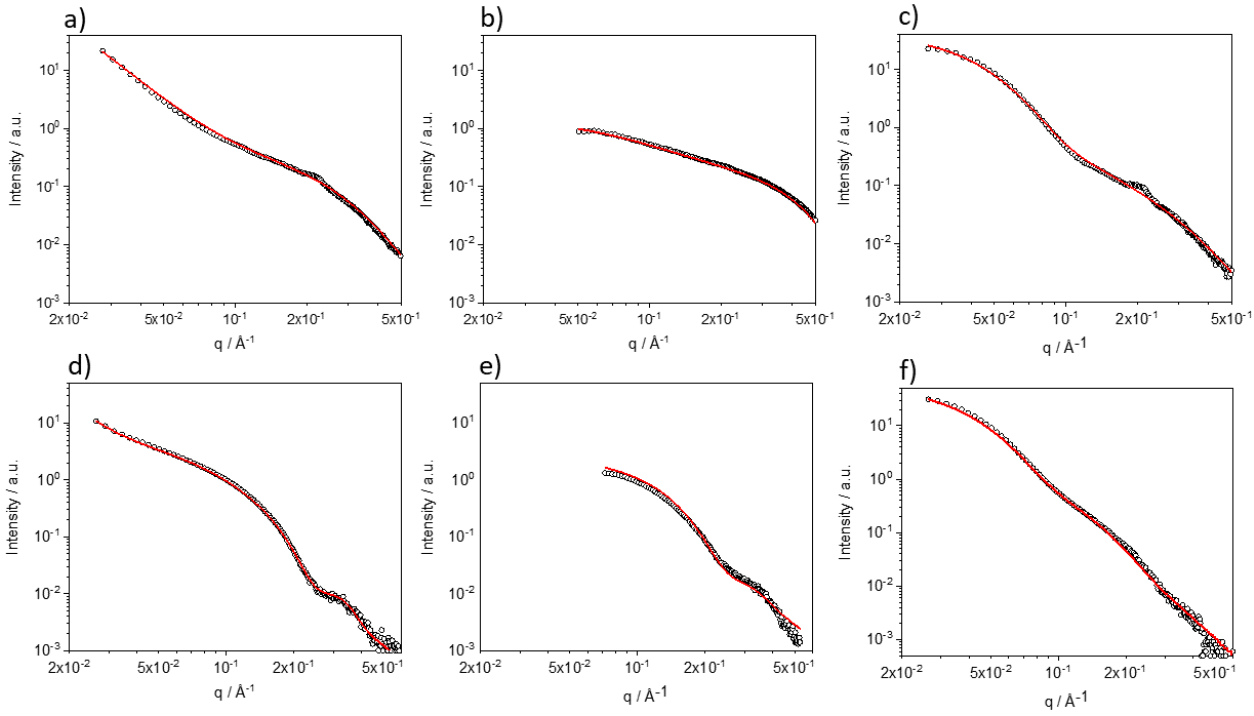

Figure S3. SAXS data and fits for the conditions before (a, b and c) and after (d, e and f) applying the degradation test. (a, d) monometallic Pt/C NPs, (b, e) Pt-IrO_2/C nanocomposite and (c, f) Pt-Au/C nanocomposite.

Table S1. Parameters of SAXS data fits and size analysis.

Samples		Power law		1st population			2nd population			Size and distribution							
		Ax 10^6	n	R_1 (Å)	σ_1	C_1	R_2 (Å)	σ_2	C_2	D_1	σ_1	D_2	σ_2	Average Diameter D (nm)	Standard Deviation of D σ (nm)	Volume fraction1	Volume fraction2
Pt/C	As prepared	180	3.25	8.0	0.30	0.008				1.7	0.5			1.7	0.5	1	0
	EOT	7	3.80	18.0	0.13	0.008	26.0	0.30	0.008	3.6	0.4	5.4	1.7	4.0	0.6	0.74	0.26
Pt-IrO_2/C	As prepared	0	2.30	6.1	0.17	0.015	14.0	0.50	0.005	1.2	0.2	3.2	1.7	1.3	0.2	0.98	0.02
	EOT	300	2.30	18.0	0.18	0.015				3.7	0.7			3.7	0.7	1	0
Pt-Au/C	As prepared	0	3.20	8.0	0.40	0.004	45.0	0.30	0.035	1.7	0.7	9.4	2.9	3.8	1.0	0.73	0.27
	EOT	20	3.00	16.0	0.25	0.003	48.0	0.30	0.038	3.3	0.8	10.0	3.0	7.0	1.7	0.45	0.55

Table S2. Particle size of the investigated catalysts before and after electrochemical measurements derived from the SAXS analysis. The standard deviation is determined from three independent measurements. BOT: before test, EOT: end of test.

		Pt/C	Pt-Au/C			Pt-IrO_2/C		
		Pt	Pt	Au	Mean size (nm)	Pt	Ir	Mean size (nm)
Particle size (nm)	BOT	1.7 ± 0.5	1.7 ± 0.7	9.4 ± 2.9	3.8 ± 1.0	3.2 ± 1.7	1.2 ± 0.2	1.3 ± 0.2
	EOT	4.1 ± 0.6	3.3 ± 0.8	10.0 ± 3.0	7.0 ± 1.7	-	-	3.7 ± 0.7

The SAXS data were recorded directly from the GDEs made from the respective catalyst by vacuum filtration. Unlike in RDE measurements no catalyst collection from multiple measurements is required as shown in our previous work[1].

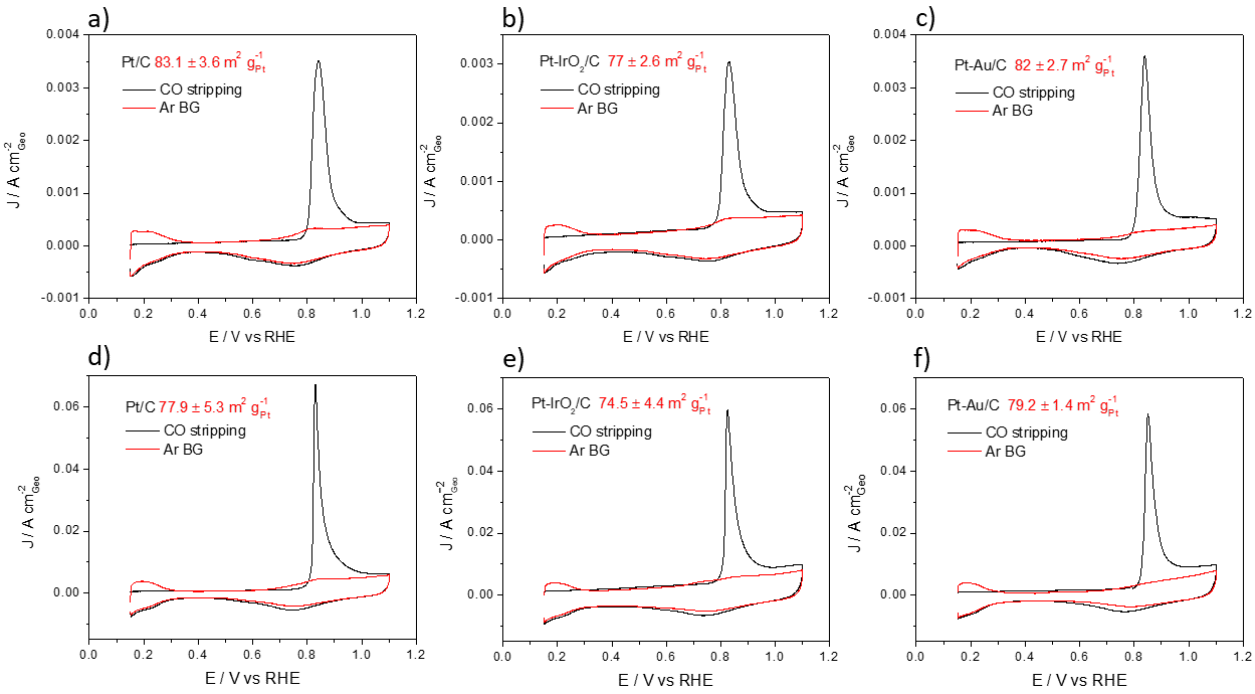

Figure S4. Representative CO stripping curves (black line) and the subsequent CVs (red line) of the monometallic Pt/C catalyst (a, d), the Pt-IrO_2/C nanocomposite (b, e) and the Pt-Au/C nanocomposite (c, f) from both RDE (a, b, c) and GDE (d, e, f) measurement approaches. The scan rate is 50 mV s^{-1}. The insert averaged ECSA value is obtained from three independent measurements from both measurement approaches. All measurements were recorded at room temperature in $HClO_4$ aqueous electrolyte.

The single CO oxidation peak can be taken as an indication that no Pt NP agglomeration is apparent in the as-prepared catalysts. The Pt surface area of the corresponding catalysts measured by the GDE approach is slightly lower than that determined by the RDE approach (Figure S4), we assume that the Nafion in catalyst ink for the GDE measurements is mainly responsible for this difference (Nafion is not added to the catalyst ink for the RDE measurement) as a portion of Pt active sites might be blocked by Nafion and the specific adsorption of sulphonate groups from Nafion on the Pt surface must also be taken into account[2,3]. The difference, however, is small. The largest determined difference in Pt area between RDE and GDE measurements is 6% (20 wt.% Pt/C).

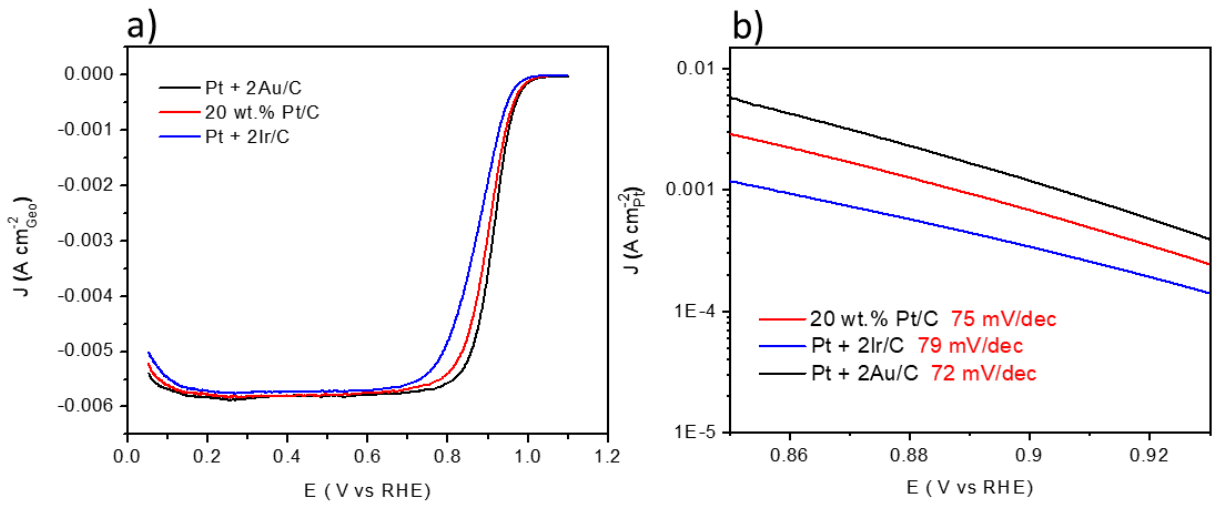

Figure S5. Comparison of linear sweep voltammograms (positive scans) of the investigated catalysts (a) and the Tafel plots extracted from the linear sweep voltammograms (b). The measurements were conducted in O_2 saturated 0.1 M $HClO_4$ aqueous electrolyte with a scan rate of 50 mV s^{-1} at room temperature. The obtained linear sweep voltammograms were corrected by Ar background and solution resistance.

The averaged polarization curves from three independent measurements are displayed in Figure S5a, these polarization curves are obtained from positive scan direction in O_2 saturated 0.1 M $HClO_4$ and after Ar background correction. We can see that the current density increases in the order of Pt-IrO_2/C to Pt/C to Pt-Au/C in the mixed of kinetic-diffusion controlled region (0.75-

1.00 V_{RHE}) which is normally used to determine ORR performance. Tafel plots are extracted from these polarization curves and depicted in Figure S5b, we can see that the Tafel plots are basically parallel to each other.

Table S3. ORR performance of the investigated catalysts from RDE and GDE approach. The ORR activity is determined at the potential of 0.85 V_{RHE} and from negative scan direction of the respective polarization curve from RDE approach. The standard deviation is determined from three independent measurements.

		Pt/C	Pt-IrO_2/C	Pt-Au/C
RDE	$SA_{0.85\ V}$ ($\mu A\ cm_{Pt}^{-2}$)	915 ± 58	416 ± 16	1280 ± 102
	$MA_{0.85\ V}$ ($A\ g_{Pt}^{-1}$)	750 ± 63	307 ± 26	1060 ± 71
GDE	$SA_{0.85\ V}$ ($\mu A\ cm_{Pt}^{-2}$)	81.8 ± 7.8	23.1 ± 2.8	107 ± 8.7
	$MA_{0.85\ V}$ ($A\ g_{Pt}^{-1}$)	63.7 ± 6.9	17.2 ± 3.1	85.1 ± 6.2

As seen, the absolute ORR activity in the RDE measurements is higher than the one determined in the GDE measurements (Table S3). This difference is related to several factors: i) a different catalyst ink composition (the ink for the GDE measurements contains Nafion while the one for the RDE measurement does not Nafion). This is also consistent with the lower ECSA obtained from the GDE measurements as compared to the RDE measurements. Nafion is known to partially block Pt active sites, and therefore insufficient Pt utilization is observed.[3] According to previous reports, an increase in the Nafion content improved the catalyst performance up to a Nafion weight percentage of 20% by Xu et al[4], while a decreased performance can be observed when the Nafion content is above 20 wt.%, same phenomenon was reported by Kim et al[5], who found 25 wt.% of Nafion content yielded the best performance in ORR activity. In our case, the Nafion content is in a range between 36 wt.% and 44 wt.% (the weight ration of Nafion/carbon is 1 in each catalyst), excess Nafion is possible to result in a suboptimal performance of the investigated catalysts in

ORR activity if referring to the above results. ii) even if ORR activity evaluation from RDE is selected from negative scan polarization curve, it is still possible to overestimate the ORR activity as a partial transient activity might contribute to the overall ORR rate evaluation from RDE measurement. iii) the configuration of the cell body from RDE and GDE approach are completely different, which can also be a source for activity deviation.

Table S4. ECSA obtained from CO stripping measurement before and after degradation test and the corresponding ECSA loss from both RDE and GDE measurement approach. Four different degradation protocols were applied for stability determination in RDE measurement while a mixed degradation protocol was applied in GDE measurement. The measurement results of Pt/C and Pt-IrO_2/C based on current mode protocol are resued from reference [6]. The standard deviation is determined from three independent measurements. BOT: before test, EOT: end of test.

Catalysts / Stability			Pt/C	Pt-IrO_2/C	Pt-Au/C
RDE ECSA (m^2 g_{Pt}^{-1})	BOT	0.6 V-1.6 V	85.6 ± 3.0	77.5 ± 2.9	86.1 ± 1.9
		1.0 V-1.5 V	81.7 ± 1.6	79 ± 1.2	82.5 ± 4.1
		0.4 V-1.4 V	84.8 ± 0.5	76.6 ± 4.1	82.7 ± 4.5
		Current mode	83.1 ± 3.6	77 ± 2.6	84.5 ± 1.7
	EOT	0.6 V-1.6 V	53.1 ± 1.3	49.2 ± 2.0	54.8 ± 1.3
		1.0 V-1.5 V	58.4 ± 1.3	65.2 ± 0.8	66 ± 2.7
		0.4 V-1.4 V	29.9 ±1.8	32.7 ± 2.3	27.2 ± 2.4
		Current mode	51.5 ± 3.4	61.9 ± 3.6	64.4 ± 4.8
Loss %	0.6 V-1.6 V		37.9 ± 0.7	36.5 ± 0.8	36.4 ± 0.5
	1.0 V-1.5 V		28.5 ± 1.0	17.5 ± 0.6	19.9 ± 2.5
	0.4 V-1.4 V		64.7 ± 2.1	57.4 ± 1.6	67.2 ± 1.1
	Current mode		38.1 ± 1.4	19.6 ± 1.3	23.7 ± 4.6
GDE ECSA (m^2 g_{Pt}^{-1})	BOT		77.9 ± 5.3	74.5 ± 4.4	79.2 ± 1.4
	EOT		52.3 ± 1.6	51.8 ± 2.0	60.2 ± 3.7
Loss %			32.9 ± 3.9	30.5 ± 4.3	24 ± 2.2

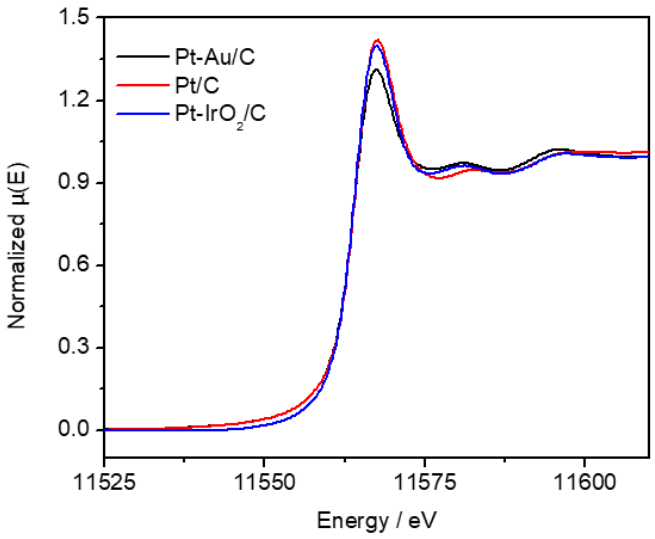

Figure S6. Normalized Pt L_3-edge XANES spectra of the supported monometallic Pt NPs and nanocomposite of Pt-Au/C and Pt-IrO_2/C.

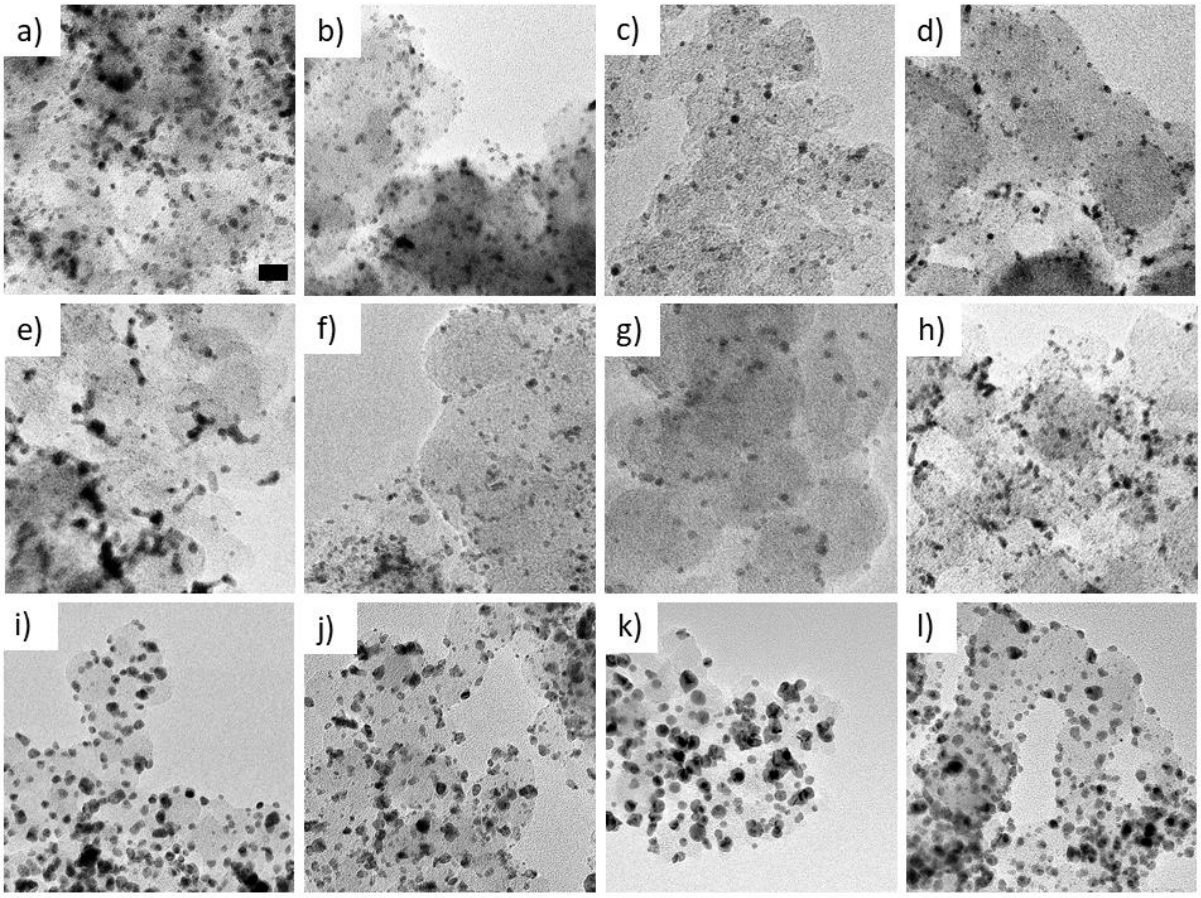

Figure S7. TEM micrographs recorded at the same magnification of the degraded catalysts with RDE approach. (a, b, c and d) Nanocomposite of Pt-IrO_2/C, (e, f, g and h) Supported monometallic Pt NPs and (i, j, k and l) Nanocomposite of Pt-Au/C. (a, e and i) are the degraded catalysts after subject to the degradation protocol as schemed in Figure S2a, (b, f and j) are the degraded catalysts after subject to the degradation protocol as schemed in Figure S2b, (c, g and k) are the degraded catalysts after subject to the degradation protocol as schemed in Figure S2c and (d, h and l) are the degraded catalysts after subject to the degradation protocol as schemed in Figure S2d. The scale bar for given in (a) is the same for all micrographs and is 20 nm.

Table S5. Weight compositions of Ir, Au and Pt that determined from TEM-EDX (RDE) and SEM-EDX (GDE). The calculated weight ratio before and after ADTs of each supported nanocomposite is obtained from five independent measurements. BOT: before test, EOT: end of test.

			Ir or Au wt. %	Pt wt. %	Ir/Pt or Au/Pt
RDE	Pt-IrO_2/C	BOT	67.0 ± 0.7	33.0 ± 0.7	2.03
		0.6 -1.6 V	34.0 ± 6.7	66.0 ± 6.7	0.52
		1.0 V-1.5 V	49.0 ± 18.7	51.0 ± 18.7	0.96
		0.4 V-1.4 V	40.0 ± 10.0	60.0 ± 10.0	0.67
		Current mode	32.0 ± 17.0	68.0 ± 17.0	0.47
	Pt-Au/C	BOT	66.0 ± 1.3	34.0 ± 1.3	1.95
		0.6 V-1.6 V	63.0 ± 2.8	37.0 ± 2.8	1.70
		1.0 V-1.5 V	69.0 ± 13.8	31.0 ± 13.8	2.23
		0.4 V-1.4 V	70.0 ± 13.6	30.0 ± 13.6	2.33
		Current mode	66.0 ± 4.2	34.0 ± 4.2	1.94
GDE	Pt-IrO_2/C	BOT	67.4 ± 2.0	32.6 ± 2.0	2.10
		EOT	49.7 ± 0.8	50.3 ± 0.8	0.99
	Pt-Au/C	BOT	65.5 ± 0.6	34.5 ± 0.6	1.90
		EOT	64.6 ± 0.7	35.4 ± 0.7	1.80

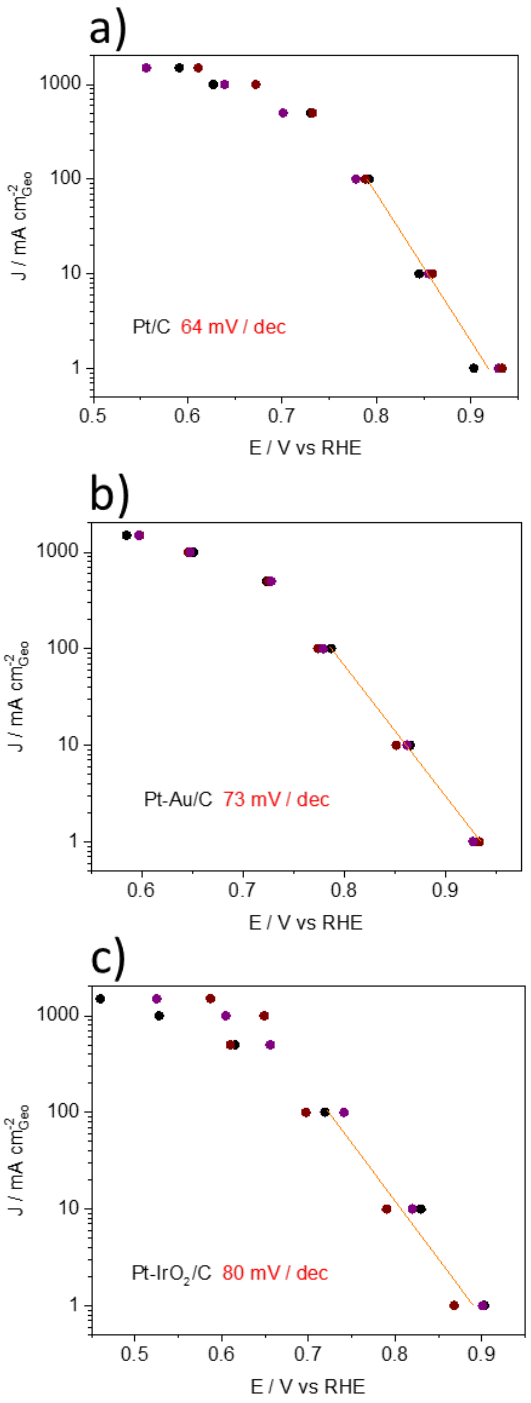

Figure S8. ORR performance before degradation test with GDE approach of supported monometallic Pt NPs (a), nanocomposite of Pt-Au/C (b) and Pt-IrO_2/C (c). Three independent measurement results are displayed in the corresponding figure, the recorded dots with the same color are from the same measurement. The current density is presented in logarithmic form. The Tafel slope is estimated from the first three measurement results.

References

(1) Schröder, J.; Quinson, J.; Mathiesen, J. K.; Kirkensgaard, J. J. K.; Alinejad, S.; Mints, V. A.; Jensen, K. M. Ø.; Arenz, M. A New Approach to Probe the Degradation of Fuel Cell Catalysts under Realistic Conditions: Combining Tests in a Gas Diffusion Electrode Setup with Small Angle X-Ray Scattering. *Journal of The Electrochemical Society* **2020**. https://doi.org/10.1149/1945-7111/abbdd2.

(2) Velázquez-Palenzuela, A.; Centellas, F.; Brillas, E.; Arias, C.; Rodríguez, R. M.; Garrido, J. A.; Cabot, P. L. Kinetic Effect of the Ionomer on the Oxygen Reduction in Carbon-Supported Pt Electrocatalysts. *International Journal of Hydrogen Energy* **2012**, *37* (23), 17828–17836. https://doi.org/10.1016/j.ijhydene.2012.09.090.

(3) Kodama, K.; Shinohara, A.; Hasegawa, N.; Shinozaki, K.; Jinnouchi, R.; Suzuki, T.; Hatanaka, T.; Morimoto, Y. Catalyst Poisoning Property of Sulfonimide Acid Ionomer on Pt (111) Surface. *Journal of The Electrochemical Society* **2014**, *161* (5), F649–F652. https://doi.org/10.1149/2.051405jes.

(4) Xu, W.; Scott, K. The Effects of Ionomer Content on PEM Water Electrolyser Membrane Electrode Assembly Performance. *International Journal of Hydrogen Energy* **2010**, *35* (21), 12029–12037. https://doi.org/10.1016/j.ijhydene.2010.08.055.

(5) Kim, K. H.; Lee, K. Y.; Kim, H. J.; Cho, E. A.; Lee, S. Y.; Lim, T. H.; Yoon, S. P.; Hwang, I. C.; Jang, J. H. The Effects of Nafion® Ionomer Content in PEMFC MEAs Prepared by a Catalyst-Coated Membrane (CCM) Spraying Method. *International Journal of Hydrogen Energy* **2010**, *35* (5), 2119–2126. https://doi.org/10.1016/j.ijhydene.2009.11.058.

(6) Du, J.; Quinson, J.; Zhang, D.; Bizzotto, F.; Zana, A.; Arenz, M. Bifunctional Pt-IrO2 Catalysts for the Oxygen Evolution and Oxygen Reduction Reactions: Alloy Nanoparticles versus Nanocomposite Catalysts. *ACS Catalysis* **2021**, *11* (2), 820–828. https://doi.org/10.1021/acscatal.0c03867.

Manuscript IV

Nanocomposite Concept for Electrochemical *in situ* Preparation of Pt-Au Alloy Nanoparticles for Formic Acid Oxidation

Jia Du[a], Jonathan Quinson[b], Damin Zhang[a], Baiyu Wang[b], Gustav K.H. Wiberg[a], Rebecca K. Pittkowski[b], Johanna Schröder[a], Søren B. Simonsen[c], Jacob J. K. Kirkensgaard[d,e], Yao Li[f], Sven Reichenberger[f], Stephan Barcikowski[f], Kirsten M. Ø. Jensen[b], Matthias Arenz[a *]

[a] University of Bern, Department of Chemistry, Biochemistry and Pharmaceutical Sciences, Freiestrasse 3, 3012 Bern, Switzerland

[b] University of Copenhagen, Department of Chemistry, Universitetsparken 5, 2100 Copenhagen Ø, Denmark

[c] Technical University of Denmark, Department of Energy Conversion and Storage, Fysikvej Bldg. 310, Lyngby, DK-2800 Kgs., Denmark

[d] University of Copenhagen, Department of Food Science, Rolighedsvej 26, 1958 Frederiksberg, Denmark

[e] University of Copenhagen, Niels Bohr Institute, Universitetsparken 5, 2100 Copenhagen Ø

[f] University of Duisburg-Essen, Technical Chemistry I and Center of Nanointegration Duisburg Essen (CENIDE), Universitätsstraße 7, Essen, North Rhine-Westphalia, 45141, Germany

ABSTRACT

Herein, we report a straightforward approach for the *in situ* preparation of Pt-Au alloy nanoparticles from Pt + xAu/C nanocomposites using monometallic colloidal nanoparticles as starting blocks. Four different compositions with fixed Pt content and varying Pt to Au mass ratio from 1:1 up to 1:7 were prepared as formic acid oxidation reaction (FAOR) catalysts. The study was carried out in a gas diffusion electrode (GDE) setup, a newly developed testing platform for fuel cell catalysts. It is shown that the presence of Au in the nanocomposites substantially improves the FAOR activity with respect to pure Pt/C which serves as a reference. The nanocomposite with a mass ratio of 1:5 between Pt and Au displays the best performance during potentiodynamic tests, with the electrooxidation rates, overpotential, and poisoning resistance being improved simultaneously. By comparison, the nanocomposites with too low or too high Au contributions lead to an unbalanced performance in the FAOR. *Operando* small-angle X-ray scattering (SAXS),

scanning transmission electron microscopy (STEM) elemental mapping, and wide-angle X-ray scattering (WAXS) reveal that a conversion between Pt and Au from separate nanoparticles to alloy nanoparticles occurred during continuous potential cycling of the catalyst with 1:5 mass ratio. By comparison, the nanocomposites with lower Au contents, e.g., 1:2, exhibit less Pt and Au *in situ* alloying, and the concomitant performance improvement is less pronounced. Applying identical location transmission electron microscopy (IL-TEM), it is revealed that the *in situ* alloying is due to Pt dissolution and re-deposition onto Au as well as Pt migration and coalescence with Au nanoparticles.

KEYWORDS

Nanocomposite electrocatalysts; formic acid oxidation reaction; gas diffusion electrode setup; small-angle X-ray scattering; in situ alloying;

1. INTRODUCTION

Fuel cells, electrochemical devices that convert the chemical energy of a fuel into electrical energy, are considered the most promising candidates for powering not only large automobile and heavy duty electric trucks,[1–3] but also for smaller devices.[4] Therefore, fuel cells attract considerable attention in both industrial and academic fields.[2,5] The most common fuels are classified as gaseous, e.g., hydrogen, and liquid, e.g., ethanol, methanol and formic acid (FA). Hydrogen-fed proton exchange membrane fuel cells (PEMFCs) have been studied intensively.[6,7] Well-known for their cleanliness and high-power density, they have been, for instance, applied in cars, busses, and trucks. However, intrinsic restrictions such as a lack of a widespread hydrogen distribution network still exist.[6,7] Alternative fuel cells using liquid fuels are the so-called direct methanol, ethanol, and formic acid fuel cells (DMFCs, DEFCs, and DFAFCs). The DFAFCs exhibit a lower crossover of

FA through the polymer membrane[8] and a smaller onset overpotential[9] compared with alcohol-based fuel cells, which makes the DFAFC promising as a power source for portable electronics.[10]

Pt is one of the most commonly used electrocatalyst materials in FAOR studies. However, Pt is prone to be poisoned by CO_{ad}, which in literature is linked to a dehydration or disproportionation pathway of FAO and which reduces the efficiency of a fuel cell.[11,12] To alleviate poisoning and to improve the FAO electrocatalytic activity, combining Pt with a foreign metal to form Pt-based bimetallic catalysts is regarded as an effective strategy.[13–15] Pt-M bimetallic (M = Bi, Pd, Au, etc.) catalysts have been developed and display improvements in FAOR catalytic performance.[16,17] Among the different bimetallic Pt-M catalysts, Pt-Au exhibits a high resistance of Au dissolution in acidic media[18,19] as well as a boosted FAO activity.[20,21] Various structures of Pt-Au bimetallic materials, such as PtAu alloys,[22,23] PtAu core-shell particles,[24,25] Pt deposited onto Au,[26,27] etc. have been synthesized. The observed improved performance is ascribed to either a modified electronic structure[28,29] or an ensemble effect.[30,31] Organic surfactants are typically needed to form a specific nanostructure. These additives are likely to block surface sites of the active phase. Removing surfactants from nanomaterials typically requires a post cleaning step to the catalyst surface that may cause adverse effects on the catalytic performance.[30] However, Guay and co-authors reported a laser ablation method to prepare surfactant-free Pt-Au bimetallic catalysts, avoiding a surfactant-removal process, and the obtained Pt-Au mixed and Pt-Au alloyed nanoparticles are used for FAO study.[32]

In the present study, we use our previously introduced nanocomposite concept,[33,34] to prepare Pt + xAu/C bimetallic nanocomposites with tunable compositions. Surfactant-free, metallic Pt and Au nanoparticles serve as starting blocks. Pt/C serves as a reference catalyst. The FAOR is probed for the different electrocatalysts in a GDE setup, a newly developed fuel cell catalyst testing platform

that was recently used to benchmark the commercial Pt/C and Pd/C for electrooxidation of small organic compounds.[35] *Operando* SAXS is combined to monitor the particle size distribution during FAOR potentiodynamic tests. The results indicate that electrochemical potentiodynamic conditions lead to *in situ* alloy formation of the initial Pt and Au composite with separate Pt and Au nanoparticles. The alloyed nanoparticles lead to a substantial improvement in FAO performance compared with the reference catalyst.

2. RESULTS AND DISCUSSION

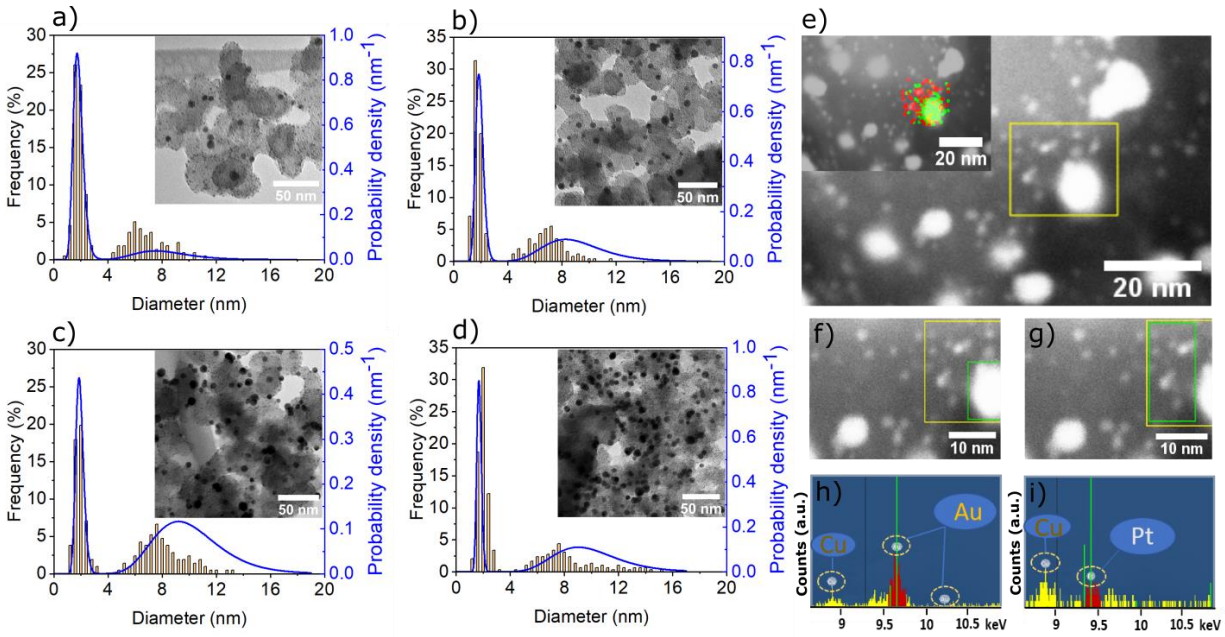

Figure 1. TEM micrographs and size distributions retrieved from TEM (bar diagrams, left axis) and SAXS (blue curves, right axis) of pristine Pt + Au/C (a), Pt + 3Au/C (b), Pt + 5 Au/C (c) and Pt + 7Au/C (d). STEM micrographs of Pt + 5Au/C with inserted EDX elemental map of Pt (red) and Au (green) (e). STEM micrographs of the selected large bright spot (green square) from Pt + 5Au/C (f) and the corresponding EDX elemental spectrum (h), as well as the selected small bright spots (green square) from Pt + 5Au/C (g) and corresponding EDX elemental spectrum (i). Copper TEM grids were used. The histograms for particle size distribution evaluation are based on an evaluation of ~300 randomly chosen nanoparticles in the TEM micrographs of the respective as-prepared catalysts. The probability density of the particle size is plotted volume weighted and obtained from analysis of the SAXS data.

2.1 Characterization of the as-prepared Electrocatalysts

Pt-Au/C nanocomposites with varying ratios of Au and Pt nanoparticles distributed over the carbon support (the number of Pt nanoparticles, expressed as mass loading in wt.%, is kept constant) were prepared from identical colloidal stock suspensions. The particle sizes of the Pt and Au colloids were chosen differently, i.e., around 2 and 10 nm respectively, to allow distinction. The obtained compositions were evaluated with ICP-MS and SEM-EDX (Table S1). In the following, the name Pt + xAu/C indicates the determined mass ratio of Pt to Au metal loadings. TEM and SAXS were used for evaluating the particle size distribution on the carbon support and one can observe that all as-prepared samples exhibit two well-distinguishable size distributions (Figure 1a-d, the physical characterization of the Pt/C reference can be seen in Figure S1). Furthermore, the Pt and Au nanoparticles are clearly separated and uniformly distributed on the carbon support. Only at high Au content, a slight aggregation of Au nanoparticles in the nanocomposites is indicated (Figure 1c-d, Table S2). In all nanocomposites, the smaller Pt nanoparticles are clearly discernable, and their particle sizes are not affected by the Au loading (Table S2). STEM EDX elemental mapping on Pt + 5Au/C allows in-depth characterization of the nanocomposites, i.e., the large bright spots relate to the Au NPs (Figure 1f, Figure 1h) while the smaller spots are related to Pt NPs (Figure 1g, Figure 1i). No element mixture is observed, which confirms that Pt and Au nanoparticles are immobilized separately on the carbon support of the pristine samples. Due to the very small size of the Pt nanoparticles in the nanocomposites (Figure 1a-d), the XRD diffractograms only display clear Au Bragg peaks (Figure S2). The structural characterization of the nanocomposites is completed by total X-ray scattering.[36] As illustrated in Figure 2, the pair distribution functions (PDFs) obtained from the four samples could all be described by a two-phase Au/Pt model, where smaller *fcc*-structured Pt nanoparticles (refined crystallite size ca. 2 nm) are identified along with

larger *fcc*-structured Au nanoparticles (refined crystallite size ca. 5-6 nm). Note, however, that the similarities between the structure and scattering power of Pt and Au make it difficult to distinguish clearly between the two phases in the PDF, and which leads to a large correlation between the refined parameter for the two phases. However, the existence of nanoparticles of two distinct crystallite sizes in the PDF is clear (Table S3), and the results are thus consistent with that from the SAXS and TEM analyses (Figure 1). In conclusion, Pt + xAu/C nanocomposites with variable compositions could be obtained with a monometallic nanoparticle preparation strategy.

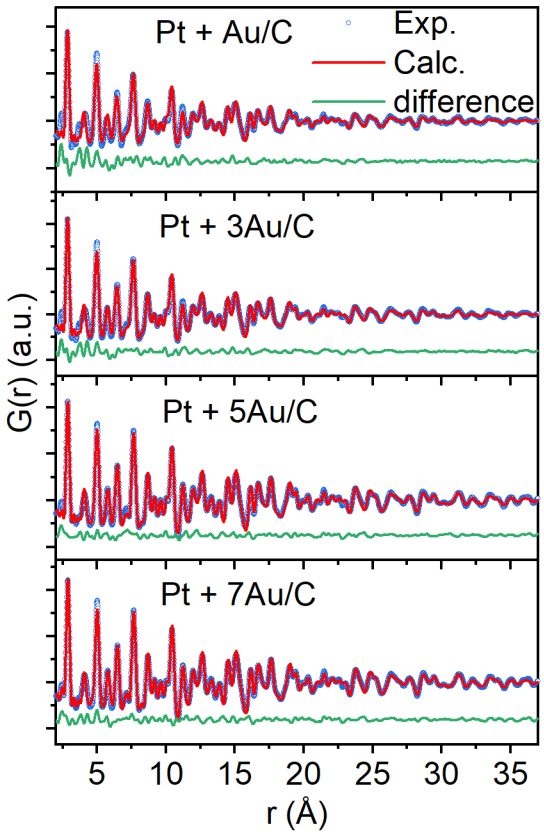

Figure 2. Fits to the PDF of the investigated pristine Pt + xAu/C nanocomposites. The fits are based on a two-phase model using both Pt and Au *fcc* structures. The blue circles show the experimental PDFs, the red lines are simulated PDFs and the green lines are the difference curves of the two. Refined parameters are given in Table S3.

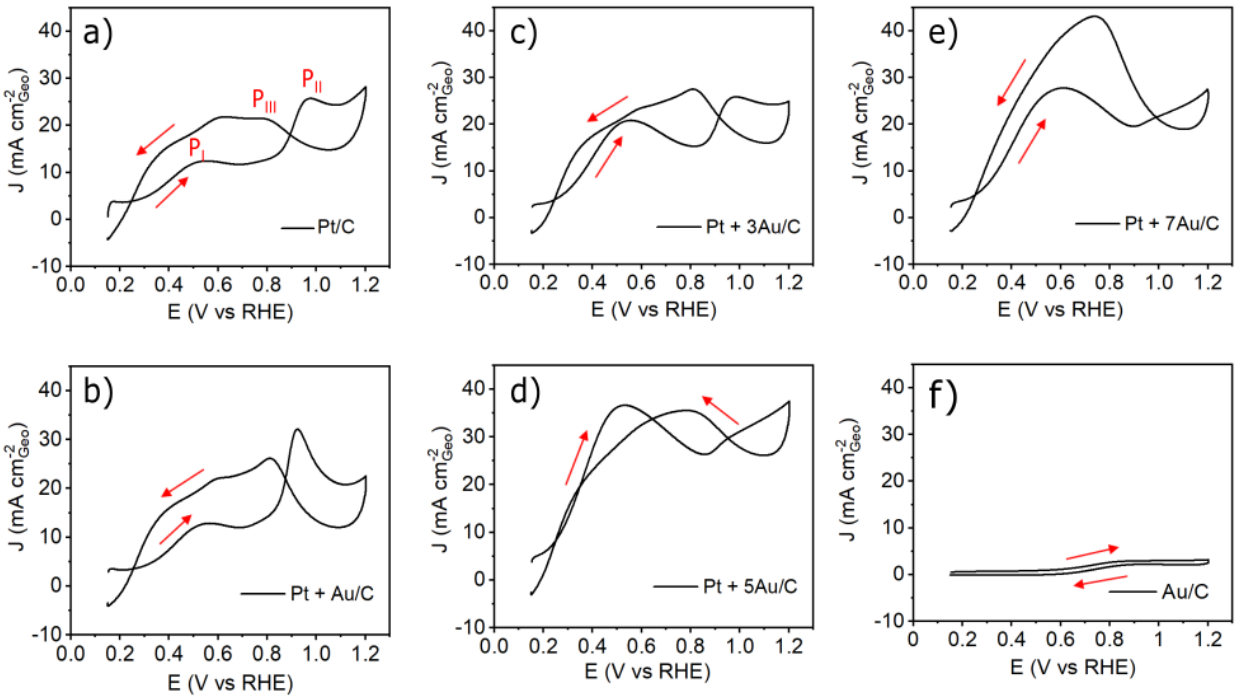

Figure 3. CVs of FAOR of the investigated catalysts in GDE setup. The bubbler is filled up with 5.0 M formic acid and the upper cell body is filled up with 1.0 M $HClO_4$. The CVs are all recorded from the second scan in potentiodynamic tests. A scanning speed of 50 mV s^{-1} is applied for all measurements.

2.2 Electrooxidation of FA on the Investigated Catalysts under Potentiodynamic Conditions

The electrooxidation of FA on the investigated electrocatalysts is carried out in a GDE setup cell, an electrochemical testing platform using a Nafion membrane to mimic fuel cell operating conditions.[37,38,39] FA is introduced to the GDE setup via FA saturated Ar gas stream. The CVs from the potentiodynamic tests (Figure 3) provide fundamental information concerning the FAOR activity. According to literature, several important characteristics can be used to describe the FAOR activity, i.e., peak currents, peak potentials and hysteresis, see Table 1 for summary of the key performance characteristics of the different Pt + xAu/C nanocomposites (the characteristics' values are extracted from Figure S3).[40] High peak currents indicate high oxidation rates, low peak potentials or high currents at a low potential are a sign of a low overpotential. A small hysteresis,

i.e., the difference between the positive and negative-going polarization curve, indicates limited poisoning and a preferential direct oxidation pathway. A "good" catalyst, therefore, exhibits high peak currents, especially in the forward-going scan, low peak potentials, and a small hysteresis between positive and negative-going scan. The well-established features of a single Pt reference catalyst for FAOR can clearly be seen in Figure 3a.[20,41] The peak in the forward-going scan corresponding to the electrooxidation of FA to CO_2 through the direct pathway (dehydrogenation) exhibits a weak intensity (P_I). The peak with strong intensity (P_{II}) in the positive-going scan is associated with CO oxidation, which occurs via the indirect pathway (dehydration) and poisons Pt-based catalysts. Therefore, in new catalyst design, we aim to increase the direct pathway (P_I) and suppress the indirect path (P_{II}) to avoid catalyst poisoning. By comparison, the current from pure Au/C is significantly smaller (Figure 3f) and pure Au seems to be inert to FAOR. However, in the case of the Pt + xAu/C nanocomposites, it is seen that the FAOR proceeds more pronounced through the direct pathway (Figure 3c-e, Pt + Au/C behaves rather similar to Pt/C as indicated in Figure 3b). The peak currents at low potential (P_I, as indicated on pure Pt/C) are boosted towards higher current densities with the introduction of Au nanoparticles, while the peak currents at high potential (P_{II}, as indicated on pure Pt/C) behave oppositely, i.e., the P_{II} currents are decreased (except for Pt + Au/C) and almost disappear on Pt + 5Au/C and Pt + 7Au/C. The accumulated FAO intermediates are oxidized at a high potential excursion, therefore, the peak currents indicated as P_{III} on pure Pt/C in the negative-going scan reflect the intrinsic activity of a "clean catalyst" towards FAOR.[41] One can see that as a result of the introduction of Au nanoparticles, the currents of P_{III} are enlarged as well, which implies that the electrooxidation rates of FA are improved in comparison to monometallic Pt/C. In addition, a reduced hysteresis in peak current (based on P_I and P_{III} current) between both scan directions is observed on Pt + 3Au/C and Pt + 5Au/C (Figure

3c-d) reflecting the improved poisoning resistance. However, the hysteresis for Pt + Au/C (Figure 3b) and Pt + 7Au/C (Figure 3e) are rather similar to that of the Pt/C reference catalyst. All of these observations indicate that the performance of FAOR can be improved by the introduced Au nanoparticles. The Au content of the nanocomposites thereby plays a significant role. Therefore, it is necessary to evaluate and compare the performance of FAOR quantitatively and systematically for the different Au contents.

2.3 Performance Comparison of FA Electrooxidation on the Investigated Catalysts

Table 1. FAOR characteristics of the investigated catalysts. The currents are evaluated and compared to each other at 0.3 V_{RHE} and at the peak positions P_I and P_{III} (as indicated in Figure 3a) from the positive-going and negative-going scans, respectively. Furthermore, the peak potentials (of P_I and P_{III}) are compared and the hysteresis is calculated from the peak currents or peak potential (P_I and P_{III}) of three different individual measurements determining the average value. The indicated errors are the standard deviation obtained from three independent measurements.

Catalysts		Pt/C	Pt + Au/C	Pt + 3Au/C	Pt + 5Au/C	Pt + 7Au/C
Forward scan	Current at 0.3 V_{RHE} (A g_{Pt}^{-1})	35.4 ± 5.4	48.8 ± 4.1	50.9 ± 6.2	98.4 ± 9.5	64.8 ± 5.9
	P_I current (A g_{Pt}^{-1})	97.0 ± 4.1	152.0 ± 8.4	181.2 ± 6.2	286.6 ± 23.5	259.9 ± 25.5
	P_I potential (mV)	546.0 ± 1.7	562.3 ± 2.3	543.0 ± 4.6	516.0 ± 6.2	621.3 ± 17.2
Backward scan	P_{III} current (A g_{Pt}^{-1})	160.5 ± 25.9	322.4 ± 10.0	228.0 ± 13.3	287.2 ± 34.0	452.5 ± 28.1
	P_{III} potential (mV)	786.7 ± 5.9	831.0 ± 16.8	807.3 ± 2.9	780.3 ± 5.1	758.3 ± 21.5
Hysteresis (from the current of P_I and P_{III}, %)		39.0 ± 6.9	52.9 ± 1.4	20.1 ± 8.6	5.2 ± 2.4	42.4 ± 6.1
Hysteresis (from the potential of P_I and P_{III}, %)		30.6 ± 0.7	32.3 ± 1.2	32.7 ± 0.8	33.9 ± 1.1	18.0 ± 2.1

We scrutinize the FAOR performance based on the Pt mass-weighted currents, as Pt is the active phase for the FAOR (the actual metal mass on the GDL is displayed in Table S1). The values of different characteristics are summarized in Table 1. A clear activity trend in peak current (P_I) is seen from the positive-going scan. The electrooxidation rate of FAOR of Pt/C is only 97.0 ± 4.1

A g_{Pt}^{-1}. This value is gradually enlarged with the introduction of Au nanoparticles, until a maximum of 286.6 ± 23.5 A g_{Pt}^{-1}, a value that is ~three times higher than the one from Pt/C, is observed for Pt + 5Au/C. Further increasing the Au content (Pt + 7Au/C) does not lead to an improvement, however, instead, a maximum in activity from the backward scan (P_{III}) is reached. A similar activity trend can also be observed at 0.3 V_{RHE}, an anodic working potential in direct formic acid fuel cells (DFAFCs),[42] in the forward-going scan. Apparently, the combination Pt + 5Au/C stands out, which is consistent with the lowest peak potential, i.e., in comparison to the reference catalyst, the value is ~30 mV shifted to lower potentials. In addition, the current hysteresis of both directions, which reflects the poisoning resistance of a catalyst in FAOR, is compared. The hysteresis from pure Pt/C is ~39%, whereas on Pt + 5Au/C it is reduced to only ~5.2%, which indicates significantly improved poisoning resistance and a preferential dehydrogenation path in the FAOR. By comparison, the nanocomposites with much lower Au content (Pt + Au/C) or a higher Au content (Pt + 7Au/C) lead to a higher current in the forward scan but also to higher peak potentials and a higher or similar (Pt + 7Au/C) hysteresis. Taking into account the boosted electrocatalytic performance in the FAOR in respect to the Au loading, the mass ratio of 1:5 (Pt:Au) displays the balanced performance improvement, we analyzed the Pt + 5Au/C catalyst further in *operando* SAXS, WAXS and IL-TEM studies.

2.4 Insights into the Improved FA Electrooxidation Performance on Pt + xAu/C Nanocomposites

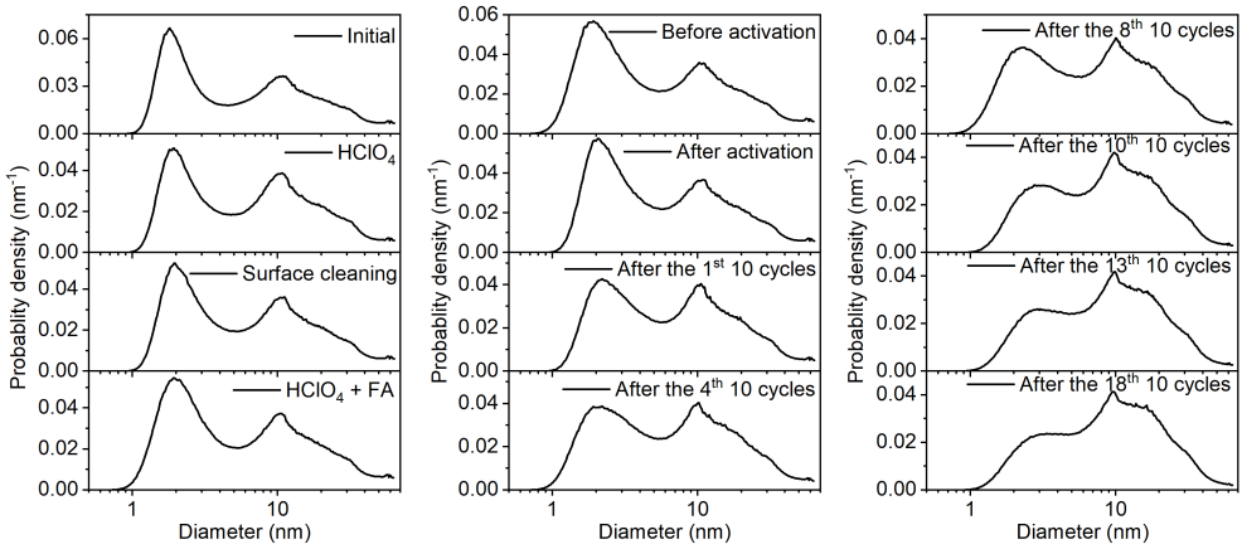

Figure 4. Size distributions of Pt + 5Au/C obtained from the analysis of *operando* SAXS data. The displayed size distribution functions are selected as a function of the duration of FAOR potentiodynamic tests. The first column shows the data before (indicated as initial) and after subjecting the catalyst to the electrolyte ($HClO_4$), after applying a cleaning procedure, and after subjecting the catalyst to formic acid (FA). The next columns show the influence of the activation procedure and the potential cycling. In the FAO potentiodynamic test, potential was swept between -0.0417 and 1.0083 $V_{Ag/AgCl}$ with a scan rate of 50 mV s^{-1}. Potential was held at 0.2683 $V_{Ag/AgCl}$ for 30 min to achieve catalyst activation. See experimental part for more details.

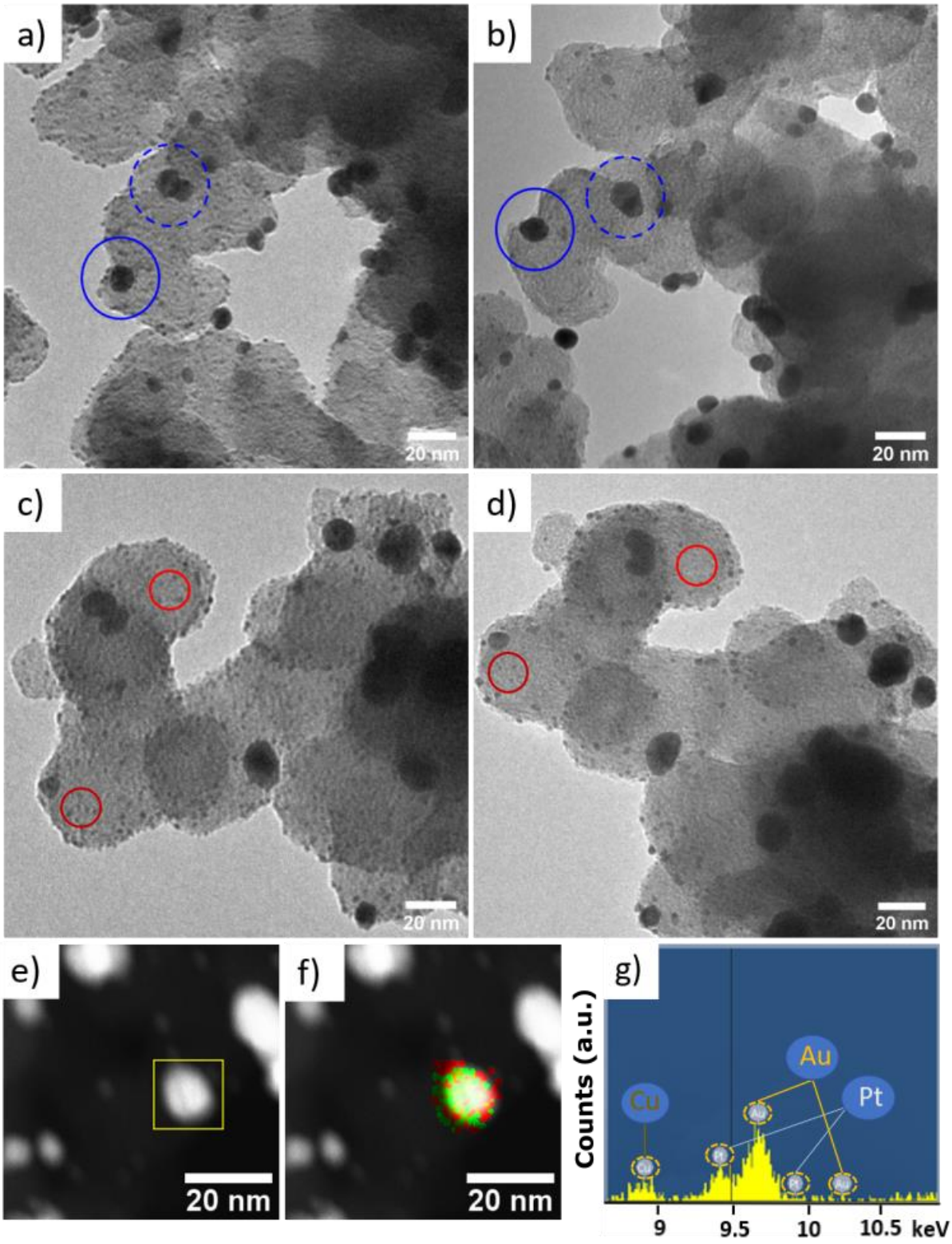

Figure 5. IL-TEM (a-d) and STEM micrographs (e), STEM-EDX mapping (f) and STEM-EDX elemental analysis (g) of the Pt + 5Au/C nanocomposite. The IL-TEM micrographs were obtained from the pristine Pt + 5Au/C sample (a, c), and the same sample exposed to the 50th scan in the

FAOR potentiodynamic test (b, d). Red solid cycles indicate a shrink of Pt nanoparticles due to dissolution; blue solid cycles indicate areas of suspected Pt nanoparticle migration and coalescence with Au islands, blue dashed cycles evidence Au nanoparticle migration and coalescence with Au nanoparticles (e), STEM-EDX elemental mapping (f) of Pt (red) and Au (green), and the corresponding EDX elemental spectrum (g) were collected after 50 CVs in the FAOR potentiodynamic test. The samples for STEM analysis were prepared by scraping catalyst powder from GDL after the potentiodynamic test, followed by dispersing into ethanol and dropping onto a copper grid.

It has been documented that catalyst surfaces restructure under continuous potential cycling, e.g., via metal dissolution and re-deposition, metal particle migration and coalescence, etc.[43,44] Therefore, it is suspected that continuous potential cycling, as typically done in catalytic testing, could trigger the formation of Pt-Au alloys from the pristine nanocomposites. This hypothesis is tested based on the Pt + 5Au/C nanocomposite by combining *operando* SAXS, IL-TEM, STEM-EDX elemental mapping, and WAXS. The *operando* SAXS data were recorded during continuous FAOR measurements in potentiodynamic mode. While the analysis of the relative ratio between Pt and Au is challenging,[45] clearly the data indicate non-static behavior. It is seen that the probability density associated with Pt NPs decreases in intensity and increases in size, indicating a gradual convergence of the two size populations associated with Pt and Au, respectively (Figure 4 and Figure S4). The observed behavior would be in line with Pt dissolution and re-deposition onto Au islands as well as Pt NP migration and coalescence with Au nanoparticles during the continuous potential cycling. To support our assumption IL-TEM is used. An Au grid deposited with Pt + 5Au/C is exposed to the same FAOR potentiodynamic conditions used in the GDE setup. In Figure 5a-d the representative IL-TEM micrographs before and after potentiodynamic test are displayed. As seen, IL-TEM indeed indicates signs of Pt nanoparticle migration and coalescence with Au nanoparticles as marked by the blue solid cycles. Pt dissolution is evident by particle shrinking as demonstrated by the red solid cycles, which is consistent with ICP-MS analysis –

small amounts of Pt are detected in the electrolyte after potentiodynamic tests (Table S4), which might re-deposit onto the Au nanoparticles. Both processes lead to an *in situ* alloying of Pt and Au. This statement is further supported by STEM-EDX and WAXS. In STEM-EDX, alloy formation on the Au nanoparticles is difficult to distinguish from migration-coalescence (i.e. alloying *versus* deposition of Pt on Au, Figure 5e-g), however, the WAXS data clearly indicate a small shift in the Bragg peak positions towards larger diffraction angles after the potentiodynamic test, see Figure 6b. Given that the Bragg peak positions from carbon (as indicated by the black vertical line) stay constant, i.e., serves as an internal standard, the small shift in peak position indicates that Pt and Au form an alloy. According to the work of Guay et al.[32] studying Pt-Au alloy nanoparticles the optimal (surface) composition of Pt-Au bimetallic catalysts for the FAO is ~50% Pt. The optimal nanocomposite composition in this study is Pt + 5Au/C, i.e., the mass contribution of Pt is roughly five times less than Au. This indicates surface enrichment of Pt, i.e., that a surface alloy of Pt and Au is formed on the Au NPs for our case. Due to the similarity of Pt and Au, Rietveld refinement did not allow to unambiguous quantification of the formed alloy. However, applying Vegard's law,[46,47] a fraction of ~10% of alloying can be estimated. Taking into account that applying Vegard's law only results in a rough estimation and does not account for surface alloying, one can assume an even higher degree of surface alloying. For comparison, for the nanocomposite with less Au content (Pt + 2Au/C, the corresponding CV in the potentiodynamic test in displayed in Figure S5) was investigated with *operando* SAXS under the same conditions. The still well-distinguishable size populations (Figure S6) and minor changes in peak intensity ratio (Figure S7) at the end of the potentiodynamic tests indicate that *in situ* alloying of Pt and Au is substantially inhibited. This might be a simple consequence of a too low amount of Au, rendering the alloying less likely. This is further evidenced by analyzing the 50th CV of the potentiodynamic

measurements. It is seen that the nanocomposites with low Au content still keep a similar feature of FAOR behavior, while a "more Pt-Au alloy" feature for the FAOR (an absence of P_{II} and a comparable peak current (P_I, P_{III}) from both directions) arises,[32] especially on Pt + 5Au/C (Figure S8). Electronic and ensemble effects are normally predominant causes to lead to an improvement in FAO performance in Pt-Au bimetallic system.[20,48,49] However, by discussing the correlation between CO oxidation peak positions and Au contents (Figure S9) in the supporting information, one can conclude that the introduced Au does not allow faster removal of CO intermediate and thus electronic effect is not a main cause for the improvement of FAO performance. Therefore, the increased FAO activity of Pt + 5Au/C surface alloy nanoparticle is achieved by facilitating direct path of FAO, which is related to ensemble effect, i.e., Pt domains are interrupted by Au (neighboring Pt atoms are required for the formation of adsorbed CO)[20] and thus suppresses CO adsorption on Pt surface.

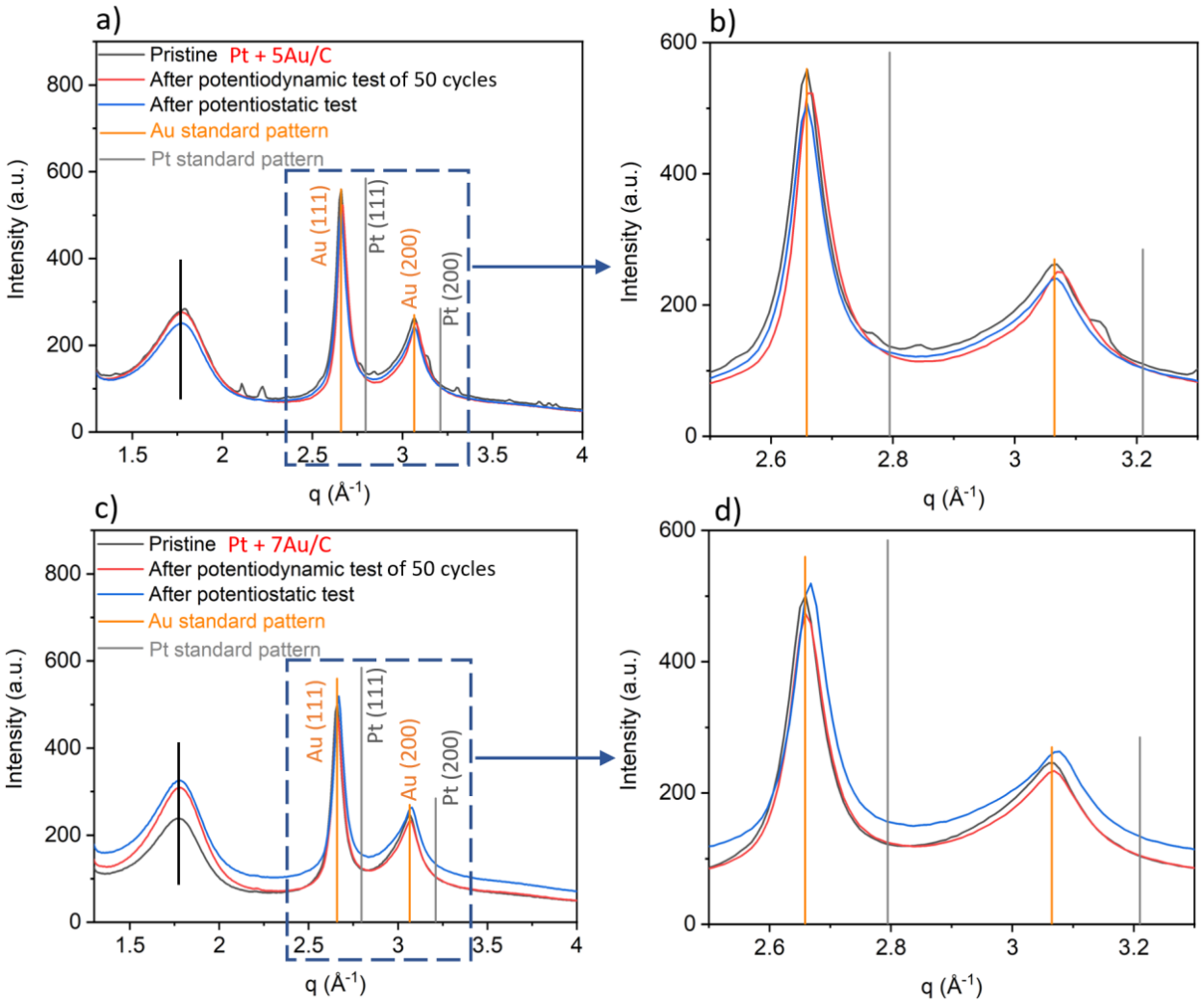

Figure 6. Profiles of WAXS diffractograms of Pt + 5Au/C (a, b) and Pt + 7Au/C (c, d). (b, d) represent the respective amplified diffraction patterns in the q range of 2.5-3.3 $Å^{-1}$. 50 CVs were applied in the potentiodynamic test for Pt + 5Au/C and Pt + 7Au/C.

2.5 Electrooxidation of FA on the Investigated Catalysts under Potentiostatic Tests

Last but not least, the catalysts were also exposed to potentiostatic tests at 0.3 V_{RHE}, which can be considered simulating a steady state DFAFC application. In these tests, a slightly different picture arises with respect to the relative performance of the catalysts (Figure 7). For all investigated catalysts, a substantial inhibition can be observed in the first 600 s. Pt + 5Au/C, which was the most suitable catalyst towards FAOR in the potentiodynamic tests, exhibits a much longer

inhibition time than the reference Pt/C catalysts or the samples with lower Au content. However, in the long-term, the sample suffers from the same performance inhibition. By comparison, the Pt + 7Au/C catalyst exhibits the best long-term performance stability. Analog to the potentiodynamic measurements, it can be assumed that *in situ* alloying of Pt and Au nanoparticles takes place under FAOR potentiostatic conditions. This indicates that the mechanisms accounted for the *in situ* alloying are more pronounced in potentiodynamic treatments than in potentiostatic ones. Therefore, under potentiostatic conditions a higher Au loading is required for the optimal result. This conclusion is supported by the particle size distributions obtained for Pt + 7Au/C from *ex situ* SAXS after the potentiostatic tests (Figure S11), which show signs of alloying of Pt and Au as well. Furthermore, also the Bragg peaks shift slightly in position (Figure 6d) as discussed before. By comparison, these changes are substantially less pronounced for the data of the Pt + 5Au/C catalyst, which display in the sample exposed to the potentiostatic tests similar peak positions as for the pristine sample (Figure 6b).

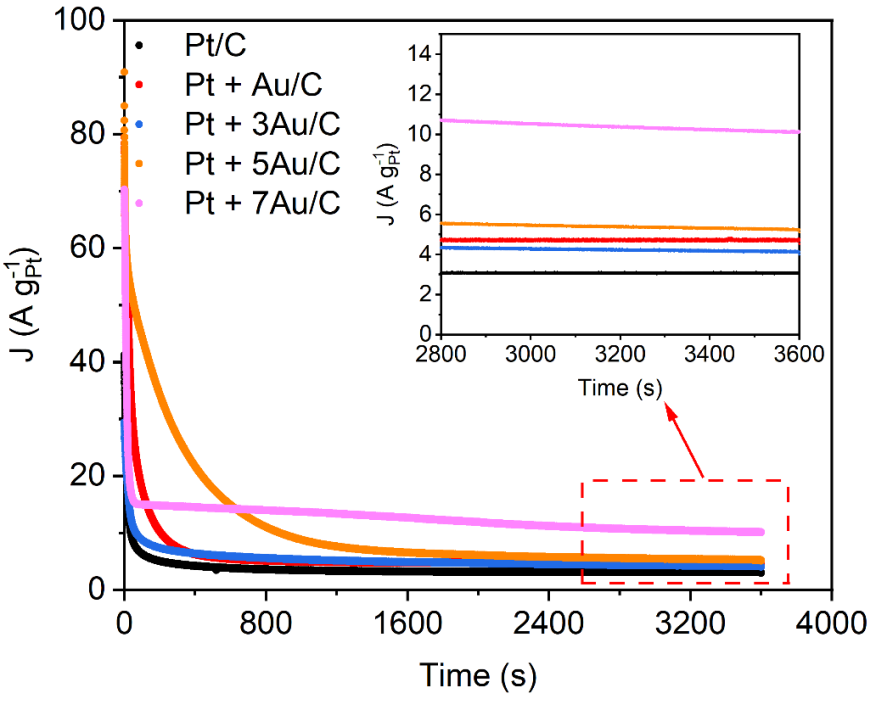

Figure 7. Potentiostatic measurements of FAOR by holding potential at 0.3 V_{RHE} for 1 hour, the inset is the magnified view of catalytic activity at steady state.

3. CONCLUSIONS

We present a concept of Pt + xAu/C nanocomposites with variable Au loadings for the FAOR. *Ex situ* and *operando* SAXS, WAXS, TEM, STEM-EDX, and PDF combined indicate that the separate deposition of Pt and Au nanoparticles onto a carbon support can be used to *in situ* form Pt-Au surface alloys with variable composition. Varying the Pt to Au ratio is easy and straightforward and requires only the preparation of two colloidal nanoparticle stocks. This is a significant advantage over the preparation of series of alloy nanoparticles with varying composition. In our work, it is demonstrated how this nanocomposite approach can be used to optimize the FAOR performance. This optimization not only on the Pt to Au ratio in the nanocomposite but also from the electrochemical conditioning. While in potentiodynamic tests Pt + 5Au/C is the optimal nanocomposite, steady state conditioning indicates improved long-term activity for Pt + 7Au/C. Although the exact amount of surface alloying is difficult to differentiate for the Pt-Au system, the results indicate that as compared to alloy nanoparticles, the nanocomposite concept does not only allow for an easier preparation and optimization, it might also show a way to optimize the use of precious and critical raw materials by surface alloying, in our case Pt onto Au nanoparticles.

4. EXPERIMENTAL

4.1 Chemicals and Materials

The following chemicals were used for platinum nanoparticles (Pt NPs) synthesis and flocculation: hexa-chloroplatinic (IV) acid hexahydrate ($H_2PtCl_6 \cdot 6H_2O$, 99.9%, Alfa Aesar), ethylene glycol (EG, 99%, Alfa Aesar), sodium hydroxide (NaOH, 99.99%, Merck), 37% hydrochloric acid (HCl, Suprapur, Merck) and acetone (for HPLC, VWR Chemicals BDH). Carbon black of Vulcan XC72R was employed as support for metal nanoparticle deposition. 37% hydrochloric acid (HCl, Suprapur, Merck) and 65% nitric acid (HNO_3, Suprapur, Merck) were used for metal nanoparticles dissolution for inductively coupled plasma mass spectrometry analysis. Isopropanol (IPA, for HPLC, VWR Chemicals BDH), Milli-Q water (resistivity>18.2 MΩ·cm, total organic carbon (TOC) <5 ppb) and Nafion (D1021, 10 wt.%, Fuel Cell Store) were used for catalyst ink preparation. 70% perchloric acid ($HClO_4$, Suprapur, Merck) and formic acid (FA, ≥95%, Sigma Aldrich) were used for electrolyte and reactant during the electrochemical measurements. Gas diffusion layer (GDL) with microporous layer (H23C8, Freudenberg) and without microporous layer (H23, Freudenberg) and Nafion membrane (Nafion 117, Fuel Cell Store) were used for catalyst layer assembly. Ar (99.999%, Air Liquide) and CO (99.97%, Air Liquide) were used for electrochemical measurements.

4.2 Synthesis of Supported Pt/C and Pt + xAu/C Nanocomposite Catalysts

The supported catalysts synthesis method includes two steps: the colloidal metal NPs preparation and the following supporting onto carbon black. A laser-based approach was applied to prepare colloidal Au NPs (solution in water). The specific method was detailed in previous studies.[50,51] Concerning the Pt NPs, a surfactant-free colloidal approach was applied[52] and cited by our recent work.[33,34] Briefly, the same volumes of NaOH EG solution (400 mM) and $H_2PtCl_6 \cdot 6H_2O$ EG

solution (40 mM) were mixed in a microwave reactor, the mixture was heated to 160 ℃ and kept under such temperature for three minutes to obtain colloidal Pt in EG with a concentration of 3.90 g_{Pt} L^{-1}. In order to support Pt NPs on carbon, the Pt colloid in EG is flocculated with 1 M HCl, and centrifuged, whereafter the Pt NPs can be separated from the EG and re-dispersed in acetone (3.90 g_{Pt} L^{-1}). Then, a carbon support (Vulcan XC72R) acetone suspension was mixed with a specific amount of Pt NPs acetone solution and homogenized by a horn sonicator for five minutes, acetone was evaporated with a rotary evaporator, and 10 wt.% Pt/C (nominal loading) catalyst powder was obtained. To prepare supported Pt + xAu/C nanocomposite catalysts, Pt NPs acetone solution (the Pt content is the same as pure Pt/C) and Au NPs water solution (0.075 g_{Au} L^{-1}) were added to the carbon acetone suspension as simultaneously as possible, under vigorous stirring, the mixture was left in the fume hood overnight under mild stirring for solvent evaporation and a dried catalyst was obtained. A similar preparation approach was applied for all Pt + xAu/C nanocomposite catalysts synthesis, during which procedure the nominal Pt content was kept as a constant, while the Au content was changeable according to experimental demand.

4.3 Electrochemical Measurements in Gas Diffusion Electrode (GDE) Setup

All electrochemical measurements were performed in a three-electrode system with a computer controlled potentiostat (ECi-200, Nordic Electrochemistry ApS) at room temperature. An in-house GDE setup is detailed in the previous studies.[37,38,39] Briefly, the GDE (working electrode) was placed on the top of the lower cell body, which is made of polytetrafluoroethylene (PTFE), on which top the upper cell body formed by PTFE was assembled. A Pt mesh used as a counter electrode (CE) and a reversible hydrogen electrode (RHE) used as a reference electrode (RE) were placed in the upper cell body, 1 M $HClO_4$ in the upper cell part served as electrolyte. A bubbler

filled up with 5 M FA was used to bring in the reactant, from which the Ar gas was introduced to FA and the FA stream was then evaporated to the GDE surface for further electrocatalytic reaction.

Concerning GDE fabrication, the catalyst (200 μg_{Pt} cm^{-2}_{geo} is the nominal loading for all catalysts) was pre-filtered on GDL (H23C8) via vacuum filtration.[53] Ø 3 mm of the filtered catalyst layer was punched and inserted to a Ø 2 cm GDL (H23C8) with a hole in the center, the Nafion membrane (Nafion 117) of 1.5 cm in diameter was pressed on top of GDL.

Prior to electrochemical measurements, the catalyst surface was cleaned by potential cycling in a region of 0.15-1.20 V_{RHE} with the scanning speed of 500 mV s^{-1}, until a stable cyclic voltammogram (CV) could be detected (normally 20-30 cycles), during which procedure, the bubbler was filled up with Milli-Q water and the Ar gas was continuously introduced into the bubbler. The CO stripping measurement was then conducted on each investigated catalyst to determine the Pt accessible surface area (ECSA). After which, the Milli-Q water in the bubbler was replaced by 5 M FA and Ar was flushed for 10 minutes (we tested 5 M FA in bubbler could be more rational compared with 2 M and 10 M FA, see Figure S13), followed by potential holding at 0.46 V_{RHE} for 30 minutes for catalyst activation and potentiodynamic tests (potential cycling in the region of 0.15- 1.20 V_{RHE} for ~50 cycles with a scanning speed of 50 mV s^{-1}) to collect the most repetitive CV (normally a stable CV could be reached within the first 20 cycles).

A similar measurement procedure was performed in potentiostatic tests, i.e., catalyst surface cleaning, CO stripping measurement, catalyst activation. The potentiostatic tests were then conducted at a static potential of 0.30 V_{RHE} for 1 hour, the corresponding current versus time was recorded to evaluate the poisoning resistance of the investigated catalysts.

4.4 Characterization

4.4.1 Small-Angle X-ray Scattering (SAXS) and Wide-Angle X-ray Scattering (WAXS)

The *ex situ* measurements were performed at the Niels Bohr Institute of the University of Copenhagen, using a Nano-inXider instrument from Xenocs (Grenoble, France) using a Cu Kα source with a 1.54 Å wavelength and a two-detector setup for simultaneous SAXS/WAXS measurements. Both detectors are Pilatus3 hybrid pixel detectors from Dectris. Using a 0.8 mm beam size the system provides a combined q-range from 0.01 $Å^{-1}$ to 4 $Å^{-1}$ with a flux on the sample of ca. 60Mph/s. Samples were measured for 30 minutes. The samples with metal NPs on GDL were placed between two mica windows in dedicated sandwich cells and the background was measured on a same GDL plus carbon black (without metal NPs). All the data fitting was conducted with a home written MATLAB code assuming log-normal size distributions. The size distribution is shown as total volume weighted probability density. The specific expressions used in the MATLAB code are detailed in previous reports.[34] All the values obtained for the free parameters in the model and the corresponding fits are shown in Table S2 and Figure S14, respectively.

4.4.2 Operando Small Angle X-ray Scattering (SAXS)

The measurements were carried out at cSAXS beamline at SLS, PSI (Villigen, Switzerland). The operando cell was adapted from Binninger et al.[54] and is detailed in our previous studies.[55] In contrast to the GDE setup, the electrolyte is directly in contact to the liquid electrolyte. A GDL (H23C8; Freudenberg) served as CE, Ag/AgCl served as RE, pre-filtered catalyst layer (punched a circle piece of 5 mm in diameter) inserted in a GDL stripe (a hole of 5 mm in diameter in the middle) served as WE. Both CE and WE were fixed on a Kapton tape with MPL side facing electrolyte (0.1 M $HClO_4$ or 0.1 M $HClO_4$ + 0.1 M FA). The electrolyte was automatically pumped

into the cell with a syringe pump (KD Scientific) throughout the measurement, the flow rate of electrolyte was kept 1 mL min^{-1}. The electrochemistry measurements were conducted in the following sequence: $HClO_4$ introduction, potential sweeping for catalyst surface cleaning (-0.0417- 1.0083 $V_{Ag/AgCl}$ with a scan speed of 500 mV s^{-1}, 25 cycles), $HClO_4$ + FA introduction, potential cycling (-0.0417- 1.0083 $V_{Ag/AgCl}$ with a scan speed of 50 mV s^{-1}, 10 repeats), catalyst activation (holding potential at 0.2683 $V_{Ag/AgCl}$ for 30 min) and potentiodynamic test with potential cycling (-0.0417- 1.0083 $V_{Ag/AgCl}$ with a scan rate of 50 mV s^{-1}, 10 cycles is a set, 18 and 10 sets in total for Pt + 5Au/C and Pt + 2Au/C, respectively). The pristine sample prior to any measurements was evaluated with *operando* SAXS, then after each electrochemistry step, *operando* SAXS was conducted to monitor the change in particle size distribution. During FAOR potentiodynamic test, after each set of potential cycling the *operando* SAXS measurements were collected. As schemed in Figure S15, four different spots on GDL were monitored in *operando* SAXS for background correction and two spots on catalyst layer for sample analysis. Sample and background spots were measured in sequence by shifting between the x-y stage of each collected scattering data in each run, then the corresponding background contribution was subtracted from SAXS analysis. It is necessary to point out that the background experiences the same electrochemical treatment as the sample in each run and a pure GDL without carbon support serves as background could lead to a wider distribution towards large particle size direction, as the carbon nanoparticles of ~30 nm[56] are included in sample analysis. All electrochemistry measurements were done with unpurged electrolyte solutions.

A home-written program was used for *operando* SAXS analysis. All SAXS fittings were conducted using Monte Carlo mode without introducing subjective factors. Before SAXS fitting, the data from two different spots for catalyst measurements and the data from the corresponding

spots for background measurements are respectively averaged in the program. The following parameters were applied for *operando* SAXS analysis: error weighing of q (for Pt + 5Au/C) and q^2 (for Pt + 2Au/C), smoothing of no weight, norm after iteration of 1000, and number of smoothings of 50, the particle sizes were logarithmically scaled.

4.4.3 Transmission Electron Microscopy (TEM) and Identical Location Transmission Electron Microscopy (IL-TEM)

The TEM analysis was conducted at the Anatomy Institute at the University of Bern. All the measurements were operated at 80 kV and equipped with an Olympus-SIS Veleta CCD Camera for micrographs recording. The as-prepared catalyst samples were prepared by dispersing catalyst powder in ethanol and dropping the catalyst solution onto TEM copper grids. The samples after electrochemical measurements and potentiostatic tests were collected by scraping the catalysts off the GDLs and dispersed in ethanol. TEM micrographs were collected from five independently selected areas for each analyzed sample.

The same equipment and a gold finder grid were applied for IL-TEM analysis. Concerning sample preparation, the Pt + 5Au/C catalyst powder was dissolved in the mixture of IPA and H_2O (V_{IPA}: V_{H2O} = 3: 1), 7 µl of Nafion was added to lead to the weight ratio between Nafion and carbon support of 1: 1. The catalyst ink was diluted by a factor of 10, 10 µl of the diluted ink was pipetted onto Au grid for IL-TEM analysis before electrochemistry. Afterwards, the same Au grid was placed between a Nafion membrane and GDL in GDE setup, after FAOR potentiodynamic test, the Au grid was analyzed with IL-TEM.

4.4.4 Scanning Electron Microscope (SEM)

The composition of the filtered Pt + xAu/C nanocomposites on GDL was determined by SEM-EDX. The Ø 3 mm GDL stuck on the carbon tape was placed on a metal holder for SEM analysis.

The analysis was performed on a Zeiss Gemini 450 SEM, which is equipped with an Oxford Instruments UltimMax 65 EDX detector, a voltage of 25 kV was used for all SEM measurements. Five random areas on the GDL were determined for each catalyst. A software of AZtec 4.2 was used to acquire the EDX spectra and to analyze the catalyst composition.

4.4.5 Scanning Transmission Electron Microscopy (STEM)

STEM imaging in combination with EDX analysis was carried out by using a 3000F JEOL transmission electron microscope equipped with a scan unit for STEM and an Oxford instruments SiLi-detector. An analytical probe with a nominal size of 1 nm and a 70 µm condenser aperture was used to maximize the EDS signal. A high-angle annular dark-field (HAADF) detector was used for imaging.

4.4.6 Pair Distribution Function (PDF)

X-ray total scattering data for Pair Distribution Function analysis were collected at the 11-ID-B beamline at the Advanced Photon Source, Argonne National Laboratory, Argonne, USA. All data were collected at room temperature using a wavelength of 0.2113 Å. The samples were measured in between two layers of Kapton films.

The detector distance and geometrical parameters were obtained from calibration in Fit2D[57] and the 2D patterns were integrated using pyFAI in Dioptas[58,59] The scattering signal from the carbon background was subtracted from the total scattering data before obtaining PDFs. The total scattering data were Fourier transformed to obtain the PDF using PDFgetX3[60] and modelled using PDFgui.[61] The following parameters were used in PDFgetX3: Qmin = 0.1 $Å^{-1}$, Qmax = 18 $Å^{-1}$, $Qmax_{inst}$ = 25 $Å^{-1}$, and rpoly = 0.9 Å.

The PDF was modelled with a two-phase model using the Pt *fcc* and Au *fcc* structures. The refinements were done in the r-range 1.5-60 Å. In the refinement of the model to the PDF from the Pt + Au/C sample, the scale factor, unit cell parameter, and crystallite size for each of the two phases were refined. An isotropic atomic displacement parameter and a parameter describing correlated motion (delta2) were furthermore refined, however, these were constrained to take the same value for the two phases due to high correlation. For the rest of the Pt + xAu/C nanocomposite samples, where Pt is the minority phase, the refinement was done in a similar way, except the unit cell parameter for Pt was kept fixed at the value obtained for the Pt + Au/C sample. Crystallite sizes of each sample were obtained from real-space Rietveld refinement by taking into account instrumental broadening. The refined parameters can be found in Table S3.

4.4.7 Inductively Coupled Plasma Mass Spectrometry (ICP-MS)

The actual metal contents after vacuum filtration on GDL were determined by ICP-MS (NexION 2000 ICP-MS), which is equipped with a cyclonic spray chamber and a PFA-nebulizer. The samples were prepared by immersing the Ø 3 mm circle GDL with filtered catalyst into aqua regia (volume ratio of HCl: HNO_3 = 3: 1) overnight, the solution was then diluted to 200 mL with Milli-Q water for ICP-MS analysis.

Table of Contents

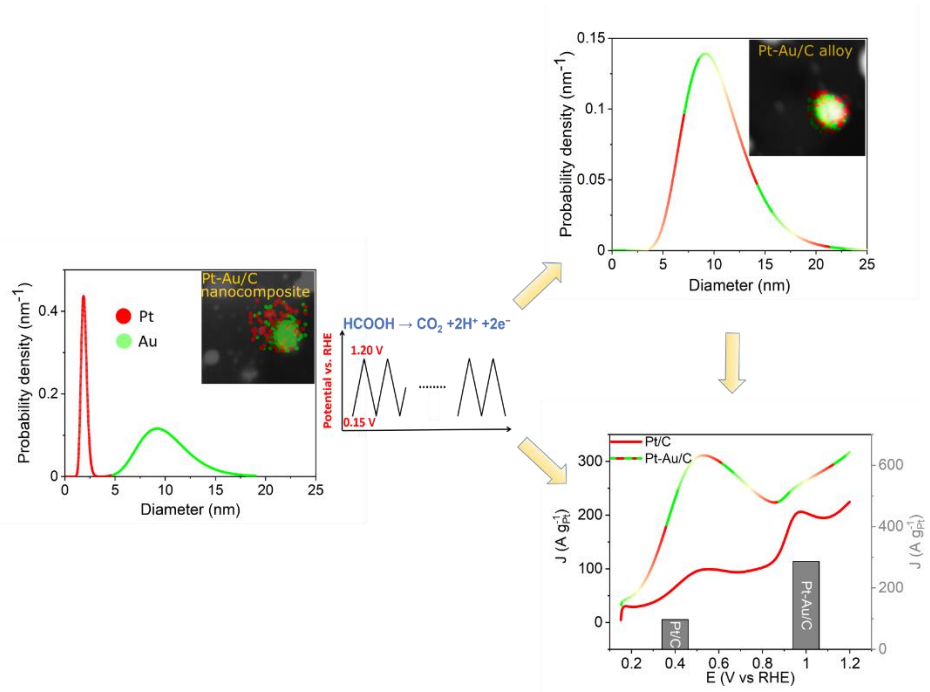

ASSOCIATED CONTENT

Supporting Information

The Supporting Information is available free of charge at DOI: XXXXXXX. Physical characterization of Pt/C reference; composition determination of nanocomposites; SAXS data fits and size analysis of the pristine catalysts; XRD patterns of pristine catalysts; PDF refinement; CO stripping measurements; quantitative analysis extracted from *operando* SAXS measurements; CVs of FAOR potentiodynamic tests after a certain repeat and with different FA concentrations; sketch of WE for *operando* SAXS measurements.

AUTHOR INFORMATION

Corresponding Author

Matthias Arenz – *Department of Chemistry, Biochemistry and Pharmaceutical Sciences, University of Bern, Freiestrasse 3, 3012 Bern, Switzerland;* ORCID: 0000-0001-9765-4315

Email: matthias.arenz@unibe.ch

Authors

Jia Du – *Department of Chemistry, Biochemistry and Pharmaceutical Sciences, University of Bern, Freiestrasse 3, 3012 Bern, Switzerland;* ORCID: 0000-0002-2387-1912

Jonathan Quinson – *Department of Chemistry, University of Copenhagen, Universitetsparken 5, 2100 Copenhagen Ø, Denmark;* ORCID: 0000-0002-9374-9330

Damin Zhang – *Department of Chemistry, Biochemistry and Pharmaceutical Sciences, University of Bern, Freiestrasse 3, 3012 Bern, Switzerland;* ORCID: 0000-0002-9037-6778

Baiyu Wang – *Department of Chemistry, University of Copenhagen, Universitetsparken 5, 2100 Copenhagen Ø, Denmark;* ORCID: 0000-0002-3777-7409

Gustav K.H. Wiberg – *Department of Chemistry, Biochemistry and Pharmaceutical Sciences, University of Bern, Freiestrasse 3, 3012 Bern, Switzerland;* ORCID: 0000-0003-1884-604X

Rebecca K. Pittkowski – *Department of Chemistry, University of Copenhagen, Universitetsparken 5, 2100 Copenhagen Ø, Denmark;* ORCID: 0000-0002-0351-4993

Johanna Schröder – *Department of Chemistry, Biochemistry and Pharmaceutical Sciences, University of Bern, Freiestrasse 3, 3012 Bern, Switzerland;* ORCID: 0000-0001-5461-4751

Søren B. Simonsen – *Department of Energy Conversion and Storage, Technical University of Denmark, Fysikvej Bldg. 310, Lyngby, DK-2800 Kgs., Denmark;* ORCID: 0000-0001-7172-1225

Jacob J. K. Kirkensgaard – Department of Food Science and Niels Bohr Institute, University of Copenhagen, Rolighedsvej 26, 1958 Frederiksberg, Denmark; ORCID: 0000-0001-6265-0314

Yao Li – *Technical Chemistry I and Center of Nanointegration Duisburg Essen (CENIDE), University of Duisburg-Essen, Universitätsstraße 7, Essen, North Rhine-Westphalia, 45141, Germany;* ORCID: 0000-0002-1151-7369

Sven Reichenberger – *Technical Chemistry I and Center of Nanointegration Duisburg Essen (CENIDE), University of Duisburg-Essen, Universitätsstraße 7, Essen, North Rhine-Westphalia, 45141, Germany;* ORCID: 0000-0002-7166-9428

Stephan Barcikowski – *Technical Chemistry I and Center of Nanointegration Duisburg Essen (CENIDE), University of Duisburg-Essen, Universitätsstraße 7, Essen, North Rhine-Westphalia, 45141, Germany;* ORCID: 0000-0002-9739-7272

Kirsten M. Ø. Jensen – *Department of Chemistry, University of Copenhagen, Universitetsparken 5, 2100 Copenhagen Ø, Denmark;* ORCID: 0000-0003-0291-217X

Author Contributions

J.D. and D.Z. conceived the project idea. J.D. performed all electrochemical measurements and analyzed experimental results. J.D. prepared Pt + xAu/C nanocomposites. J.Q. performed SAXS and WAXS measurements and did SAXS analysis. S.B.S. performed STEM-EDX measurements. J.J.K.K. performed WAXS measurements. G.K.H.W wrote a program for SAXS analysis. J.D. analyzed *operando* SAXS data. B.W. and K.M. Ø. J. analyzed PDF data. J.D. did TEM, IL-TEM and SEM-EDX measurements. D.Z. did IL-TEM and ICP-MS measurements. J.D., R.K.P. and J.S. did *operando* SAXS measurements. Y.L., S.R. and S.B. prepared Au colloids. M.A. supervised the overall project. J.D. wrote the first manuscript of the paper. R.K.P., J.Q. and G.K.H.W corrected language in the paper. M.A. determined the final version of the manuscript. All authors commented on the final version of the manuscript.

ACKNOWLEDGEMENTS

This work was supported by the Swiss National Science Foundation (SNSF) via the project No. 200021_184742 and the Danish National Research Foundation Center for High Entropy Alloy Catalysis (CHEAC) DNRF-149. Jia Du and Damin Zhang acknowledge funding from the China Scholarship Council (CSC). Jonathan Quinson acknowledges the European Union's Horizon 2020 research and innovation program under the Marie Skłodowska-Curie grant agreement No. 840523 (CoSolCat). WAXS data was generated via a research infrastructure at University of Copenhagen, partly funded by FOODHAY (Food and Health Open Innovation Laboratory, Danish Roadmap for Research Infrastructure). This research used resources of the Advanced Photon Source, a U.S. Department of Energy (DOE) Office of Science User Facility operated for the DOE Office of Science by Argonne National Laboratory under Contract No. DE-AC02-06CH11357 (11-ID-B beamline, proposal GUP-72059). Beamline scientists O. J. Borkiewicz, L. Gallington and T. Tinnibrugh are thanked for their help and support. Furthermore, we acknowledge the Paul Scherrer Institute, Villigen, Switzerland for provision of synchrotron radiation beamtime at the cSAXS (X12SA) beamline of the SLS and would like to thank Dr. A. Menzel for assistance (Proposal 20201725).

REFERENCES

(1) Gangloff, J. J.; Kast, J.; Morrison, G.; Marcinkoski, J. Design Space Assessment of Hydrogen Storage Onboard Medium and Heavy Duty Fuel Cell Electric Trucks. *Journal of Electrochemical Energy Conversion and Storage* **2017**, *14* (2). https://doi.org/10.1115/1.4036508.

(2) Zhang, H.; Shen, P. K. Recent Development of Polymer Electrolyte Membranes for Fuel Cells. *Chemical Reviews* **2012**, *112* (5), 2780–2832. https://doi.org/10.1021/cr200035s.

(3) Pollet, B. G.; Staffell, I.; Shang, J. L. Current Status of Hybrid, Battery and Fuel Cell Electric Vehicles: From Electrochemistry to Market Prospects. *Electrochimica Acta* **2012**, *84*, 235–249. https://doi.org/10.1016/j.electacta.2012.03.172.

(4) Bashir, S.; Hanumandla, P.; Huang, H. Y.; Liu, J. L. Nanostructured Materials for Advanced Energy Conversion and Storage Devices: Safety Implications at End-of-Life Disposal. *Nanostructured Materials for Next-Generation Energy Storage and Conversion: Fuel Cells* **2018**, *4* (May), 517–542. https://doi.org/10.1007/978-3-662-56364-9_18.

(5) Li, Z.; Zheng, Z.; Xu, L.; Lu, X. A Review of the Applications of Fuel Cells in Microgrids: Opportunities and Challenges. *BMC Energy* **2019**, *1* (1), 1–23. https://doi.org/10.1186/s42500-019-0008-3.

(6) Tellez-Cruz, M. M.; Escorihuela, J.; Solorza-Feria, O.; Compañ, V. Proton Exchange Membrane Fuel Cells (Pemfcs): Advances and Challenges. *Polymers* **2021**, *13* (18), 1–54. https://doi.org/10.3390/polym13183064.

(7) Kraytsberg, A.; Ein-Eli, Y. Review of Advanced Materials for Proton Exchange Membrane Fuel Cells. *Energy and Fuels* **2014**, *28* (12), 7303–7330. https://doi.org/10.1021/ef501977k.

(8) Wang, X.; Hu, J. M.; Hsing, I. M. Electrochemical Investigation of Formic Acid Electro-Oxidation and Its Crossover through a Nafion ® Membrane. *Journal of Electroanalytical Chemistry* **2004**, *562* (1), 73–80. https://doi.org/10.1016/j.jelechem.2003.08.010.

(9) Willsau, J.; Heitbaum, J. Analysis of Adsorbed Intermediates and Determination of Surface Potential Shifts by Dems. *Electrochimica Acta* **1986**, *31* (8), 943–948. https://doi.org/10.1016/0013-4686(86)80008-1.

(10) Rice, C.; Ha, S.; Masel, R. I.; Waszczuk, P.; Wieckowski, A.; Barnard, T. Direct Formic Acid Fuel Cells. *Journal of Power Sources* **2002**, *111* (1), 83–89. https://doi.org/10.1016/S0378-7753(02)00271-9.

(11) Parsons, R.; VanderNoot, T. The Oxidation of Small Organic Molecules. A Survey of Recent Fuel Cell Related Research. *Journal of Electroanalytical Chemistry* **1988**, *257* (1–2), 9–45. https://doi.org/10.1016/0022-0728(88)87028-1.

(12) Marković, N. M.; Ross, P. N. Surface Science Studies of Model Fuel Cell Electrocatalysts. *Surface Science Reports* **2002**, *45* (4–6), 117–229. https://doi.org/10.1016/s0167-5729(01)00022-x.

(13) Yajima, T.; Uchida, H.; Watanabe, M. In-Situ ATR-FTIR Spectroscopic Study of Electro-Oxidation of Methanol and Adsorbed CO at Pt-Ru Alloy. *Journal of Physical Chemistry B* **2004**, *108* (8), 2654–2659. https://doi.org/10.1021/jp037215q.

(14) Arenz, M.; Stamenkovic, V.; Schmidt, T. J.; Wandelt, K.; Ross, P. N.; Markovic, N. M. The Electro-Oxidation of Formic Acid on Pt-Pd Single Crystal Bimetallic Surfaces.

Physical Chemistry Chemical Physics **2003**, *5* (19), 4242–4251. https://doi.org/10.1039/b306307k.

(15) Arenz, M.; Stamenkovic, V.; Ross, P. N.; Markovic, N. M. Surface (Electro-)Chemistry on Pt(111) Modified by a Pseudomorphic Pd Monolayer. *Surface Science* **2004**, *573* (1), 57–66. https://doi.org/10.1016/j.susc.2004.05.144.

(16) Kang, Y.; Qi, L.; Li, M.; Diaz, R. E.; Su, D.; Adzic, R. R.; Stach, E.; Li, J.; Murray, C. B. Highly Active Pt 3Pb and Core-Shell Pt 3Pb-Pt Electrocatalysts for Formic Acid Oxidation. *ACS Nano* **2012**, *6* (3), 2818–2825. https://doi.org/10.1021/nn3003373.

(17) Chen, Q. S.; Zhou, Z. Y.; Vidal-Iglesias, F. J.; Solla-Gullón, J.; Feliu, J. M.; Sun, S. G. Significantly Enhancing Catalytic Activity of Tetrahexahedral Pt Nanocrystals by Bi Adatom Decoration. *Journal of the American Chemical Society* **2011**, *133* (33), 12930–12933. https://doi.org/10.1021/ja2042029.

(18) Jovanovič, P.; Može, M.; Gričar, E.; Šala, M.; Ruiz-Zepeda, F.; Bele, M.; Marolt, G.; Hodnik, N. Effect of Particle Size on the Corrosion Behaviour of Gold in the Presence of Chloride Impurities: An EFC-ICP-MS Potentiodynamic Study. *Coatings* **2019**, *9* (1). https://doi.org/10.3390/coatings9010010.

(19) Cherevko, S.; Topalov, A. A.; Zeradjanin, A. R.; Katsounaros, I.; Mayrhofer, K. J. J. Gold Dissolution: Towards Understanding of Noble Metal Corrosion. *RSC Advances* **2013**, *3* (37), 16516–16527. https://doi.org/10.1039/c3ra42684j.

(20) Krstajić Pajić, M. N.; Stevanović, S. I.; Radmilović, V. v.; Gavrilović-Wohlmuther, A.; Zabinski, P.; Elezović, N. R.; Radmilović, V. R.; Gojković, S. L.; Jovanović, V. M. Dispersion Effect in Formic Acid Oxidation on PtAu/C Nanocatalyst Prepared by Water-in-Oil Microemulsion Method. *Applied Catalysis B: Environmental* **2019**, *243* (July 2018), 585–593. https://doi.org/10.1016/j.apcatb.2018.10.064.

(21) Fan, H.; Cheng, M.; Wang, L.; Song, Y.; Cui, Y.; Wang, R. Extraordinary Electrocatalytic Performance for Formic Acid Oxidation by the Synergistic Effect of Pt and Au on Carbon Black. *Nano Energy* **2018**, *48* (January), 1–9. https://doi.org/10.1016/j.nanoen.2018.03.018.

(22) Xu, J. B.; Zhao, T. S.; Liang, Z. X. Carbon Supported Platinum-Gold Alloy Catalyst for Direct Formic Acid Fuel Cells. *Journal of Power Sources* **2008**, *185* (2), 857–861. https://doi.org/10.1016/j.jpowsour.2008.09.039.

(23) Zhang, S.; Shao, Y.; Liao, H. G.; Liu, J.; Aksay, I. A.; Yin, G.; Lin, Y. Graphene Decorated with PtAu Alloy Nanoparticles: Facile Synthesis and Promising Application for Formic Acid Oxidation. *Chemistry of Materials* **2011**, *23* (5), 1079–1081. https://doi.org/10.1021/cm101568z.

(24) Xue, Q.; Bai, X. Y.; Zhao, Y.; Li, Y. N.; Wang, T. J.; Sun, H. Y.; Li, F. M.; Chen, P.; Jin, P.; Yin, S. bin; Chen, Y. Au Core-PtAu Alloy Shell Nanowires for Formic Acid

Electrolysis. *Journal of Energy Chemistry* **2021**, *65*, 94–102. https://doi.org/10.1016/j.jechem.2021.05.034.

(25) Liu, C. W.; Wei, Y. C.; Liu, C. C.; Wang, K. W. Pt-Au Core/Shell Nanorods: Preparation and Applications as Electrocatalysts for Fuel Cells. *Journal of Materials Chemistry* **2012**, *22* (11), 4641–4644. https://doi.org/10.1039/c2jm16407h.

(26) Park, I. S.; Lee, K. S.; Choi, J. H.; Park, H. Y.; Sung, Y. E. Surface Structure of Pt-Modified Au Nanoparticles and Electrocatalytic Activity in Formic Acid Electro-Oxidation. *Journal of Physical Chemistry C* **2007**, *111* (51), 19126–19133. https://doi.org/10.1021/jp0739566.

(27) Kristian, N.; Yan, Y.; Wang, X. Highly Efficient Submonolayer Pt-Decorated Au Nano-Catalysts for Formic Acid Oxidation. *Chemical Communications* **2008**, *1* (3), 353–355. https://doi.org/10.1039/b714230g.

(28) Wang, R.; Wang, C.; Cai, W. bin; Ding, Y. Ultralow-Platinum-Loading High-Performance Nanoporous Electrocatalysts with Nanoengineered Surface Structures. *Advanced Materials* **2010**, *22* (16), 1845–1848. https://doi.org/10.1002/adma.200903548.

(29) Zhang, G. R.; Zhao, D.; Feng, Y. Y.; Zhang, B.; Su, D. S.; Liu, G.; Xu, B. Q. Catalytic Pt-on-Au Nanostructures: Why Pt Becomes More Active on Smaller Au Particles. *ACS Nano* **2012**, *6* (3), 2226–2236. https://doi.org/10.1021/nn204378t.

(30) Rizo, R.; Roldan Cuenya, B. Shape-Controlled Nanoparticles as Anodic Catalysts in Low-Temperature Fuel Cells. *ACS Energy Letters* **2019**, *4* (6), 1484–1495. https://doi.org/10.1021/acsenergylett.9b00565.

(31) Obradović, M. D.; Tripković, A. v.; Gojković, S. L. The Origin of High Activity of Pt-Au Surfaces in the Formic Acid Oxidation. *Electrochimica Acta* **2009**, *55* (1), 204–209. https://doi.org/10.1016/j.electacta.2009.08.038.

(32) Oko, D. N.; Zhang, J.; Garbarino, S.; Chaker, M.; Ma, D.; Tavares, A. C.; Guay, D. Formic Acid Electro-Oxidation at PtAu Alloyed Nanoparticles Synthesized by Pulsed Laser Ablation in Liquids. *Journal of Power Sources* **2014**, *248*, 273–282. https://doi.org/10.1016/j.jpowsour.2013.09.045.

(33) Du, J.; Quinson, J.; Zhang, D.; Bizzotto, F.; Zana, A.; Arenz, M. Bifunctional Pt-IrO2Catalysts for the Oxygen Evolution and Oxygen Reduction Reactions: Alloy Nanoparticles versus Nanocomposite Catalysts. *ACS Catalysis* **2021**, *11* (2), 820–828. https://doi.org/10.1021/acscatal.0c03867.

(34) Du, J.; Quinson, J.; Zana, A.; Arenz, M. Elucidating Pt-Based Nanocomposite Catalysts for the Oxygen Reduction Reaction in Rotating Disk Electrode and Gas Diffusion Electrode Measurements. *ACS Catalysis* **2021**, *11* (12), 7584–7594. https://doi.org/10.1021/acscatal.1c01496.

(35) Zhang, D.; Du, J.; Quinson, J.; Arenz, M. On the Electro-Oxidation of Small Organic Molecules: Towards a Fuel Cell Catalyst Testing Platform Based on Gas Diffusion Electrode Setups. *Journal of Power Sources* **2022**, *522*, 230979. https://doi.org/10.1016/j.jpowsour.2022.230979.

(36) Christiansen, T. L.; Cooper, S. R.; Jensen, K. M. O. There's No Place like Real-Space: Elucidating Size-Dependent Atomic Structure of Nanomaterials Using Pair Distribution Function Analysis. *Nanoscale Advances* **2020**, *2* (6), 2234–2254. https://doi.org/10.1039/d0na00120a.

(37) Alinejad, S.; Inaba, M.; Schröder, J.; Du, J.; Quinson, J.; Zana, A.; Arenz, M. Testing Fuel Cell Catalysts under More Realistic Reaction Conditions: Accelerated Stress Tests in a Gas Diffusion Electrode Setup. *JPhys Energy* **2020**, *2* (2). https://doi.org/10.1088/2515-7655/ab67e2.

(38) Wiberg, G. K. H.; Fleige, M.; Arenz, M. Gas Diffusion Electrode Setup for Catalyst Testing in Concentrated Phosphoric Acid at Elevated Temperatures. *Review of Scientific Instruments* **2015**, *86* (2). https://doi.org/10.1063/1.4908169.

(39) Inaba, M.; Jensen, A. W.; Sievers, G. W.; Escudero-Escribano, M.; Zana, A.; Arenz, M. Benchmarking High Surface Area Electrocatalysts in a Gas Diffusion Electrode: Measurement of Oxygen Reduction Activities under Realistic Conditions. *Energy and Environmental Science* **2018**, *11* (4), 988–994. https://doi.org/10.1039/c8ee00019k.

(40) Cabello, G.; Davoglio, R. A.; Hartl, F. W.; Marco, J. F.; Pereira, E. C.; Biaggio, S. R.; Varela, H.; Cuesta, A. Microwave-Assisted Synthesis of Pt-Au Nanoparticles with Enhanced Electrocatalytic Activity for the Oxidation of Formic Acid. *Electrochimica Acta* **2017**, *224*, 56–63. https://doi.org/10.1016/j.electacta.2016.12.022.

(41) Obradović, M. D.; Rogan, J. R.; Babić, B. M.; Tripković, A. V.; Gautam, A. R. S.; Radmilović, V. R.; Gojković, S. L. Formic Acid Oxidation on Pt-Au Nanoparticles: Relation between the Catalyst Activity and the Poisoning Rate. *Journal of Power Sources* **2012**, *197*, 72–79. https://doi.org/10.1016/j.jpowsour.2011.09.043.

(42) Yu, X.; Pickup, P. G. Recent Advances in Direct Formic Acid Fuel Cells (DFAFC). *Journal of Power Sources* **2008**, *182* (1), 124–132. https://doi.org/10.1016/j.jpowsour.2008.03.075.

(43) Hartl, K.; Nesselberger, M.; Mayrhofer, K. J. J.; Kunz, S.; Schweinberger, F. F.; Kwon, G.; Hanzlik, M.; Heiz, U.; Arenz, M. Electrochemically Induced Nanocluster Migration. *Electrochimica Acta* **2010**, *56* (2), 810–816. https://doi.org/10.1016/j.electacta.2010.10.005.

(44) Zana, A.; Speder, J.; Roefzaad, M.; Altmann, L.; Bäumer, M.; Arenz, M. Probing Degradation by IL-TEM: The Influence of Stress Test Conditions on the Degradation Mechanism. *Journal of The Electrochemical Society* **2013**, *160* (6), F608–F615. https://doi.org/10.1149/2.078306jes.

(45) Schröder, J.; Pittkowski, R. K.; Martens, I.; Chattot, R.; Drnec, J.; Quinson, J.; Kirkensgaard, J. J. K.; Arenz, M. Tracking the Catalyst Layer Depth-Dependent Electrochemical Degradation of a Bimodal Pt/C Fuel Cell Catalyst: A Combined Operando Small- and Wide-Angle X-Ray Scattering Study . *ACS Catalysis* **2022**, 2077–2085. https://doi.org/10.1021/acscatal.1c04365.

(46) King, H. W.; Vegard, Y. Lo. Yon Lo Vegard. *Journal of Materials Science* **1921**, *1* (1), 79–90.

(47) Denton, A. R.; Ashcroft, N. W. *Vegard's Law*; 1991; Vol. 43.

(48) Zhang, Q.; Yue, R.; Jiang, F.; Wang, H.; Zhai, C.; Yang, P.; Du, Y. Au as an Efficient Promoter for Electrocatalytic Oxidation of Formic Acid and Carbon Monoxide: A Comparison between Pt-on-Au and PtAu Alloy Catalysts. *Gold Bulletin* **2013**, *46* (3), 175–184. https://doi.org/10.1007/s13404-013-0098-5.

(49) Liu, J.; Cao, L.; Huang, W.; Li, Z. Preparation of AuPt Alloy Foam Films and Their Superior Electrocatalytic Activity for the Oxidation of Formic Acid. *ACS Applied Materials and Interfaces* **2011**, *3* (9), 3552–3558. https://doi.org/10.1021/am200782x.

(50) Kohsakowski, S.; Seiser, F.; Wiederrecht, J. P.; Reichenberger, S.; Vinnay, T.; Barcikowski, S.; Marzun, G. Effective Size Separation of Laser-Generated, Surfactant-Free Nanoparticles by Continuous Centrifugation. *Nanotechnology* **2020**, *31* (9). https://doi.org/10.1088/1361-6528/ab55bd.

(51) Letzel, A.; Reich, S.; dos Santos Rolo, T.; Kanitz, A.; Hoppius, J.; Rack, A.; Olbinado, M. P.; Ostendorf, A.; Gökce, B.; Plech, A.; Barcikowski, S. Time and Mechanism of Nanoparticle Functionalization by Macromolecular Ligands during Pulsed Laser Ablation in Liquids. *Langmuir* **2019**, *35* (8), 3038–3047. https://doi.org/10.1021/acs.langmuir.8b01585.

(52) Quinson, J.; Kunz, S.; Arenz, M. Beyond Active Site Design: A Surfactant-Free Toolbox Approach for Optimized Supported Nanoparticle Catalysts. *ChemCatChem* **2021**, *13* (7), 1692–1705. https://doi.org/10.1002/cctc.202001858.

(53) Yarlagadda, V.; McKinney, S. E.; Keary, C. L.; Thompson, L.; Zulevi, B.; Kongkanand, A. Preparation of PEMFC Electrodes from Milligram-Amounts of Catalyst Powder. *Journal of The Electrochemical Society* **2017**, *164* (7), F845–F849. https://doi.org/10.1149/2.1461707jes.

(54) Binninger, T.; Fabbri, E.; Patru, A.; Garganourakis, M.; Han, J.; Abbott, D. F.; Sereda, O.; Kötz, R.; Menzel, A.; Nachtegaal, M.; Schmidt, T. J. Electrochemical Flow-Cell Setup for In Situ X-Ray Investigations. *Journal of The Electrochemical Society* **2016**, *163* (10), H906–H912. https://doi.org/10.1149/2.0201610jes.

(55) Schröder, J.; Quinson, J.; Kirkensgaard, J. J. K.; Arenz, M. Operando SAXS Study of a Pt/C Fuel Cell Catalyst with an X-Ray Laboratory Source. *Journal of Physics D: Applied Physics* **2021**, *54* (29). https://doi.org/10.1088/1361-6463/abfa39.

(56) Zana, A.; Speder, J.; Reeler, N. E. A.; Vosch, T.; Arenz, M. Investigating the Corrosion of High Surface Area Carbons during Start/Stop Fuel Cell Conditions: A Raman Study. *Electrochimica Acta* **2013**, *114*, 455–461. https://doi.org/10.1016/j.electacta.2013.10.097.

(57) Hammersley, A. P. FIT2D: A Multi-Purpose Data Reduction, Analysis and Visualization Program. *Journal of Applied Crystallography* **2016**, *49* (2), 646–652. https://doi.org/10.1107/S1600576716000455.

(58) Kieffer, J.; Karkoulis, D. PyFAI, a Versatile Library for Azimuthal Regrouping. *Journal of Physics: Conference Series* **2013**, *425* (PART 20). https://doi.org/10.1088/1742-6596/425/20/202012.

(59) Prescher, C.; Prakapenka, V. B. DIOPTAS: A Program for Reduction of Two-Dimensional X-Ray Diffraction Data and Data Exploration. *High Pressure Research* **2015**, *35* (3), 223–230. https://doi.org/10.1080/08957959.2015.1059835.

(60) Juhás, P.; Davis, T.; Farrow, C. L.; Billinge, S. J. L. PDFgetX3: A Rapid and Highly Automatable Program for Processing Powder Diffraction Data into Total Scattering Pair Distribution Functions. *Journal of Applied Crystallography* **2013**, *46* (2), 560–566. https://doi.org/10.1107/S0021889813005190.

(61) Farrow, C. L.; Juhas, P.; Liu, J. W.; Bryndin, D.; Boin, E. S.; Bloch, J.; Proffen, T.; Billinge, S. J. L. PDFfit2 and PDFgui: Computer Programs for Studying Nanostructure in Crystals. *Journal of Physics Condensed Matter* **2007**, *19* (33). https://doi.org/10.1088/0953-8984/19/33/335219.

Supporting Information of Manuscript IV

Supporting Information

Nanocomposite Concept for Electrochemical *in situ* Preparation of Pt-Au Alloy Nanoparticles for Formic Acid Oxidation

Jia Du[a], Jonathan Quinson[b], Damin Zhang[a], Baiyu Wang[b], Gustav K.H. Wiberg[a], Rebecca K. Pittkowski[b], Johanna Schröder[a], Søren B. Simonsen[c], Jacob J. K. Kirkensgaard[d,e], Yao Li[f], Sven Reichenberger[f], Stephan Barcikowski[f], Kirsten M. Ø. Jensen[b], Matthias Arenz[a *]

[a] University of Bern, Department of Chemistry, Biochemistry and Pharmaceutical Sciences, Freiestrasse 3, 3012 Bern, Switzerland

[b] University of Copenhagen, Department of Chemistry, Universitetsparken 5, 2100 Copenhagen Ø, Denmark

[c] Technical University of Denmark, Department of Energy Conversion and Storage, Fysikvej Bldg. 310, Lyngby, DK-2800 Kgs., Denmark

[d] University of Copenhagen, Department of Food Science, Rolighedsvej 26, 1958 Frederiksberg, Denmark

[e] University of Copenhagen, Niels Bohr Institute, Universitetsparken 5, 2100 Copenhagen Ø

[f] University of Duisburg-Essen, Technical Chemistry I and Center of Nanointegration Duisburg Essen (CENIDE), Universitätsstraße 7, Essen, North Rhine-Westphalia, 45141, Germany

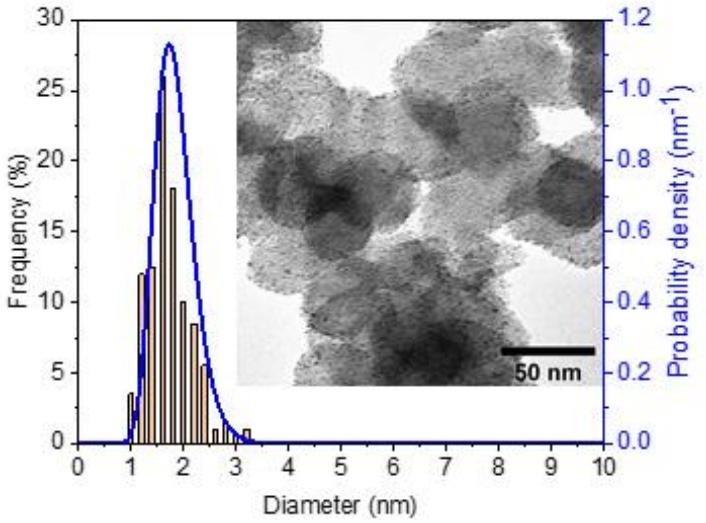

Figure S1. TEM micrographs and size distribution of the Pt/C reference. The histograms for particle size distribution evaluation are based on a statistical analysis of 200 Pt particles of the as-prepared Pt/C catalysts from TEM micrograph and the volume weighted probability density of the particle size is derived from SAXS measurement.

Table S1. The actual metal loading on GDL after vacuum filtration and the respective mass ratio between Au and Pt of the investigated electrocatalysts. The actual Pt and Au loading on GDL are determined by ICP-MS, the mass ratio of Au:Pt is checked by SEM-EDX and calculated from ICP-MS results, respectively.

	Pt mass on GDL (µg)	Au mass on GDL (µg)	Au:Pt (ICP-MS)	Au:Pt (SEM-EDX)
Pt/C	8.8	-	-	-
Pt + Au/C	5.6	5.8	1.04	1.10
Pt + 3Au/C	8.3	21.9	2.64	3.03
Pt + 5Au/C	8.3	39.3	4.73	5.33
Pt + 7Au/C	7.1	52.1	7.34	6.82
Au/C	-	6.0	-	-

Table S2. Parameters of SAXS data fits and size analysis of the pristine samples.

Catalysts	Power law		1st population			2nd population			Size and distribution							
									Smaller NPs 'Pt'			Larger NPs 'Au'			Overall	
	A x 10^6	n	R_1 (Å)	σ_1	C_1	R_2 (Å)	σ_2	C_2	D_1 (nm)	σ_1 (nm)	Volume fraction 1	D_2 (nm)	σ_2 (nm)	Volume fraction 2	Overall Diameter D (nm)	Overall Standard Deviation of D σ (nm)
Pt/C	25	3.5	9.0	0.20	0.0055	27.0	0.30	0	1.8	0.4	1.00	-	-	0	1.8	0.4
Pt + Au/C	23	3.5	9.0	0.20	0.0020	40.0	0.25	0.01	1.8	0.4	0.81	8.3	2.1	0.19	3.0	0.4
Pt + 3Au/C	50	3.8	9.5	0.15	0.0022	44.0	0.25	0.05	1.9	0.3	0.53	9.1	2.3	0.47	5.3	1.1
Pt + 5Au/C	35	4.0	9.5	0.15	7E-4	49.0	0.25	0.05	1.9	0.3	0.31	10.1	2.6	0.69	7.6	1.8
Pt + 7Au/C	50	4.0	8.5	0.10	7E-4	48.0	0.25	0.05	1.7	0.2	0.36	9.9	2.5	0.64	6.9	1.6

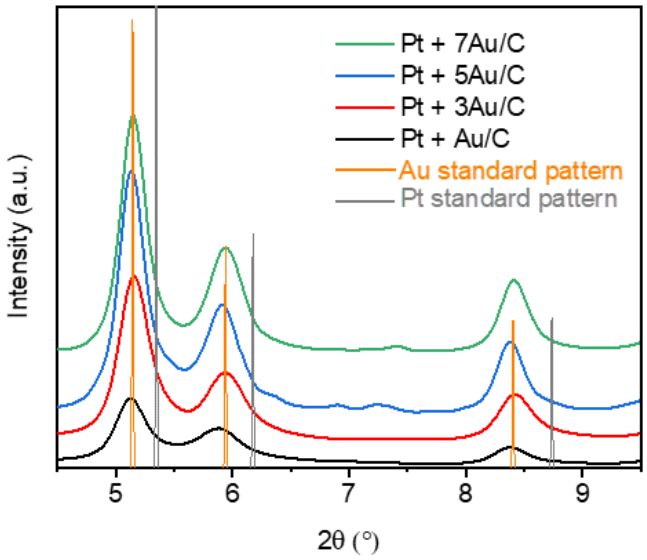

Figure S2. XRD diffractograms of the pristine Pt + xAu/C nanocomposites. The results are based on the total scattering data the PDFs were obtained from.

Table S3. Results from PDF refinements.

Catalysts	Au unit cell (Å)	Pt unit cell (Å)	Au/Pt Uiso ($Å^2$)	Au/Pt delta2 (Å)	Au crystallite size (Å)	Pt crystallite size (Å)	Au mass fraction	Pt mass fraction	Rw (%)
Pt + Au/C	4.09	3.97	0.010	4.3	50	17	0.65	0.35	26.4
Pt + 3Au/C	4.10	3.97	0.010	4.5	50	20	0.75	0.25	18.2
Pt + 5 Au/C	4.10	3.97	0.009	4.3	62	21	0.85	0.15	13.3
Pt + 7Au/C	4.11	3.97	0.010	4.8	63	17	0.72	0.28	12.5

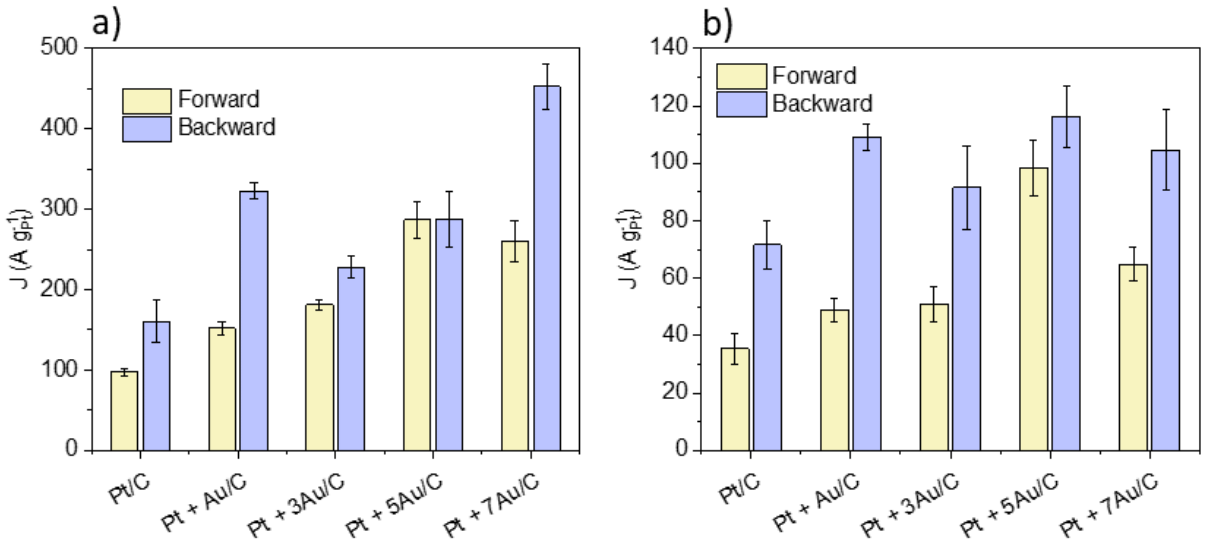

Figure S3. FAOR performance comparison of the investigated electrocatalysts with oxidation current recorded at (a) peak position (P_I for forward scanning and P_{III} for backward scanning, as displayed in Figure 3 in main text) and (b) potential of 0.3 V_{RHE} from both scanning directions. The standard deviation is obtained from at least three independent measurements for each investigated catalyst.

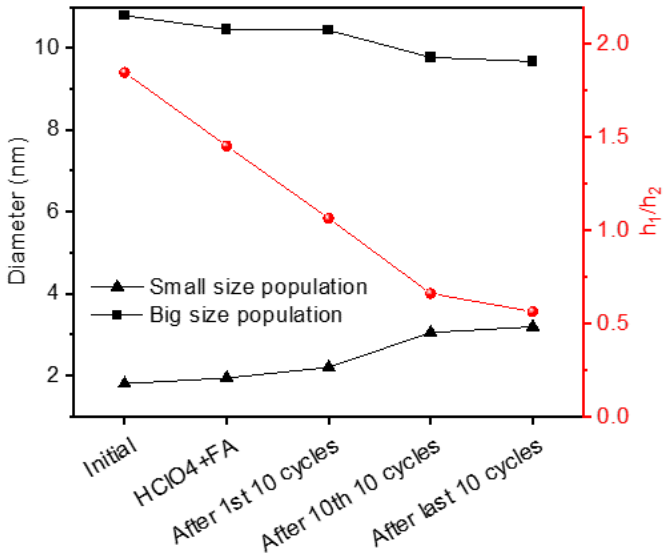

Figure S4. Particle characteristics of Pt + 5Au/C extracted from *operando* SAXS analysis. The corresponding particle size distributions are displayed in Figure 4 in the main text. The particle diameters of both populations reported here are based on the respective peak positions of maximum probability (mode) retrieved from the distribution functions presented in Figure 4. The h_1/h_2 ratios are calculated from the relative peak intensities at the mode for the small and big size populations on distribution functions.

Table S4. Pt and Au mass in 1.0 M $HClO_4$ electrolyte determined by ICP-MS. The electrolyte is filled in upper cell body of GDE setup. 5 mL of electrolyte in upper cell body is used for ICP-MS test before and after potentiodynamic test, respectively.

Pt + 5Au/C	Pt mass in electrolyte (µg)	Au mass in electrolyte (µg)
Before potentiodynamic test	0.0080	0.0000
After potentiodynamic test	0.1470	0.0009

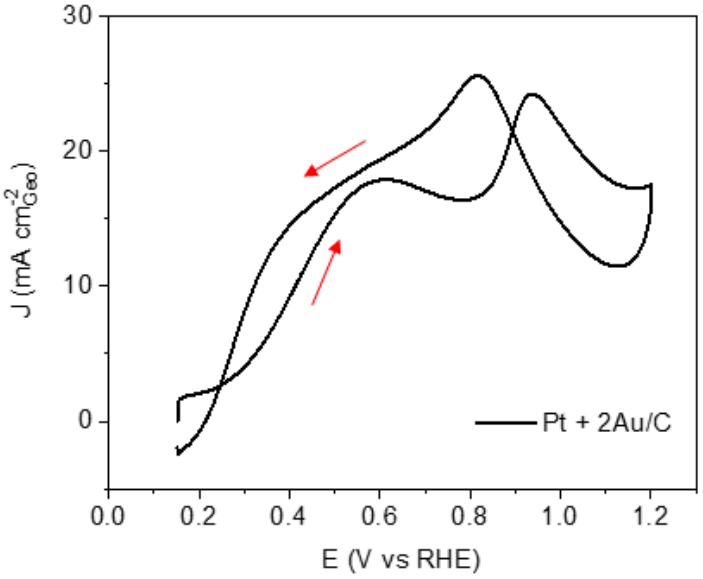

Figure S5. CV of FAOR potentiodynamic test of Pt + 2Au/C nanocomposite in GDE setup. The bubbler is filled up with 5.0 M formic acid and the upper cell body is filled up with 1.0 M $HClO_4$. A scanning speed of 50 mV s^{-1} is applied for measurements.

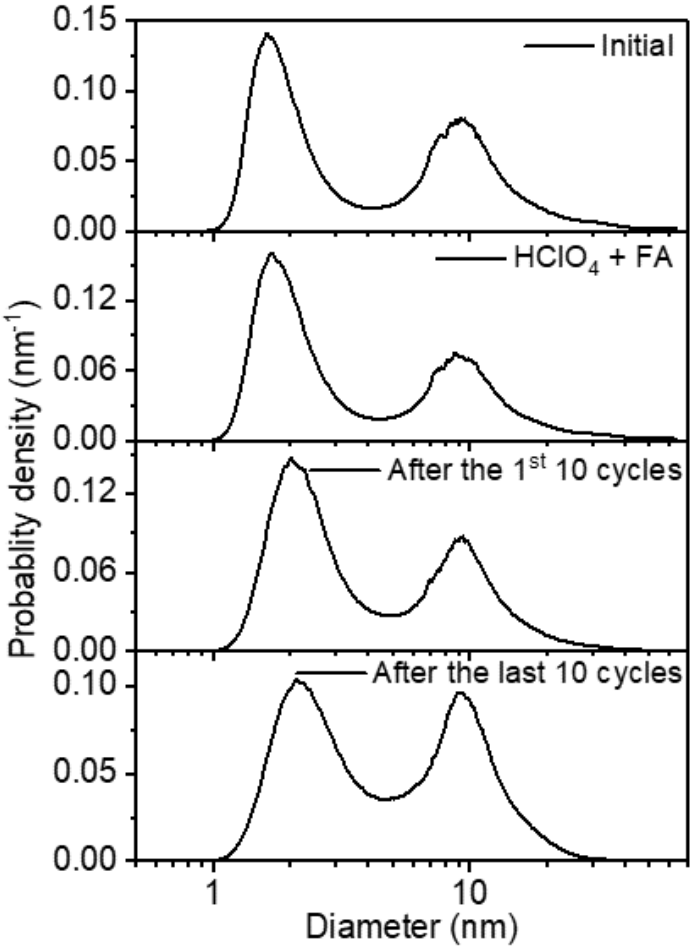

Figure S6. Size distributions of Pt + 2Au/C from operando SAXS analysis. The displayed size distribution functions are selected after a certain step of FAOR potentiodynamic test and in an order of top to the bottom as proceeding sequential measurement steps. A pure GDL serves as background for each background subtraction. Background and sample data are respectively averaged before SAXS fitting.

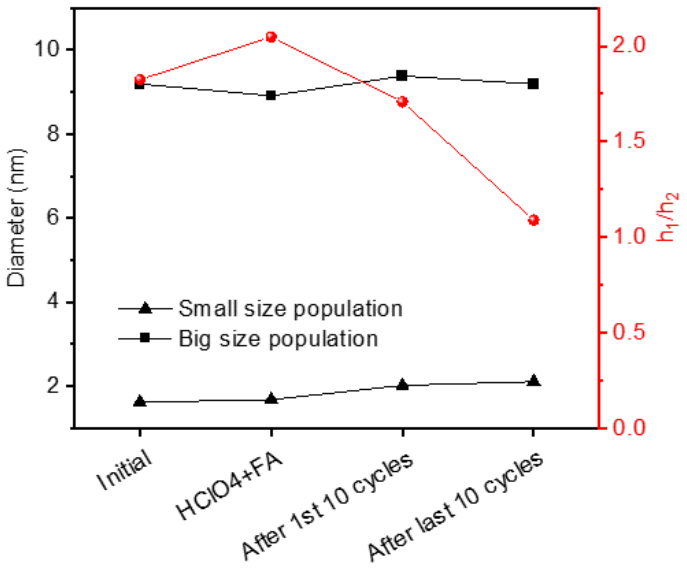

Figure S7. Particle characteristics of Pt + 2Au/C extracted from *operando* SAXS analysis. The corresponding particle size distributions are displayed in Figure S6. The particle diameters of both populations reported here are based on the respective peak positions of maximum probability (mode) retrieved from the distribution functions presented in Figure S6. The h_1/h_2 ratios are calculated from the relative peak intensities at the mode for the small and big size populations on distribution functions.

It is necessary to point out that less cycles were done in potentiodynamic test on Pt + 2Au/C. Ten times of potential cycling in each repeat and ten repeats in total. The last 10 cycles is corresponded to the 10^{th} 10 cycles on Pt + 2Au/C. It is seen that the ratio value of h_1/h_2 is decreased from 1.82 the initial value to 1.09 after potentiodynamic test, by comparison, h_1/h_2 value is decreased from 1.85 to 0.66 after the 10^{th} 10 potential sweeping on Pt + 5Au/C.

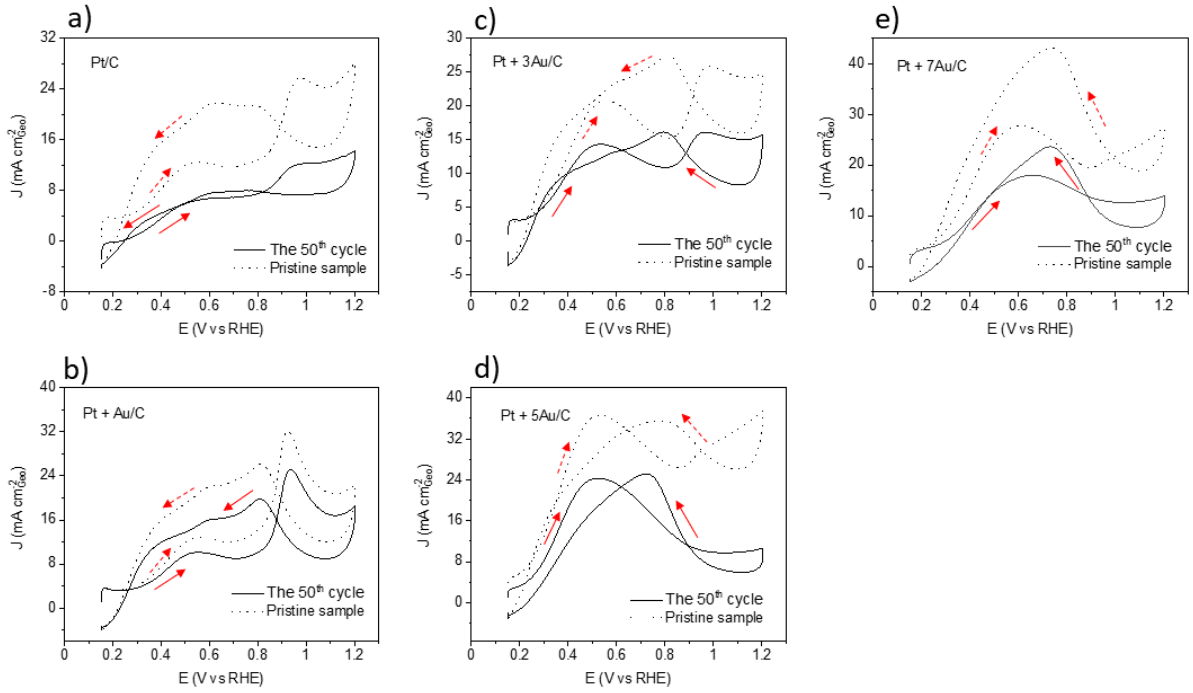

Figure S8. Comparison of CVs recorded from the pristine sample and the samples experience 50 times of potential sweeping in the FAOR potentiodynamic test in GDE setup. The bubbler is filled up with 5.0 M formic acid and the upper cell body is filled up with 1.0 M $HClO_4$. A scanning speed of 50 mV s^{-1} is applied for all measurements.

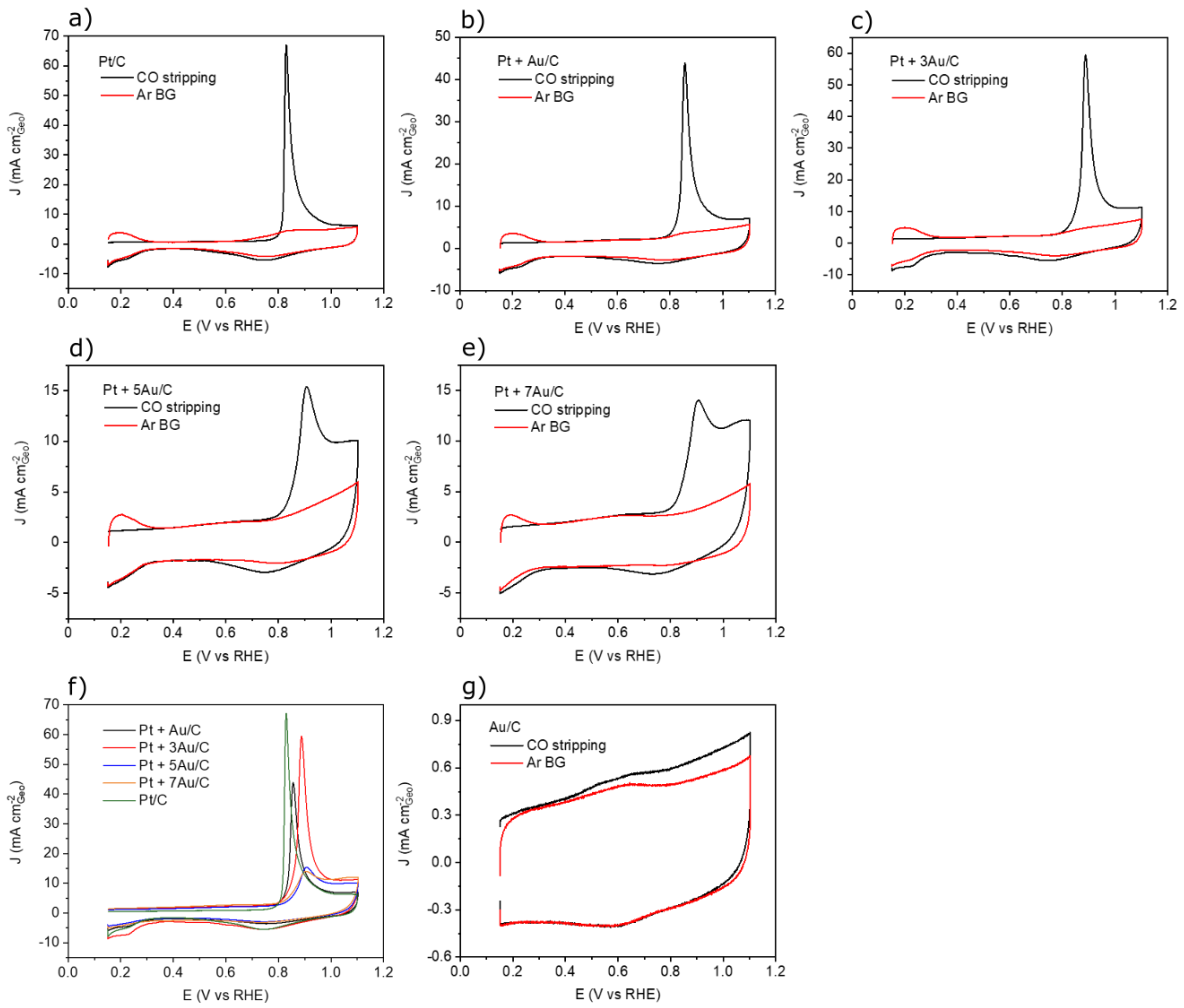

Figure S9. CO stripping curves and the subsequent CVs of the studied catalysts recorded in GDE measurements. The CO stripping curves of Pt-based catalysts are compared in Figure S9f. Scanning speed of 50 mV s^{-1} and 1.0 M $HClO_4$ serves as electrolyte in the upper cell body are applied for the measurements.

One can clearly observe the difference of CO stripping curves of the investigated catalysts. The catalysts with low Au content (one and three times higher of Au mass than Pt in composition) basically display the same feature as pure Pt/C, however, with Au loading increases to five (Figure S9d) and seven times (Figure S9e) higher than Pt, the CO oxidation peak seems to be incomplete in the standard potential window (0.15-1.10 V_{RHE}), therefore, an extended upper potential to 1.40 V_{RHE} is applied for these two catalysts and the CO stripping curves are exhibited in Figure S10, one can see a complete CO oxidation peak and thus only used to determine the ECSA of Pt +

5Au/C and Pt + 7Au/C. In addition, one can clearly observe that CO oxidation peaks are positively shifted with Au content (Figure S9f), as more Pt atoms are in direct contact with Au and thus the electronic modification is more pronounced. That is also the reason the standard potential window (0.15-1.10 V_{RHE}) is not sufficient for Pt + 5Au/C and Pt + 7Au/C in the CO stripping measurement.

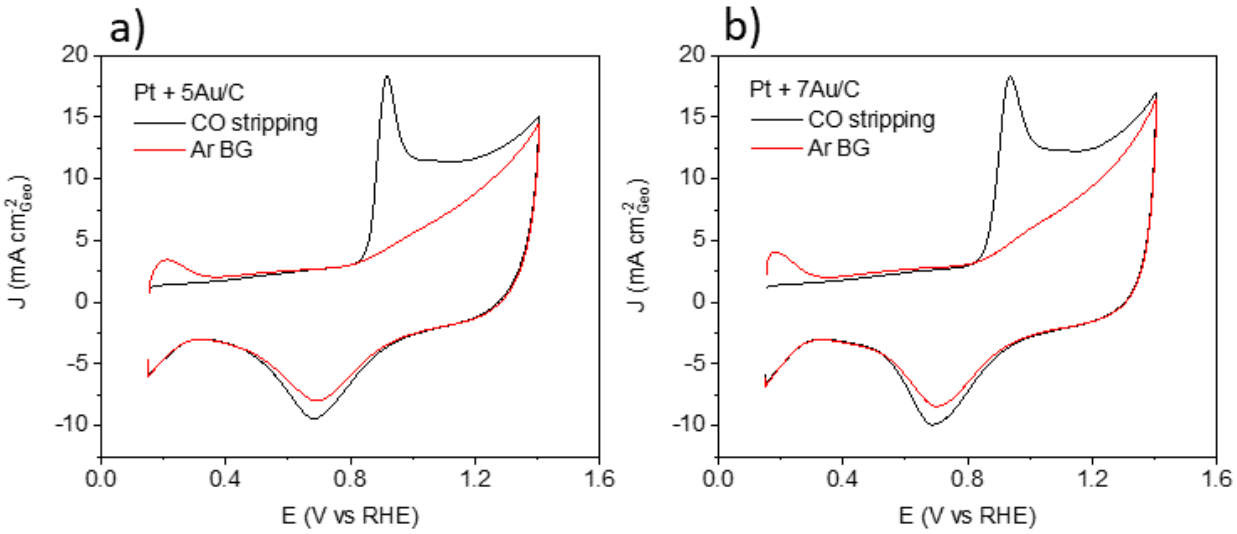

Figure S10. CO stripping curves and the subsequent CVs of the supported Pt + xAu/C nanocomposites (five and seven times higher than Pt composition in mass) with extended upper potential to 1.40 V_{RHE} in GDE setup. The scanning speed is 50 mV s^{-1} and the measurements are conducted with 1.0 M $HClO_4$ serves as electrolyte in the upper cell body in room temperature. The samples for the measurements are "one time" with no additional FAO measurements, to avoid pre-alloy of Pt and Au.

Table S5. The actual Pt loading (via ICP-MS) on GDL after vacuum filtration and the electrochemically Pt surface area (ECSA) of the investigated electrocatalysts. The ECSA values are normalized by the actual Pt mass on GDL. The upper potential in CO stripping measurements for ECSA determination is 1.10 V_{RHE} for Pt/C, Pt + Au/C and Pt + 3Au/C (Figure S9a-c), while an extended upper potential of 1.40 V_{RHE} is applied for Pt + 5Au/C and Pt + 7Au/C (Figure S10) to obtain a complete CO oxidation peak. Three independent CO stripping measurements are performed to add the standard deviations.

	Pt/C	Pt + Au/C	Pt + 3Au/C	Pt + 5Au/C	Pt + 7Au/C
Pt mass on GDL (µg)	8.8	5.6	8.3	8.3	7.1
ECSA ($m^2\ g_{Pt}^{-1}$)	110.8 ± 6.6	116.4 ± 8.6	123.0 ± 2.0	104.4 ± 5.8	104.8 ± 7.6

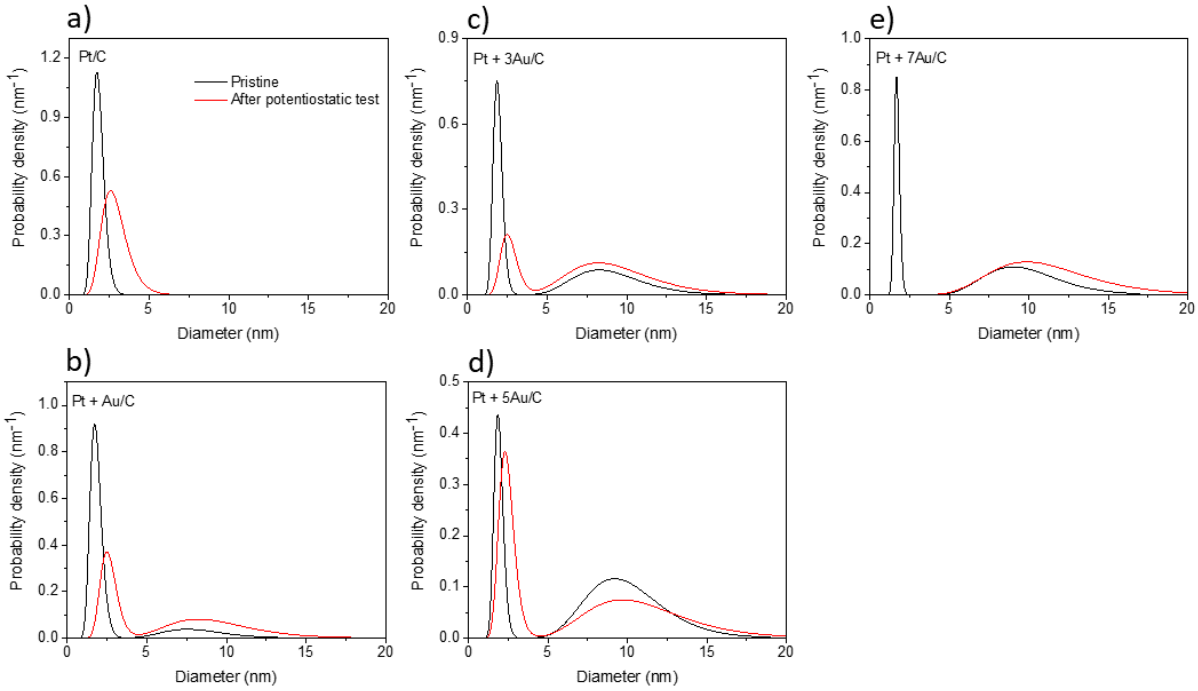

Figure S11. Size distribution comparison of the studied catalysts before and after potentiostatic test. All black curves represent the size distributions of each pristine sample, while all red curves are for the catalysts after potentiostatic test. The probability density of the particle size is derived from SAXS analysis with volume weighted.

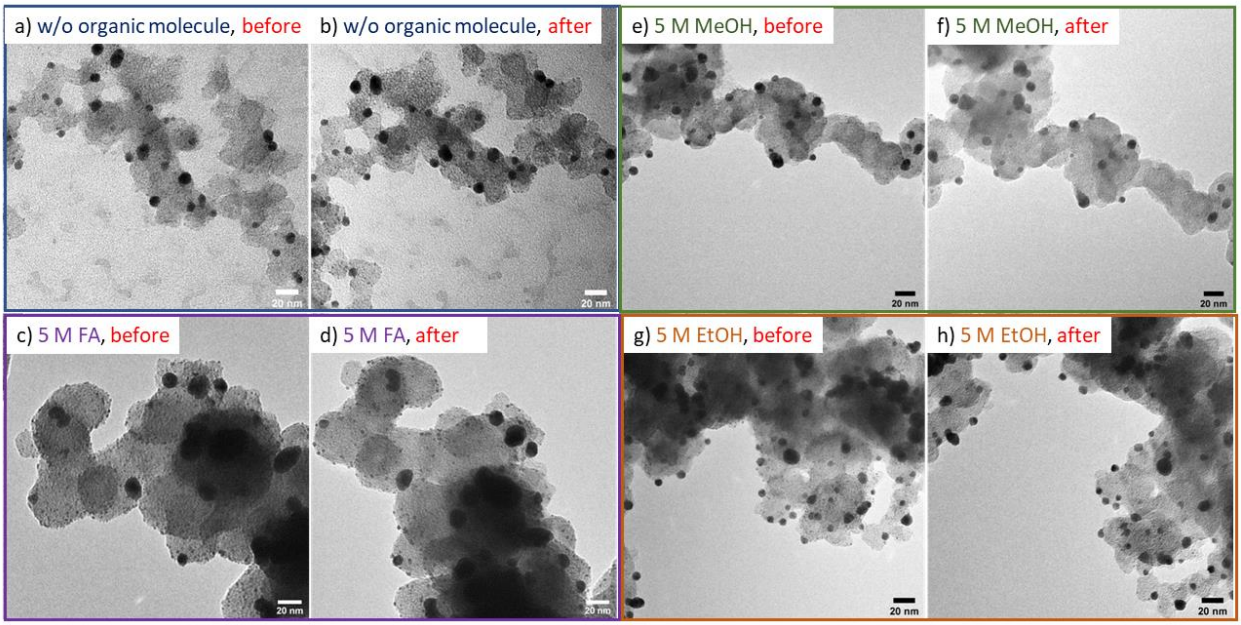

Figure S12. IL-TEM of Pt + 5Au/C before (pristine sample) and after (after 50 CVs in the potentiodynamic test) electrochemical treatment in GDE setup. The bubbler is filled with various organic solvent to differentiate measurement environment, and the evaporated liquid is carried by the purged Ar to reach catalyst layer for further reactions. A sweeping rate of 50 mV s^{-1} is applied for all measurements.

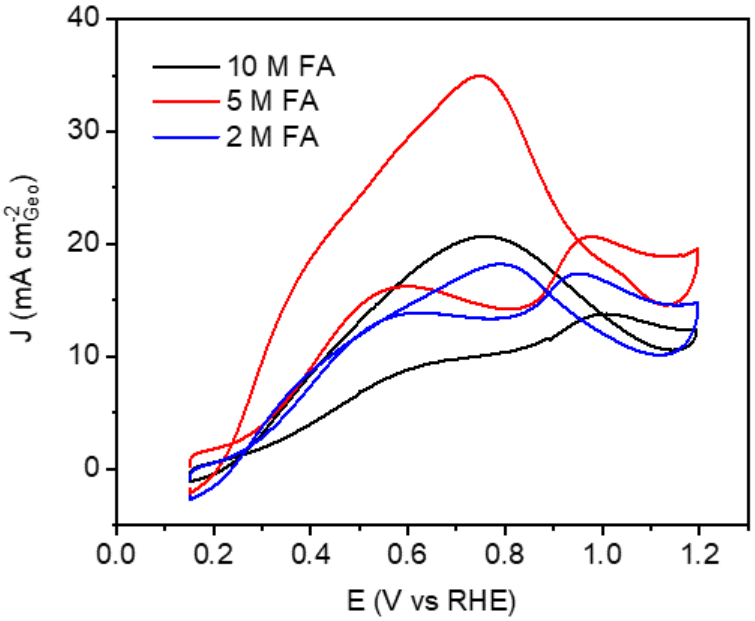

Figure S13. CVs of FAOR potentiodynamic test with different FA concentration in bubbler in GDE setup. The measurement is conducted on 2Pt + 4Au/C nanocomposite (the nominal Pt loading

is 20% in weight, all the rest nanocomposites in the study with a nominal Pt loading of 10% in weight). The upper cell body is filled up with 1.0 M $HClO_4$. A scanning speed of 50 mV s^{-1} is applied for all measurements.

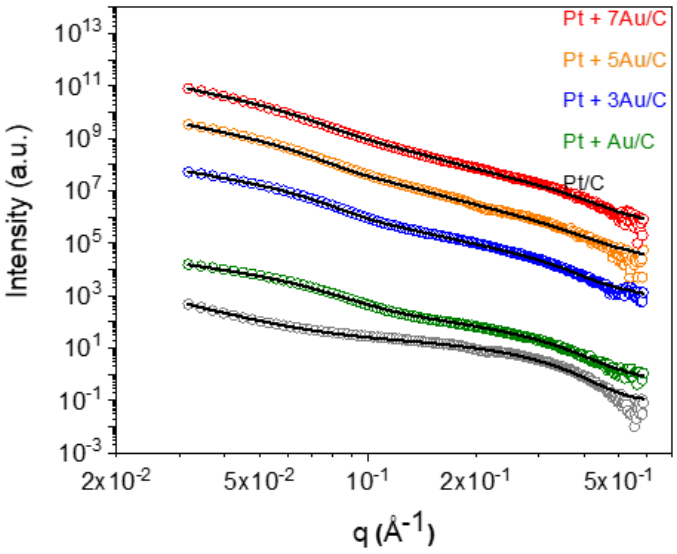

Figure S14. SAXS data and fits of the investigated pristine catalysts.

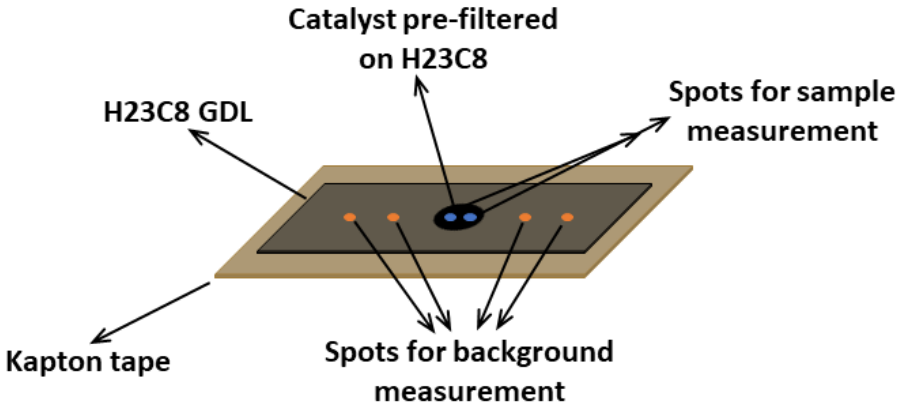

Figure S15. Sketch of WE inserted in a GDL stripe and fixed on the Kapton tape for *operando* SAXS measurements.

Manuscript V

On the Selective Dissolution of Ir and IrO_2 in Nanocomposite Electrocatalysts: A Pathway for Electrochemical Ir Recycling?

Jia Du[a+], Matej Zlatar[b+], Damin Zhang[a], Daniel Escalara[b], Jonathan Quinson[c], Serhiy Cherevko[b], Matthias Arenz[a *]

[a] University of Bern, Department of Chemistry, Biochemistry and Pharmaceutical Sciences, Freiestrasse 3, 3012 Bern, Switzerland

[b] Helmholtz-Institute Erlangen-Nürnberg for Renewable Energy (IEK-11), Forschungszentrum Jülich GmbH, 91058 Erlangen, Germany

[c] Department of Chemistry, University of Copenhagen, Universitetsparken 5, 2100 Copenhagen Ø, Denmark

[+] Equally contributing first authors

ABSTRACT

Herein, we report metal dissolution studies to scrutinize the degradation of bifunctional electrocatalysts used for mitigating cell reversal damages in the anode of proton exchange membrane fuel cells (PEMFCs). During cell reversal, substantial carbon corrosion occurs that can be mitigated by adding an IrO_2 oxygen evolution reaction (OER) catalyst to the anode. The OER catalyst will selectively promote the water oxidation rather than the carbon oxidation reaction (COR). For the concept to be implementable the stability of IrO_2 is essential, but previous reports suggest limited resistance to degradation. In the presented work, it is shown with the help of carbon supported bifunctional Pt-Ir/C and Pt-IrO_2/C nanocomposite catalysts that depending on the applied conditions, Ir/IrO_2 dissolution is substantially more pronounced than Pt dissolution. Thereby a hydrogen atmosphere, that was proposed to trigger a reduction of IrO_2 to Ir prior to dissolution, is not essential. While the demonstrated dissolution of IrO_2 and Ir limits the applicability of functional anode catalysts for cell reversal mitigation, it is shown here that electrochemistry provides a promising and much-needed pathway for selective Ir recycling of

catalyst coated membranes (CCMs). In particular, it is demonstrated that current based protocols can be used that enable simple two electrode setups in recycling.

KEYWORDS

Nanocomposite electrocatalysts; Ir/IrO_2 dissolution; Pt dissolution; Ir/IrO_2 recycling;

One of the main challenges that hinders the widespread commercialization of electrochemical energy conversion devices such as fuel cells and water electrolysis cells is meeting long-term durability targets[1–5]. In PEMFCs, one of the conditions limiting the lifetime of the catalyst is cell reversal which can occur due to undersupply of hydrogen fuel at the anode during transient operation. This leads to a temporarily rise in anode potential to values well above the one of the cathode (> 1 V_{RHE}) and thus substantial carbon corrosion as well as Pt dissolution at the anode catalyst[5]. To mitigate this effect, bifunctional Pt – IrO_2 catalysts, also called co-catalysts, have been introduced to catalyze the oxygen evolution reaction (OER) instead of the COR during cell reversal. Even though IrO_2 is the most stable OER catalyst, it has been reported that the H_2 gas at the PEMFC anode can chemically reduce a few outer monolayers of the surface of IrO_2 nanoparticles to metallic Ir which then is more prone to dissolution[5]. Furthermore, bifunctional Pt-IrO_2 catalysts have been proposed for the use of so-called unitized regenerative fuel cells (URFCs) that would allow a closed loop system to use and produce hydrogen on demand. Similarly, as for mitigating cell reversal, in URFCs the electrocatalyst needs to accommodate different reaction conditions to produce electricity as well as to re-generate the hydrogen fuel when connected to an external energy source[6]. Two different concepts exist, the constant-gas (CG) and the constant-electrode (CE) configuration[6], i.e., either an oxygen electrode needs to sustain the oxygen reduction reaction (ORR) and OER and a hydrogen electrode for the hydrogen oxidation and the

hydrogen evolution reactions (HOR/HER), or the two electrodes are a HOR/OER and an ORR/HER electrode. However, these different reaction conditions challenge the stability of the catalysts[7] similar as mitigation of cell reversal effects. In PEMWEs, IrO_2 is the most promising anode catalyst for the OER. It demonstrates a slightly lower OER activity in comparison to Ru but that is compensated by the much higher stability against corrosion[8]. However, although Ir(IV)-based catalysts are stable in water, the OER is dominated by the transition of Ir(V) to Ir (III) at lower potentials, which, inevitably leads to iridium dissolution[9]. In addition, PEMWEs may have to be overloaded when coupled with renewable energy sources, which means IrO_2 anode catalyst should maintain stability at least for short intervals at higher potentials, e.g., a potential is above 2.0 V_{RHE}[10]. However, a change in valence of Ir from Ir(V) to Ir (VI) at higher potentials triggers even more significant Ir transient dissolution[9]. All these discussions suggest that the stability of Ir largely limits the long-term durability of PEMWEs and thus inhibiting their entry into a mature market.

In the acidic conditions of a PEM electrochemical device, Pt and Pt-alloys are the state-of-the-art catalysts for the HOR, HER, and ORR[11,12], whereas IrO_2 is the best compromise between activity and stability for the OER[3,13]. In the presented work, we use the concept of nanocomposites combining different nanoparticles on the same catalyst support to study Ir, IrO_2 and Pt dissolution in Ar and air saturated electrolyte. The inert/air atmosphere and Ir as well as IrO_2 were chosen to distinguish dissolution via a reduction of IrO_2 to Ir pathway under hydrogen atmosphere (HOR conditions) or a more direct IrO_2 dissolution pathway.

Results

We start the investigations comparing the metal dissolution of a standard Pt/C and Pt-Ir/C nanocomposite catalysts with a fixed respective metal loading and similar particle size of Pt and

Ir[7]. We apply thin catalyst films in a scanning flow cell with inductively coupled plasma mass spectrometry analytics in the downstream (SFC-ICP-MS measurements)[14]. A mild degradation protocol is chosen, i.e., potential steps between 0.8 and 1.1 V vs. RHE to avoid Ir activation and the formation of an IrO_2 phase. It is seen (Figure 1) that upon establishing potential contact an initial metal dissolution occurs. Interestingly, in the bifunctional Pt-Ir/C catalyst, the dissolution of Ir is substantially more pronounced than the dissolution of Pt. However, starting the degradation protocol, Ir and Pt dissolution occurs at similar rates in the Pt-Ir/C catalyst. A comparison to the standard Pt/C catalyst indicates an inhibition of Pt dissolution by the presence of Ir. That indicates bifunctional Pt-Ir/C catalysts can indeed mitigate the dissolution of the active HOR catalyst (not that in this work we did not study the COR of the support that should be mitigated as well).

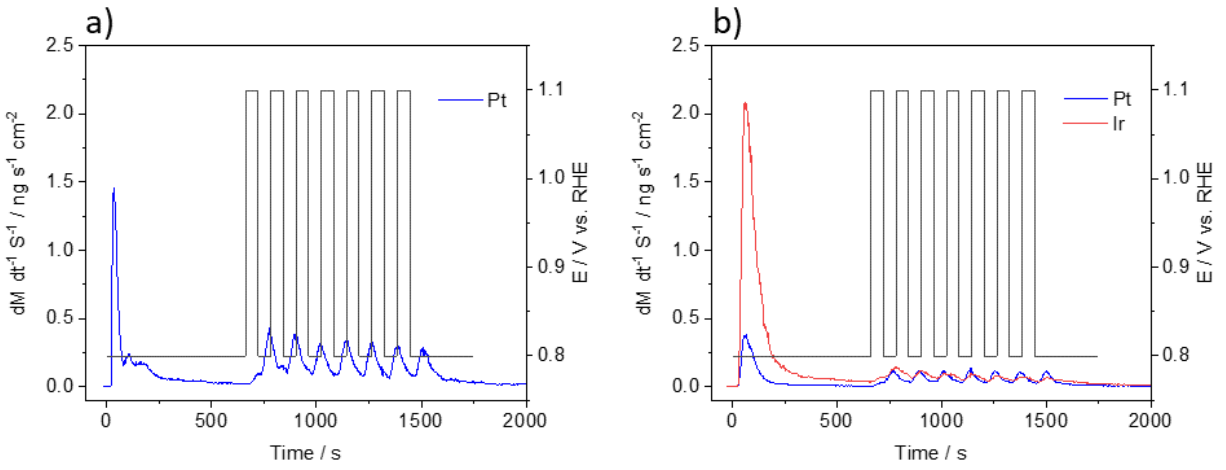

Figure 1. Mass-specific Pt dissolution rates of 20 wt.% Pt/C (a) and the respective metal dissolution rate of Ir (red curve) and Pt (blue curve) of 20 wt.% Pt + 20 wt.% Ir/C (Pt-Ir/C) nanocomposite (b). Applied potential control protocol is plotted at the same time scale, the applied potential steps between 0.8 V_{RHE} and 1.1 V_{RHE} with a rest time of 60 s on each potential, the total treatment is repeated for 7 times.

Nevertheless, our findings are in line with previous studies showing that the introduction of bifunctional or co-catalysts to enhance the OER during cell reversal conditions can lead to substantial performance limitations due to the dissolution of metallic Ir[5]. Dissolved Ir ions can

diffuse through the proton exchange membrane from the anode to the cathode where they lead to a reduction of the ORR activity[5]. In the mechanism proposed by the authors of the previous study[5], the reduction of IrO_2 to Ir in the hydrogen atmosphere of a PEMFC anode plays an essential role for the Ir dissolution. Therefore, we tested if Ir dissolution is limited to metallic Ir formed under highly reductive conditions or if IrO_2 is prone to dissolution as well. For this the Pt-Ir/C catalyst was activated to form a Pt-IrO_2/C nanocomposite active for the OER[7,15,16] before subjecting it to a treatment triggering dissolution. The results presented in Figure 2 indicate that Ir dissolution is not restricted to a reductive hydrogen atmosphere, but that during potential excursions from typical anode potentials, i.e., 0 V vs. RHE, to very high potentials, i.e., 2 V vs. RHE as occurring during cell reversal, a pronounced Ir dissolution takes place even without a reducing gas atmosphere. Independent if Ir or activated IrO_2 is present in the catalyst, our results show that the protection of the Pt anode catalyst and the carbon support during cell reversal by introducing bifunctional catalysts is at the expense of substantial Ir dissolution limiting long-term stability and performance. Therefore, avoiding or minimizing the reduction of IrO_2 to Ir in a hydrogen atmosphere as suggested previously[5] is unlikely to mitigate the IrO_2 stability problem which seems more intrinsic to the applied potential.

However, the results presented in Figure 2 also reveal an interesting selectivity of Ir dissolution. Similar to the contact dissolution but in contrast to the potential steps shown for the case of metallic Ir (Figure 1), applying a degradation protocol to the Pt-IrO_2/C catalyst, the relative amount of dissolved Ir as compared to dissolved Pt is substantially higher. In other words, the potential excursions lead to an almost selective Ir dissolution whereas the Pt nanoparticles remain relatively stable. While this phenomenon does not alleviate the limitations of bifunctional catalysts to mitigate the COR during cell reversal, in the following we focus on developing an electrochemical

pathway for Ir recycling that utilizes the observed selectivity. Ir recycling is an essential process for re-using the Ir containing CCMs of electrolysis cells[17,18] and other electrocatalysts based on Ir[19]. For example, a water electrolysis cell contains a CCM with an IrO_2 anode and a Pt based cathode. In a first step, the precious metals need to be removed from the CCM and thereafter selectively recovered. If the removal from the CCM can be achieved selectively, the selective recovery of Ir and Pt would not be required.

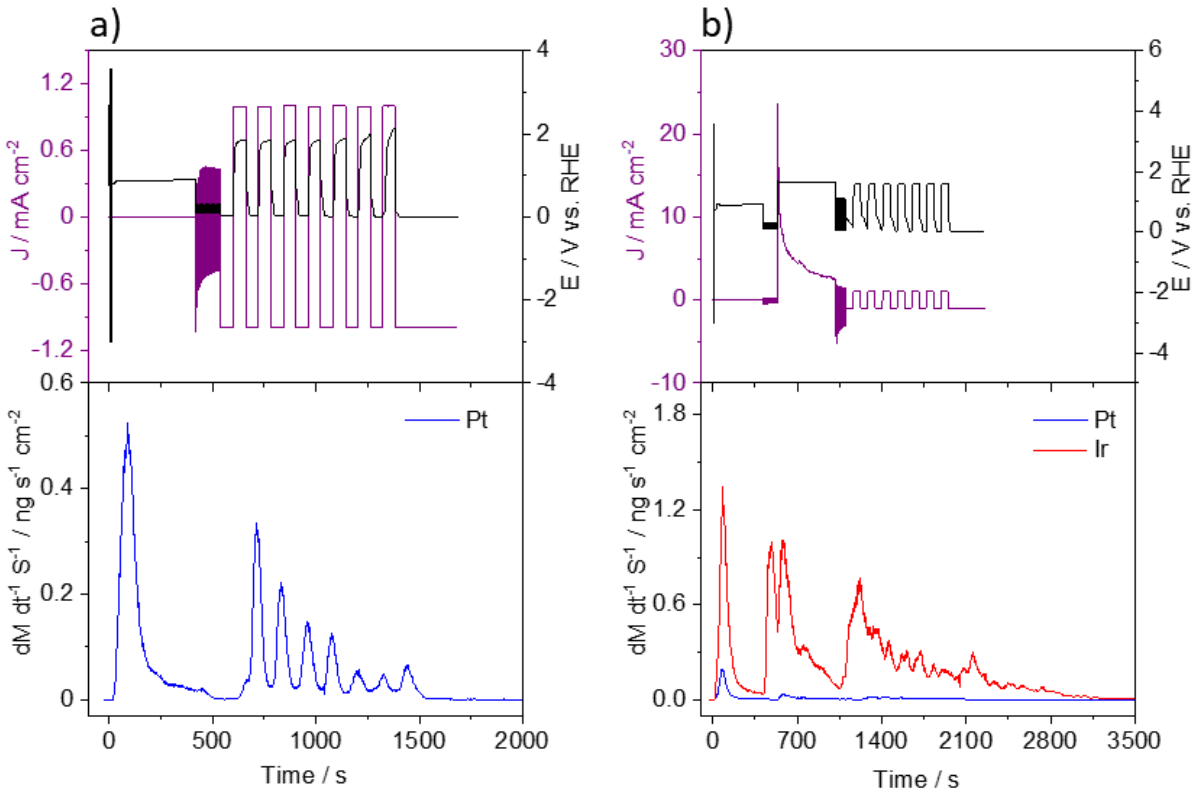

Figure 2. Mass-specific Pt dissolution rate of 20 wt.% Pt/C (a) and Pt (blue curves) and Ir (red curves) dissolution rates of 20 wt.% Pt + 20 wt.% Ir/C (Pt-IrO_2/C) nanocomposites (b). Applied electrochemical measurement protocols and metal dissolution rates are plotted at the same time scale. The measurements are started with catalyst surface cleaning as indicated at ~400 s, potential cycling between 0.1 V_{RHE} and 0.3 V_{RHE} at a scan rate of 100 mV s^{-1} for 30 cycles is applied as displayed by the black curves in both figures, followed by Ir activation of Pt-IrO_2/C nanocomposite by holding potential at 1.6 V_{RHE} for 8 min and subsequently sweeping potential between 0.05 V_{RHE}

and 1.1 V_{RHE} at a scan rate of 500 mV s^{-1} for 20 cycles to stabilize the catalyst. Afterwards, the measurement protocols are switched to current control mode with current stepping between -1 mA cm^{-2} and 1 mA cm^{-2}, for each current the holding time is 60 s and 7 repeats in total, as shown from the purple curves in both figures.

We therefore investigated if the observed selectivity in Ir dissolution from the Pt-IrO_2/C catalyst can be observed also for Pt-Ir/C catalyst. Changing the upper potential limit from 1.1 (shown in Figure 1b) to 0.9 V vs RHE to avoid the formation of Pt-oxide, which is prone to dissolution during its reduction[20,21], does not improve the selectivity of Ir dissolution substantially, see Figure 3a. However, when changing the lower limit in the degradation protocol from 0.8 to 0.05 V vs RHE has a significant influence on the Ir dissolution. The highest selectivity in Ir dissolution could be observed in potential jumps between 0.9 to 0.05 V vs RHE. The upper potential limit avoids the formation of Pt-oxide, while at such lower potential limit, the selective Ir dissolution process is almost continuous as demonstrated for the extended hold time (900 s) shown in Figure 3b.

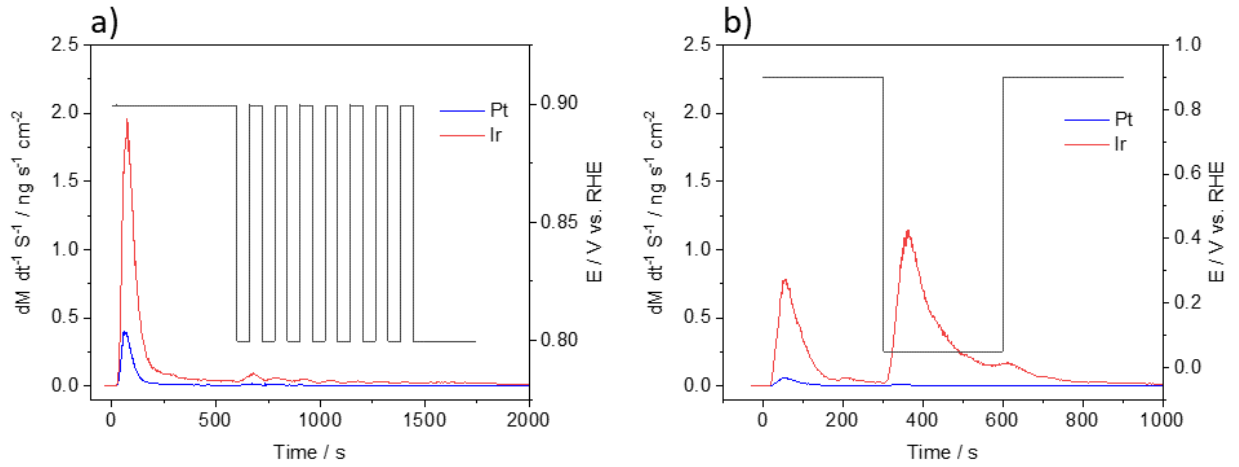

Figure 3. Mass-specific metal dissolution rate of Ir (red curve) and Pt (blue curve) of 20 wt.% Pt + 20 wt.% Ir/C (Pt-Ir/C) nanocomposite exposed to different potential control protocols. (a) the applied potential steps between 0.9 V_{RHE} and 0.8 V_{RHE} with 60 s of each holding time, the treatment is lasted for 7 repeats and (b) the applied potential steps between 0.9 V_{RHE} and 0.05 V_{RHE}, on each applied potential the rest time is 300 s.

For an industrial recycling process, the use of an electrochemical three-electrode setup, as required in the SFC-ICP-MS measurements is not favorable. It would be cost intensive and limit its applicability. Two electrode processes are considerably less complex and do not require a potentiostat but a simple power source (current or potential controlled). In the following, we therefore optimized the electrochemical protocol for selective Ir dissolution further by introducing a current control (galvanostatic) protocol instead of the typically applied potential protocol. In the summary of Figure 4 it is demonstrated that with the help of a protocol switching the electrode current between + 1 mA cm^{-2} and -1 mA cm^{-2} it is possible to almost selectively dissolve all Ir (96 %) from a Pt-IrO_2/C catalyst. Such a current-based protocol has furthermore the advantage of being feasible in a simple two electrode configuration instead of a three-electrode configuration that requires a potentiostat.

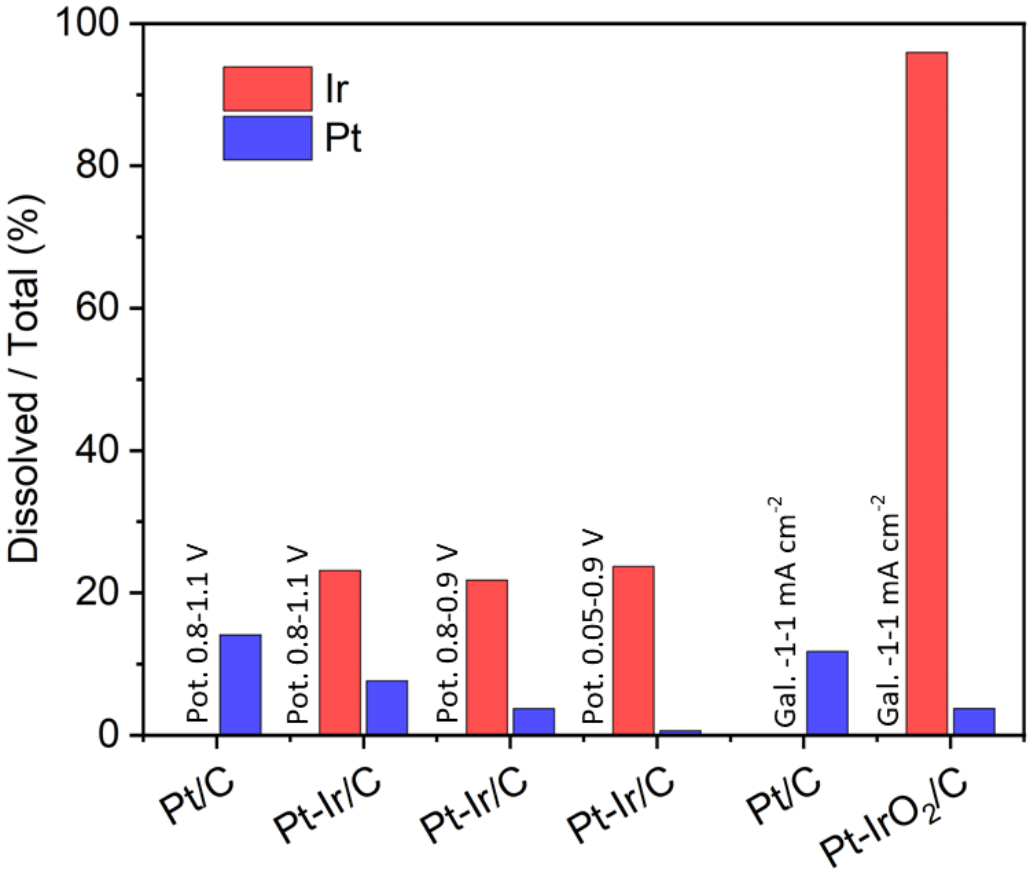

Figure 4. The summary of total metal dissolution rates during measurements with different treatment protocols. Pt-Ir/C and Pt-IrO_2/C are used to differentiate the metallic and the activated Ir in the nanocomposites, respectively. Pt and Ir are introduced with a same weight ratio (20 wt.%, respectively) to constitute the nanocomposites.

Certainly, a commercial protocol for the recycling of Ir from used water electrolysis CCMs would require further optimization of the parameters. Here we settle with a simple proof of concept from Pt-IrO_2/C nanocomposite catalyst films deposited onto carbon gas diffusion layers (GDLs) at high metal loading (200 $\mu g_{Pt/Ir}$ cm^{-2}) as compared to the SFC-ICP-MS measurements, see Table 1. The measurements were performed in a simple jacketed H-cell type electrochemical cell and the dissolution determined by ICP-MS analysis of the bulk electrolyte. Scanning electron microscopy coupled to energy dispersive X-ray spectroscopy was used to determine the selectivity of the Ir dissolution.

Table1. The calculated Ir / Pt weight ratio via SEM-EDX analysis before and after treatment, the change in Ir / Pt weight ratio and the dissolved Pt and Ir amount determined by ICP-MS during treatment of 20 wt.% Pt + 20 wt.% Ir/C (Pt-IrO_2/C). The averaged composition values in weight fraction are calculated from five different areas of catalyst layers (200 $\mu g_{Pt/Ir}$ cm^{-2}), the calculation of Ir / Pt ratio change is based on the averaged Wt. Ir / Pt values before and after treatment. All measurements are performed under 40 °C in air, and in a jacketed H-cell type electrochemical cell. The error is the standard deviation of five independent measurements. 5 ml of electrolyte after treatment is taken out and diluted to an ideal concentration for ICP-MS measurements. BOT: before test, EOT: end of test.

	BOT Wt. Ir/Pt	EOT Wt. Ir/Pt	Wt. Ir/Pt change (%)	Pt in electrolyte (µg)	Ir in electrolyte (µg)
1 M H_2SO_4	1.14 ± 0.07	0.44 ± 0.11	61.4	0.570	2.025
	1.15 ± 0.05	0.56 ± 0.10	51.3	-	-
1 M $HClO_4$	1.16 ± 0.09	0.93 ± 0.06	19.8	0.105	0.255
	1.10 ± 0.08	0.86 ± 0.04	21.8	-	-
1 M HNO_3	1.15 ± 0.18	0.63 ± 0.07	45.2	-	-
	1.16 ± 0.12	0.58 ± 0.02	50.0	0.555	1.755
1 M H_2SO_4 + 0.5 M CH_3OH	1.19 ± 0.03	0.36 ± 0.03	69.7	-	-
	1.20 ± 0.06	0.42 ± 0.03	65.0	-	-
1 M H_2SO_4 + 0.1 mM HCl	0.87 ± 0.04	0.49 ± 0.05	43.7	0.525	1.545
1 M H_2SO_4 + 0.01 mM HCl	0.87 ± 0.04	0.47 ± 0.02	46.0	0.520	1.800

It is seen that the chosen electrolyte has a pronounced effect on the selectivity of Ir dissolution. Selective Ir dissolution occurs in all tested electrolyte media, however, a H_2SO_4-based aqueous electrolyte shows best results. Adding trace amounts of Cl^- by comparison decreases the selectively.

Methods

Synthesis of supported metallic Pt and nanocomposite. The synthesis methods for supported catalysts are detailed in previous studies[7,22], which includes the microwave-assisted preparation of metal (Pt and Ir) NPs and the post-immobilization of metal NPs onto carbon support (Vulcan XC72R). Pure Pt NPs solution, or Pt and Ir NPs solution were simultaneously added to carbon suspension to differentiate the obtained catalyst was supported monometallic or nanocomposite catalysts. The content of Pt NPs was kept 20% in weight throughout the prepared supported catalysts.

Transmission electron microscopy (TEM). TEM was used for physical characterization of the as-prepared catalysts. A Jeol 2100 transmission electron microscope operated at 200 kV was used for TEM analysis. The catalyst dispersion diluted in ethanol was dropped on carbon coated copper TEM grids (Quantifoil) for TEM sample preparation. Images were recorded at least three randomly selected areas. The representative TEM micrographs of the studied catalysts are displayed in Figure 5.

Small angle X-ray scattering (SAXS). The size distributions of the studied catalysts were evaluated by SAXS and shhown in Figure 5. SAXS measurements and data analysis were performed as detailed in the previous study[23]. The scattering data are fitted to the expression:

$$I(q) = A \cdot q^{-n} + C \cdot \int P(q,R)V(R)D(R)dR$$

Where $A \cdot q^{-n}$ is the power law in which A and n are free parameters, C is a scaling constant, P is a sphere form factor, V is the particle volume, and D the log-normal size distribution, and the scattering vector $q = 4\pi \cdot \sin(\theta)/\lambda$, The sphere form factor is expressed as:

$$P_s(q,R) = \left(3\frac{\sin(qR) - qR\cos(qR)}{(qR)^3}\right)^2$$

and the log-normal distribution is expressed as:

$$D(R) = \frac{1}{R\sigma\sqrt{2\pi}}e^{\left(\frac{-\left[\ln\left(\frac{R}{R_0}\right)\right]^2}{2\sigma^2}\right)}$$

The fitting was conducted with a home written MATLAB code. The values obtained for free parameters in the model are listed in Table 2.

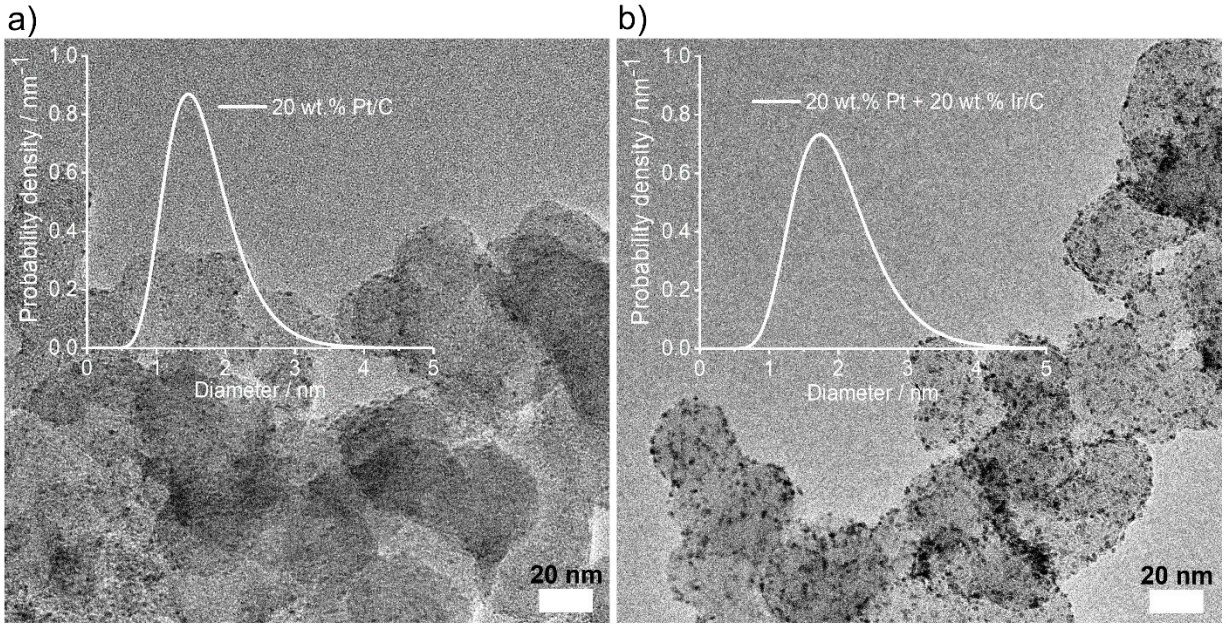

Figure 5. TEM micrographs and size distributions of the studied 20 wt.% Pt/C (a) and 20 wt.% Pt + 20 wt.% Ir/C (Pt-Ir/C) (b). The SAXS data of 20 wt.% Pt were already reported in previous study[23] and shown here compared to the 20 wt.% Pt + 20 wt.% Ir/C (Pt-Ir/C).

Table 2. Parameters of SAXS data fits and size analysis.

Samples	Power law		1st population			2nd population			Size and distribution							
Parameters	Ax 10^6	n	R_1 (Å)	σ_1	C_1	R_2 (Å)	σ_2	C_2	D_1	$\sigma_{1'}$	D_2	$\sigma_{2'}$	Average Diameter D (nm)	Standard Deviation of D σ (nm)	Volume fraction1	Volume fraction2
20 wt.% Pt/C	180	3.25	8.0	0.3	0.008				1.7	0.5			1.7	0.5	1	0
20 wt.% Pt + 20 wt.% Ir/C (Pt-Ir/C)	140	3.00	9.5	0.3	0.007	1.0	1.0	0.000	2.0	0.6			2.0	0.6	1	0

Scanning electron microscope (SEM)-based energy dispersive X-ray spectroscopy (EDX). The compositions of nanocomposites before and after treatments were evaluated with SEM-EDX. An equipment of Zeiss Gemini 450 SEM coupled with an Oxford Instruments UltimMax 65 EDX detector was used and a voltage of 25 kV was applied for analysis. Before treatment, a Ø 3 mm of pre-filtered catalyst layer was punched and fixed on top of a sticky carbon tape, which was placed on the metallic sample holder. The catalyst layer after composition analysis served as working electrode and used for electrochemical treatment. Afterwards, the Ø 3 mm catalyst layer was transferred again to SEM-EDX to determine the change of relative Pt / Ir weight ratio during electrochemical treatment. Five independent spots of a catalyst layer were selected for analysis for each studied sample.

Inductively coupled plasma mass spectrometry (ICP-MS). The contents of the dissolved Pt and Ir in electrolyte after jacketed H-cell-based electrochemical treatment were evaluated with ICP-MS (NexION 2000 ICP-MS). The ICP-MS was equipped with a cyclonic spray chamber and a PFA-nebulizer. 5 mL of electrolyte in cell after electrochemical treatment was taken and diluted with milli-Q water to an ideal concentration for further ICP-MS analysis.

Preparation of working electrode (WE). The catalyst layer (nominal loading of 200 $\mu g_{Pt/Ir}$ cm^{-2}_{geo}) was fabricated via vacuum filtration, which was detailed elsewhere[24]. Afterwards, a

rectangular GDL (1 cm × 3 cm, with MPL on the top) was applied for WE fixing, in which, a Ø 3 mm of the pre-filtered catalyst layer was punched and placed on top of the rectangular GDL, which was further fixed with Teflon tape wrapped surrounding to be sure the Ø 3 mm WE was stabilized and exposed to electrochemical treatments.

Electrochemical treatments. All electrochemical treatments based on the more realistic catalyst loading (200 $\mu g_{Pt/Ir}$ cm^{-2}_{geo}) were performed in a three-electrode system connected with a potentiostat (ECi-200, Nordic Electrochemistry ApS), which was controlled by a computer. A jacketed H-cell type electrochemical cell with a hollow outer layer for water circulation for temperature controlling, was used for electrochemical treatments. A carbon rod was used as counter electrode (CE), the WE was detailed in the last section. All potentials were determined with respect to a reversible hydrogen electrode (RHE), which was prepared prior to each measurement. All electrochemical treatments were performed in air under 40 °C, which was controlled by the circulated water in the outer layer of jacketed cell, ten more minutes was waited after the set temperature was reached, to confirm the temperature of electrolyte in the inner space of jacket cell was correct. Different electrolyte (1 M H_2SO_4, 1 M $HClO_4$, 1 M HNO_3, 1 M H_2SO_4 + 0.5 M CH_3OH, 1 M H_2SO_4 + 0.1 mM HCl and 1 M H_2SO_4 + 0.01 mM HCl) was used for electrochemical treatments. The following procedures were implemented sequentially in treatments: catalyst surface cleaning, catalyst activation (only for nanocomposite), and degradation. For supported monometallic Pt/C, continuously swept potential between 0.05 V_{RHE} and 1.10 V_{RHE} at a scan rate of 500 mV s^{-1} served as a typical protocol for catalyst surface cleaning, ~30 repeats were performed to obtain a stable cyclic voltammograms. For supported Pt-Ir/C nanocomposite, potentials were swept in a limited window of 0.10 V_{RHE} - 0.30 V_{RHE} to avoid Ir to be pre-oxidized, a scanning speed of 100 mV s^{-1} for ~20 cycles was employed for catalyst surface cleaning. The

solution resistance was compensated to between 2 and 3 Ω via an analog positive feedback scheme during catalyst surface cleaning. An additional catalyst activation procedure by holding potential at 1.60 V_{RHE} for 8 minutes was needed for Pt-Ir/C nanocomposites, during which the metallic Ir was irreversibly oxidized to IrO_2. Afterwards, sweeping potential between 0.05 V_{RHE} and 1.10 V_{RHE} at a scan rate of 500 mV s^{-1} to reach a stable cyclic voltammograms. Concerning degradation test, a current control mode was employed, in which, the applied current was stepped between -1 mA and 1 mA with a rest time of 1 second at each current, the total treatment lasted for 1 hour. After electrochemical treatments, 5 ml of electrolyte was preserved for ICP-MS analysis.

References

(1) Han, B.; Carlton, C. E.; Kongkanand, A.; Kukreja, R. S.; Theobald, B. R.; Gan, L.; O'Malley, R.; Strasser, P.; Wagner, F. T.; Shao-Horn, Y. Record Activity and Stability of Dealloyed Bimetallic Catalysts for Proton Exchange Membrane Fuel Cells. *Energy and Environmental Science* **2015**, *8* (1), 258–266. https://doi.org/10.1039/c4ee02144d.

(2) Sun, Y.; Polani, S.; Luo, F.; Ott, S.; Strasser, P.; Dionigi, F. Advancements in Cathode Catalyst and Cathode Layer Design for Proton Exchange Membrane Fuel Cells. *Nature Communications* **2021**, *12* (1), 1–14. https://doi.org/10.1038/s41467-021-25911-x.

(3) Chen, L.-W.; Liang, H.-W. Ir-Based Bifunctional Electrocatalysts for Overall Water Splitting. *Catalysis Science & Technology* **2021**, *11* (14), 4673–4689. https://doi.org/10.1039/D1CY00650A.

(4) She, L.; Zhao, G.; Ma, T.; Chen, J.; Sun, W.; Pan, H. On the Durability of Iridium-Based Electrocatalysts toward the Oxygen Evolution Reaction under Acid Environment. *Advanced Functional Materials*. John Wiley and Sons Inc January 1, 2022. https://doi.org/10.1002/adfm.202108465.

(5) Fathi Tovini, M.; Damjanovic, A. M.; El-Sayed, H. A.; Speder, J.; Eickes, C.; Suchsland, J.-P.; Ghielmi, A.; Gasteiger, H. A. Degradation Mechanism of an IrO2 Anode Co-Catalyst for Cell Voltage Reversal Mitigation under Transient Operation Conditions of a PEM Fuel Cell. *Journal of The Electrochemical Society* **2021**, *168* (6), 064521. https://doi.org/10.1149/1945-7111/ac0d39.

(6) Regmi, Y. N.; Peng, X.; Fornaciari, J. C.; Wei, M.; Myers, D. J.; Weber, A. Z.; Danilovic, N. A Low Temperature Unitized Regenerative Fuel Cell Realizing 60% Round Trip Efficiency and 10 000 Cycles of Durability for Energy Storage Applications. *Energy & Environmental Science* **2020**, *13* (7), 2096–2105. https://doi.org/10.1039/C9EE03626A.

(7) Du, J.; Quinson, J.; Zhang, D.; Bizzotto, F.; Zana, A.; Arenz, M. Bifunctional Pt-IrO2Catalysts for the Oxygen Evolution and Oxygen Reduction Reactions: Alloy Nanoparticles versus Nanocomposite Catalysts. *ACS Catalysis* **2021**, *11* (2), 820–828. https://doi.org/10.1021/acscatal.0c03867.

(8) McCrory, C. C. L.; Jung, S.; Ferrer, I. M.; Chatman, S. M.; Peters, J. C.; Jaramillo, T. F. Benchmarking Hydrogen Evolving Reaction and Oxygen Evolving Reaction Electrocatalysts for Solar Water Splitting Devices. *J Am Chem Soc* **2015**, *137* (13), 4347–4357. https://doi.org/10.1021/ja510442p.

(9) Kasian, O.; Grote, J.-P.; Geiger, S.; Cherevko, S.; Mayrhofer, K. J. J. The Common Intermediates of Oxygen Evolution and Dissolution Reactions during Water Electrolysis on Iridium. *Angewandte Chemie International Edition* **2018**, *57* (9), 2488–2491. https://doi.org/10.1002/anie.201709652.

(10) Gago, A. S.; Bürkle, J.; Lettenmeier, P.; Morawietz, T.; Handl, M.; Hiesgen, R.; Burggraf, F.; Valles Beltran, P. A.; Friedrich, K. A. Degradation of Proton Exchange Membrane (PEM) Electrolysis: The Influence of Current Density. *ECS Transactions* **2018**, *86* (13), 695–700. https://doi.org/10.1149/08613.0695ecst.

(11) Sheng, W.; Zhuang, Z.; Gao, M.; Zheng, J.; Chen, J. G.; Yan, Y. Correlating Hydrogen Oxidation and Evolution Activity on Platinum at Different PH with Measured Hydrogen Binding Energy. *Nature Communications* **2015**, *6*. https://doi.org/10.1038/ncomms6848.

(12) Pu, Z.; Cheng, R.; Zhao, J.; Hu, Z.; Li, C.; Li, W.; Wang, P.; Amiinu, I. S.; Wang, Z.; Min Wang; Chen, D.; Mu, S. Anion-Modulated Platinum for High-Performance Multifunctional Electrocatalysis toward HER, HOR, and ORR. *iScience* **2020**, *23* (12), 101793. https://doi.org/10.1016/j.isci.2020.101793.

(13) Reier, T.; Oezaslan, M.; Strasser, P. Electrocatalytic Oxygen Evolution Reaction (OER) on Ru, Ir, and Pt Catalysts: A Comparative Study of Nanoparticles and Bulk Materials. *ACS Catalysis* **2012**, *2* (8), 1765–1772. https://doi.org/10.1021/cs3003098.

(14) Shkirskiy, V.; Speck, F. D.; Kulyk, N.; Cherevko, S. On the Time Resolution of Electrochemical Scanning Flow Cell Coupled to Downstream Analysis. *Journal of The Electrochemical Society* **2019**, *166* (16), H866–H870. https://doi.org/10.1149/2.1401915jes.

(15) Bizzotto, F.; Quinson, J.; Schröder, J.; Zana, A.; Arenz, M. Surfactant-Free Colloidal Strategies for Highly Dispersed and Active Supported IrO2 Catalysts: Synthesis and Performance Evaluation for the Oxygen Evolution Reaction. *Journal of Catalysis* **2021**. https://doi.org/10.1016/J.JCAT.2021.07.004.

(16) Bizzotto, F.; Quinson, J.; Zana, A.; Kirkensgaard, J. J. K.; Dworzak, A.; Oezaslan, M.; Arenz, M. Ir Nanoparticles with Ultrahigh Dispersion as Oxygen Evolution Reaction (OER) Catalysts: Synthesis and Activity Benchmarking. *Catalysis Science and Technology* **2019**, *9* (22), 6345–6356. https://doi.org/10.1039/c9cy01728c.

(17) Minke, C.; Suermann, M.; Bensmann, B.; Hanke-Rauschenbach, R. Is Iridium Demand a Potential Bottleneck in the Realization of Large-Scale PEM Water Electrolysis? *International Journal of Hydrogen Energy* **2021**, *46* (46), 23581–23590. https://doi.org/10.1016/j.ijhydene.2021.04.174.

(18) Carmo, M.; Keeley, G. P.; Holtz, D.; Grube, T.; Robinius, M.; Müller, M.; Stolten, D. PEM Water Electrolysis: Innovative Approaches towards Catalyst Separation, Recovery and Recycling. *International Journal of Hydrogen Energy* **2019**, *44* (7), 3450–3455. https://doi.org/10.1016/j.ijhydene.2018.12.030.

(19) Huang, B.; Zhao, Y. Iridium-based Electrocatalysts toward Sustainable Energy Conversion. *EcoMat* **2022**, *4* (2). https://doi.org/10.1002/eom2.12176.

(20) Topalov, A. A.; Katsounaros, I.; Auinger, M.; Cherevko, S.; Meier, J. C.; Klemm, S. O.; Mayrhofer, K. J. J. Dissolution of Platinum: Limits for the Deployment of Electrochemical Energy Conversion? *Angewandte Chemie - International Edition* **2012**, *51* (50), 12613–12615. https://doi.org/10.1002/anie.201207256.

(21) Cherevko, S.; Kulyk, N.; Mayrhofer, K. J. J. Durability of Platinum-Based Fuel Cell Electrocatalysts: Dissolution of Bulk and Nanoscale Platinum. *Nano Energy* **2016**, *29*, 275–298. https://doi.org/10.1016/j.nanoen.2016.03.005.

(22) Quinson, J.; Inaba, M.; Neumann, S.; Swane, A. A.; Bucher, J.; Simonsen, S. B.; Theil Kuhn, L.; Kirkensgaard, J. J. K.; Jensen, K. M.; Oezaslan, M.; Kunz, S.; Arenz, M. Investigating Particle Size Effects in Catalysis by Applying a Size-Controlled and Surfactant-Free Synthesis of Colloidal Nanoparticles in Alkaline Ethylene Glycol: Case Study of the Oxygen Reduction Reaction on Pt. *ACS Catalysis* **2018**, *8* (7), 6627–6635. https://doi.org/10.1021/acscatal.8b00694.

(23) Du, J.; Quinson, J.; Zana, A.; Arenz, M. Elucidating Pt-Based Nanocomposite Catalysts for the Oxygen Reduction Reaction in Rotating Disk Electrode and Gas Diffusion Electrode Measurements. *ACS Catalysis* **2021**, *11* (12), 7584–7594. https://doi.org/10.1021/acscatal.1c01496.

(24) Yarlagadda, V.; McKinney, S. E.; Keary, C. L.; Thompson, L.; Zulevi, B.; Kongkanand, A. Preparation of PEMFC Electrodes from Milligram-Amounts of Catalyst Powder. *Journal of The Electrochemical Society* **2017**, *164* (7), F845–F849. https://doi.org/10.1149/2.1461707jes.

Declaration of consent

on the basis of Article 18 of the PromR Phil.-nat. 19

Name/First Name:

Registration Number:

Study program:

Bachelor ☐ Master ☐ Dissertation ☐

Title of the thesis:

Supervisor:

I declare herewith that this thesis is my own work and that I have not used any sources other than those stated. I have indicated the adoption of quotations as well as thoughts taken from other authors as such in the thesis. I am aware that the Senate pursuant to Article 36 paragraph 1 litera r of the University Act of September 5th, 1996 and Article 69 of the University Statute of June 7th, 2011 is authorized to revoke the doctoral degree awarded on the basis of this thesis.
For the purposes of evaluation and verification of compliance with the declaration of originality and the regulations governing plagiarism, I hereby grant the University of Bern the right to process my personal data and to perform the acts of use this requires, in particular, to reproduce the written thesis and to store it permanently in a database, and to use said database, or to make said database available, to enable comparison with theses submitted by others.

Place/Date

Signature Jia Du